Biocatalytic Metal Nanoparticle Synthesis & Investigation of Catalytic Properties of Metal Nanoparticle-Enzyme Hybrids



Lucy Beatrice Faed Browne

University of Oxford

St Peter's College

Trinity Term 2024

A Thesis submitted to the Board of the Faculty of Physical Sciences, for the degree of

Doctor of Philosophy, University of Oxford

Biocatalytic Metal Nanoparticle Synthesis & Investigation of Catalytic Properties of Metal Nanoparticle-Enzyme Hybrids

Lucy Beatrice Faed Browne, St Peter's College, University of Oxford

A Thesis submitted for the degree of Doctor of Philosophy, Trinity Term 2024

Biocatalysis and heterogeneous metal catalysis, traditionally may be thought of as very opposing fields. However recent developments in these areas have shown how combining these together can bring enhanced catalytic properties. There are now several examples of using biocatalysts and heterogeneous metal catalysts together in one-pot to provide a cascade reaction, where intermediate products do not need to be isolated and purified before the next desired step; thus, making improvements in process sustainability by cutting down the amount of waste produced. Despite homogeneous metal complexes often being found to inactivate enzymes, metals in the form of small nanoparticles (NPs) have been shown in many systems to be compatible with enzymes, therefore there is a huge area of unexplored reaction space involving both metal NPs and enzymes which may bring about very useful reaction pathways. Already demonstrated are examples where metal NPs can provide the electron source, by supply of a specific reduced "cofactor" molecule or by generating H_2O_2, required by the enzyme to carry out its selective transformation on an organic molecule. Combining protein structures and metals has also been carried out by either inserting artificial metal centres into proteins or by attaching metal NPs and enzymes together, often in the presence of a non-reactive support material, to make chemo-bio hybrids.

To synthesise metal NPs, often very harsh conditions and/or toxic reagents are used. Therefore, alternative methods employing a bio-based material such as a plant-extract have been widely investigated, with numerous examples showing their ease-of-application. The use of a living organism (bacteria, fungi) has also been explored for the mild biosynthesis of metal

NPs. Alternatively, use of an isolated enzyme has been shown to give some advantages over the plant or whole cell approach, namely due to the high uniformity of the size and shapes of the NPs which form, while still using very mild conditions for the metal reduction.

Thus, in this thesis the synthesis of metal NPs by isolated enzymes is explored and the reactivity of the resulting metal NPs and enzyme hybrids is investigated. Successful well-controlled NP formation was demonstrated by supplying an enzyme (an NAD^+ reductase) with its reduced cofactor, which it oxidises while reducing Au^{3+} salts, thereby forming Au NPs (*Chapter 3*). This was extended to make Au core-Pt shell NPs and the resulting metal NP-enzyme hybrids were tested for NAD^+ reduction under H_2, where Pt oxidises H_2 and the enzyme uses those electrons generated to selectively reduce NAD^+. Without the metal NP, the enzyme has no activity, and without the enzyme, Pt metal alone unselectively reduces NAD^+ to a mixture of non-biologically-relevant products. Therefore, this demonstrated the synergistic behaviour of both components of the biohybrid.

In a separate study (*Chapter 5*), another type of enzyme (a hydrogenase) was also investigated for Au NP synthesis, using H_2 as the electron source, therefore providing a NP synthesis with no carbon-containing sacrificial reductant. The resulting biohybrids were then found to give increased reaction rates compared to the enzyme alone, therefore demonstrating an electron-transfer rate-enhancement effect due to contact between the enzyme and NP.

This system was also investigated for synthesising a heterogeneous supported hybrid catalyst (*Chapter 6*) to extend the potential scope of application of these hybrids in biocatalytic processes.

Another topic explored was the potential to use a significantly cheaper cofactor, riboflavin, in place of the native flavin cofactors, FMN and FAD, for applications in biocatalysis (*Chapter 4*). The reduction of riboflavin was tested using an efficient H_2-driven process utilising the natural H_2-oxidising activity of a hydrogenase enzyme and subsequently a recycling system was demonstrated for supplying reduced riboflavin to an enzyme (an ene-reductase) to allow for

the chemically useful transformation of a selective alkene to alkane reduction, under mild conditions.

Overall, this thesis demonstrates scope for a new class of self-assembled metal NP enzyme hybrid catalysts, whereby supplying the enzyme with its native reduced substrate (or cheaper, synthetic analogue) allowed it to control the synthesis of metal NPs. The resulting hybrid catalysts showcased advantageous catalytic properties, by combining both the enzyme and metal NP reactivities, thus offering promise for potential further catalytic applications.

Acknowledgements

Most importantly I would like to sincerely thank my supervisor, Kylie Vincent. I am very grateful to you for giving me the opportunity to carry out this DPhil at the University of Oxford and to work in this exciting area of research. Thanks for all the helpful project advice and for encouraging me to present my work in posters and talks at various conferences.

I thank all the members of the Vincent group, of which there are too many to individually mention but I sincerely thank all those who have helped me in the lab or have provided their good nature, contributing to a wonderful place to work. There are some members who deserve a notable mention; firstly, Tim Sudmeier who I owe a considerably sized thanks to – for giving me guidance and day-to-day support at the beginning of the project, which I would have been lost without. Your unwavering patience and never-ending ideas are truly inspiring! To Maya Landis, I thank you for your friendship over the years, for the coffee breaks and for your calming presence always bringing me joy. I also thank you for always being willing to help me with the microscopy analysis of my nanoparticle samples. For the success of this project, I also am indebted to Steve Carr and Miguel Ramirez for their help in preparing the enzymes, both of whose intelligence and dedication is inspiring. I also thank Hazel Rycroft for her hard work and patience during her master's project which led to some of the results I have been able to include in this thesis.

Thanks also to the microscopy experts, Christopher Allen, David Hopkinson and Michal Klosowski, who have helped me during this project, without which I would not have been able to obtain some of the nanoparticle analysis included in this thesis. I also thank Caroline Paul for kindly supplying the artificial cofactors I tested in this thesis.

I would like to thank my family, for the encouragement and support over the years. You have all believed in me and gotten me to where I am today. Lastly, but not least, I am very thankful to James, for supporting me throughout this journey and for always being able to make me laugh, even when I don't feel like laughing.

Abbreviations

a.u.	absorbance units
AmNAH	1-carbamoylmethyl-1,4-dihydronicotinamide
BNAH	1-benzyl-1,4-dihydronicotinamide
CV	cyclic voltammetry
Da	Dalton
DLS	dynamic light scattering
DMSO	dimethyl sulfoxide
e^-	electron
E. coli	*Escherichia coli*
e.e.	enantiomeric excess
EDX	energy dispersive X-ray
FAD	flavin adenine dinucleotide
Fe-S	iron-sulfur
FMN	flavin mononucleotide
HR-STEM	high resolution scanning transmission electron microscopy
Hyd1	Hydrogenase 1
KPi	potassium phosphate buffer
NAD^+	nicotinamide adenine dinucleotide
NADH	1,4-dihydronicotinamide adenine dinucleotide
NaPi	sodium phosphate buffer

NMR	nuclear magnetic resonance
NP	nanoparticle
NRase	NAD^+ Reductase
PDB	Protein Data Bank
PGE	pyrolytic graphite edge
ppm	parts per million
RF	riboflavin
rpm	rotations per minute
SCE	saturated calomel electrode
SHE	Standard hydrogen electrode
SPR	surface plasmon resonance
TEM	transmission electron microscopy
TN	turnover number
TOF	turnover frequency
TTN	total turnover number
UV-vis	Ultraviolet-visible
V	Volts
XRD	X-ray diffraction
λ_{max}	wavelength of maximum absorbance

Table of Contents

Chapter 1. Introduction 1

1.1. Metal NP Properties and Applications 2

1.1.1. Introduction to Metal NPs 2

1.1.2. Metal NPs in Biomedical Applications 3

1.1.3. Metal NPs in Electronic Applications 5

1.1.4. Metal NPs in Catalysis Applications 6

1.2. Metal NP Synthesis Procedures 11

1.2.1. Overview of Metal NP Synthesis 11

1.2.2. Chemical Methods 12

1.2.3. Biosynthesis Methods 15

1.2.4. Synthesis of Core-Shell NPs 18

1.3. Hydrogenase and NAD^+ Reductase Enzymes 19

1.3.1. Introduction to Hydrogenase 19

1.3.2. Introduction to NAD^+ Reductase 23

1.4. Combining Metals with Enzymes 26

1.4.1. Linking Enzymes to Gold Surface for Electrochemical Studies 26

1.4.2. Enzymes and Metals in Biocatalysis 27

1.5. Cofactor Recycling for Biocatalysis 29

1.6. Aims of This Project 35

1.7. This Thesis Explained 37

1.8. References 39

Chapter 2. Theory of Characterisation Methods 45

2.1. Techniques Core to This Thesis Work 46

2.1.1. UV-vis 46

2.1.1.1. Theory of UV-vis Spectroscopy 46

2.1.1.2. UV-vis Spectroscopy Applied to Cofactors 47

2.1.1.3. UV-vis Spectroscopy Applied to Metal NPs 49

2.1.1.4. UV-vis Procedure for Metal NP Analysis 50

2.1.1.5. UV-vis Procedure for Enzyme Kinetics 51

2.1.2. CV 52

2.1.2.1. Theory of CV 52

2.1.2.2. CV Procedure for Metal NP Analysis 54

2.1.2.3. Procedure for Determining Reduction Potential of Organic Compound 55

2.1.2.4. CV Procedure for Enzyme Activity Analysis 56

2.1.3. DLS 56

2.1.3.1. Theory of DLS 56

2.1.3.2. DLS Procedure for Metal NP Analysis 57

2.1.4. Zeta Potential 58

2.1.4.1. Theory of Zeta Potential 58

2.1.4.2. Zeta Potential Procedure for Metal NP Analysis 59

2.2. Additional Techniques Used by Collaborators 59

2.2.1. TEM 59

2.2.1.1. Principle of TEM 59

2.2.1.2. TEM Sample Preparation 60

2.2.2. EDX 60

2.2.2.1. Principle of EDX 60

2.2.2.2. EDX Sample Preparation 63

2.2.3. XRD 63

2.2.3.1. Principle of XRD 63

2.2.3.2. XRD Sample Preparation 65

2.2.4. XPS 65

2.2.4.1. Principle of XPS 65

2.2.4.2. XPS Sample Preparation 66

2.3. Summary of Characterisation Techniques for Metal NPs 66

2.4. References 68

Chapter 3. Biocatalytic Synthesis of Metal Nanoparticles, using *NAD^+ Reductase*, and Application of Resulting Biohybrids 70

3.1. Introduction 71

3.2. Paper 1: Controlled Biocatalytic Synthesis of a Metal Nanoparticle-Enzyme Hybrid: Demonstration for Catalytic H_2-driven NADH Recycling 71

Chapter 4. H_2-Driven Riboflavin Recycling 108

4.1. Introduction 109

4.2. Paper 2: Riboflavin with H_2-Driven or Electrochemical Recycling is a Cheap Cofactor System for Supporting Biocatalytic Alkene Reduction 109

Chapter 5. Biocatalytic Synthesis of Metal Nanoparticles, using *Hydrogenase*, and Application of Resulting Biohybrids 142

5.1. Introduction 143

5.2. Paper 3: Using Low Pressure H_2 with Hydrogenase for the Synthesis of Enzyme-Gold Nanoparticle Biohybrids; Demonstrating their Catalytic Rate Enhancement in Ene-Reductase Biocatalysis 143

Chapter 6. Biocatalytic Synthesis of Supported Metal NPs and their Potential Applications 189

6.1. Introduction 190

6.2. Synthesis of Supported Metal NPs 190

6.2.1. Initial Work 190

6.2.2. General Procedure for Synthesis of Supported NPs 191

6.2.3. Analysis of Au Supported NPs 192

6.2.4. Analysis of Cu Supported NPs 195

6.3. Application of Supported Metal NPs 200

6.3.1. Indole Synthesis Background 200

6.3.2. Investigating the Synthesis of Indoles using Hyd1-Au/C 201

6.4. References 208

Chapter 7. Conclusions and Future Directions 210

Appendix: Reaction Set-up 216

Chapter 1. Introduction

1.1. Metal NP Properties and Applications

1.1.1. Introduction to Metal NPs

Metal nanoparticles (NPs) are metal particles that are usually in the 1 to 500 nanometre size range.[1] This small size causes them to have highly different physicochemical properties to their corresponding bulk metal. This is largely attributed to their high surface area to volume ratio, which brings about their suitability in a wide range of applications, covering the fields of biomedicine, electronics, and catalysis. Metal NPs have been used as long ago as the Ancient Roman times – where colloidal gold was used in stained glass for decorative purposes.[2] However, it was not until the 1850s when Michael Faraday investigated the properties of gold NPs and discovered how different they were to bulk gold.[3]

In bulk metal, light waves are reflected off the metal surface thereby exciting an electron cloud (also called a plasmon) and causing their displacement with respect to their positive lattice (**Figure 1. 1. A**). This effect is known as propagating surface plasmon polaritons (PSPPs). Below the surface, plasmons will not be excited by light in bulk metal. The unique optical property of gold NPs (Au NPs) which makes them appear bright red or purple in solution is due to a phenomenon known as surface plasmon resonance (SPR). This effect arises since NPs are smaller than the wavelength of light which means light penetrates through NPs and causes the conduction electrons to be polarised. These polarised electrons will oscillate (also called a plasmon) parallel to the electric field of the incident light (**Figure 1. 1. B**).[4] The oscillating electrons are localised over the whole NP volume therefore giving the term surface plasmon resonance, or localised surface plasmons (LSPs). These can be thought of as similar to the spring-mass harmonic oscillator model, with the negatively charged electrons being pulled back to the positively charged lattice (**Figure 1. 1. C**). This gives rise to absorbance spectra exhibiting a peak in the visible region, with the wavelength of the peak maximum (λ_{max}) between 500-600 nm. The λ_{max} can be tuned based on the size of the NPs.[4-5] This effect will

be described in more detail in relation to metal NP analysis by UV-vis spectroscopy later in the thesis (**2.1.1.3**).

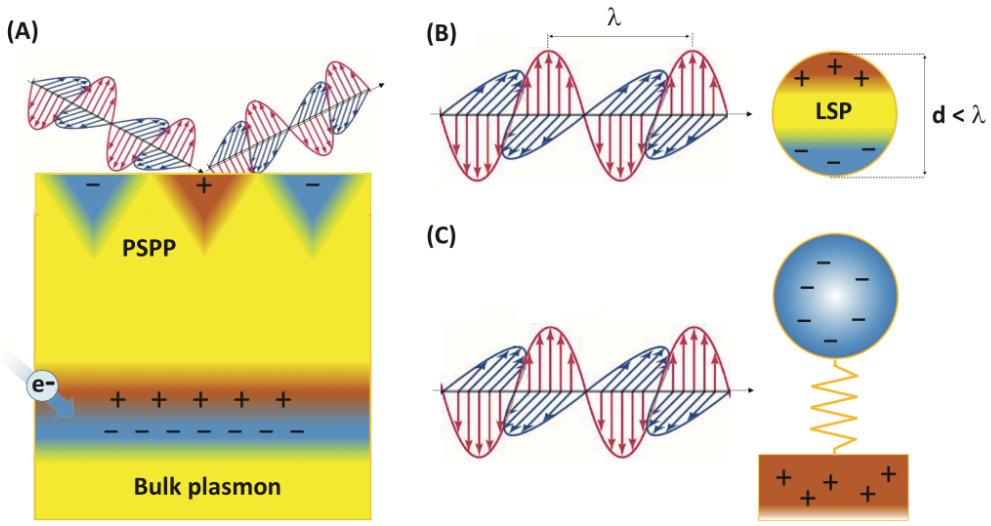


Figure 1. 1. Illustration comparing plasmons in bulk gold and in small gold NPs. **A)** In bulk gold, light can excite the surface plasmons creating a propagating surface plasmon polaritons (PSPPs). Beyond the metal penetration depth, light cannot excite the plasmons, but an electron beam can. **B)** Once a particle is smaller than the wavelength of light, localised surface plasmons (LSPs) can exist, with the oscillating cloud of electrons parallel to the incident light. **C)** Depiction of the LSP modelled as a spring-mass harmonic oscillator. The figure is taken from reference,[4] with permission from Institute of Physics (IOP) publisher, license number: 1478785-1.

1.1.2. Metal NPs in Biomedical Applications

Metal NPs of gold in particular have attracted a lot of scientific attention in the biomedical industry due to their tuneable optical properties as well as good biocompatibility (due to the relative chemical inertness of gold). These properties make them desirable for disease diagnostic and drug delivery applications. Au NPs can be synthesised with a specific capping ligand (a capping/stabilising ligand will always be present as will be explained in **1.2**) which upon binding to a target biomarker will cause an effect on the physical or chemical properties of the NPs.[6] This change in property can be measured and thus used as a detection method for biomolecules of interest. One of the first examples in this area, reported in 1996, used Au NPs functionalised with oligonucleotides which upon binding to their target DNA caused the NPs to aggregate, resulting in a red to blue colour change due to the loss of the well-defined SPR absorbance peak.[7] A more recent example used antibody-conjugated Au NPs which

bound to influenza virus protein antigens in an immunoassay, giving a greater signal for detection at low concentrations of the antigen compared to other immunoassay methods.[8] Similarly Au NPs have been used for cancer imaging, where using Au NPs with a high light scattering ability allows cancer cells to be detected under a confocal microscope by the presence of Au NPs which selectively bind to the cell membranes of cancerous cells over non-cancerous ones.[9] For drug delivery applications, Au NPs with bound drug molecules, which can be released once the bio-nanoconjugates have reached the target area, have been investigated using near-UV irradiation to cleave the drug from the NP.[10] Photothermal therapy is another area of biomedicine where the use of Au NPs shows promise. Again antibody-conjugated Au NPs can be used to selectively bind to cancer cells, and then by using pulsed lasers in the visible region, photon energy can be converted to heat, causing selective cell death of the Au NP-covered cancer cells over the non-cancerous cells.[11]

So far the examples given have used spherical Au NPs, however it is important to note that many studies have focused on Au NPs with non-spherical morphologies – also known as anisotropic – such as stars, cubes and rods, for biomedical applications.[12-14] It is therefore worthwhile to discuss how these different morphologies can provide advantages over spherical NPs for these type of applications.

Star shaped Au NPs will generally have absorbance, and SPR peak maxima, at much higher wavelengths (i.e. the near-infrared region) than spherical NPs, offering a greater suitability for applications such as in photothermal cancer therapy, where drug molecules can be adsorbed onto the NPs and released at the targeted cancer sites using fast pulses of light at the SPR wavelength.[15] Additionally these star shapes can introduce different physicochemical properties of adsorbed molecules, due to their branches and areas of negative curvature; for example, they have been found to increase the loading of DNA molecules compared to spherical NPs of similar size.[16]

Gold nanocubes have been investigated for biosensing applications in detection of biological molecules with SERS (surface enhanced Raman spectroscopy).[17] This allows for very low

concentrations of molecules to be detected, when they are adsorbed to the surface of the gold nanostructure. The edges and corners of a gold nanocube give enhanced localised electromagnetic field thus favouring their use over spherical NPs for applications using SERS.[18]

Similarly, to gold nanocubes, gold nanorods have also been investigated for their diagnostic applications. Their electromagnetic field is strongly affected by the presence of bound protein molecules which causes a shift in their SPR peak.[19] The absorbance spectra of a gold nanorod exhibits two SPR peaks, a smaller one usually around 520 nm which arises from a similar effect to that in spherical NPs, and a much larger one in the visible to near-infrared region which arises from the surface plasmon from the longitudinal direction of the NP. The position of this peak can be selectively tuned by varying the length to width aspect ratio of the NP.[20]

1.1.3. Metal NPs in Electronic Applications

Due to the conducting properties of metal NPs, there is interest in using them to create "nanowires" as the electronics industry continues with its trend of attempting to build smaller and smaller devices. By employing Au NPs as conductive inks, these can allow for printed circuit boards and flexible displays.[21]

Au NPs can also be used in solar cells, using the absorbance properties of Au NPs (by excitement of localised surface plasmon resonance) to boost solar energy conversion efficiencies.[22] A Au NP less than 2 nm, also known as a nanocluster or quantum dot (QD), no longer exhibits a surface plasmon effect (explained in more detail in **2.1.1.3**), and can instead emit fluorescence at visible wavelengths by electrons being excited from absorbing near UV-light.[23] Due to the quantum confinement effect, as the size of the particle (less than the Bohr radius) decreases, the band gap between the discrete valence band and conduction band increases, and therefore higher energy (smaller wavelengths) fluorescence is emitted.[24] Au

QDs have been combined with Au NPs in a study demonstrating their synergistic effects on enhancing solar cell performance.[23] The fluorescence emitted by QDs can increase the surface plasmon effect of the NPs while concurrently the enhanced electric field, increases the QD fluorescence.[25] Therefore the absorbance of the incident light is significantly increased thereby increasing the power conversion efficiency metric, up to 13% increase compared to a reference organic solar cell.[23]

1.1.4. Metal NPs in Catalysis Applications

For catalysis, generally smaller sized metal NPs are desired, i.e. 1-10 nm,[26] as this gives a very high surface area to volume ratio as well as high surface curvature. On a metal surface there can be a number of differently coordinated surface atoms, depending on the exposed lattice plane – lattice plane examples in **Figure 1. 2.**

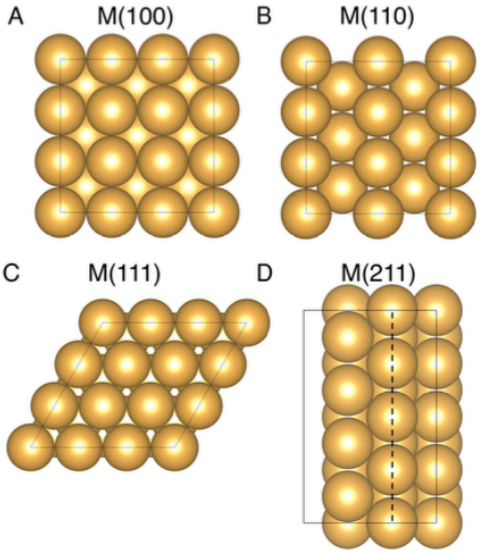


Figure 1. 2. Top views of lattice planes on a metal surface. Black lines indicate a unit cell and dashed black line indicates a stepped site. Image taken from reference,[27] with ACS AuthorChoice license.

The edge or corner atoms or atoms on a step, indicated by the dashed line of (211) plane in **Figure 1. 2.**, found in these lattice planes are low coordinating atoms which will be in a higher percentage, out of total surface atoms, in smaller NPs, as illustrated in **Figure 1. 3.**

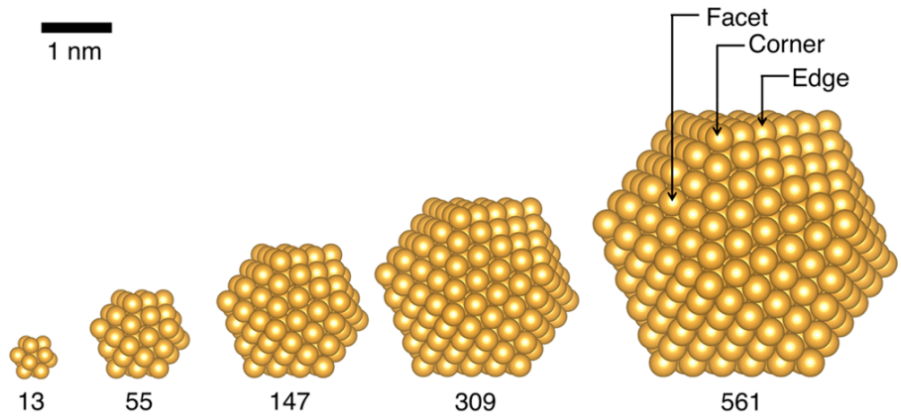


Figure 1. 3. NPs of increasing size (number of atoms indicated). Image taken from reference,[27] with ACS AuthorChoice license.

Most of the studies investigating the influence of the NP structure on its reactivity have been carried out for Pt or Pd NPs. Within the 1-5 nm size range there is a significant change in NP structure, for example for a Pt NP, 92% of atoms exist on the surface of 1 nm NP and the percentage of surface atoms decreases rapidly with 28% in a 5 nm NP.[26] As well as the surface area to volume ratio, another factor to consider is the spacing of the atoms which increases with particle size.[28] This results in an increase in binding energy of adsorbed molecules to the metal surface (as modelled for CO) which fits with the theory of bond order conservation, as the valences are more saturated for the metal atoms in the larger NPs.[29] Due to a similar effect, the interaction energies are higher for atoms with lower coordination number, i.e. the bridge sites on edges of NPs have the highest interaction energies.[30] The ratio of edge sites to non-edge sites is inherently higher for smaller NPs than larger ones (of comparable geometries). There is a factor which causes an opposite trend: in decreasing binding energy as NP size increases, which is due to the increase in energy of the centre of the d-band due to a decrease in the ratio of low coordinated atoms on the NP surface. This factor is more dominant for smaller sizes – a Pd cluster of around 50 atoms in size was

therefore calculated, by DFT methods, to have the lowest binding energies for the adsorption of CO molecules.[31]

The effect these electronic and structural properties have on catalytic activity depends on the reaction studied but is strongly linked to the number of available low-coordination sites and the effect of the NP structure on stabilising reaction intermediates.[29] There have been many experimental studies investigating the effect of the size and shape of Pt NPs, as catalysts in hydrogenation reactions, on their reactivity and selectivity towards different products.[26] For both furan and pyrrole hydrogenation, the smallest size of Pt NPs tested (1 nm) gave the highest selectivity for reduced ring products over ring opened products.[32-33] The higher preference for butanol (from furan hydrogenation and ring opening) was also seen when tested over a Pt(100) single crystal surface compared to Pt(111).[32] Therefore demonstrating that the type of surface facets that are present in NPs of different sizes may lead to different reaction outcomes. As well as different sizes, different shapes of NPs will have different surface facets. Tetrahedral Pt NPs which only have (111) planes exposed were compared to spherical NPs for their effect on cis-trans isomerisation of alkenes. The tetrahedral NPs were found to give a faster rate of conversion from trans to cis isomers while spherical NPs gave a faster rate for cis to trans.[34]

For Au NPs similar trends have been observed based on decreasing catalytic activity for increasing NP size. Small Au NPs were shown to catalyse glucose oxidation in O_2 to produce H_2O_2 and gluconic acid, giving glucose oxidase-like behaviour.[35] Increasing the NP size from 3 to 10 nm was found to decrease the activity. Interestingly Au was found to give much higher activity than other metals tested alongside: Cu, Ag, Pd and Pt. Another application of Au NPs as an enzyme mimic, is in breaking down H_2O_2 while oxidising a substrate such as 3,3′,5,5′-tetramethylbenzidine (TMB), showing peroxidase-like activity.[36] Upon investigating the surface activity by selectively blocking Au(I) sites using sulfide ions, it was found that surface Au(I) was key to the reactivity.

The reduction of 4-nitrophenol, a pollutant from the textile and drug industry, to 4-aminophenol, which is less toxic, has been widely studied using $NaBH_4$ and metal NPs, including Au NPs as catalysts.[37] The Au NPs are often combined with a support, such as a carbon-based support or magnetic Fe_3O_4 NPs, to make the catalyst easier to recycle and separate from reaction products.[37-38]

Electrochemical reduction of CO_2 to CO can be catalysed by small Au NPs. Studies have shown that an increased number of edge sites gives greater reactivity due to the low coordination of Au atoms which allow for stabilisation of CO_2 reduction intermediates and weakening of CO binding. This has inspired the investigation of unusual Au NP structures such as concave rhombic dodecahedral NPs which showed higher electrocatalytic performance.[39]

Au NPs have also been investigated for catalysing CO oxidation to CO_2.[40] For improved catalytic rates, bimetallic NPs such as AuPt NPs have also been studied for this application. A mixed metal species is found to alter the binding properties of substrates to the NP surface.[41] As therefore implied, controlling the structural composition of bimetallic NPs can be beneficial for control over their reactivity. The composition of Au and Pt NPs were investigated for their electrocatalytic properties for methanol oxidation reaction and oxygen reduction reaction which can be applied to fuel cells.[42] A positive shift in the oxygen reduction potential was seen when comparing Au, Pt@Au (Pt core-Au shell), Au@Pt (Au core-Pt shell), Pt NPs (in order from lowest to highest). The mass activities (normalised to the total mass of metal) also followed this order, due to increasing number of surface Pt atoms. For the CO oxidation reaction, the activity was improved by increasing the number of surface Au atoms surrounding single Pt atoms which causes an electronic structure change of Pt thereby decreasing the binding strength of CO and thus limiting the CO poisoning effect that is often seen in standard Pt/C catalysts.[43] The use of Au@Pt core-shell-satellite NPs (i.e. mostly Au with small Pt particles over the surface, as shown in **Figure 1. 4.**) over Pt NPs can lead to improved stability under electrocatalytic oxidation conditions since oxygen species can adsorb

to Au and encourages interaction between oxygen and CO-derivatives.[44] This is also beneficial due to the scarcity and higher cost of Pt compared to Au.

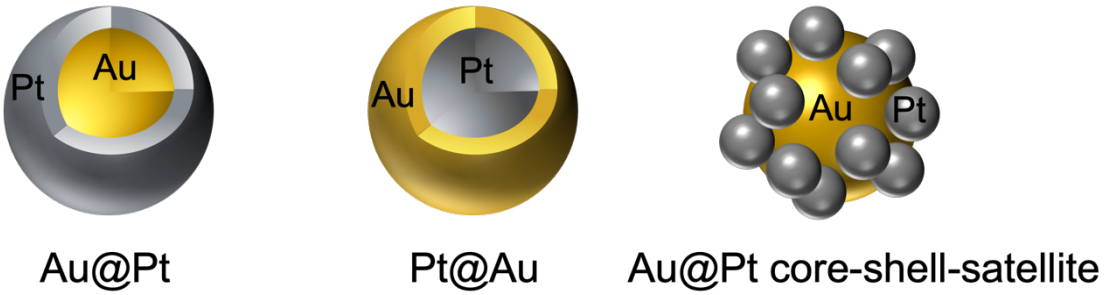


Figure 1. 4. Different structures of core-shell NPs.

As well as the dependence of catalytic activity on the size of NPs, the presence of a support also plays a role in the catalytic activity. The sole purpose of a support is therefore not just to provide an easier to recycle catalyst. For CO oxidation using a Au NP supported catalyst (TiO_2 support) it was found that catalysts prepared using different methods influenced the CO oxidation activity; the catalyst preparation that resulted in the greatest interaction of NP and support showed the highest activity – explained by the minimising of the distance for surface diffusion between reactive species.[45-46] It is also noted that the interaction of Au and TiO_2 support results in more electron-rich Au species which contributes to increased activity.[47] As well as altering the method for preparation of supported metal NPs, another way to increase the interaction between metal and support is by changing the type of support used. Carbon supports are commonly used in heterogeneous catalysis due to their high stability, high porosity and electrical conductivity.[48] In a graphitic support, most of the carbon bonds will be sp^2-hybridised, forming a very inert planar structure which can only have weak van der Waals interactions with metal NP species.[49] However defects in the structure introduce stronger bonding sites where either a so-called “dangling carbon” can form a covalent bond to the metal or a doped species such as nitrogen can undergo hybridisation of N π-orbitals and metal d-orbitals.[50] This σ-donation from filled N π-orbital to an empty metal d-orbital and π back-donation from filled metal d-orbital to N antibonding π^*-orbital therefore creates strong bonding

between metal and support and influences the electronic properties of the metal NP.[49] Thus using a defect-introduced support, improves the stability of the catalyst and introduces higher possibility of interfacial charge transfer between metal and support.[51]

The other notable area of applications of metal NPs is in photocatalysis, for example using supported Au NPs for reduction or oxidation reactions by using light at the wavelength of the SPR to excite the NPs.[52-53] For photocatalytic H_2 production, it was shown that attaching a silver nanocluster to an O_2-tolerant hydrogenase enzyme (which under neutral conditions is not efficient at producing H_2) can drive H_2 production by photoexcited electrons from the silver nanocluster being passed onto the enzyme which carries out the proton reduction.[54]

1.2. Metal NP Synthesis Procedures

1.2.1. Overview of Metal NP Synthesis

As was demonstrated by some of the examples of metal NP applications in the previous section, the size and shape of the NP can dramatically affect the NP properties and hence change its suitability for certain applications. Therefore, it is important that a NP synthesis method provides precise control over the NP size and shape with maximum uniformity. This is sometimes referred to as the monodispersity of a sample with “near-monodisperse” defined as NPs with size differences ≤ ±15%.[55]

There are a huge number of different methods reported for metal NP synthesis with their own advantages and disadvantages which may depend on the desired NP application. The general types of methods are sometimes referred to as “top-down” or “bottom-up” approaches: meaning either starting with the bulk metal and breaking it down into smaller pieces until nanometre-sized particles are made (top-down) or by starting with metal ions, reducing these to atoms and agglomerating these atoms together to form NPs (bottom-up). The types of

methods used for these approaches can be classed as physical, chemical, or biological (biosynthesis) methods.

Physical methods are usually energy-intensive involving something such as a pulsed focused laser (laser ablation) to break down the bulk metal into NPs in solution. Other physical methods include thermal evaporation-condensation, ball milling and spluttering.[56] They can provide advantages such as the lack of needing to use reagents which may bind to the NP and limit its reactivity and with not needing to remove any unwanted reagents from the NP solution.[57]

A key feature of the chemical and biosynthesis methods discussed in the following sub-sections is the presence of a reductant and a capping/stabilising agent. In some cases, the reductant is also involved as the stabilising agent and in others a separate reagent is added to act as the stabiliser. The ratio of reductant and/or stabiliser to the metal precursor is often an important factor for controlling the size/shape of the resulting metal NPs.

The methods discussed in the following sub-sections are focused on the synthesis of small, spherical NPs which are the type generally used for catalysis applications (most relevant for this thesis area). The reasons for the greatest suitability of small, spherical NPs have already been discussed in **1.1.4**. If however anisotropic NPs are desired, a set of conditions/reagents which direct the growth of the NPs into the desired shapes is required.[58] A common approach involves starting with Au NP seeds, followed by the addition of more Au^{3+} precursor, a reductant and cetyltrimethylammonium bromide (CTAB), a cationic stabiliser, to form shapes such as Au nanorods.[59] During this synthesis, CTAB directs the growth into nanorods due to its preference for adsorbing to (100) and (110) facets over (111) facets which are present at the tips of the nanorods.[60]

1.2.2. Chemical Methods

One of the first and most frequently cited methods for the synthesis of spherical Au NPs is known as the Turkevich method: this uses sodium citrate as the reductant and NP stabilising

agent.[61] An aqueous solution of $HAuCl_4$ and sodium citrate is boiled and the colour change to the characteristic red colour of Au NPs is observed within 1 minute, with an increase in intensity of the colour over the remaining reaction time as the concentration of Au NPs increases. After many studies into the mechanism for this reaction, it is now commonly accepted (by evidence from different analytical techniques) that there is a short nucleation period where small Au seeds form, which then attract the remaining Au^{3+} ions which then undergo reduction onto the Au seeds causing growth of these particles while the number of NPs remains constant – thereby called a seed-mediated growth mechanism.[62]

Many studies investigating reaction parameters such as temperature, ratio of $HAuCl_4$ to sodium citrate and pH have been carried out with these parameters being shown to be key to controlling the size of the NPs which form.[63-64] The pH of the solution was also found to be an important parameter in minimising agglomeration of the resulting NPs, which gave evidence for the role of citrate molecules in stabilising the NPs: since the pH needs to be higher than pH 3.1 to stop NP precipitation. Below pH 3.1 citrate will be fully protonated (pK_a values of 6.4, 4.8, 3.2) therefore there will no longer be electrostatic repulsion between NPs covered in citrate ions.[65] A modified Turkevich method which starts with Au seeds, of around 10 nm in size, (prepared also by boiling $HAuCl_4$ with sodium citrate) and then uses successive additions of sodium citrate and $HAuCl_4$, at adequately low concentration to minimise new nucleation sites, allows for controlled growth of Au NPs to desired sizes, up to 180 nm (procedure and TEM images shown in **Figure 1. 5.** and **Figure 1. 6.**).[65]

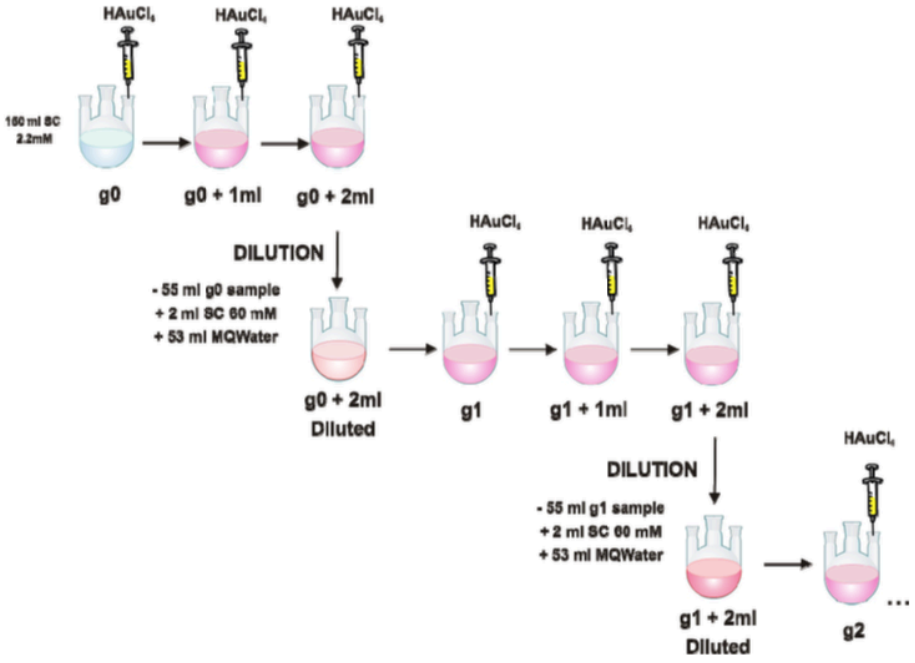


Figure 1. 5. Preparation method for controlled growth of Au NPs, starting from making 10 nm sized Au NP seeds and with sequential additions and dilutions to prepare NPs of desired size, up to 180 nm. Reprinted from reference[65] with permission from American Chemical Society.

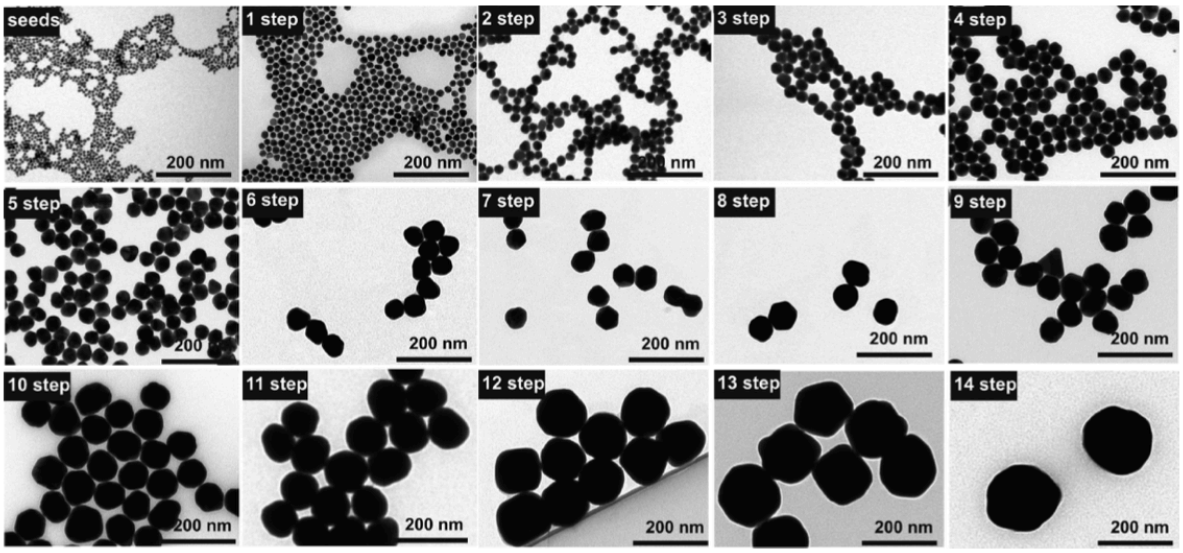


Figure 1. 6. TEM images of Au NPs after preparing initial Au NP seeds and after growth steps. Reprinted from reference[65] with permission from American Chemical Society.

Other methods have been used which avoid the need to boil the solution and can instead be carried out at room temperature. For example, UV-irradiation can be used to initiate the

reduction reaction of $HAuCl_4$ in presence of sodium citrate. The NPs obtained are comparable in size to those from the thermal sodium citrate method, however a population of triangular and plate-like shaped NPs are also formed under the UV conditions.[66] Other reductants, instead of sodium citrate, can also be used, such as ascorbic acid or sodium borohydride.[66] A mixture of sodium citrate and sodium borohydride can prepare 5 nm sized Au NPs at room temperature.[67] Sodium borohydride has also been shown to synthesise stable, small Au NPs without the need for an additional capping reagent.[68] It is proposed that the NPs can be stabilised by BH_4^- and H^-.[69] There have also been studies on controlling the size of the NPs using sodium borohydride as the reductant and thiol-terminated ligands or peptides as capping agents.[70-71]

1.2.3. Biosynthesis Methods

Biosynthesis methods differ to that of chemical methods in that the reductants are bio-based materials including plant extracts, micro-organisms and enzymes, thus avoiding the use of toxic reagents. Most of these methods are carried out at room temperature without any organic solvents therefore the mild conditions offer a more sustainable synthesis route to metal NPs than the chemical methods.

There are a vast number of publications using different plant extracts to make metal NPs with the methods being generally very simple and thus convenient for large scale production.[72-73] For example, a seaweed (*Gracilaria crassa*) was used to prepare Au NPs by firstly washing, drying and blending the seaweed into a fine powder which was then used to make an aqueous broth by boiling in water and filtering.[74] A solution of $HAuCl_4$ was then added to the broth, which was shaken at room temperature, resulting in the appearance of a purple-coloured solution indicating Au NPs were formed. These NPs were relatively large, 32 ± 4 nm, so could be centrifuged to remove excess water-soluble biomolecules.

However, there is often a lack of understanding of the mechanism for the NP synthesis due to the large number of different compounds which may be present in any one plant extract. There can also be batch to batch variations when different plants contain different chemical compositions which can be difficult to analyse. These factors can result in a lack of good size and shape control over the NPs with often relatively large NPs and varying shapes present.[75-76] Nevertheless, the ease-of-application and the benign and easily sourceable reagents, has meant this is still an attractive synthesis route which many are further investigating particularly for anti-bacterial and biomedical applications.[72]

Using living micro-organisms, e.g. bacteria and fungi, is another NP synthesis option that has been explored.[77] Enzymes found inside or on the cell walls of bacteria and fungi are able to reduce metal ions and stabilise the metal NPs which form. Similarly to plant extracts, these offer an attractive low toxicity synthesis route. Some micro-organisms can tolerate high metal concentrations therefore there have been examples exploring their use in bioremediation of metal-contaminated water. During this process the micro-organisms extract metal ions from solution and reduce them, with metal NPs forming as a result.[78-79] With Pd NPs, usually supported on a carbon material, being prominent in traditional heterogeneous catalysis there have been many investigations into making Pd NPs, under mild conditions, supported on biomass.[80-81] Thus, using bacteria offers promise for this purpose. One of the first examples of using bacteria to make Pd NPs, reported in 1998, used the sulfate-reducing bacterium, *Desulfovibrio desulfuricans*.[82] Pd NPs were shown to form in the presence of either pyruvate, formate or H_2 as the sacrificial electron donors. Other later studies moved to using *Escherichia coli* of which it was found that high populations of Pd NPs formed along the cell membranes (**Figure 1. 7.**).[83] After preparing mutants which did not express specific enzymes (hydrogenase) and where a much slower rate of Pd^{2+} reduction occurred and where larger Pd aggregates formed outside the cell, it was proposed that these enzymes played an active role in the mechanism for the Pd^{2+} reduction and localised NP formation.[83] Metal reduction by

bacteria is not unique to Pd, for example *Escherichia coli* (*E. coli*) has also been shown to be active for Au reduction.[84]

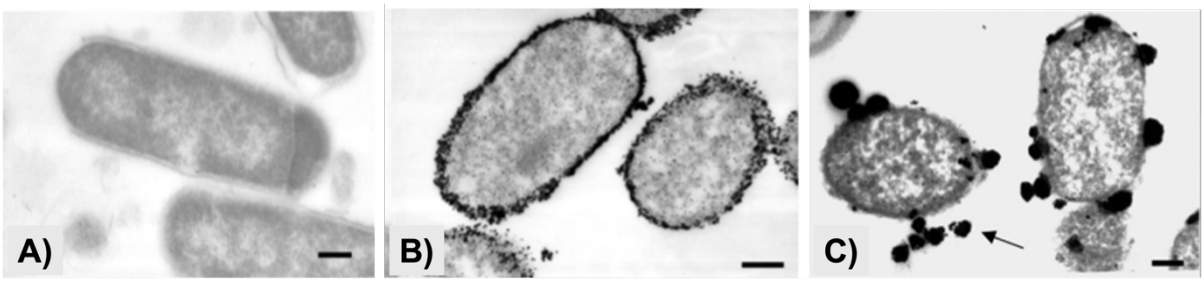


Figure 1. 7. TEM of *E. coli* cells, **A)** parent strain, untreated, **B)** parent strain, treated with Pd, **C)** hydrogenase-deficient mutant, treated with Pd (arrow pointing to large aggregate outside cell). Cells were in presence of sodium formate as electron source. Scale bars indicate 200 nm. Image taken from reference[83] with permission from Microbiology Society publisher, license number: 1480122-1.

By extracting enzymes grown in micro-organisms, these can be used as isolated enzymes for the synthesis of metal NPs.[85-86] This can make purification easier as NPs do not need to be extracted from the cell after synthesis. Some examples have been shown to use exposed thiol groups (from cysteines) on the surface of enzymes as the reducing agents: α-amylase was found to form spherical Au NPs around 10 nm in size which were also stable due to the presence of the enzyme acting as a capping agent.[87] A denatured form of this enzyme also formed Au NPs, and at a faster rate, therefore indicating the role of the thiols in reducing Au^{3+}. The α-amylase activity in the resulting Au NP-α-amylase hybrid was found to be lower than the free enzyme which is often common in enzyme immobilisation strategies. Another example uses glutathione reductase which oxidises NADPH while reducing Au^{3+} with the Au NPs found to form at its cysteine-containing active site.[88] The active site is in a cleft of the enzyme therefore directing the size of the Au NPs such that, with careful control over the ratio of enzyme to Au^{3+}, their diameter matches the size of the cleft (2 nm). Since the catalytic cysteines are involved in the enzyme's natural activity in reducing oxidised glutathione via a disulfide exchange reaction, it is found that this activity is lost after reduction of Au^{3+} (since the NPs are now blocking the active site cysteines). A sulfite reductase has similarly been used to make spherical, 10 nm sized Au NPs in the presence of Na_2SO_3, gelatin and NADPH.[89] A

control with denatured enzyme where no NPs formed confirmed the enzymatic process for the Au^{3+} reduction. Interestingly in this case, the authors found that a capping agent such as gelatin was needed, as well as the enzyme, to observe Au NP formation.

1.2.4. Synthesis of Core-Shell NPs

Chemical synthesis of core-shell NPs generally involves a two-step procedure where the first metal is reduced followed by addition of the second metal to be reduced on the surface of the already formed cores of the first metal. For example a procedure described to synthesise around 8 nm sized Au@Pt NPs (Au core, Pt shell), starts with the synthesis of Au cores, made using a two-phase procedure (water/toluene),[71] with $NaBH_4$ as reductant and with tetraoctylammonium capping ligands, followed by addition of Pt precursor and oleylamine with 1,2-hexadecanediol as the reducing agent for Pt reduction onto the Au seeds.[42] A similar procedure, reversing the order of the steps can be followed to prepare Pt@Au NPs (Pt core, Au shell). For the second step, a high boiling point solvent, octyl ether, is used since control over the thickness of the shell was found to be achieved by controlling the temperature of this step between 100 and 180 °C. The presence of strong capping ligands was key to controlling the NP growth and providing stability however it is also known that the capping ligands can decrease the reactivity of the NPs by making the surface sites less accessible to the reaction substrates.[90] Therefore other methods using less strongly binding capping agents have been reported, such as using ascorbic acid as reductant and stabilising agent (still requiring heating, at 90 °C, for reduction of Pt^{4+} onto Au seeds).[44]

Another example uses UV-irradiation to break down the initially-used stabilising ligands, in the synthesis of carbon supported Au@Pt NPs with 2 nm sized Au cores surrounded by a few layers of Pt atoms.[91] In this procedure small Au NPs are firstly made using the two-phase procedure described earlier. Then these Au NPs are mixed with a carbon support material and ethanol is added to remove excess thiol. The carbon supported Au NPs are then mixed with

H_2O_2 and ethanol and UV-irradiation is used to photo-oxidise the thiol stabiliser and thereafter H_2PtCl_6 and ascorbic acid is added to make small, carbon supported Au@Pt NPs.

Due to the lower reduction potentials of Pt^{4+} (to Pt^{2+} and Pt^{2+} to Pt^0) there have been less examples of plant-material synthesis methods than for Au^{3+} reduction to Au^0. Consequently, there are very few biological methods for synthesising Au@Pt core shell NPs. One method however uses gallic acid (phenolic acid found in many plants) as reductant and stabiliser which involves heating an aqueous solution of $HAuCl_4$ and H_2PtCl_6 with gallic acid.[92] Depending on the temperature used this method formed NPs sized between 50 to 80 nm. Despite a one-step approach being used, Au@Pt NPs formed selectively. The explanation for this was proposed based on the difference between the metal reduction potentials, meaning that Au reduction is favoured therefore making Au NP seeds first which then catalyses the Pt reduction, forming the core-shell NPs.

An example of core-shell NPs made using bacteria was reported for the synthesis of Au@Pd NPs, with average sizes around 2 nm, prepared using *E. coli* cells and H_2.[93] Despite the metal salts being added in a two-step process, unusually with Pd^{2+} added first, the resulting NPs exhibit a Au core and Pd shell structure. This is explained by a mechanism where Pd^{2+} is first biocatalytically reduced to Pd^0 seeds by the enzymes found in *E. coli*, then the Pd^0 seeds catalyse Au^{3+} reduction due to the difference in their redox potentials meaning Pd^{2+} is reformed which then gets re-reduced on the Au surface, forming the Au@Pd structures.

1.3. Hydrogenase and NAD^+ Reductase Enzymes

1.3.1. Introduction to Hydrogenase

Hydrogenases are a class of enzymes which undergo reversible H_2 oxidation ($H_2 \rightleftharpoons 2\ H^+ + 2\ e^-$). This occurs at a buried metal-containing active site with a hydrophobic gas channel leading

to this active site, allowing small H_2 molecules to reach the metal centre where they are heterolytically cleaved ($H_2 \rightleftharpoons H^+ + H^- \rightarrow 2\ H^+ + 2\ e^-$).[94] This mechanism is different to the homolytic cleavage of H_2, usually favoured on metal surfaces of NPs or in metal complexes.[95]

Evolution has designed these enzymes to act selectively on H_2; they have existed since early Earth where H_2 levels were high and where H_2 levels have since rapidly declined and O_2 levels increased.[96] Despite this, CO has been found to be a competitive inhibitor of H_2 with fast reversible binding at the active site.[97]

Hydrogenases can be broadly split into three groups based on their metal centre, as either [NiFe], [FeFe] or [Fe]. Depending on their physiological function, they exhibit a catalytic bias towards either H_2 oxidation or proton reduction: [NiFe] hydrogenases have a bias towards H_2 oxidation while [FeFe] hydrogenases are more efficient at proton reduction (H_2 evolution).[96] These hydrogenases have been widely studied through electrochemical and spectroscopic analysis for determination of their structure-activity relationships. Thus, activity differences between different hydrogenases have been observed by cyclic voltammetry (CV) studies, or more specifically called protein film electrochemistry (PFE), where the enzyme in contact with the electrode causes a change in current over the potential range.[96] A large negative current in the potential range for H_2 evolution with [FeFe] hydrogenases demonstrates their high activity as H_2 generation catalysts.[98] Even within a class of hydrogenases there is a range in activities observed; for example, two different [NiFe] hydrogenases from *E. coli* known as “hydrogenase 1” (Hyd1) and “hydrogenase 2” (Hyd2) display very different redox properties. PFV of Hyd1 shows an over-potential of around 50 mV with respect to the thermodynamic $2H^+/H_2$ couple meaning that it is biased towards H_2 oxidation, whereas Hyd2 has no over-potential and so can more easily undergo proton reduction to H_2.[99] H_2 inhibition for H_2 evolution has also been observed to occur for hydrogenases, as measured by comparing the current at negative potentials from PFV under H_2 compared to Ar.[97]

E. coli Hyd1 is natively bound to the cell membrane. In 2012 the first crystal structure of Hyd1 from *E. coli* was reported.[100] This identified the isolated enzyme as a dimer of heterodimers,

with each monomer containing a small and large subunit. The membrane-anchoring hydrophobic domain was disordered and therefore not seen in this crystal structure. Soon after a crystal structure of a Hyd1 variant was reported including the transmembrane domains and cytochrome (**Figure 1. 8.**).[101]

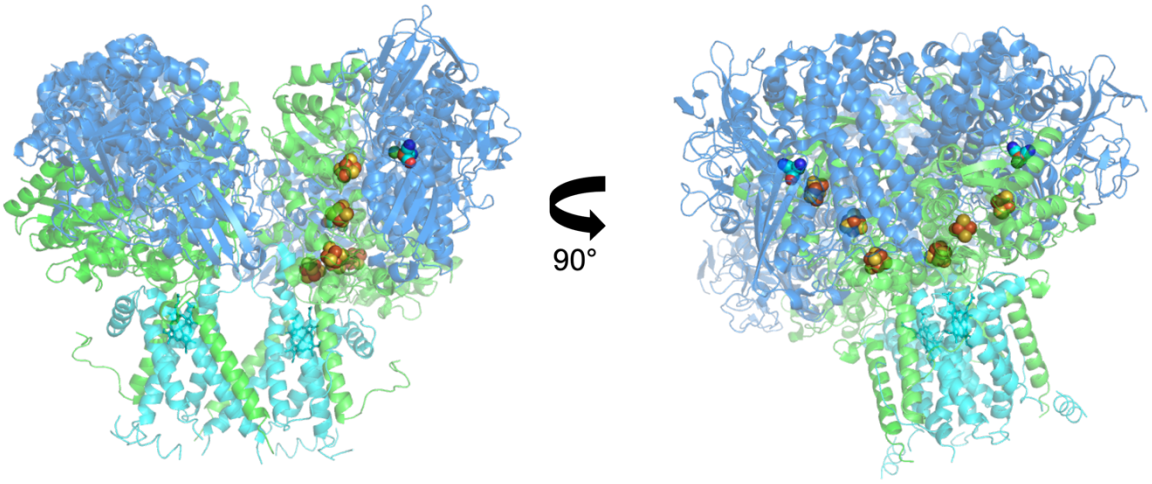


Figure 1. 8. Crystal structure of *E. coli* Hyd1 variant (PDB: 4GD3),[101] shown as the dimer of heterodimers, from two viewpoints. Fe-S clusters (orange and yellow spheres) and NiFe active site (coloured spheres) only shown in one dimer for clarity. Each monomer made up of blue large-subunit, green small-subunit with cyan cytochrome.

Spectroscopic studies investigating the redox states of the metals in the active site have found that for [NiFe] hydrogenases, during the catalytic cycle, Fe remains in the (II) state whereas Ni exists as either (I), (II) or (III) depending on the stage of the cycle (**Figure 1. 9.**).[102] The Fe is coordinated to one CO ligand and two CN ligands. Their corresponding IR bands are sensitive to changes in electron density at the active site therefore are a useful probe for determining catalytic states.[103]

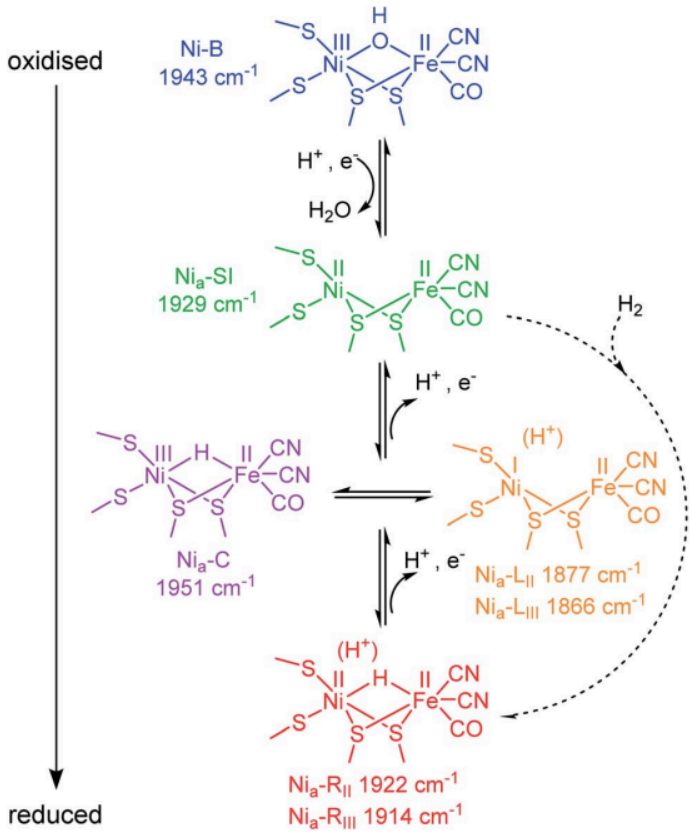


Figure 1. 9. Representation of the active site of [NiFe] hydrogenase. Dashed arrow shows H_2 binding during catalytic H_2 oxidation where H_2 is heterolytically cleaved across NiFe bridging site. IR CO stretching band positions can be assigned to the different redox states, as labelled. Figure taken from reference[102] with permission from the Royal Society of Chemistry under the Creative Commons Attribution 3.0 Unported Licence.

As well as the active site, another key feature of these enzymes is the presence of multiple Fe-S clusters, leading from the active site to the surface of the enzyme. The small distance between these Fe-S clusters (<14 Å) is considered short enough for electron tunnelling therefore allowing them to act as a highly efficient electron transport chain.[104-105] The Fe-S clusters are known as proximal, medial and distal for clusters of increasing distance away from the active site. Spectroscopic studies comparing the Fe-S clusters of Hyd1 and Hyd2, reveal that the proximal cluster for Hyd1 has a higher redox potential than the proximal cluster for Hyd2 thus indicating a likely reason for their activity differences.[106]

Hyd1 is found to have greater O_2 tolerance than some of the other hydrogenases. There have been four identified contributing factors. Firstly, the proximal Fe-S cluster (nearest the active site) is unusually a [4Fe-3S] structure instead of the standard [4Fe-4S].[107] There are four

coordinated cysteine ligands around the standard [4Fe-4S] cluster whereas there are six coordinated around [4Fe-3S]. This replacement of a bridging sulfide with a sulfur atom from one of the extra cysteine ligands (with the other extra cysteine coordinated as a terminal ligand) changes the coordination structure of the Fe-S cluster into a more open, distorted conformation instead of the standard cuboidal conformation. This allows the proximal cluster to be able to reach a higher redox potential therefore allowing the cluster to promote the immediate transport of two of the four electrons needed to reduce O_2 to H_2O, via the following two redox transitions: $[4Fe\text{-}3S]^{3+} \rightleftharpoons [4Fe\text{-}3S]^{4+} \rightleftharpoons [4Fe\text{-}3S]^{5+}$. In the final transition the unusual structure of this cluster allows for an Fe-N(amide) bond to stabilise the valence-localized Fe^{3+}. The final two electrons required for O_2 reduction to H_2O are supplied by the oxidation of the Ni in the active site (Ni^{2+} to Ni^{3+}) and from the medial Fe-S cluster which is also found to be important for the O_2-tolerance of Hyd1 (due to its higher potential than found in medial clusters of other [NiFe] hydrogenases).[108-109] Another structural difference between O_2-tolerant and O_2-sensitive hydrogenases is the presence of hydrophilic channels from the active site to the protein surface which therefore help the transport of H_2O, from the oxidation of O_2, away from the active site.[110] Lastly, the dimeric structure is observed to help with the O_2-tolerance: the distance between the distal Fe-S clusters of each monomer is around 12 Å which means electrons can be easily transported between them.[104] This means in the presence of a mixture of H_2 and O_2, if H_2 is being oxidised at one monomer, it is possible for those electrons to be transported to the other monomer, if it is under O_2 attack, to allow for fast O_2 reduction.

1.3.2. Introduction to NAD^+ Reductase

An NAD^+ reductase is an enzyme which can undergo bidirectional reduction of NAD^+ or oxidation of NADH depending on the conditions. It is naturally found as an enzyme moiety associated to a hydrogenase moiety – together known as “soluble hydrogenase”. Thus, the NAD^+ reductase is one half of the soluble hydrogenase structure which exists as a heterohexameric protein, with the six subunits, $HoxHYFUI_2$.[111] The $HoxI_2$ subunits are found

to be unstable under the conditions used to isolate and purify the enzyme.[112] HoxHYFU, however, can be isolated and used for H_2-driven NAD^+ reduction where the HoxHY carries out H_2 oxidation and separately the HoxFU subunit carries out the NAD^+ reduction.[113] There is a chain of iron-sulfur clusters found between the buried [NiFe] active site of the HoxHY and the flavin mononucleotide (FMN) active site of the HoxFU (**Figure 1. 10.**). These are a common feature of redox proteins and are known to function as an electron transport chain,[114] thus here they transport the electrons from H_2 oxidation to the site of NAD^+ reduction (and reverse).[115]

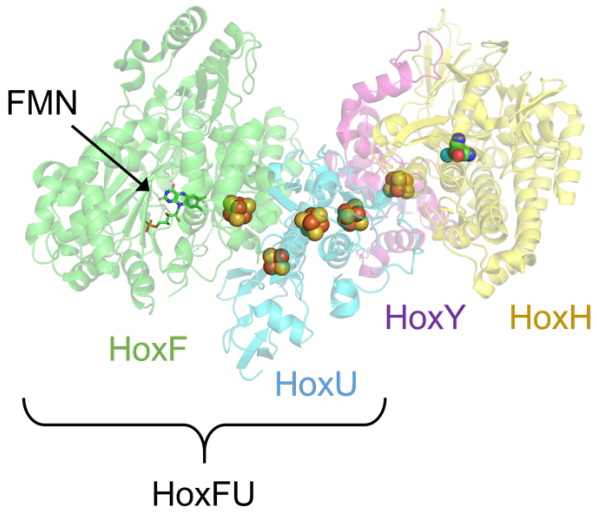


Figure 1. 10. Crystal structure of isolated soluble hydrogenase from *Hydrogenophilus thermoluteolus* (PDB: 5XF9)[115] showing the four subunits (HoxHYFU) with five Fe-S clusters between the NiFe H_2 oxidation active site and the buried FMN at the NAD^+ reduction active site.

Since there is currently no crystal structure for soluble hydrogenase of *Ralstonia eutropha (now known as Cupriavidus necator)*, instead complex I of *Thermus thermophilus*, which has high homology to the HoxF in soluble hydrogenase, can be used to aid investigation of the NAD^+ reductase mechanism.[116] The crystal structure of bound NADH (PDB: 3IAM)[117] shows how the external cofactor and prosthetic FMN interact in the active site (**Figure 1. 11.**). The positioning of the NAD^+ with respect to the FMN is such that the H^- transfer is regio- and stereo- selective: with the H^- transferred from FMN onto the *si* face of the NAD^+ cofactor at the

4-position of the nicotinamide ring, yielding 1,4-NADH. Studies in the presence of D_2O validate the stereoselectivity of the NAD^+ reductase, by forming an isotopically induced stereocenter, with complete selectivity for [4*S*-^{2}H]-NADH observed by ^{1}H NMR spectroscopy.[116]

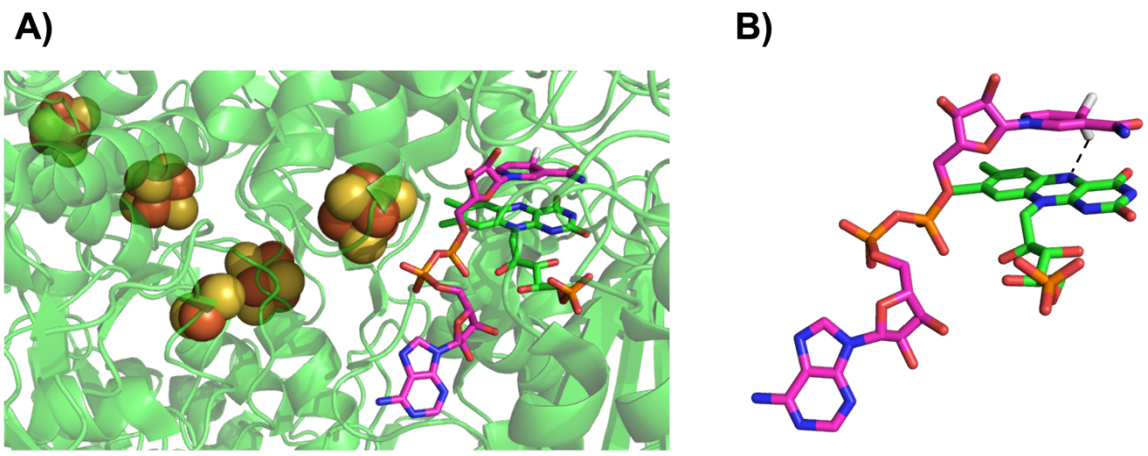


Figure 1. 11. Crystal structure of complex I of *Thermus thermophilus* (PDB: 3IAM)[117] with bound NADH, which has a high homology to HoxF at the bound FMN NADH binding site. **A)** The binding site of NADH within the protein structure. **B)** Proteins chains omitted to show clearly how the H^- is transferred from NADH to FMN (dashed line).

The HoxHY and HoxFU subunits can be expressed and isolated separately.[118-119] In this thesis HoxFU was expressed in *E. coli* and isolated and thus was used as an NAD^+ reductase operating without a hydrogenase. Despite soluble hydrogenase of *Ralstonia eutropha* being shown to give high turnover frequency numbers for the reduction of NAD^+, it has also been found to have limited long-term stability under reaction conditions,[118, 120] while the HoxFU subunit alone has significantly higher stability.[119] Thus, strategies have been employed to couple the NAD^+ reductase with a more robust hydrogenase such as Hyd1, via co-immobilisation to a carbon support,[121-122] or by combining NAD^+ reductase with a palladium or platinum on carbon catalyst where the metal can carry out the H_2 oxidation and electrons are transferred to the NAD^+ reductase for the selective NAD^+ reduction.[116, 123]

1.4. Combining Metals with Enzymes

1.4.1. Linking Enzymes to Gold Surface for Electrochemical Studies

Gold electrodes due to their chemical inertness are often used to study catalytic mechanisms using electrochemical control over the electrode-bound chemical or enzyme.[124] Due to the electronic properties of gold, surface-enhanced infrared absorption spectroscopy can also be carried out to study which surface groups on the protein are involved in the interaction to the gold surface and whether any changes occur to the protein at different potentials.[125] Since enzymes will not generally adsorb directly onto a Au electrode, a self-assembled monolayer (SAM) is commonly used. The general principle of a SAM is to use an alkanethiol to act as a linker between the electrode and enzyme by covalently attaching to the gold surface via a Au-S bond and then at the other end, functional groups can be tailored for optimal immobilisation of the enzyme studied.[126] The formation of the enzyme-alkanethiol monolayer on the gold surface thereby occurs by a spontaneous process. Ideally incorporation of a redox mediator into the thiol linker means electrons can be transferred directly between electrode and enzyme.

A study has shown that the introduction of Au NPs immobilised onto a Au electrode can increase electron transfer rates between an immobilised enzyme and the electrode. The Au NPs are bound to the Au electrode surface by a dithiol linker, followed by the non-covalent enzyme attachment to the Au NPs by a hydrophobic linker. The resulting system showed enhanced interfacial electron transfer of 20-fold compared to enzyme immobilised via an alkanethiol directly onto the Au electrode, without Au NPs (comparison of assembly structure shown in **Figure 1. 12.**).[127] This effect was attributed to the plasmonic delocalisation that Au NPs $\geq$ 2.5 nm can exhibit.

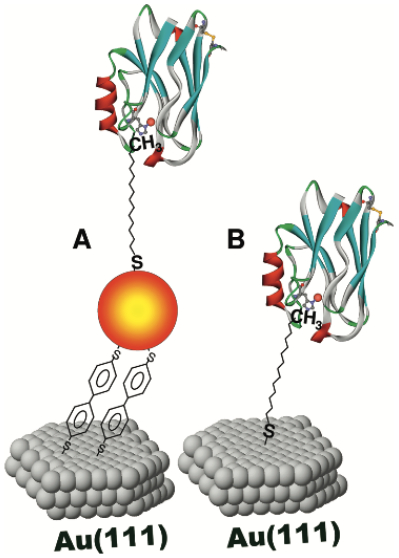


Figure 1. 12. Diagram representing molecular assembly of azurin protein on Au electrode, attached either by: **A)** a hydrophobic linker covalently bound to a Au NP which is covalently bound to the Au electrode or, **B)** the hydrophobic linker directly covalently bound to the Au electrode. Figure taken from reference[127] with permission from American Chemical Society.

1.4.2. Enzymes and Metals in Biocatalysis

Although not mainstream in biocatalysis, there have been several examples where combining enzymes and metals have shown advantages in being able to obtain certain reaction products or provide more efficient systems.

An interesting study showed that to convert a nitro group to an amine, V_2O_5 can be added to a reaction solution containing a nitroreductase. The nitroreductase alone will only form the hydroxylamine therefore V_2O_5 is required to catalyse the disproportionation of hydroxylamine to amine (and nitroso).[128] Another study used $HAuCl_4$ with lipase for a tandem lipase-catalysed kinetic resolution of a racemic allenic acetate followed by a gold-catalysed cycloisomerisation.[129]

Another area of significant research interest is artificial metalloenzymes where a synthetic metal complex is incorporated into a protein scaffold.[130-131] This has allowed for new reactions to be accessed by biocatalytic transformations such as Diels-Alder, Friedel-Crafts, asymmetric hydrogenation and alkene metathesis. The use of artificial metalloenzymes over small

molecule metal complexes can help to improve the reaction sustainability (allowing aqueous and low temperature conditions to be effective) and selectivity.

In terms of combining metal NPs with enzymes for catalytic applications, there have been some notable examples which show how the catalytic properties of the metal NP can be used to aid biocatalytic processes. AuPd NPs have been used to produce H_2O_2 from a H_2 and O_2 mixture for *in situ* supply of H_2O_2 for unspecific peroxygenases (UPO) enzymes, allowing them to carry out hydroxylation reactions on substrates such as cyclohexane and ethylbenzene as well as for oxidation of a styrene to an alcohol.[129, 132] An advantage of this chemo-bio tandem approach over other known methods for H_2O_2 production is the clean reaction that making H_2O_2 from H_2 and O_2 provides – with only H_2O as a by-product. The other benefit is by not using a UV-light irradiation procedure reactive oxidative species, which can cause enzyme instability, are minimised. Another example of the cooperative behaviour of metal NP and enzyme was described when using a hybrid catalyst comprising of co-immobilised lipase from *Candida antarctica* fraction B (CALB) and Au NPs on a support for a chemo-enzymatic cascade reaction to convert *p*-nitrophenyl esters into p-aminophenol.[133] In this cascade the CALB enzyme carries out the *p*-nitrophenyl ester hydrolysis and the Au NPs in the presence of $NaBH_4$ then undergo the nitro reduction to amine. It was found that co-immobilising the enzyme and Au NPs on the same support gave significant rate enhancement compared to a method where they were separately immobilised, therefore having the two catalytic sites in close proximity gave the best results. Another chemo-enzymatic cascade demonstrated the dual activity of gold or silver NPs and CALB enzyme as a bioconjugate where CALB was used to make the metal NPs.[134] The hybrid catalysts were successful for the stereoselective hydrolysis/cyclisation cascade reaction of allenic acetate to a 2,5-dihydrofuran.

1.5. Cofactor Recycling for Biocatalysis

Biocatalysis is becoming an increasingly attractive route choice in chemical manufacturing, particularly in the pharmaceutical industry, due to the societal push to reduce energy-consumption and waste and due to the progress in enzyme development.[135] Methods such as directed enzyme evolution have allowed for significant improvements in enzyme activity on substrates non-natural to the wild-type enzyme.[136] Thus, the substrate and reaction scope for biocatalysis is increasingly growing. Improvements in enzyme stability under reaction conditions have also increased their suitability for large-scale reaction synthesis.[135]

Approximately 50% of known enzymes require a so-called “cofactor” to be able to carry out their function; they typically oxidise the cofactor while reducing their substrate.[137] These cofactors can often be very expensive due to their complex structure and with no simple way to make them.[138] Thus, a cofactor recycling system must be used to make the biocatalysis reaction economically viable. Common cofactors include 1,4-dihydronicotinamide adenine dinucleotide (NADH) and the phosphorylated version (NADPH), flavin-containing cofactors (FMN and FAD), deazaflavins (F_{420}), quinones (PQQ), adenosine 5’-triphosphaye (ATP), coenzyme A (CoA) and S-adenosylmethionine (SAM).

The nicotinamide-containing cofactors (full structures shown in **Figure 1. 13.**) undergo a two-electron reduction and a proton transfer while being reduced from $NAD(P)^+$ to NAD(P)H. In an alcohol dehydrogenase, NAD(P)H binds to the prosthetic flavin found in the active site and is then used to transfer the hydride required for enantioselective reduction of a ketone to an alcohol.[139]

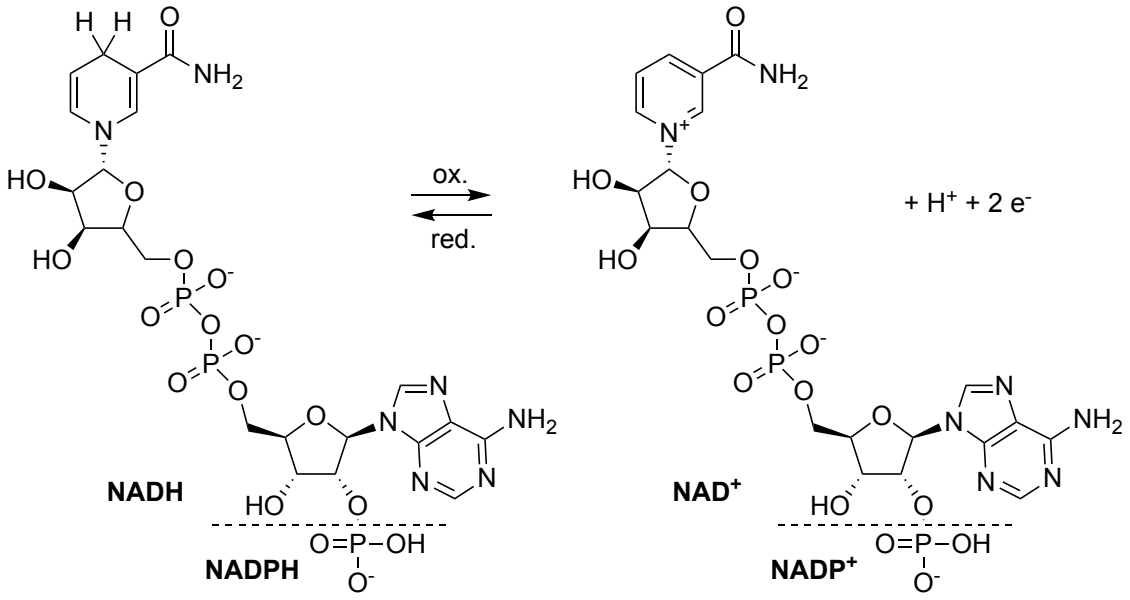


Figure 1. 13. Structures of 1,4-NADH, 1,4-NADPH and their respective oxidised forms, showing the hydrogen at the top of the left structure where the oxidation/reduction occurs.

For flavin-containing cofactors, a one or two electron reduction is possible.[140] The two-electron reduction pathway is accompanied by a loss of two protons, i.e. flavin mononucleotide (FMN) is reduced to the hydroquinone flavin mononucleotide ($FMNH_2$). **Figure 1. 14.** shows the chemical structures of the oxidised and reduced states from the two-electron reduction. The reverse direction of this pathway is observed when supplying an ene-reductase enzyme with $FMNH_2$, which the enzyme can use to reduce its covalently-bound flavin group which then transfers the hydride onto a docked alkene substrate, reducing it to an alkane (a so called ping-pong bi-bi mechanism).[141-142]

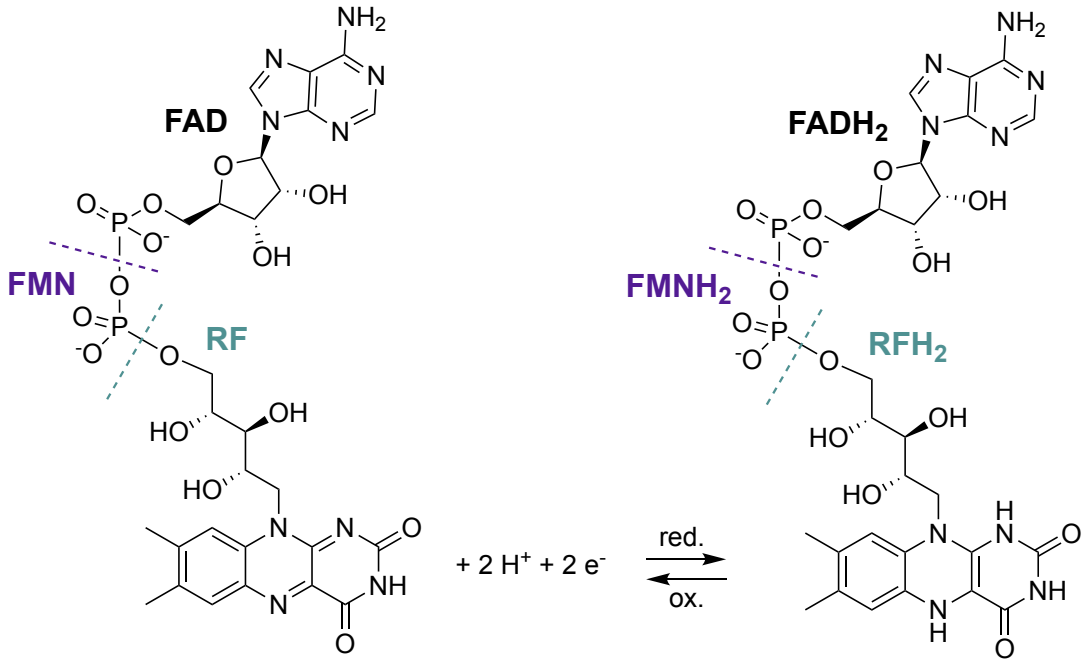


Figure 1. 14. Two-electron reduction of flavin cofactors: flavin adenine dinucleotide (FAD) is whole structure as shown, flavin mononucleotide (FMN) is shorter structure without the adenine and ribose, riboflavin (RF) is shorter again with a terminal hydroxyl group instead of phosphate group found in FMN. In all of these flavins the reduction occurs at the isoalloxazine fragment.

One-electron pathways have also been observed in biological systems which involve the formation of semi-quinone flavin radical species (**Figure 1. 15.**). For example, flavins are often found bound inside a protein (flavoenzyme) and in a NADPH-dependent cytochrome P450 enzyme, it is found that the bound flavin accepts two electrons from NADPH but then only transfers one-electron at a time towards other electron-acceptor proteins, leaving the flavin in a semi-quinone transient state.[143]

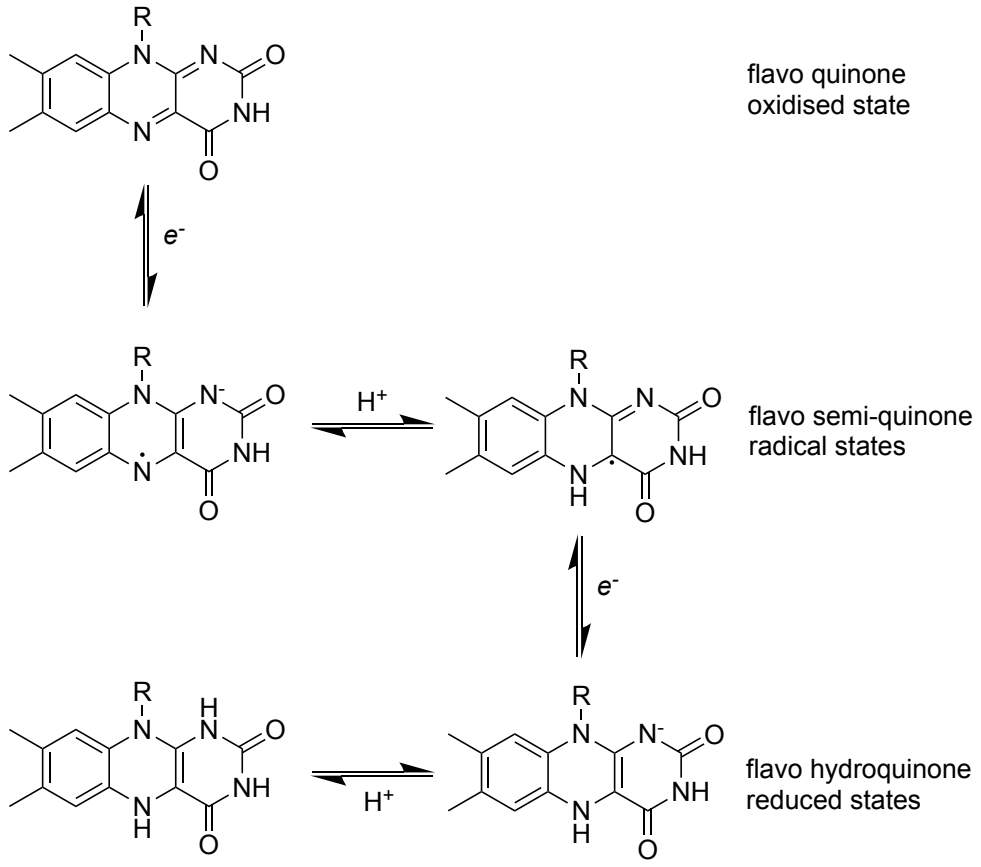


Figure 1. 15. One-electron reduction steps from oxidised flavin states to reduced hydroquinone, via radical semi-quinone states.

A typical recycling system for NAD(P)H cofactor involves the use of another enzyme to selectively reduce NAD(P)$^+$ to 1,4-NAD(P)H. The importance of complete selectivity to 1,4-NAD(P)H (and not to other NAD(P)H isomers, i.e. 1,6- or 1,2-NAD(P)H or over-reduced products) is such that only 1,4-NAD(P)H is accepted by the redox enzymes thus incorrect forms will limit the reaction rate and cause complete consumption of the expensive cofactor over multiple cycles making it no longer recyclable. Routinely, glucose dehydrogenase with glucose as the sacrificial reductant is used as the cofactor recycling system.[139] During the reaction there will be a build-up of gluconolactone which often involves reaction engineering steps to minimise the change to pH that this causes as well as separation from reaction products at the end of the reaction.[144]

A H_2-driven cofactor recycling system provides the advantage of providing an atom-efficient process with no build-up of waste.[145] For NADH this has been demonstrated with the use of soluble hydrogenase enzymes and with some homogeneous iridium complexes.[146-147] Despite the iridium catalysts showcasing high selectivity for the desired NADH isomer, subsequent studies found enzyme incompatibility of these complexes.[148] As discussed in **1.3.2**, despite soluble hydrogenases displaying very fast initial turnover numbers, they suffer with long-term stability. Thus the strategies mentioned in **1.3.2** were investigated to provide more robust recycling systems: where multiple enzymes were co-immobilised[121-122] or a chemo-bio combined system was used.[116, 123] These strategies could not be directly transferred for NADPH recycling due to the specificity of the soluble hydrogenases for NADH over NADPH. However, it has been shown that by performing some amino acid mutations near the cofactor binding pocket, the resulting variant allows $NADP^+$ to be accommodated and therefore carry out $NADP^+$ reduction.[149]

For H_2-driven flavin cofactor recycling, again it has been shown to be possible to use soluble hydrogenase.[145] Thereafter, the more robust Hyd1 was used and coupled to flavin-dependent ene-reductases, giving Hyd1 turnover frequencies of up to 20.4 min^{-1} and high total turnover numbers of up to 20,200 (with corresponding flavin turnover number of 240).[150] This system was also demonstrated coupled with nitroreductases for reducing nitro groups to amines.[151]

Other flavin recycling systems have been reported using photoreduction, direct electrochemical reduction or by using artificial cofactor analogues to be sacrificially oxidised while flavin is reduced.[152] For photoreduction, flavins have been shown to be reduced by light in the presence of a sacrificial electron donor, i.e. ethylenediaminetetraacetate (EDTA).[153-154] The light irradiation causes oxidised flavin to be excited and thus able to oxidise EDTA, forming a semi-quinone species. Two semi-quinone species can synproportionate, forming one hydroquinone flavin and one oxidised flavin. This photoreduction recycling method showed good compatibility coupled with ene-reductase type enzymes where high turnover frequencies (e.g. TOF = 194 h^{-1}) were achieved.[153, 155] Care was required to remove O_2 from

reaction solutions due to the formation of H_2O_2 in the presence of flavin, light and O_2. Therefore this system had less success in a biocatalytic oxidation reaction, using a monooxygenase which uses O_2 for the oxidation of a ketone.[154] For a similar biocatalytic reaction, using a monooxygenase carrying out alkene epoxidation, an electrochemical approach was shown to be successful for the regeneration of flavin cofactor. In this, a potential of -550 mV vs $Ag/AgCl_{sat.}$ (-353 mV vs SHE) was applied to the reaction solution containing the monooxygenase, flavin, catalase (added to convert any H_2O_2 into O_2 and H_2O) and styrene derivative substrate.[156]

In the case of the artificial cofactor analogues, these are based on the NADH structure but with a shorter side chain off the nicotinamide ring in place of the adenine dinucleotide, which therefore simplifies their chemical synthesis, making them significantly cheaper, alternative cofactors (selected examples shown in **Figure 1. 16.**).[157] For example, 1-benzyl-1,4-dihydronicotinamide (BNAH) has been used to directly reduce FAD to $FADH_2$, for $FADH_2$-dependent monooxygenase in the styrene epoxidation reaction.[158]

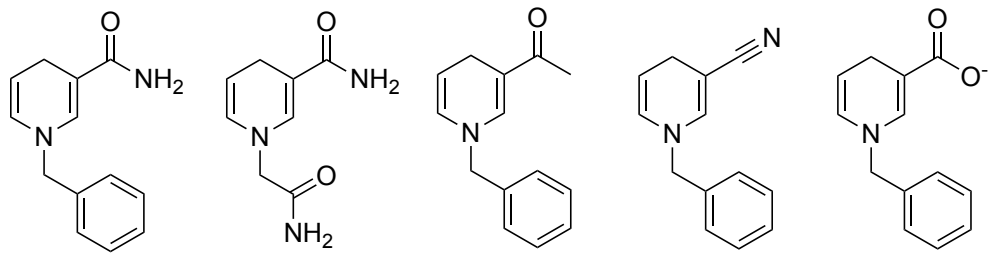


Figure 1. 16. Structures of selected artificial nicotinamide cofactors.[159]

However, using the artificial cofactors stoichiometrically for the reduction of flavin is not ideal for reaction intensification where high amounts would be needed to reach high flavin turnover numbers and fast reaction conversions. A H_2-driven recycling approach of these artificial cofactors has now been demonstrated.[159] Some enzymes have been found to directly accept

these cofactors therefore avoiding the need for expensive NADH or flavin cofactors.[160] Thus combining the advantages of using H_2-driven cofactor recycling and the cheap synthetic cofactors provides a very attractive biocatalytic process. Unfortunately, more research effort, likely in enzyme engineering, is required to expand the scope of enzymes which accept these synthetic cofactors.

1.6. Aims of This Project

This project was based on the hypothesis that an enzyme, when supplied with a sacrificial reductant could reduce metal ions, which have higher reduction potentials than the sacrificial reductant, and consequently form metal NPs. Additionally, the site-directed metal reduction by the presence of Fe-S clusters, transporting electrons from the site of oxidation to the enzyme surface, would allow for a controlled NP synthesis where monodisperse NPs are expected and well-stabilised by the enzyme through electrostatics. Thus, an isolated enzyme could act as a reductant and stabilising agent for metal NPs. The mild conditions, aqueous and room temperature, under which an enzyme typically functions would also provide an attractive synthesis route for making metal NPs, with low energy-consumption and no toxic chemicals required.

Two enzymes were chosen to be explored for this application, each with their own sacrificial reductant. Firstly, an NAD^+ reductase which could be supplied with NADH and secondly, a hydrogenase which could be supplied with H_2 gas. The NAD^+ reductase used was an isolated NAD^+ reductase moiety (i.e. no hydrogenase subunit attached) of *Hydrogenophilus thermoluteolus* soluble hydrogenase, expressed in *E. coli*. The hydrogenase used was [NiFe] hydrogenase 1 (Hyd1) from *E. coli*. Both enzymes have previously been investigated in the group for other applications and have been demonstrated to have good practicality due to

relative ease of preparation (suitable for expression in *E. coli*, allowing for high protein yields), stability and O_2-tolerance.

Previous work has shown that Hyd1 is able to reduce non-native flavin substrates, under 1 bar H_2, where it is proposed that the electrons released from H_2 oxidation occurring at the buried [NiFe] active site are passed through the Fe-S cluster chain which ends near the surface of Hyd1, thus accessible for the flavin substrates to be reduced.[150] Thus, it is proposed that a similar mechanism could occur for the reduction of metal ions. In the case of Hyd1, which oxidises H_2 at a potential approximately 50 mV higher than the thermodynamic $2H^+/H_2$ couple,[99] the reduction potential of the metal would need to be higher than this for the reduction to be thermodynamically feasible. For example, at pH 7, 25 °C, 1 bar H_2, this would equate to a potential of -0.35 V vs SHE. For utilising the NAD^+ reductase, its native cofactor NAD^+ has a reduction potential of -0.32 V vs SHE,[161] therefore the desired metal to be reduced would need to have a higher reduction potential than +0.32 V vs SHE (for the oxidation of NADH to occur).

Once metal NPs had been made, instead of investigating the reactivity of the metal NPs alone, the focus was on investigating whether there were synergistic behaviours of the metal and enzyme, based on the hypothesis that the enzyme molecules would remain in contact with the metal NPs after the NP synthesis. Thus, the reversible flow of electrons between metal NP and enzyme would be exploited. For the biohybrid NPs prepared using NAD^+ reductase (which are shown for making Au@Pt core-shell NPs) these were demonstrated for NADH cofactor recycling where the Pt metal can carry out H_2 oxidation and these electrons can be transported to the NAD^+ reductase flavin active site where the selective NAD^+ reduction can occur. In the absence of enzyme, Pt NPs are known to cause non-selective NAD^+ reduction thus analysis of NAD^+ reduction products would indicate whether there is optimal contact between the metal and enzyme. In the case of the NPs prepared using Hyd1, the effect of having an enhanced surface area for electronic contact between the enzyme and flavin cofactor was investigated by measuring the rate of flavin reduction.

Both cofactor recycling systems were also demonstrated in the presence of a cofactor-dependent enzyme and its substrate. Thus, showcasing the compatibility of the biohybrid enzyme-metal NPs with other redox enzymes and the potential advantage that this system can provide.

Lastly to expand the possible scope of applications for enzyme-metal NP biohybrids, their synthesis was investigated in the presence of a carbon support, thus creating a catalyst system more analogous to traditional heterogeneous catalysts. In this way, the catalyst system is more easily recycled for a reaction carried out in batch or implemented in a continuous flow reaction set-up.

1.7. This Thesis Explained

The following chapter (*Chapter 2*) explains the theory and technical details of the methods used for characterising the metal NPs synthesised in this project. It also details the methods used for enzyme kinetics and for onset reduction potential determination.

The first results chapter of this thesis (*Chapter 3*) discusses results obtained from synthesising metal NPs using an NAD^+ reductase and from testing the resulting enzyme-metal biohybrids in a biocatalytic application. These results have been included in a paper which has been published by the journal *Angewandte Chemie*, with the following title and citation:

> Controlled Biocatalytic Synthesis of a Metal Nanoparticle-Enzyme Hybrid: Demonstration for Catalytic H_2-driven NADH Recycling
>
> Lucy B. F. Browne, Tim Sudmeier, Maya A. Landis, Christopher S. Allen, Kylie A. Vincent, *Angew. Chem. Int. Ed.* **2024**, *63*, e202404024

Chapter 4 explores the scope for H_2-driven reduction of the cheap cofactor riboflavin in biotechnology; this study was conducted as preparatory work for the research described in

the next chapter. These results are included in a manuscript which also includes the work from other members of the group. The working title and authors list for this manuscript are as follows:

Riboflavin with H_2-Driven or Electrochemical Recycling is a Cheap Cofactor System for Supporting Biocatalytic Alkene Reduction

Lucy B. F. Browne, Charlotte C. Hancox, Sofia M. Helin, Peter M. T. Todd, Kylie A. Vincent

Chapter 5 moves onto exploring the synthesis of Au NPs using hydrogenase (Hyd1) under 1 bar H_2. In this chapter, a manuscript has been prepared to include the results of the NP synthesis as well as results from investigating the differences in riboflavin reduction rate observed with the Au NP biohybrids compared to Hyd1 alone. The working title and authors list for this manuscript are as follows:

Using Low Pressure H_2 with Hydrogenase for the Synthesis of Enzyme-Gold Nanoparticle Biohybrids; Demonstrating their Catalytic Rate Enhancement in Ene-Reductase Biocatalysis

Lucy B. F. Browne, Tim Sudmeier, Maya A. Landis, Kylie A. Vincent

The final results chapter (*Chapter 6*) describes work done on preparing biohybrid NPs supported on carbon. Characterisation of these NPs has been performed but further work is required to demonstrate their application and thus make this work suitable for publication. These hybrid catalysts were prepared by firstly immobilising Hyd1 on a carbon support then Au^{3+} reduction is carried out by Hyd1, resulting in Au NPs which are stabilised onto the carbon support (Hyd1-Au/C). Preliminary tests found the Hyd1 remains active in the hybrid catalyst, giving recently discovered activity for nitro to amine reduction which only occurs in the presence of both enzyme and support.[162] It is hypothesised that the presence of Au NPs in this hybrid catalyst could then be utilised for a cascade/tandem reaction where the enzyme carries out the first step followed by a Au NP catalysed step.

Chapter 7 of this thesis provides conclusions from each results chapter and the significance of the work as a whole. Ideas for future experiments and directions related to this project are also included.

1.8. References

[1] V. V. Mody, R. Siwale, A. Singh, H. R. Mody, *J Pharm Bioallied Sci* **2010**, *2*, 282-289.
[2] D. A. Giljohann, D. S. Seferos, W. L. Daniel, M. D. Massich, P. C. Patel, C. A. Mirkin, *Angew. Chem. Int. Ed. Engl.* **2010**, *49*, 3280-3294.
[3] M. Faraday, *Philos. Trans. R. Soc. London* **1857**, *147*, 145-181.
[4] V. Amendola, R. Pilot, M. Frasconi, O. M. Maragò, M. A. Iatì, *J. Phys.: Condens. Matter* **2017**, *29*, 203002.
[5] X. Huang, M. A. El-Sayed, *J. Adv. Res.* **2010**, *1*, 13-28.
[6] N. L. Rosi, C. A. Mirkin, *Chem. Rev.* **2005**, *105*, 1547-1562.
[7] C. A. Mirkin, R. L. Letsinger, R. C. Mucic, J. J. Storhoff, *Nature* **1996**, *382*, 607-609.
[8] H. Yabu, S. Yokokura, S. Shimizu, *Langmuir* **2024**, *40*, 3268-3273.
[9] K. Sokolov, J. Aaron, B. Hsu, D. Nida, A. Gillenwater, M. Follen, C. MacAulay, K. Adler-Storthz, B. Korgel, M. Descour, R. Pasqualini, W. Arap, W. Lam, R. Richards-Kortum, *Technology in Cancer Research & Treatment* **2003**, *2*, 491-504.
[10] G. Han, C.-C. You, B.-j. Kim, R. S. Turingan, N. S. Forbes, C. T. Martin, V. M. Rotello, *Angew. Chem. Int. Ed.* **2006**, *45*, 3165-3169.
[11] C. M. Pitsillides, E. K. Joe, X. Wei, R. R. Anderson, C. P. Lin, *Biophys. J.* **2003**, *84*, 4023-4032.
[12] K. Chandra, K. S. B. Culver, S. E. Werner, R. C. Lee, T. W. Odom, *Chem. Mater.* **2016**, *28*, 6763-6769.
[13] J.-E. Park, Y. Lee, J.-M. Nam, *Nano Lett.* **2018**, *18*, 6475-6482.
[14] C. J. Murphy, L. B. Thompson, A. M. Alkilany, P. N. Sisco, S. P. Boulos, S. T. Sivapalan, J. A. Yang, D. J. Chernak, J. Huang, *The Journal of Physical Chemistry Letters* **2010**, *1*, 2867-2875.
[15] D. H. M. Dam, J. H. Lee, P. N. Sisco, D. T. Co, M. Zhang, M. R. Wasielewski, T. W. Odom, *ACS Nano* **2012**, *6*, 3318-3326.
[16] M. J. Eller, K. Chandra, E. E. Coughlin, T. W. Odom, E. A. Schweikert, *Anal. Chem.* **2019**, *91*, 5566-5572.
[17] S. Anwar, M. B. Khawar, M. Ovais, A. Afzal, X. Zhang, *J. Pharm. Biomed. Anal.* **2023**, *226*, 115242.
[18] C. Deeb, X. Zhou, R. Miller, S. K. Gray, S. Marguet, J. Plain, G. P. Wiederrecht, R. Bachelot, *J. Phys. Chem. C* **2012**, *116*, 24734-24740.
[19] W. Shi, J. Casas, M. Venkataramasubramani, L. Tang, *ISRN Nanomaterials* **2012**, *2012*, 659043.
[20] L. Zhang, K. Xia, Z. Lu, G. Li, J. Chen, Y. Deng, S. Li, F. Zhou, N. He, *Chem. Mater.* **2014**, *26*, 1794-1798.
[21] M. M. Ghobashy, S. A. Alkhursani, H. A. Alqahtani, T. K. El-damhougy, M. Madani, *Materials Science and Engineering: B* **2024**, *301*, 117191.
[22] D. Zheng, C. Schwob, Y. Prado, Z. Ouzit, L. Coolen, T. Pauporté, *Nano Energy* **2022**, *94*, 106934.
[23] S. Phetsang, A. Phengdaam, C. Lertvachirapaiboon, R. Ishikawa, K. Shinbo, K. Kato, P. Mungkornasawakul, K. Ounnunkad, A. Baba, *Nanoscale Adv.* **2019**, *1*, 792-798.

[24] D. Sumanth Kumar, B. Jai Kumar, H. M. Mahesh, in *Synthesis of Inorganic Nanomaterials* (Eds.: S. Mohan Bhagyaraj, O. S. Oluwafemi, N. Kalarikkal, S. Thomas), Woodhead Publishing, **2018**, pp. 59-88.
[25] K. G. Stamplecoskie, P. V. Kamat, *The Journal of Physical Chemistry Letters* **2015**, *6*, 1870-1875.
[26] K. An, G. A. Somorjai, *ChemCatChem* **2012**, *4*, 1512-1524.
[27] S. Back, M. S. Yeom, Y. Jung, *ACS Catal.* **2015**, *5*, 5089-5096.
[28] I. V. Yudanov, R. Sahnoun, K. M. Neyman, N. Rösch, *The Journal of Chemical Physics* **2002**, *117*, 9887-9896.
[29] F. Viñes, J. R. B. Gomes, F. Illas, *Chem. Soc. Rev.* **2014**, *43*, 4922-4939.
[30] I. V. Yudanov, R. Sahnoun, K. M. Neyman, N. Rösch, J. Hoffmann, S. Schauermann, V. Johánek, H. Unterhalt, G. Rupprechter, J. Libuda, H.-J. Freund, *J. Phys. Chem. B* **2003**, *107*, 255-264.
[31] I. V. Yudanov, A. Genest, S. Schauermann, H.-J. Freund, N. Rösch, *Nano Lett.* **2012**, *12*, 2134-2139.
[32] C. J. Kliewer, C. Aliaga, M. Bieri, W. Huang, C.-K. Tsung, J. B. Wood, K. Komvopoulos, G. A. Somorjai, *J. Am. Chem. Soc.* **2010**, *132*, 13088-13095.
[33] J. N. Kuhn, W. Huang, C.-K. Tsung, Y. Zhang, G. A. Somorjai, *J. Am. Chem. Soc.* **2008**, *130*, 14026-14027.
[34] F. Zaera, *Acc. Chem. Res.* **2009**, *42*, 1152-1160.
[35] M. Comotti, C. Della Pina, R. Matarrese, M. Rossi, *Angew. Chem. Int. Ed.* **2004**, *43*, 5812-5815.
[36] C.-P. Liu, K.-C. Chen, C.-F. Su, P.-Y. Yu, P.-W. Lee, *Catalysts* **2019**, *9*, 517.
[37] H. Rodríguez Molina, J. L. Santos Muñoz, M. I. Domínguez Leal, T. R. Reina, S. Ivanova, M. Á. Centeno Gallego, J. A. Odriozola, *Front. Chem.* **2019**, *7*.
[38] F.-h. Lin, R.-a. Doong, *Applied Catalysis A: General* **2014**, *486*, 32-41.
[39] H.-E. Lee, K. D. Yang, S. M. Yoon, H.-Y. Ahn, Y. Y. Lee, H. Chang, D. H. Jeong, Y.-S. Lee, M. Y. Kim, K. T. Nam, *ACS Nano* **2015**, *9*, 8384-8393.
[40] M. Haruta, M. Daté, *Applied Catalysis A: General* **2001**, *222*, 427-437.
[41] C. Song, Q. Ge, L. Wang, *J. Phys. Chem. B* **2005**, *109*, 22341-22350.
[42] J. Luo, L. Wang, D. Mott, P. N. Njoki, Y. Lin, T. He, Z. Xu, B. N. Wanjana, I. I. S. Lim, C.-J. Zhong, *Adv. Mater.* **2008**, *20*.
[43] J. Suntivich, Z. Xu, C. E. Carlton, J. Kim, B. Han, S. W. Lee, N. Bonnet, N. Marzari, L. F. Allard, H. A. Gasteiger, K. Hamad-Schifferli, Y. Shao-Horn, *J. Am. Chem. Soc.* **2013**, *135*, 7985-7991.
[44] L. Yang, H. Feng, W. Liang, X. He, Y. Wang, D. Li, J. Zhang, Y. Sun, C. Tan, L. Jiang, *Energy Technology* **2022**, *10*, 2200202.
[45] S. Tsubota, T. Nakamura, K. Tanaka, M. Haruta, *Catal. Lett.* **1998**, *56*, 131-135.
[46] D. R. Rolison, *Science* **2003**, *299*, 1698-1701.
[47] T. V. Choudhary, D. W. Goodman, *Applied Catalysis A: General* **2005**, *291*, 32-36.
[48] L. He, F. Weniger, H. Neumann, M. Beller, *Angew. Chem. Int. Ed.* **2016**, *55*, 12582-12594.
[49] Y. Lou, J. Xu, Y. Zhang, C. Pan, Y. Dong, Y. Zhu, *Materials Today Nano* **2020**, *12*, 100093.
[50] R. Arrigo, M. E. Schuster, Z. Xie, Y. Yi, G. Wowsnick, L. L. Sun, K. E. Hermann, M. Friedrich, P. Kast, M. Hävecker, A. Knop-Gericke, R. Schlögl, *ACS Catal.* **2015**, *5*, 2740-2753.
[51] D. S. Su, S. Perathoner, G. Centi, *Chem. Rev.* **2013**, *113*, 5782-5816.
[52] H. Zhu, X. Ke, X. Yang, S. Sarina, H. Liu, *Angew. Chem. Int. Ed.* **2010**, *49*, 9657-9661.
[53] J. Wang, R. A. Ando, P. H. C. Camargo, *Angew. Chem. Int. Ed.* **2015**, *54*, 6909-6912.
[54] L. Zhang, G. Morello, S. B. Carr, F. A. Armstrong, *J. Am. Chem. Soc.* **2020**, *142*, 12699-12707.
[55] J. D. Aiken, Y. Lin, R. G. Finke, *J. Mol. Catal. A: Chem.* **1996**, *114*, 29-51.
[56] N. Baig, I. Kammakakam, W. Falath, *Materials Advances* **2021**, *2*, 1821-1871.

[57] G. Palazzo, G. Valenza, M. Dell'Aglio, A. De Giacomo, *J. Colloid Interface Sci.* **2017**, *489*, 47-56.
[58] J. E. Ortiz-Castillo, R. C. Gallo-Villanueva, M. J. Madou, V. H. Perez-Gonzalez, *Coord. Chem. Rev.* **2020**, *425*, 213489.
[59] N. R. Jana, L. Gearheart, C. J. Murphy, *Adv. Mater.* **2001**, *13*, 1389-1393.
[60] A. Chhatre, R. Thaokar, A. Mehra, *Crystal Growth & Design* **2018**, *18*, 3269-3282.
[61] J. Turkevich, P. C. Stevenson, J. Hillier, *Discuss. Faraday Soc.* **1951**, *11*, 55-75.
[62] M. Wuithschick, A. Birnbaum, S. Witte, M. Sztucki, U. Vainio, N. Pinna, K. Rademann, F. Emmerling, R. Kraehnert, J. Polte, *ACS Nano* **2015**, *9*, 7052-7071.
[63] Y. Gao, L. Torrente-Murciano, *Nanoscale* **2020**, *12*, 2740-2751.
[64] X. Ji, X. Song, J. Li, Y. Bai, W. Yang, X. Peng, *J. Am. Chem. Soc.* **2007**, *129*, 13939-13948.
[65] N. G. Bastús, J. Comenge, V. Puntes, *Langmuir* **2011**, *27*, 11098-11105.
[66] J. Kimling, M. Maier, B. Okenve, V. Kotaidis, H. Ballot, A. Plech, *J. Phys. Chem. B* **2006**, *110*, 15700-15707.
[67] W. Haiss, N. T. K. Thanh, J. Aveyard, D. G. Fernig, *Anal. Chem.* **2007**, *79*, 4215-4221.
[68] C. Deraedt, L. Salmon, S. Gatard, R. Ciganda, R. Hernandez, J. Ruiz, D. Astruc, *Chem. Commun.* **2014**, *50*, 14194-14196.
[69] S. M. Ansar, F. S. Ameer, W. Hu, S. Zou, C. U. Pittman, Jr., D. Zhang, *Nano Lett.* **2013**, *13*, 1226-1229.
[70] Z. Wang, B. Tan, I. Hussain, N. Schaeffer, M. F. Wyatt, M. Brust, A. I. Cooper, *Langmuir* **2007**, *23*, 885-895.
[71] M. Brust, M. Walker, D. Bethell, D. J. Schiffrin, R. Whyman, *J. Chem. Soc., Chem. Commun.* **1994**, 801-802.
[72] A. Guleria, H. Sachdeva, K. Saini, K. Gupta, J. Mathur, *Appl. Organomet. Chem.* **2022**, *36*, e6778.
[73] A. Gour, N. K. Jain, *Artificial Cells, Nanomedicine, and Biotechnology* **2019**, *47*, 844-851.
[74] C. Kamaraj, S. Karthi, A. D. Reegan, G. Balasubramani, G. Ramkumar, K. Kalaivani, A. A. Zahir, P. Deepak, S. Senthil-Nathan, M. M. Rahman, A. R. Md Towfiqul Islam, G. Malafaia, *Environ. Res.* **2022**, *213*, 113711.
[75] K. X. Lee, K. Shameli, Y. P. Yew, S.-Y. Teow, H. Jahangirian, R. Rafiee-Moghaddam, T. J. Webster, *Int. J. Nanomedicine* **2020**, *15*, 275-300.
[76] N. Joudeh, A. Saragliadis, G. Koster, P. Mikheenko, D. Linke, *Frontiers in Nanotechnology* **2022**, *4*.
[77] M. Kitching, M. Ramani, E. Marsili, *Microb. Biotechol.* **2015**, *8*, 904-917.
[78] N. J. Creamer, V. S. Baxter-Plant, J. Henderson, M. Potter, L. E. Macaskie, *Biotechnol. Lett* **2006**, *28*, 1475-1484.
[79] A. N. Mabbett, D. Sanyahumbi, P. Yong, L. E. Macaskie, *Environmental Science & Technology* **2006**, *40*, 1015-1021.
[80] W. D. Windt, P. Aelterman, W. Verstraete, *Environ. Microbiol.* **2005**, *7*, 314-325.
[81] N. J. Creamer, I. P. Mikheenko, P. Yong, K. Deplanche, D. Sanyahumbi, J. Wood, K. Pollmann, M. Merroun, S. Selenska-Pobell, L. E. Macaskie, *Catal. Today* **2007**, *128*, 80-87.
[82] R. Lloyd Jon, P. Yong, E. Macaskie Lynne, *Appl. Environ. Microbiol.* **1998**, *64*, 4607-4609.
[83] K. Deplanche, I. Caldelari, I. P. Mikheenko, F. Sargent, L. E. Macaskie, *Microbiology* **2010**, *156*, 2630-2640.
[84] K. Deplanche, L. E. Macaskie, *Biotechnol. Bioeng.* **2008**, *99*, 1055-1064.
[85] I. A. Adelere, A. Lateef, *Nanotechnol. Rev.* **2016**, *5*, 567-587.
[86] M. Durán, C. P. Silveira, N. Durán, *IET Nanobiotechnology* **2015**, *9*, 314-323.
[87] A. Rangnekar, T. K. Sarma, A. K. Singh, J. Deka, A. Ramesh, A. Chattopadhyay, *Langmuir* **2007**, *23*, 5700-5706.
[88] D. Scott, M. Toney, M. Muzikár, *J. Am. Chem. Soc.* **2008**, *130*, 865-874.

[89] M. Gholami-Shabani, M. Shams-Ghahfarokhi, Z. Gholami-Shabani, A. Akbarzadeh, G. Riazi, S. Ajdari, A. Amani, M. Razzaghi-Abyaneh, *Process Biochem.* **2015**, *50*, 1076-1085.
[90] M. Luo, Y. Hong, W. Yao, C. Huang, Q. Xu, Q. Wu, *Journal of Materials Chemistry A* **2015**, *3*, 2770-2775.
[91] A. Dorjgotov, Y. Jeon, J. Hwang, B. Ulziidelger, H. S. Kim, B. Han, Y.-G. Shul, *Electrochim. Acta* **2017**, *228*, 389-397.
[92] G. Zhang, H. Zheng, M. Shen, L. Wang, X. Wang, *J. Phys. Chem. Solids* **2015**, *81*, 79-87.
[93] K. Deplanche, M. L. Merroun, M. Casadesus, D. T. Tran, I. P. Mikheenko, J. A. Bennett, J. Zhu, I. P. Jones, G. A. Attard, J. Wood, S. Selenska-Pobell, L. E. Macaskie, *Journal of The Royal Society Interface* **2012**, *9*, 1705-1712.
[94] Y. Montet, P. Amara, A. Volbeda, X. Vernede, E. C. Hatchikian, M. J. Field, M. Frey, J. C. Fontecilla-Camps, *Nature Structural Biology* **1997**, *4*, 523-526.
[95] D. R. Aireddy, K. Ding, *ACS Catal.* **2022**, *12*, 4707-4723.
[96] K. A. Vincent, A. Parkin, F. A. Armstrong, *Chem. Rev.* **2007**, *107*, 4366-4413.
[97] C. Léger, S. Dementin, P. Bertrand, M. Rousset, B. Guigliarelli, *J. Am. Chem. Soc.* **2004**, *126*, 12162-12172.
[98] K. A. Vincent, A. Parkin, O. Lenz, S. P. J. Albracht, J. C. Fontecilla-Camps, R. Cammack, B. Friedrich, F. A. Armstrong, *J. Am. Chem. Soc.* **2005**, *127*, 18179-18189.
[99] M. J. Lukey, A. Parkin, M. M. Roessler, B. J. Murphy, J. Harmer, T. Palmer, F. Sargent, F. A. Armstrong, *J. Biol. Chem.* **2010**, *285*, 3928-3938.
[100] A. Volbeda, P. Amara, C. Darnault, J.-M. Mouesca, A. Parkin, M. M. Roessler, F. A. Armstrong, J. C. Fontecilla-Camps, *Proceedings of the National Academy of Sciences* **2012**, *109*, 5305-5310.
[101] A. Volbeda, C. Darnault, A. Parkin, F. Sargent, F. A. Armstrong, J. C. Fontecilla-Camps, *Structure* **2013**, *21*, 184-190.
[102] P. A. Ash, S. E. T. Kendall-Price, R. M. Evans, S. B. Carr, A. R. Brasnett, S. Morra, J. S. Rowbotham, R. Hidalgo, A. J. Healy, G. Cinque, M. D. Frogley, F. A. Armstrong, K. A. Vincent, *Chem. Sci.* **2021**, *12*, 12959-12970.
[103] K. A. Bagley, C. J. Van Garderen, M. Chen, W. H. Woodruff, E. C. Duin, S. P. J. Albracht, *Biochemistry* **1994**, *33*, 9229-9236.
[104] P. Wulff, C. Thomas, F. Sargent, F. A. Armstrong, *JBIC Journal of Biological Inorganic Chemistry* **2016**, *21*, 121-134.
[105] C. C. Page, C. C. Moser, X. Chen, P. L. Dutton, *Nature* **1999**, *402*, 47-52.
[106] R. M. Evans, P. A. Ash, S. E. Beaton, E. J. Brooke, K. A. Vincent, S. B. Carr, F. A. Armstrong, *J. Am. Chem. Soc.* **2018**, *140*, 10208-10220.
[107] T. Goris, A. F. Wait, M. Saggu, J. Fritsch, N. Heidary, M. Stein, I. Zebger, F. Lendzian, F. A. Armstrong, B. Friedrich, O. Lenz, *Nature Chemical Biology* **2011**, *7*, 310-318.
[108] R. M. Evans, A. Parkin, M. M. Roessler, B. J. Murphy, H. Adamson, M. J. Lukey, F. Sargent, A. Volbeda, J. C. Fontecilla-Camps, F. A. Armstrong, *J. Am. Chem. Soc.* **2013**, *135*, 2694-2707.
[109] M. M. Roessler, R. M. Evans, R. A. Davies, J. Harmer, F. A. Armstrong, *J. Am. Chem. Soc.* **2012**, *134*, 15581-15594.
[110] J. Fritsch, P. Scheerer, S. Frielingsdorf, S. Kroschinsky, B. Friedrich, O. Lenz, C. M. T. Spahn, *Nature* **2011**, *479*, 249-252.
[111] T. Burgdorf, E. van der Linden, M. Bernhard, Y. Yin Qing, W. Back Jaap, F. Hartog Aloysius, O. Muijsers Anton, G. de Koster Chris, P. J. Albracht Simon, B. Friedrich, *J. Bacteriol.* **2005**, *187*, 3122-3132.
[112] L. Lauterbach, O. Lenz, K. A. Vincent, *The FEBS Journal* **2013**, *280*, 3058-3068.
[113] J. Preissler, S. Wahlefeld, C. Lorent, C. Teutloff, M. Horch, L. Lauterbach, S. P. Cramer, I. Zebger, O. Lenz, *Biochim. Biophys. Acta - Bioenerg.* **2018**, *1859*, 8-18.
[114] J. C. Fontecilla-Camps, A. Volbeda, C. Cavazza, Y. Nicolet, *Chem. Rev.* **2007**, *107*, 4273-4303.

[115] Y. Shomura, M. Taketa, H. Nakashima, H. Tai, H. Nakagawa, Y. Ikeda, M. Ishii, Y. Igarashi, H. Nishihara, K.-S. Yoon, S. Ogo, S. Hirota, Y. Higuchi, *Science* **2017**, *357*, 928-932.
[116] J. S. Rowbotham, H. A. Reeve, K. A. Vincent, *ACS Catal.* **2021**, *11*, 2596-2604.
[117] J. M. Berrisford, L. A. Sazanov, *J. Biol. Chem.* **2009**, *284*, 29773-29783.
[118] L. Lauterbach, J. Liu, M. Horch, P. Hummel, A. Schwarze, M. Haumann, K. A. Vincent, O. Lenz, I. Zebger, *Eur. J. Inorg. Chem.* **2011**, *2011*, 1067-1079.
[119] L. Lauterbach, Z. Idris, K. A. Vincent, O. Lenz, *PLOS ONE* **2011**, *6*, e25939.
[120] J. Ratzka, L. Lauterbach, O. Lenz, M. B. Ansorge-Schumacher, *Biocatal. Biotransform.* **2011**, *29*, 246-252.
[121] H. A. Reeve, L. Lauterbach, O. Lenz, K. A. Vincent, *ChemCatChem* **2015**, *7*, 3480-3487.
[122] H. A. Reeve, L. Lauterbach, P. A. Ash, O. Lenz, K. A. Vincent, *Chem. Commun.* **2012**, *48*, 1589-1591.
[123] X. Zhao, S. E. Cleary, C. Zor, N. Grobert, H. A. Reeve, K. A. Vincent, *Chem. Sci.* **2021**, *12*, 8105-8114.
[124] J. C. Love, L. A. Estroff, J. K. Kriebel, R. G. Nuzzo, G. M. Whitesides, *Chem. Rev.* **2005**, *105*, 1103-1170.
[125] H. Krassen, S. T. Stripp, N. Böhm, A. Berkessel, T. Happe, K. Ataka, J. Heberle, *Eur. J. Inorg. Chem.* **2011**, *2011*, 1138-1146.
[126] X. Yan, J. Tang, D. Tanner, J. Ulstrup, X. Xiao, in *Catalysts, Vol. 10*, **2020**.
[127] P. S. Jensen, Q. Chi, J. Zhang, J. Ulstrup, *J. Phys. Chem. C* **2009**, *113*, 13993-14000.
[128] S. Bisagni, A. Bornadel, A. H. Cherney, S. J. Hedley, J. LePaih, S. M. Mennen, A. Pushpanath, I. Slabu, J. Tedrow, B. Dominguez, *Current Research in Chemical Biology* **2022**, *2*, 100026.
[129] M. Asikainen, N. Krause, *Adv. Synth. Catal.* **2009**, *351*, 2305-2309.
[130] A. G. Jarvis, *Curr. Opin. Chem. Biol.* **2020**, *58*, 63-71.
[131] F. Schwizer, Y. Okamoto, T. Heinisch, Y. Gu, M. M. Pellizzoni, V. Lebrun, R. Reuter, V. Köhler, J. C. Lewis, T. R. Ward, *Chem. Rev.* **2018**, *118*, 142-231.
[132] D. Wilbers, J. Brehm, R. J. Lewis, J. van Marwijk, T. E. Davies, D. J. Morgan, D. J. Opperman, M. S. Smit, M. Alcalde, A. Kotsiopoulos, S. T. L. Harrison, G. J. Hutchings, S. J. Freakley, *Green Chem.* **2021**, *23*, 4170-4180.
[133] H. R. de Barros, L. Y. Tanaka, R. T. P. da Silva, J. Santiago-Arcos, S. I. C. de Torresi, F. López-Gallego, *Particle & Particle Systems Characterization* **2021**, *38*, 2100136.
[134] J. M. Naapuri, N. Losada-Garcia, J. Deska, J. M. Palomo, *Nanoscale* **2022**, *14*, 5701-5715.
[135] R. A. Sheldon, D. Brady, M. L. Bode, *Chem. Sci.* **2020**, *11*, 2587-2605.
[136] S. P. France, R. D. Lewis, C. A. Martinez, *JACS Au* **2023**.
[137] J. D. Fischer, G. L. Holliday, S. A. Rahman, J. M. Thornton, *J. Mol. Biol.* **2010**, *403*, 803-824.
[138] S. Mordhorst, J. N. Andexer, *Natural Product Reports* **2020**, *37*, 1316-1333.
[139] F. Hollmann, D. J. Opperman, C. E. Paul, *Angew. Chem. Int. Ed.* **2021**, *60*, 5644-5665.
[140] S. A. Baker Dockrey, A. R. H. Narayan, *Tetrahedron* **2019**, *75*, 1115-1121.
[141] M. Hall, C. Stueckler, H. Ehammer, E. Pointner, G. Oberdorfer, K. Gruber, B. Hauer, R. Stuermer, W. Kroutil, P. Macheroux, K. Faber, *Adv. Synth. Catal.* **2008**, *350*, 411-418.
[142] P. A. Karplus, K. M. Fox, V. Massey, *FASEB J.* **1995**, *9*, 1518-1526.
[143] R. M. Davydov, G. Jennings, B. M. Hoffman, L. M. Podust, *Arch. Biochem. Biophys.* **2019**, *673*, 108080.
[144] V. Kaswurm, W. V. Hecke, K. D. Kulbe, R. Ludwig, *Adv. Synth. Catal.* **2013**, *355*, 1709-1714.
[145] A. Al-Shameri, S. J. P. Willot, C. E. Paul, F. Hollmann, L. Lauterbach, *Chem. Commun.* **2020**, *56*, 9667-9670.
[146] R. Mertens, L. Greiner, E. C. D. van den Ban, H. B. C. M. Haaker, A. Liese, *J. Mol. Catal. B: Enzym.* **2003**, *24-25*, 39-52.

[147] Y. Maenaka, T. Suenobu, S. Fukuzumi, *J. Am. Chem. Soc.* **2012**, *134*, 367-374.
[148] V. Köhler, Y. M. Wilson, M. Dürrenberger, D. Ghislieri, E. Churakova, T. Quinto, L. Knörr, D. Häussinger, F. Hollmann, N. J. Turner, T. R. Ward, *Nat. Chem.* **2013**, *5*, 93-99.
[149] J. Preissler, H. A. Reeve, T. Zhu, J. Nicholson, K. Urata, L. Lauterbach, L. L. Wong, K. A. Vincent, O. Lenz, *ChemCatChem* **2020**, *12*, 4853-4861.
[150] S. Joseph Srinivasan, S. E. Cleary, M. A. Ramirez, H. A. Reeve, C. E. Paul, K. A. Vincent, *Angew. Chem. Int. Ed.* **2021**, *60*, 13824-13828.
[151] M. A. Ramirez, S. Joseph Srinivasan, S. E. Cleary, P. M. T. Todd, H. A. Reeve, K. A. Vincent, *Frontiers in Catalysis* **2022**, *2*.
[152] W. Zhang, F. Hollmann, *Chem. Commun.* **2018**, *54*, 7281-7289.
[153] F. Hollmann, A. Taglieber, F. Schulz, M. T. Reetz, *Angew. Chem. Int. Ed.* **2007**, *46*, 2903-2906.
[154] A. Taglieber, F. Schulz, F. Hollmann, M. Rusek, M. T. Reetz, *ChemBioChem* **2008**, *9*, 565-572.
[155] M. M. Grau, J. C. van der Toorn, L. G. Otten, P. Macheroux, A. Taglieber, F. E. Zilly, I. W. C. E. Arends, F. Hollmann, *Adv. Synth. Catal.* **2009**, *351*, 3279-3286.
[156] F. Hollmann, K. Hofstetter, T. Habicher, B. Hauer, A. Schmid, *J. Am. Chem. Soc.* **2005**, *127*, 6540-6541.
[157] C. E. Paul, I. W. C. E. Arends, F. Hollmann, *ACS Catal.* **2014**, *4*, 788-797.
[158] C. E. Paul, D. Tischler, A. Riedel, T. Heine, N. Itoh, F. Hollmann, *ACS Catal.* **2015**, *5*, 2961-2965.
[159] H. A. Reeve, J. Nicholson, F. Altaf, T. H. Lonsdale, J. Preissler, L. Lauterbach, O. Lenz, S. Leimkühler, F. Hollmann, C. E. Paul, K. A. Vincent, *Chem. Commun.* **2022**, *58*, 10540-10543.
[160] C. E. Paul, S. Gargiulo, D. J. Opperman, I. Lavandera, V. Gotor-Fernández, V. Gotor, A. Taglieber, I. W. C. E. Arends, F. Hollmann, *Org. Lett.* **2013**, *15*, 180-183.
[161] C. Greening, F. H. Ahmed, A. E. Mohamed, B. M. Lee, G. Pandey, A. C. Warden, C. Scott, J. G. Oakeshott, M. C. Taylor, C. J. Jackson, *Microbiol Mol Biol Rev* **2016**, *80*, 451-493.
[162] D. Sokolova, T. C. Lurshay, J. S. Rowbotham, G. Stonadge, H. A. Reeve, S. E. Cleary, T. Sudmeier, K. A. Vincent, *ChemRxiv preprint* **2024**.

Chapter 2. Theory of Characterisation Methods

2.1. Techniques Core to This Thesis Work

The techniques discussed in this section were the primary characterisation tools I used for *in situ* analysis of metal NPs – UV-visible (UV-vis) spectroscopy – and *ex situ* analysis of metal NPs – cyclic voltammetry (CV), dynamic light scattering (DLS) and zeta potential. UV-vis was also used for enzyme kinetics and CV was additionally used for identifying the reduction potential of a substrate desired to be reduced enzymatically.

2.1.1. UV-vis

2.1.1.1. Theory of UV-vis Spectroscopy

The radiation of light causes electrons to be excited from lower to higher energy levels. The following equation relates the energy of the electronic transition and the wavelength of absorbed light (λ):

$$\Delta E = \frac{hc}{\lambda}$$

ΔE is the energy difference between two electronic energy levels, h is Planck's constant and c is the speed of light. Thus, the higher the energy transition between orbitals, the lower the wavelength of absorbance. The type of electronic transition will depend on what energy levels are occupied in a species, with the most likely transition occurring from the highest occupied molecular orbital (HOMO) to the lowest unoccupied molecular orbital (LUMO). The possible electronic transitions are shown in **Figure 2. 1.**

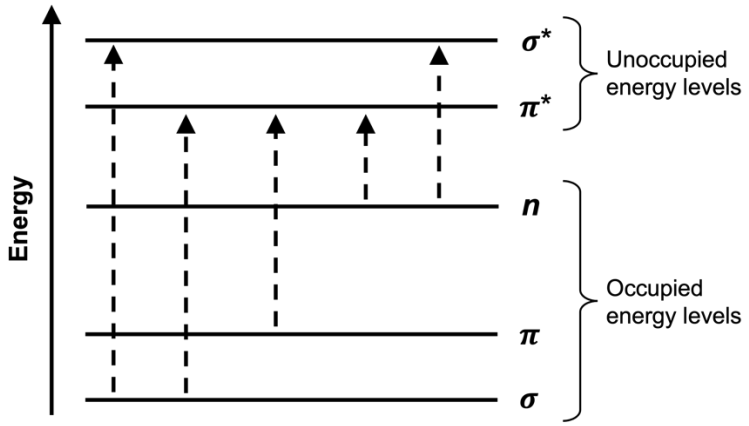


Figure 2. 1. Diagram of energy levels and possible electronic transitions.

Most of these transitions will absorb wavelengths in the ultraviolet (UV) to visible regions of the electromagnetic spectrum, covering a range of 100-800 nm. Therefore, most UV-visible (UV-vis) spectrophotometers are built to detect absorbance from at least 200-800 nm. Since different species will have different absorbance spectra this allows us to study what species are present and at what concentration.

The Beer Lambert Law describes the relationship between the absorbance (*A*) at a particular wavelength of a species in solution:

$$A = \varepsilon C l$$

Where ε is the molar extinction coefficient for a specific species (M^{-1} cm^{-1}), *C* (M) is the concentration of the species in solution and *l* (cm) is the path length of light through the solution (in practical terms, the width of the cuvette which holds your solution of sample in the direction light passes through).

2.1.1.2. UV-vis Spectroscopy Applied to Cofactors

The UV-vis spectra of biological cofactors NAD^+ and NADH, which are used in this thesis, display an absorbance peak at 260 nm which arises from the π to π^* electronic transitions from

their aromatic adenine groups as well as aromatic nicotinamide group for NAD^+. Once NAD^+ has been reduced to NADH, the nicotinamide is converted to a dihydronicotinamide, hence losing aromaticity, and the electronic transition (which is now *n* to π^*) is lower in energy, hence there is an absorbance peak at higher wavelength (λ_{max} at 340 nm). Thus UV-vis spectroscopy can be used to monitor the rate of NADH formation by the increase in absorbance at 340 nm.

Similarly, for flavin cofactors, which are also studied in this thesis, the UV-vis absorbance can be used to determine what redox states (and protonation states) are present in solution.[1] The isoalloxazine fragment of a flavin gives rise to their characteristic absorbance spectra. Upon a two-electron reduction of oxidised flavin, the α-diimine bond is reduced to an ethene-1,2-diamine group. This changes which molecular orbitals are occupied; in the oxidised form, the π_3 orbital is the LUMO and allows a relatively low energy π to π^* (π_2 to π_3) transition to take place, giving rise to a strong absorbance around 450 nm.[2] In the hydroquinone state (the fully reduced state) the π_3 orbital is now fully occupied therefore there is no absorbance at 450 nm; the next available energy transition, at higher energy, is from the π_3 to π_5 orbitals which gives absorbance around 320 nm. Therefore, monitoring the decrease of the absorbance around 450 nm is a useful method to determine rate data for the reduction of oxidised flavin to hydroquinone flavin (or in reverse for the oxidation). However, what can complicate the spectra is the appearance of semi-reduced, radical species (known as semi-quinones) which can occur from a one-electron reduction of the oxidised flavin. These can exist as either anionic or neutral protonation states (structures shown in *Chapter 1*, **Figure 1. 15.**). These will also have the π_2 to π_3 transition that was seen for the oxidised flavin, but this will give absorbance at higher wavelengths as the energy gap between orbitals gets smaller upon reduction. These will also have a very strong absorbance peak around 340 nm due to the transition from the singly occupied molecular orbital (SOMO) to LUMO, π_3 to π_5.

2.1.1.3. UV-vis Spectroscopy Applied to Metal NPs

A solution of metal NPs is usually strongly coloured: with yellow, red, purple or brown being common. The colour will depend on the type of metal as well as the size and shape of the NPs which are present. These visible colours originate from their absorbance across wavelengths of 400-800 nm. A material which absorbs across all visible regions appears black in colour therefore a very broad absorbance with no significant peak in the spectrum will appear brown to black in colour which is the case for Pt or Pd NPs in solution.

Gold NPs have been widely studied for their photophysical properties due to their tuneable λ_{max} giving rise to a range of colours.[3] Their absorbance spectra will typically exhibit a peak with the λ_{max} between 500-600 nm. If there is a sharp absorbance peak with its λ_{max} around 500 nm the solution will be red in colour and as the λ_{max} is increased to around 600 nm (or the absorbance peak broadens: increasing the absorbance at higher wavelengths) the solution will be more purple. With even higher wavelengths of absorbance, the solution will appear blue. The origin of the absorbance peak is due to the surface plasmon resonance (SPR) effect that was introduced in **1.1**.

The absorbance spectra therefore have contributions from SPR and scattering effects. SPR dominates in smaller NPs, up to around 50 nm, above which scattering begins to dominate.[4]

Smaller sized NPs will have a λ_{max} at lower wavelengths because of two effects: the extrinsic and intrinsic effects.[5] The extrinsic effect can be simplified as when the NP size is increased, the oscillating electron cloud becomes less uniformly polarised at different points in the NP. This phenomenon has been described by Mie's theory and means that λ_{max} will increase with the size of the NP as well as give rise to a broadening effect of the SPR peak.[6] The intrinsic effect starts to effect Au NPs which are < 30 nm: at this size the mean free path of the conducting electrons is the same as the size of the NPs which therefore quenches the SPR effect, until about 2 nm where the SPR effect has been fully quenched and there is no longer a peak seen in the absorbance spectra.[5]

It is also worth noting that the surroundings of the NP (stabilising ligands and solvent) will also have an impact on the position of the λ_{max}. As the size of the NP decreases, the effect of the surroundings will increase, as the percentage of surface atoms increases.[7]

The reason the SPR absorbance peak is unique to Au, Ag, Cu (and Al) is due to their electronic structure since they have filled d-shells which minimises intraband transitions.[8] Intraband transitions cause electron-electron scattering which increases SPR relaxation frequency. Thus electron-electron scattering has a high probability in metal NPs such as Pt and Pd, which have partially filled d-states, which is the reason for no observed SPR peak in their spectra.

UV-vis spectroscopy is therefore a very useful tool to detect the formation of metal NPs of sizes greater than 2 nm. For gold NPs, the position and shape of the SPR peak indicates the size and size distribution of the NPs. The ratio of the absorbance at the SPR peak to the absorbance at 450 nm was used in this thesis to estimate the average NP size.[9]

2.1.1.4. UV-vis Procedure for Metal NP Analysis

The UV-vis spectroscopy described in this thesis was all carried out using a Cary 60 UV-visible spectrophotometer (Agilent) which was set-up inside a glovebox with inert atmosphere. A Peltier accessory was used to control the temperature of the cuvette which was set to 25 °C, unless otherwise stated.

For most of the analysis of metal NPs, this was carried out using a plastic micro-cuvette (1 cm path length) which allowed for small volumes to be analysed (minimum volume of 60 μL). For monitoring reaction progress of NP formation, the reaction solution was added to the micro-cuvette and the spectra were recorded from 800 to 200 nm (after running a baseline with the appropriate reaction buffer/water).

In the case of the NPs prepared using NADH and NRase enzyme (described in *Chapter 3*), to observe the NADH oxidation to NAD^+, small aliquots of the NP reaction solutions were diluted

with pH 8 water (made to pH 8 by addition of NaOH) by a factor of 10 (e.g. 10 µL reaction solution and 90 µL pH 8 water) so that the peak at 340 nm for NADH could be fully observed in the measurable absorbance range.

For the NPs made using hydrogenase under H_2 (described in *Chapter 4 and 5*), some *in situ* analysis was carried out by adding the reagents to a quartz 1 mL cuvette (1 cm path length) with a H_2 flow (set-up the same as described in next section, **2.1.1.5**), and setting the UV-vis spectrophotometer to record scans regularly throughout an experiment.

2.1.1.5. UV-vis Procedure for Enzyme Kinetics

For studying the kinetics of hydrogenase (specifically Hyd1 in this thesis), it is useful to perform *in situ* analysis with the UV-vis cuvette under H_2.

A typical procedure for measuring the activity of Hyd1 for the reduction of a flavin under H_2 was as follows. The settings on the Scan software were set to record a spectrum from 800 to 200 nm every 30 seconds during an assay. A background spectrum of pH 7, 50 mM potassium phosphate in a quartz 1 mL cuvette was recorded before beginning the experiment. A 0.103 mM solution of flavin in pH 7, 50 mM potassium phosphate was prepared. 880 µL of this solution was then added to the cuvette. A Suba-seal® was used to seal the UV-vis cuvette and two needles were added through the top of the Suba-seal®. A H_2 gas line and an outlet line were attached to the needles and the inlet needle was moved below the surface of the flavin solution to sparge the solution with H_2 for a minimum of 15 minutes. Meanwhile pH 7, 50 mM potassium phosphate buffer was used to make the volume of the Hyd1 solution up to 20 µL (thus making the flavin concentration in each assay experiment as 0.1 mM and Hyd1 concentration as 0.05 mg mL^{-1}). After the sparging of the flavin solution was complete, both needles were lifted out of the solution so they were now in the cuvette headspace. The UV-vis spectrophotometer was set to start scanning every 30 seconds before the Hyd1 solution was added to the cuvette, using a needle and syringe to do so, using 200 µL of flavin solution

to aid transfer. The flavin reduction rate was then measured by the decrease in absorbance of the λ_{max} around 445 nm, over time, using the data from the linear section of the graph.

2.1.2. CV

2.1.2.1. Theory of CV

Cyclic voltammetry (CV) is a form of electrochemical analysis which is widely used to identify reduction/oxidation potentials and intermediate reaction species. A redox reaction, a reaction where electrons are transferred between oxidised (*Ox*) and reduced (*Red*) species, can be represented by the following equation:

$$Ox_y + ne^- \leftrightharpoons Red_z$$

Where *y* and *z* are the stoichiometric coefficients of these species in the redox half-cell reaction and *n* is the number of electrons transferred. A CV experiment is usually run so that a current is firstly supplied from a potentiostat to a working electrode, which is the site where reduction will occur, starting at a more positive potential than the potential range of interest and scanning down to more negative potentials (cathodic direction) until a chosen potential, beyond the region of interest, where it is then reversed (anodic direction), therefore capturing any oxidation features on the return direction (**Figure 2. 2.**). The current can then be applied again to reduce the oxidised species and CV can be continued to collect as many scans as desired. The reduction features are therefore measured as negative current (electrons are pulled away from the electrode) and the oxidation features as positive current (electrons pushed back towards the electrode). These peaks which arise in the CV scans are due to the equilibrium of species present at the potential of the cell (*E*), which are described by the Nernst equation:

$$E_{red} = E^0_{red} + \frac{RT}{nF} ln \frac{a^z_{red}}{a^y_{ox}}$$

Here E^0 is the standard potential of a species, a_{red} and a_{ox} are the activities of the reduced and oxidised species respectively with their stoichiometric coefficients *z* and *y*, *R* is the universal gas constant, *F* is Faraday's constant, *T* is the temperature and *n* is the number of electrons involved in the transfer between reduced and oxidised species.

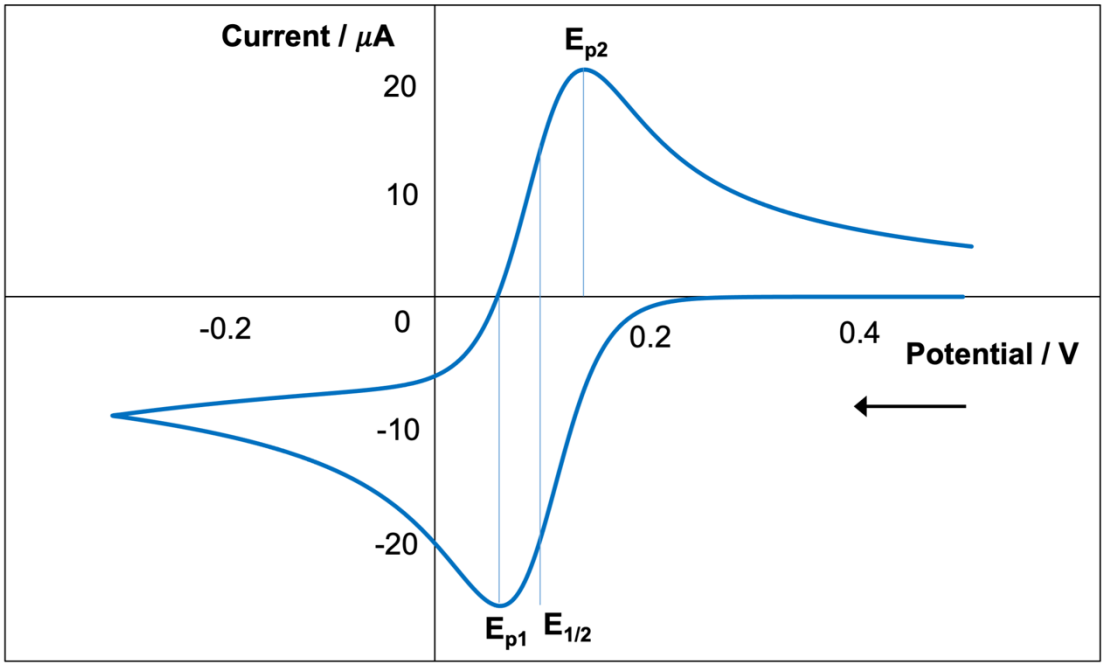


Figure 2. 2. Example of a CV scan of a reversible electron transfer. Arrow showing scan direction where potentials are scanned down to low potentials first resulting in the reduction peak (E_{p1}) and then oxidation peak (E_{p2}) when potentials are increased on the reverse scan. $E_{1/2}$ is the potential in the middle of the two peaks and is where the number of oxidised and reduced species in solution is equal. For a reversible one-electron transfer the difference in potentials between E_{p1} and E_{p2} is around 60 mV.[10]

The potential values measured are relative to the potential of the reference electrode used. In this thesis a saturated calomel electrode (SCE) is used as the reference therefore the potentials are converted to the standard hydrogen electrode (SHE) by the following equation:

$$E_{SHE} = E_{SCE} + 0.241\ V$$

A counter electrode must also be present to act as an electron sink and therefore minimise current reaching the reference electrode and causing its potential to drift. Thus, the components of a standard CV set-up are the three electrodes and the electrolyte (which contains ions which move to compensate the charge from the electrode to the solution).[11]

The main variables needed to be chosen for running a CV experiment are whether the working electrode is held stationary or rotated and what scan rate is used. The decision on whether to use a stationary or rotating electrode is based on what information is desired; using a stationary electrode means that any species which are oxidised may be reduced again at the electrode (since they are not spun away), therefore features corresponding to very low concentration of species may be detected. This therefore allows for identification of reversible reaction intermediates. Whereas with a rotating electrode set-up, any oxidised species will be removed from the electrode surface and therefore the reduction of this species will not be observed in the following scan. Currents are however likely to be significantly larger in a rotating electrode set-up since it will not be experiencing mass transport limitations which are seen when the electrode is stationary. Thus, for measuring reduction potentials with greater accuracy, a rotating electrode may be used. The rate at which the potentiostat varies the potentials over time (scan rate) also must be considered based on the nature of the experiment. Increasing the scan rate can sometimes cause peak splitting: this is since a faster scan rate can allow, otherwise unobservable, electron transfer steps, which occur faster than the lower scan rate, to be observed.[12] Changing scan rate may also change the apparent reversibility of a redox wave in cases where there is a following chemical step after a redox process which may be sufficiently slow to be outrun at faster scan rates. It is therefore possible to identify possible reaction mechanisms and extract kinetic data from CVs by varying the scan rate.[11]

2.1.2.2. CV Procedure for Metal NP Analysis

The following three electrode set-up was used: a pyrolytic graphite edge (PGE) working electrode (which was polished using silicon carbide paper to a high shine before use), a coiled platinum wire was used as the counter electrode and a saturated calomel electrode (SCE) was used as the reference electrode. The following steps were taken to set up the electrochemical cell. A glass cell with a temperature-controlled water-cooling jacket and with

side arms for the Pt wire and SCE electrode was used (these were both then inserted). The electrolyte which in this case was an aqueous buffer (8 mL) was added to the cell. The PGE electrode was then attached to a rotator, positioned above the cell, and lowered into the cell so that it was submerged into the electrolyte (without touching the bottom or the sides or the other two electrodes). It was then checked that the electrolyte was still in good contact with the Pt wire and SCE electrode and that there were no gas bubbles on the PGE. The electrodes were then connected to a PalmSens4 potentiostat using the relevant wire connectors before the experiment could then be started. A "blank" with nothing added to the electrode was always performed first to check that the electrode was clean and so any redox features seen in the following experiments were ensured to originate from the material studied.

For carrying out CVs of metal NPs, such as those in *Chapter 5* which were supported on carbon, a small sample of the material (e.g. 1 μL) was pipetted onto the PGE and allowed to dry completely before the electrode was submerged in the electrolyte and the CV was started.

2.1.2.3. Procedure for Determining Reduction Potential of Organic Compound

The same electrochemical set-up as was described in the previous section was used for studying the redox potentials of an organic compound (desired to be used as a substrate in a biocatalytic reaction). This differed however in that instead of the material to be studied being dried onto the PGE electrode, it was instead dissolved in the electrolyte.

Stationary and rotating PGE electrode CV scans were performed to investigate different properties of the redox potentials. To estimate the onset potential for the reduction of a nitro compound (to the amine) the first scan from a CV experiment (with 3000 rpm rotation, to minimise mass transport effects) was used. The potential at which the measured current began to deviate exponentially away from a linear baseline (where activity was zero), by a value of 10 nA, was taken as the onset potential. This was the same procedure as was used by others in the group when carrying out a broad screening of nitro compounds for their onset

reduction potentials and thus suitability to be reduced by Hyd1/C under H_2.[13] It was thereby found to be a reliable method with a very small experimental error between repeats using independent PGE electrodes.

2.1.2.4. CV Procedure for Enzyme Activity Analysis

For measuring enzyme activity, the same electrochemical set-up can again be used. In this case however, the enzyme is dropcast as a film (also known as PFE, protein film electrochemistry) onto the PGE electrode and not allowed to dry completely, only allowing it to adsorb on for a few seconds before the electrode is transferred into the cell. The analyte to be reduced/oxidised by the enzyme is present in the electrolyte. Thus, for studying the activity of a NAD^+ reductase enzyme, NAD^+ is dissolved in an aqueous buffer solution at the desired pH. Thus, when applying the thermodynamic driving force (by applying potential) active NAD^+ reductase should be able to carry out NAD^+ reduction which will be seen by a peak in the cathodic sweep direction ($E^{0'}$ of 2 e^- transfer of NAD^+ to NADH is -0.32 V vs SHE).[14] If the activity of a hydrogenase enzyme is desired to be investigated using an electrochemical approach, H_2 needs to be flowed through the cell thus requiring a gas-tight cell to be used. The activity of the enzyme is then measured by the oxidation of H_2 (E^0 for $2H^+/H_2$ couple is -0.41 V vs SHE, at pH 7, 1 bar H_2, 25 °C) and depending on the type of hydrogenase and conditions used it can also be possible to observe a peak in the cathodic direction for H^+ reduction to H_2.[15]

2.1.3. DLS

2.1.3.1. Theory of DLS

Dynamic light scattering (DLS) is a highly sensitive technique which measures the sizes of particles in solution. In contrast to other techniques such as TEM (discussed later in **2.2.1**), it will measure the size of the metal NP as well as the ligand molecules which are surrounding

the metal – this is known as the hydrodynamic diameter. DLS operates by measuring the scattering of light over time by the particles which are in Brownian motion and then applying the Stokes-Einstein equation which relates the molecular movement of particles in solution with their hydrodynamic radii (*r*).[16]

$$D = \frac{RT}{N} \cdot \frac{1}{6\pi Zr}$$

D is the diffusion constant, *R* is the gas constant, *T* is the temperature, *N* is Avogadro's number, *Z* is the viscosity of the solvent. This equation assumes spherical shaped particles therefore DLS is generally used most accurately to determine the size of spherical NPs.[17] Larger sized particles also cause greater amounts of scattering than smaller particles, therefore calculations (in built in DLS software) are needed to interpret the data and convert scattering to the number of particles of that size.[18]

2.1.3.2. DLS Procedure for Metal NP Analysis

Samples can be analysed by DLS and zeta potential using the same instrument, Malvern Panalytical Zetasizer, and the same cell, as long as a cell with conducting capability is used, i.e. a Malvern folded capillary zeta cell: DTS1070. Therefore, typically a diluted sample can be measured by DLS followed by zeta potential and then by DLS again to investigate sample stability to the zeta potential conditions. It is also generally a good procedure to analyse a sample with increasing dilution to make sure that the concentration of NPs is not impacting the results, thus avoiding multiple scattering events which occur at high concentration.[18]

Milli-Q water and samples were filtered using a disposable filter with 0.45 µm pore size (Cytiva Whatman™ Puradisc™ 13 mm) before adding to the cell.

In this thesis, ZS XPLORER 2.1.0.15 software (from Malvern Panalytical) was used.

2.1.4. Zeta Potential

2.1.4.1. Theory of Zeta Potential

The zeta potential of a NP solution describes the surface charge of the NPs. It therefore gives an indication of the stability of the NPs since the electrostatic repulsion between NPs is what stops them from aggregating. A value of 0 mV means there are equal positive and negative charges in solution (also known as an isoelectric point) which would suggest the particles are completely aggregated. A value of +30 mV or higher (or -30 mV or lower) is generally considered to reflect “stable particles”.[18-19]

A zeta-sizer instrument works by applying a low voltage across a cell (with two electrodes at either side) while illuminating the sample with a laser. The voltage causes charged particles to be attracted to the oppositely charged electrode and the speed at which these particles move at is measured by the frequency shift (Δf) of the scattered light by the charged, moving particles.[20] The following equation is therefore used to measure the particle velocity (v):

$$\Delta f = \frac{2v \ sin\left(\frac{\theta}{2}\right)}{\lambda}$$

Where λ is the laser wavelength and θ is the scattering angle. Henry’s equation is then used to determine the zeta potential (ζ) from the electrophoretic mobility (U_E), which is the particle velocity divided by the electric field strength, as follows:

$$U_E = \frac{2\varepsilon\zeta F(\kappa a)}{3\eta}$$

Where ε is the dielectric constant of the solvent, $F(\kappa a)$ is the Henry function and n is the solvent viscosity.[20]

2.1.4.2. Zeta Potential Procedure for Metal NP Analysis

As described in **2.1.3.2**, the same procedure for DLS and zeta potential analysis can be carried out.

2.2. Additional Techniques Used by Collaborators

The following additional techniques were used to aid further characterisation of metal NPs. Transmission electron microscopy (TEM) and x-ray diffraction (XRD) were mainly used to corroborate with analysis performed using UV-vis, while energy dispersive x-ray (EDX) was used to provide more insight into the elemental composition of mixed-metal NPs. TEM was mostly performed by Maya A. Landis using the facilities in the David Cockayne Centre for Electron Microscopy, Department of Materials, University of Oxford. TEM of some samples were performed by Dr Michal Klosowski, Electron Microscopy Specialist at the UKRI research complex at Harwell. EDX (coupled to high resolution scanning transmission electron microscopy (HR-STEM) was performed by Dr Christopher S. Allen, Principal Scientist at the electron Physical Science Imaging Centre (ePSIC), Diamond Light Source. XRD was carried out by Hazel Rycroft with assistance from Dr Tim Sudmeier using facilities in the Inorganic Chemistry Laboratory, University of Oxford. X-ray photoelectron spectroscopy (XPS) was carried out and analysed by Dr Phil Holdway, Department of Materials, University of Oxford, with samples prepared by Hazel Rycroft.

2.2.1. TEM

2.2.1.1. Principle of TEM

In transmission electron microscopy (TEM), a beam of electrons is irradiated at a thin sample and the electrons which have subsequently been scattered by the sample are analysed to build up an image of the sample. With good enough microscopes, it is possible to observe

single atoms – this high resolution is since elastic scattering originates from the highly localised charges of an atomic nucleus – this is known as high resolution TEM (HR-TEM).[21]

Another microscopy technique, called scanning transmission electron microscopy (STEM or HR-STEM for the high resolution version), uses an electron beam which is highly focused on a small area of sample, which then scans over the sample point by point, instead of the broad beam used in TEM. This can bring improvements in resolution, especially when a sample is non-uniform in thickness.[22]

TEM and STEM therefore yield images of metal NPs, giving information on their size and shape. With high enough resolution, lattice planes in the crystalline metal NPs can be observed.

2.2.1.2. TEM Sample Preparation

TEM was used for the characterisation of selected metal NPs in either the presence of a carbon support or as unsupported metal NPs. In both cases holey carbon film (300 or 400 mesh) Cu TEM grids (Agar Scientific) were used. For samples without carbon support, these were prepared by dropcasting onto the Cu grids, blotting away excess sample after 10 minutes using filter paper and leaving grids in a vacuum overnight to dry completely. For the supported metal NPs, samples were firstly sonicated and diluted in Milli-Q water (i.e. 20 x dilution and sonicated for 30 minutes) to break up any large aggregates. These were then dropcast onto Cu grids and allowed to dry completely.

2.2.2. EDX

2.2.2.1. Principle of EDX

Energy dispersive x-ray (EDX) analysis is performed *in situ* with TEM, STEM or SEM (scanning electron microscopy).[23] These techniques all involve the bombardment of a sample

with electrons and an EDX detector allows for the analysis of the x-rays which are produced during that process. The impact of the high energy electrons causes electrons in lower shells of an atom to be ejected out of the atom, leaving behind a hole which is then filled by an electron from a higher shell, with the difference in energy between these shells being released in the form of x-rays (as depicted in **Figure 2. 3.**).[24] The electrons can move down from different shells, with the shells known as K, L, M in order of increasing distance from the nucleus, and can move down to a shell one or two lower than the starting shell the electron originated from. Thus, the notation used for these transitions indicates the shell where the hole originated and the size of the transition, e.g. Kα: electron transition to K shell from one shell above (L shell) whereas Kβ: larger sized electron transition to K shell from two shells above (M shell). The x-rays released from each transition will have a unique energy characteristic of the element and the electron transition type. The measured frequencies recorded by an EDX detector are represented by Moseley's law:[25]

$$\sqrt{\nu} = k_1 \cdot (Z - k_2)$$

Where v is the frequency of the emission line, k_1 and k_2 are constants depending on the type of line and Z is the atomic number of the element. For the highest intensity lines (these are from $K\alpha$ and $L\alpha$ emissions since these are the most probable transitions) this equates to:

$$\nu(K_\alpha) = R \cdot \frac{3}{4} \cdot (Z - 1)^2$$

$$\nu(L_\alpha) = R \cdot \frac{5}{36} \cdot (Z - 7.4)^2$$

Where R is the Rydberg frequency (3.29×10^{15} Hz).[26]

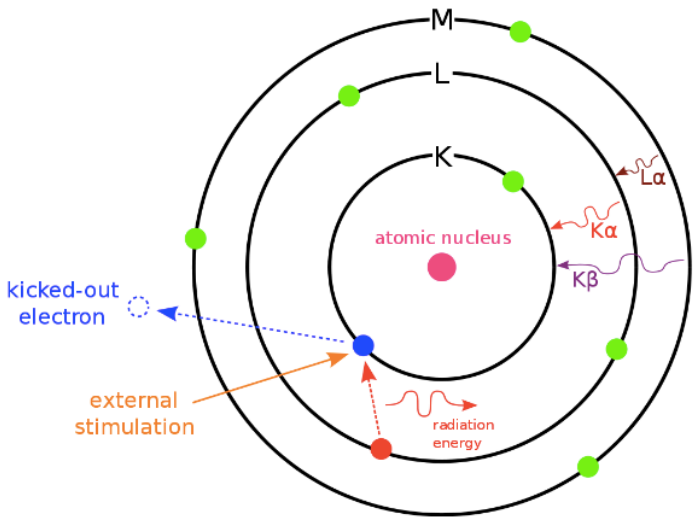


Figure 2. 3. Diagram of electron shells and x-rays emitted as a result of bombardment of atom with high energy electrons, ejecting lower shell electrons. Figure used under the Creative Commons Attribution Share Alike 3.0 License.

A computer program can therefore be used to convert the position on the x-axis (electron energy) of peaks recorded on a EDX spectra into the quantification of elements present in a sample. Using EDX in combination with HR-STEM allows for compositional data to be obtained by either carrying out line scans across particles or mapping an area of a sample. For example, the most intense peak in the EDX spectra of gold or silver NPs shown in **Figure 2. 4.** (apart from the copper peak which arises from the copper grids which the samples are deposited on) is, as expected, from x-ray emissions generated by electron transitions in gold or silver atoms. An elemental map shows the distribution of gold or silver across the sample.

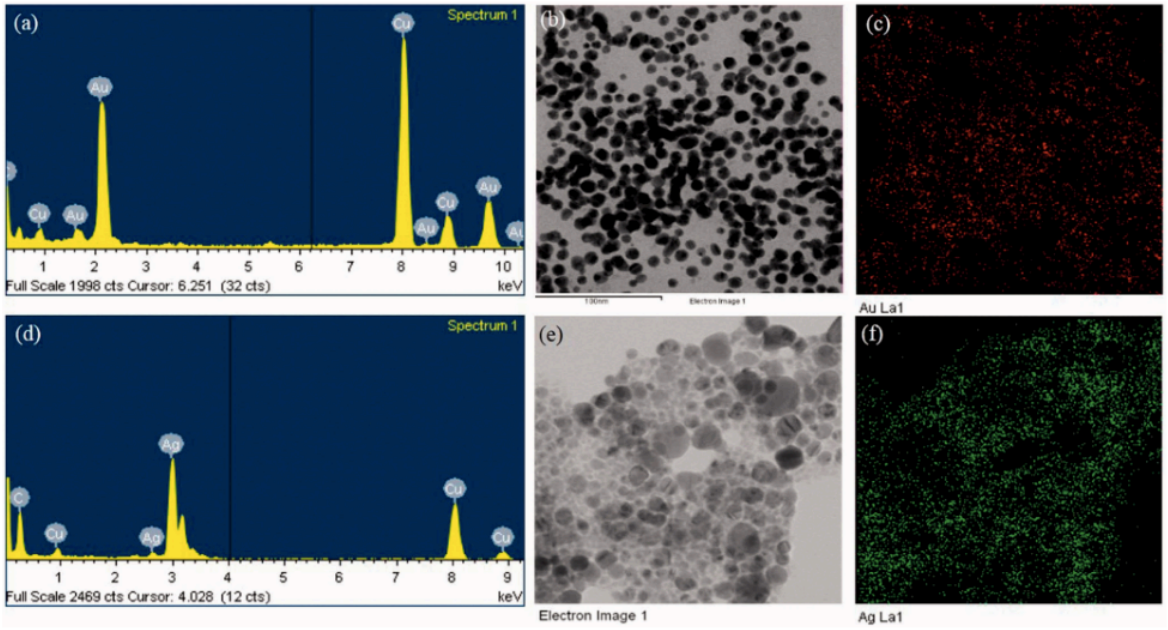


Figure 2. 4. EDX spectra of **A)** gold and **D)** silver NPs and their respective electron microscopy images **B)** and **E)** and elemental mapping **C)** and **F)**. Image from reference[27] with permission from Taylor & Francis.

2.2.2.2. EDX Sample Preparation

Since EDX analysis was performed *in situ* with HR-STEM, samples were prepared the same way as described for TEM sample preparation, i.e. the same samples on Cu grids were used for HR-STEM imaging as well as EDX analysis.

2.2.3. XRD

2.2.3.1. Principle of XRD

X-ray diffraction (XRD) is a technique which provides information about crystalline materials, which thereby diffract a beam of x-rays and the diffracted pattern can be analysed to extract information about the composition and crystal structure of the material. The identification of the material is possible due to the dependence of the diffraction on the interplanar spacing of crystal lattice planes of atoms.

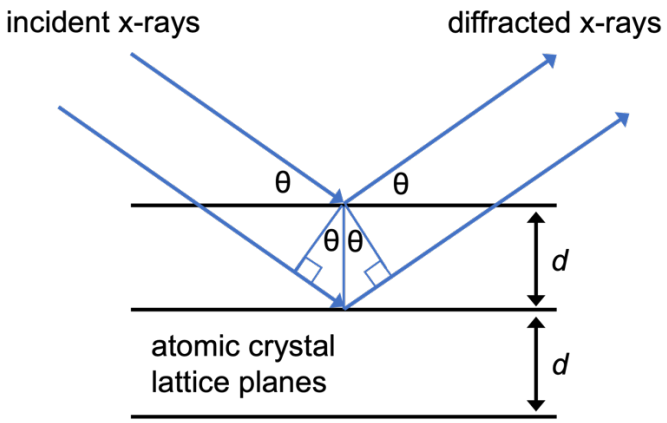


Figure 2. 5. Diagram of the principle of XRD where a beam of x-rays are fired at a sample and crystalline materials will diffract the x-rays away from the material at an angle equalling the angle of incidence.

This is due to the feature that the diffracted x-rays with a travel path length which are a whole number integer of the wavelength of the x-rays will 'constructively interfere' meaning that they create a new beam with higher amplitude. This leads to a stronger signal at that angle of diffraction as recorded in the XRD pattern. The angle of diffraction (θ) can be used to calculate the interplanar spacing (*d*) using Bragg's Law:

$$\sin\theta = \frac{n\,\lambda}{2\,d}$$

Thus an XRD pattern contains peaks of which their position and intensities can determine what elements are present and in what lattice structure.[18] An unknown material can be identified by comparison to a reference database such as the Inorganic Crystal Structure Database (ICSD).

The crystallite size (*D*) can also be estimated from the XRD pattern by using the most intense peak and the Scherrer equation:

$$D = \frac{K\lambda}{\beta\cos\theta}$$

Where *K* is the Scherrer constant, λ is the wavelength of x-ray beam used, β is the full width at half maximum (FWHM) of the peak and θ is the Bragg angle.[28] The Scherrer constant takes

into account the shape of the crystallite and usually a value of 0.9 is used for spherical particles.[29-31]

2.2.3.2. XRD Sample Preparation

XRD was used in this thesis for the characterisation of selected carbon supported metal NPs. Samples (e.g. 50 µL of 10 mg mL^{-1} carbon suspension) were dropcast onto a glass slide and left to dry under a flow of N_2.

2.2.4. XPS

2.2.4.1. Principle of XPS

X-ray photoelectron spectroscopy (XPS) is similar in principle to EDX, except instead of the x-rays which are released upon electron bombardment, in XPS x-rays are fired at a sample and the electrons which are ejected from inner atomic shells are analysed. This is based on Einstein's photoelectric effect where Einstein theorised that if an atom is fired with an energy source of higher energy than the binding energy of the electrons, then electrons will be emitted from the atom and their kinetic energies (E_{KE}) will be proportional to the frequency (hv) of the incident radiation. Their energies will also be dependent on what element and what orbital they came from. Thus, the following equation (Einstein relationship) is used to determine the electron binding energies (E_{BE}) and corresponding element:

$$E_{KE} = hv - E_{BE} - \phi_{sp}$$

Where hv is the photon energy and ϕ_{sp} is the work function constant of the spectrometer used (which is the energy difference between the vacuum energy level and the Fermi level).[32]

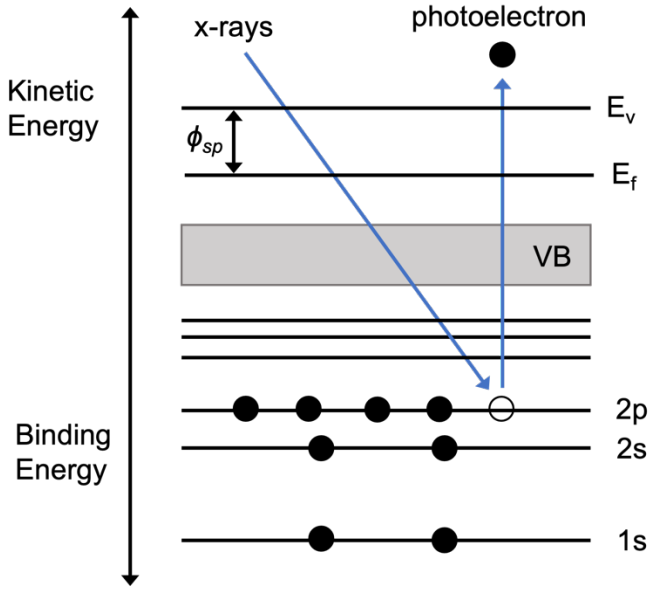


Figure 2. 6. Diagram of the principle of XPS where a beam of x-rays are fired at a sample and inner shell electrons are ejected (photoelectron) with their kinetic energies dependent on the energy of the x-rays and of the binding energy from the orbital and element they came from. (VB: valence band, E_v: vacuum energy level, E_f: Fermi level, ϕ_{sp}: work function constant of spectrometer)

An XPS spectra gives the counts and kinetic energies of emitted electrons from the surface of materials (1-10 nm depth) and a computer program can be used to convert this data into elemental quantification of a sample.

2.2.4.2. XPS Sample Preparation

XPS was used in this thesis for the characterisation of selected carbon supported metal NPs. Samples (e.g. 50 µL of 10 mg mL^{-1} carbon suspension) were dropcast onto a silicon wafer (Agar Scientific) and left to dry under a flow of N_2.

2.3. Summary of Characterisation Techniques for Metal NPs

Table 2. 1. shows a summary of the information that can be gained from the different techniques used in this thesis for characterising the synthesised metal NPs, as well as some associated pros and cons of these methods. To note, this is not an exhaustive list of all

characterisation methods for metal NPs and there are others which could provide further insight into the structure of these or other metal NPs: BET (Brunauer-Emmett-Teller) for surface area analysis, AFM (atomic force microscopy) for 3D shape analysis and ICP-MS (inductively coupled plasma mass spectrometry) for concentration quantification, to name a few.

Table 2. 1. Summary of techniques used in this thesis for the characterisation of metal NPs.

Technique	**Information**	**Size range for greatest accuracy of average size (nm)**	**Pros**	**Cons**
UV-vis [a]	Size, size distribution	5 to 100 [9] (minimum detection 2 nm)	In situ analysis, easy to use	Non-spherical NPs will affect spectra and introduce inaccuracies for size analysis
CV	Composition	n/a	Highly sensitive for detection of low concentrations of metal, useful for analysis of supported NPs where the support excludes analysis by UV-vis	Difficult to use in quantitative manner due to large variance in sample-electrode preparation
DLS	Hydrodynamic diameter and dispersity	0.3 to 10,000 [b]	Measurement of metal NP and its surrounding stabilising groups and is kept in solution	Concentration of solution effects results
Zeta potential	Surface charge	n/a	Useful for determining stability of NPs	Solutions need to not contain multiple reagents as these will complicate interpretation of results
TEM	Size, size distribution, shape, crystal structure (depending on microscope)	1-2 minimum, no maximum	Obtaining images of the NPs gives insightful information on their shape, useful for analysis of NPs on a support	Drying solutions may lead to flocculation of NPs (that are not present in solution) and accurate size analysis can be difficult due to requiring a large number of well-dispersed (not overlapping) NPs
EDX	Composition, structure of composition	n/a	Very useful in determining the compositional structure of bimetallic NPs	Time-costly analysis for compositional maps of samples
XRD	Composition, average crystallite size, lattice parameters	>3 to 50 [18]	Reference to databases allows ease of analysis	Very small NPs or too low concentrations may not be detected
XPS	Composition (including surface species), oxidation states	n/a	Useful for detecting the NP stabilising ligands, highly sensitive technique to low concentrations of elements	Contamination or sample damage during analysis may occur, affecting results [33]

[a] Information relating to analysis of metals which exhibit an SPR effect (Ag, Au, Al) as much less information can be gained for analysis of non-SPR metal NPs by UV-vis. [b] Quoted on Malvern Panalytical website for the Zetasizer.

2.4. References

[1] V. Massey, P. Hemmerich, *Biochem. Soc. Trans.* **1980**, *8*, 246-257.
[2] P. Mondal, K. Schwinn, M. Huix-Rotllant, *Journal of Photochemistry and Photobiology A: Chemistry* **2020**, *387*, 112164.

[3] X. Huang, M. A. El-Sayed, *J. Adv. Res.* **2010**, *1*, 13-28.
[4] P. K. Jain, K. S. Lee, I. H. El-Sayed, M. A. El-Sayed, *J. Phys. Chem. B* **2006**, *110*, 7238-7248.
[5] V. Amendola, R. Pilot, M. Frasconi, O. M. Maragò, M. A. Iatì, *J. Phys.: Condens. Matter* **2017**, *29*, 203002.
[6] G. Mie, *Annalen der Physik* **1908**, *330*, 377-445.
[7] K. L. Kelly, E. Coronado, L. L. Zhao, G. C. Schatz, *J. Phys. Chem. B* **2003**, *107*, 668-677.
[8] M. G. Blaber, M. D. Arnold, M. J. Ford, *J. Phys.: Condens. Matter* **2010**, *22*, 143201.
[9] W. Haiss, N. T. K. Thanh, J. Aveyard, D. G. Fernig, *Anal. Chem.* **2007**, *79*, 4215-4221.
[10] C. Sandford, M. A. Edwards, K. J. Klunder, D. P. Hickey, M. Li, K. Barman, M. S. Sigman, H. S. White, S. D. Minteer, *Chem. Sci.* **2019**, *10*, 6404-6422.
[11] N. Elgrishi, K. J. Rountree, B. D. McCarthy, E. S. Rountree, T. T. Eisenhart, J. L. Dempsey, *J. Chem. Educ.* **2018**, *95*, 197-206.
[12] P. S. Jensen, Q. Chi, J. Zhang, J. Ulstrup, *J. Phys. Chem. C* **2009**, *113*, 13993-14000.
[13] D. Sokolova, T. C. Lurshay, J. S. Rowbotham, G. Stonadge, H. A. Reeve, S. E. Cleary, T. Sudmeier, K. A. Vincent, *ChemRxiv preprint* **2024**.
[14] W. Buckel, R. K. Thauer, *Biochim. Biophys. Acta - Bioenerg.* **2013**, *1827*, 94-113.
[15] K. A. Vincent, A. Parkin, F. A. Armstrong, *Chem. Rev.* **2007**, *107*, 4366-4413.
[16] C. C. Miller, J. Walker, *Proceedings of the Royal Society of London. Series A, Containing Papers of a Mathematical and Physical Character* **1924**, *106*, 724-749.
[17] P. Arenas-Guerrero, Á. V. Delgado, K. J. Donovan, K. Scott, T. Bellini, F. Mantegazza, M. L. Jiménez, *Scientific Reports* **2018**, *8*, 9502.
[18] S. Mourdikoudis, R. M. Pallares, N. T. K. Thanh, *Nanoscale* **2018**, *10*, 12871-12934.
[19] A. Carone, S. Emilsson, P. Mariani, A. Désert, S. Parola, *Nanoscale Adv.* **2023**, *5*, 2017-2026.
[20] M. Kaszuba, J. Corbett, F. M. Watson, A. Jones, *Philos Trans A Math Phys Eng Sci* **2010**, *368*, 4439-4451.
[21] H. Kohl, L. Reimer, in *Transmission Electron Microscopy: Physics of Image Formation*, Springer New York, New York, NY, **2008**, pp. 1-15.
[22] Y. Lin, M. Zhou, X. Tai, H. Li, X. Han, J. Yu, *Matter* **2021**, *4*, 2309-2339.
[23] R. W. Welker, in *Developments in Surface Contamination and Cleaning* (Eds.: R. Kohli, K. L. Mittal), William Andrew Publishing, Oxford, **2012**, pp. 179-213.
[24] S. P. Kumar, D. Balaji, T. R. Mandlimath, in *Advanced Flexible Ceramics* (Eds.: R. K. Gupta, A. Behera, S. Farhad, T. A. Nguyen), Elsevier, **2023**, pp. 25-43.
[25] H. G. J. Moseley, *Philosophical Magazine* **1914**, *27*, 703-713.
[26] B. de Beauvoir, F. Nez, L. Julien, B. Cagnac, F. Biraben, D. Touahri, L. Hilico, O. Acef, A. Clairon, J. J. Zondy, *Phys. Rev. Lett.* **1997**, *78*, 440-443.
[27] C. Wang, P. Singh, Y. J. Kim, R. Mathiyalagan, D. Myagmarjav, D. Wang, C.-G. Jin, D. C. Yang, *Artificial Cells, Nanomedicine, and Biotechnology* **2016**, *44*, 1714-1721.
[28] V. S. Vinila, J. Isac, in *Design, Fabrication, and Characterization of Multifunctional Nanomaterials* (Eds.: S. Thomas, N. Kalarikkal, A. R. Abraham), Elsevier, **2022**, pp. 319-341.
[29] J. I. Langford, A. J. C. Wilson, *J. Appl. Crystallogr.* **1978**, *11*, 102-113.
[30] S. A. Disha, M. Sahadat Hossain, M. L. Habib, S. Ahmed, *Results in Materials* **2024**, *21*, 100496.
[31] P. M. Kibasomba, S. Dhlamini, M. Maaza, C.-P. Liu, M. M. Rashad, D. A. Rayan, B. W. Mwakikunga, *Results in Physics* **2018**, *9*, 628-635.
[32] N. H. Turner, *Applied Spectroscopy Reviews* **2000**, *35*, 203-254.
[33] D. R. Baer, M. H. Engelhard, *J. Electron. Spectrosc. Relat. Phenom.* **2010**, *178-179*, 415-432.

Chapter 3. Biocatalytic Synthesis of Metal Nanoparticles, using *NAD^+ Reductase*, and Application of Resulting Biohybrids

3.1. Introduction

This chapter discusses experiments testing an isolated NAD^+ reductase (NRase) for metal NP synthesis, including characterisation of the metal NPs by UV-vis, TEM, HR-STEM-EDX. After finding suitable conditions for the NP synthesis, the effect of changing the concentration of NRase at the same concentration of metal salt was investigated. The properties of the resulting biohybrids were investigated by analysing their selectivity for NAD^+ reduction to 1,4-NADH, with selective results indicating electronic contact between enzyme and metal NP. Demonstration of the biohybrids as H_2-driven NAD^+ reduction catalysts coupled to a NADH-dependent enzyme, an alcohol dehydrogenase, was also carried out.

3.2. Paper 1: Controlled Biocatalytic Synthesis of a Metal Nanoparticle-Enzyme Hybrid: Demonstration for Catalytic H_2-driven NADH Recycling

This manuscript has been published by the journal *Angewandte Chemie*, with the following citation:

Lucy B. F. Browne, Tim Sudmeier, Maya A. Landis, Christopher S. Allen, Kylie A. Vincent, *Angew. Chem. Int. Ed.* **2024**, *63*, e202404024

The paper followed by the supporting information can be found on the following pages in the format of the 'Accepted Article.'

As is stated in the supporting information, I carried out all the experimental work included in this work, except for the TEM imaging which was performed by Maya A. Landis and the HR-STEM-EDX which was performed by Christopher S. Allen. I carried out the formal analysis and wrote the original draft of this manuscript. Tim Sudmeier and Kylie A. Vincent advised on initial project ideas and experimental work. All authors reviewed the manuscript.

Controlled Biocatalytic Synthesis of a Metal Nanoparticle-Enzyme Hybrid: Demonstration for Catalytic H_2-driven NADH Recycling

Lucy B. F. Browne,[a] Tim Sudmeier,[a] Maya A. Landis,[a] Christopher S. Allen,[b] and Kylie A. Vincent*[a]

[a] L. B. F. Browne, Dr. T. Sudmeier, M. A. Landis, Prof. K. A. Vincent
Department of Chemistry, University of Oxford
Inorganic Chemistry Laboratory, South Parks Rd, Oxford, OX1 3QR (United Kingdom)
E-mail: kylie.vincent@chem.ox.ac.uk

[b] Dr. C. S. Allen
Electron Physical Science Imaging Centre
Diamond Light Source, Oxford, OX11 0DE (United Kingdom)
Department of Materials, University of Oxford
Parks Rd, Oxford, OX1 3PH (United Kingdom)

Supporting information for this article is given via a link at the end of the document.

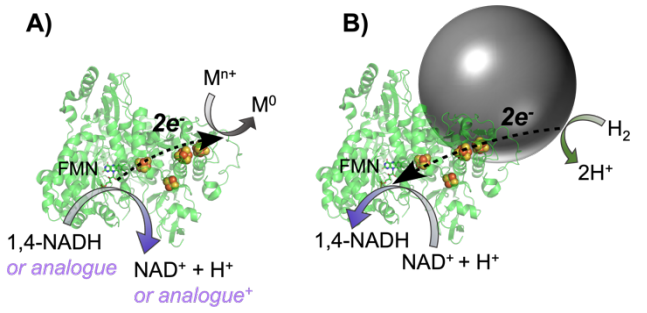
Abstract: Here we demonstrate the preparation of enzyme-metal biohybrids of NAD^+ reductase with biocatalytically-synthesised small gold nanoparticles (NPs, <10 nm) and core-shell gold-platinum NPs for tandem catalysis. Despite the variety of methods available for NP synthesis, there remains a need for more sustainable strategies which also give precise control over the shape and size of the metal NPs for applications in catalysis, biomedical devices, and electronics. We demonstrate facile biosynthesis of spherical, highly uniform, gold NPs under mild conditions using an isolated enzyme moiety, an NAD^+ reductase, to reduce metal salts while oxidising a nicotinamide-containing cofactor. By subsequently introducing platinum salts, we show that core-shell Au@Pt NPs can then be formed. Catalytic function of these enzyme-Au@Pt NP hybrids was demonstrated for H_2-driven NADH recycling to support enantioselective ketone reduction by an NADH-dependent alcohol dehydrogenase.

The need to maintain size and shape control over metal nanoparticles (NPs), while transitioning to more sustainable conditions for their synthesis and catalytic operation, present key drivers for finding new synthetic routes to NPs.[1-2] Achieving high uniformity of metal NPs is crucial for applications ranging from catalysis, drug delivery, biosensing to electronics.[3] In particular, gold NPs have received significant attention, largely due to their biocompatibility and optical properties.[4] The traditional method for making gold NPs involves boiling tetrachloroauric acid ($HAuCl_4$) and sodium citrate.[5-6] This method produces larger sized NPs (10-200 nm, depending on the procedure) which have uses in biomedical applications. For catalysis, however, smaller sized NPs (<10 nm) are more desirable due to their increased surface area to volume ratio, with a higher number of catalytically active surface sites, leading to greater reactivity.[7] Methods to make small Au NPs include using sodium borohydride as reductant with additional stabilising/capping agents such as alkane thiols or thiol-containing polymers.[8-9]

In search of more sustainable synthesis routes for gold NPs, numerous bio-based strategies have been explored using plant extracts or micro-organisms; these often allow milder conditions to be employed, however, the resulting NPs tend to have poor uniformity.[10-12] There have been some examples reported for using isolated enzymes in the synthesis of gold NPs, and these can give improved NP uniformity.[13-14] These include utilising surface exposed thiols, on proteins, as reducing agents.[13] Another example used a glutathione reductase enzyme where Au(III) reduction and size-controlled NP formation occurred at the enzyme active site which however lead to a loss of enzyme activity for its natural substrate.[14]

Although gold NPs show relatively low activity for many catalytic processes, gold is often used in combination with scarcer platinum group metals, either in a core-shell or alloy, which can offer advantageous reactivity and/or stability properties.[15] There are very few examples of synthesis of core-shell NPs by "green" methods, and organic solvents which rate poorly on *GSK's Solvent Sustainability Guide,*[16] such as toluene (rated amber), are common. Even syntheses involving aqueous conditions still require high temperatures or the use of metal surface-binding ligands such as carbon monoxide to achieve uniform core-shell structures.[17-19]

Here, we describe a pathway to synthesise metal NPs using an isolated enzyme which allows for mild synthesis conditions in water, while enabling high uniformity of NP size and shape. Specifically, we use an NAD^+ reductase enzyme moiety (NRase),



Scheme 1. A) Synthesis of metal NPs using an NAD^+ reductase moiety (NRase) and NADH or synthetic analogue as the reductant while metal salt (M^{n+}) is reduced to M^0. **B)** Depiction of H_2 oxidation occurring at the metal NP surface and subsequent electron transfer to the NRase active site (FMN), where selective NAD^+ reduction can occur.

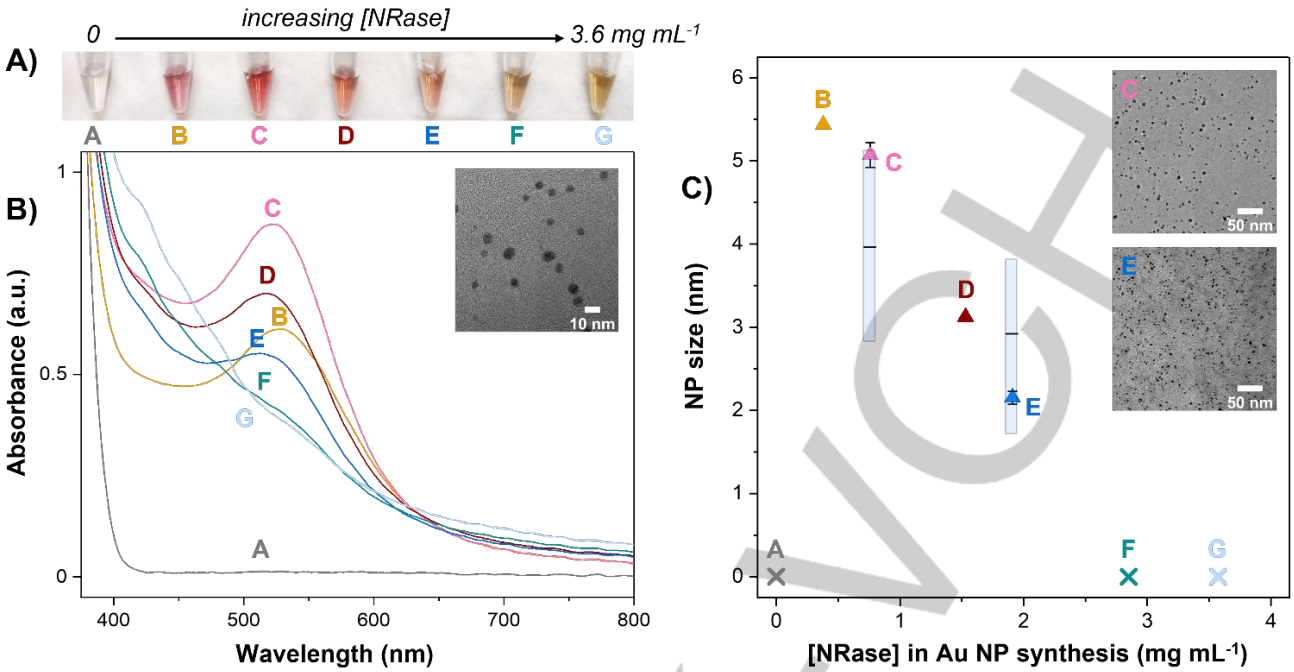


Figure 1. Size-controlled synthesis of Au NPs using NRase and NADH. **A)** Photograph, taken after 16 h, of reactions all containing the same initial concentration of $HAuCl_4$ and NADH, with different amounts of NRase (mg mL^{-1}): A: 0, B: 0.4, C: 0.8, D: 1.5, E: 1.9, F: 2.9, G: 3.6. **B)** The corresponding UV-vis spectra for the reactions photographed in A). The inset shows an example of a TEM image of these NPs (from sample C). **C)** The UV-vis spectra can be used to estimate the average NP diameter, shown by the coloured symbols in this graph, with respect to the concentration of NRase used in the synthesis. The error bars are from results of replicate experiments. The vertical bars shown for C and E indicate the NP size distribution (capturing 25-75% of the NP sizes, with the average shown by the black horizontal line) measured from TEM images such as those shown in the inset images (samples C and E pictured).

expressed in *E. coli* (HoxFU subunits of *Hydrogenophilus thermoluteolus* soluble hydrogenase, see Supporting Information, sections S.1.3 and S.2.1 for more details).[20] NRase contains a bound flavin mononucleotide (FMN) which is the catalytic site for reversible oxidation of 1,4-dihydronicotinamide adenine dinucleotide (hereafter, NADH), releasing electrons to the surface of the protein via a chain of iron-sulfur (FeS) clusters. Here we exploit this directed flow of electrons during oxidation of NADH (or cheaper synthetic analogues) for reduction of metal salts to form biohybrid Au NPs, as well as Au core, Pt shell (Au@Pt) NPs, Scheme 1A.

We show that the biohybrid Au@Pt NPs have catalytic activity which differs from that of the metal NPs or NRase alone. Our results demonstrate that Au@Pt NPs made using the enzyme, NRase, can be used for their H_2 oxidation properties, under mild pressure and temperature (e.g. 1 bar and 25 °C) to supply electrons back to NRase which selectively reduces NAD^+ to the bioactive NADH cofactor (Scheme 1B). This provides a novel route for continuous H_2-driven atom-efficient recycling of NADH. Use of H_2 as reductant for NADH has been previously explored using methods including intact soluble hydrogenase enzymes;[21] co-immobilised hydrogenase and NRase on carbon particles;[22] Pt nanoparticles;[23] and homogeneous Ir catalysts.[24] Despite having good selectivity, the Ir catalysts face bio-incompatibility issues.[25] A key limitation with Pt based systems is poor selectivity for making 1,4-NADH, but in previous work we showed that this limitation could be overcome by adsorbing an NRase onto a commercial carbon-supported platinum or palladium catalyst.[26-27] In this work we investigate whether NPs made via a bio-based method can obtain the desired selectivity for 1,4-NADH; using the already-present NRase and NPs together. As an example, we demonstrate coupling this with an NADH-dependent alcohol dehydrogenase (ADH) for an enantioselective ketone reduction. NADH-dependent enzymes are widely used in industrial biotechnology for fine chemical manufacturing, but are typically run with atom-uneconomical, glucose-driven, NADH recycling.[28] Hence we demonstrate one application for the biohybrid Au@Pt NPs is in selective, H_2-driven NADH recycling to support the activity of ADH in an enantioselective ketone reduction.

First, to investigate the synthesis of metal NPs using NRase: NADH and $HAuCl_4$ were added to different concentrations of NRase enzyme, Figure 1A. Over time the reaction solutions with NRase were observed to change colour, while the control, without enzyme, remained colourless (Figure 1A shows solutions after 16 h). As shown by the UV-vis spectra, these colour changes correspond to the growth of a surface plasmon peak with the absorbance maximum (λ_{max}) around 520 nm, indicative of Au NP formation, which was confirmed by TEM analysis (Figure 1B and inset). (The iron-sulfur clusters of NRase absorb in the 400-500 nm region,[20] and these spectral contributions increase with enzyme concentration; see Figure S3 for further spectra recorded at the start of the reaction.) The position and broadness of the surface plasmon peak for Au NPs is well-established to show a correlation with NP size and uniformity.[29] We use this correlation to estimate an average NP diameter for each reaction mixture (Figure 1C, triangle symbols), showing that NPs range from 5.4 nm (0.4 mg mL^{-1} NRase), down to 2.2 nm ± 0.1 nm (1.9 mg mL^{-1} NRase), with very small variation between experimental repeats (see S.2.4 for more details). Thus, there is a strong correlation between the NP size and the concentration of NRase used (samples B to E).

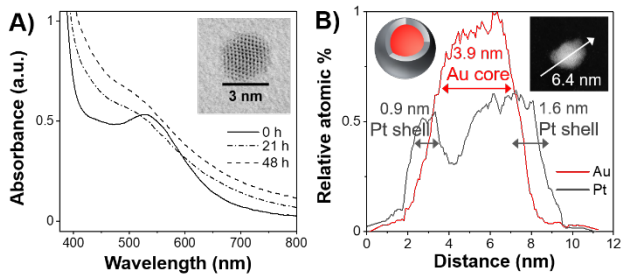


Figure 2. Synthesis of core-shell Au@Pt NPs using NRase to reduce Au(III) followed by Pt(IV). **A)** UV-vis spectra recorded after addition of K_2PtCl_6 and NADH to a solution of NRase and Au NPs (0 h) and after 21 and 48 h. Inset is a HR-STEM (BF) image of a NP after 48 h. **B)** EDX data of the line scan shown in the inset HR-STEM (HAADF) image, of sample after 48 h, showing a Pt shell and gold core, as depicted in the inset diagram (top left).

Nanoparticle formation and size distribution was corroborated from TEM analysis of samples C and E (see Figure 1C inset). TEM images showed spherical metal NPs with typical *fcc* lattice type with a size distribution in reasonable agreement with the UV-vis analysis (vertical bars on Figure 1C; for details see S.2.5 and S.2.6). The trend of increasing NRase concentration leading to smaller NP sizes is consistent with particle seeding on the surface of the enzyme, where electrons are released via the FeS relay, since a higher concentration of enzyme leads to more nucleation sites and thus smaller particles (i.e. the same number of metal atoms are split between more sites). This is consistent with the NRase templating NP formation.[30-31]

The NRase is highly selective for NADH over the related cofactor NADPH which differs only in an additional phosphate group (Figure S9) and has a very similar reduction potential.[32] To confirm that NADH oxidation at the active site of NRase is critical for electron supply to allow NP synthesis, we ran experiments under identical conditions with NRase, Au(III) and either NADH or NADPH. The latter experiment remained colourless, and UV-vis spectroscopy confirmed NP formation only in the experiment with NADH (Figure S10).

Given the high cost of the biological nicotinamide cofactors, we then explored whether the NP synthesis could be replicated with cheaper, synthetic cofactor analogues which are known to be tolerated by NRase.[33] Two synthetic cofactors, 1-benzyl-1,4-dihydronicotinamide (BNAH) and 1-carbamoylmethyl-1,4-dihydronicotinamide (AmNAH),[34] were found to give NPs with similar UV-vis spectra, as when using NADH: all with a narrow surface plasmon peak with its maxima at the same wavelength (±1 nm) for a given NRase concentration (Figure S11A). Thus, this implies the size of the NPs from the synthesis in the presence of NRase is controlled by the enzyme and not by the type of cofactor/reductant used. Controls were also carried out without any NRase. In contrast to the control with NADH and no NRase, in which no NPs formed, the BNAH and AmNAH synthetic cofactors were able to cause reduction of Au(III) and formation of NPs. However, they gave poor size-control over the NPs as evidenced by a very broad surface plasmon peak (Figure S11B) and subsequent precipitation, suggesting the cofactors could not provide long-term stabilization of the NPs.

Experiments were then conducted to try to generate a Pt shell over the Au NP core by subsequent reduction of Pt(IV) by NRase using NADH as reductant. Figure 2A shows that the surface plasmon peak is dampened after the addition of Pt(IV) and further NADH to the preformed biohybrid NRase-Au NPs. This is consistent with the formation of a core-shell structure since the plasmon peak has been shown to decrease in absorbance when Au is no longer exposed.[19] The average Au NP size in the starting NRase-Au biohybrids was estimated to be 2.7 ± 0.2 nm from the UV-vis spectrum; after Pt(IV) reduction, TEM analysis showed that the average NP size was 6.4 ± 2.4 nm (Figure S14). The Au-Pt NPs were also investigated by HR-STEM-EDX (Figure 2B and Figure S16). The EDX line scan data is consistent with a core-shell structure, with a higher ratio of Pt versus Au detected in the outer layers of the NPs (0.9 ± 0.4 nm Pt shell thickness) and a higher ratio of Au versus Pt in the centre (3.8 ± 0.1 nm core). We subsequently refer to these as *biohybrid NRase-Au@Pt NPs*.

Two types of control experiments were performed. (i) 'no NRase': Pt(IV) was added to a reaction solution which had no NRase, but which had NADH and Au(III) "incubated" for the same length of time as the solutions used to form the NRase-Au NPs. (ii) '1-step': Pt(IV) and Au(III) were added at the same time to a solution of NADH and NRase. Although these samples gave rise to a broad absorbance in the UV-vis region (Figure S18), no evidence for defined core-shell Au@Pt structures was observed in HR-STEM-EDX analysis. Instead, these reaction mixtures showed some evidence of Pt-core Au-layer and thin Pt-shell, as well as alloy structures (Figure S17). These will be referred to as (i) *non-bio-Au-Pt NPs* and (ii) *NRase-Au-Pt NPs*. Further control experiments under the same conditions, but without gold, showed only very low concentrations of Pt NPs in both the absence and presence of NRase (Figure S19). A catalytic role for gold in reduction of platinum salts has been shown previously in the case of making Au@Pt core-shell nanostructures of around 50 nm in size using gallic acid, a mild reducing agent, where it was proposed that Au NPs can behave as seeds for Pt reduction.[19] The Pt(IV) to Pt(II) and Pt(II) to Pt(0) couples have more negative reduction potentials than the Au(III) to Au(0) couple, hence Au(III) would be expected to be reduced before Pt(IV) in a mixture containing salts of both metals and a reducing agent.[35]

We then tested a series of NP samples for their selectivity and activity in NAD^+ reduction using H_2 as the electron source (as depicted in Scheme 1B). Using a non-enzymatic catalyst for NAD^+ reduction often leads to a mixture of products including 1,6-NADH, 1,2-NADH, NAD_2 dimers as well as over-reduced products (Figure S22), all of which cannot be utilised by enzymes such as alcohol dehydrogenase, which are selective for 1,4-NADH (Figure S22).[26] The *non-bio-Au-Pt NPs* converted all NAD^+, but after 21

Table 1. The selectivity and conversion in H_2-driven NAD^+ reduction catalysed by *non-bio-Au-Pt NPs* and *biohybrid NRase-Au@Pt NPs* made using different amounts of NRase in the NP synthesis.

Entry	[NRase] (mg mL^{-1})[a]	Selectivity for 1,4-NADH (%)[b]	Conversion of NAD^+ (%)[c]
1	0	0	100
2	0.2	17	100
3	0.5	64	88
4[d]	0.8	74 ± <1	35 ± 2
5	1.9	>99	20
6	3.2	n/a	0

[a] Concentration of NRase that was introduced during the synthesis of the NPs. [b] Selectivity measures the content of 1,4-NADH as a percentage of the total reaction products, as analysed by ^1H NMR spectroscopy. [c] Conversion

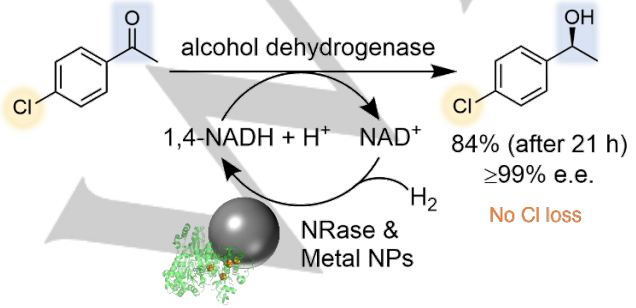
measures the consumption of NAD^+ starting material, as analysed by ^1H NMR. [d] This entry reflects duplicate measurements (from two separate reaction set-ups). Reactions conditions: NAD^+ (1 mM) in potassium phosphate (5 mM, pH 8.0), H_2 (1 bar), 20-25 °C, 21 hours, using general procedure – S.1.7.1.

hours, the ^1H NMR spectrum showed no trace of 1,4-NADH and instead showed exclusively over-reduced products, i.e. with two double bonds on the pyridine ring now reduced (Table 1, entry 1 and Figure S24). The *biohybrid NRase-Au@Pt NPs* prepared using different amounts of NRase were next compared (Table 1, entries 2-6).

As the concentration of NRase used in the synthesis was increased, the selectivity for 1,4-NADH increased, albeit with lower conversion. The decrease in conversion with increasing enzyme concentration can likely be explained by blocking of metal surface sites by additional enzyme. At an NRase concentration of 1.9 mg mL^{-1}, solely 1,4-NADH and NAD^+ was observed, indicating the enzyme is able to suppress any non-selective reduction of NAD^+ at the metal surface. We have previously observed a similar effect when using a biohybrid catalyst comprising NRase adsorbed onto a commercial carbon-supported platinum or palladium catalyst, in which higher loadings of enzyme resulted in good selectivity for 1,4-NADH (i.e. again suppressing the metal-catalysed cofactor reduction).[26-27] The fact that NRase remains catalytically active for NAD^+ reduction in the biohybrid system provides strong evidence that the enzyme remains structurally intact and in electronic communication with the Pt where electrons are released from H_2 oxidation. We therefore hypothesise that the metal NPs are formed on the enzyme surface, close to the external iron-sulfur cluster, where electrons would be released from NADH oxidation during the NP synthesis for reduction of the metal salts, and where electrons would be taken up for NAD^+ reduction during subsequent H_2-driven catalysis.

Lowering the Pt(IV) concentration used to form the Pt-shell in *biohybrid NRase-Au@Pt NPs* resulted in negligible conversion of NAD^+ to NADH (Table S4, entries 7 and 8). Similarly, NPs made with Pt(IV) and Au(III) added at the same time, *NRase-Au-Pt NPs*, which were shown by HR-STEM-EDX to have a thinner outer Pt shell, gave no conversion (Figure S17, Table S4, entry 9). This suggests the need for significant coverage of the original Au NPs with Pt for H_2 oxidation to drive NAD^+ reduction. Overall, this illustrates that the structure of the metal NPs, as well as the presence of sufficient amounts of NRase in this biohybrid catalyst system are both crucial for achieving selective NAD^+ reduction.

We further investigated this by adding a small amount of extra NRase (0.07 mg mL^{-1}) to *biohybrid NRase-Au@Pt NPs* and subjecting to NAD^+ reduction conditions. The presence of NRase added after the NP synthesis was found to significantly increase conversion of NAD^+ as well as selectivity for 1,4-NADH



Scheme 2. Enantioselective ketone reduction of 4'-chloroacetophenone using gold-platinum NPs with NRase as a H_2-driven NADH recycling catalyst.

(Table S4, compare entries 3 and 4 with entries 12 and 13 respectively). For example, improving the result obtained with *biohybrid NRase-Au@Pt NPs* made using 0.5 mg mL^{-1} NRase from 88% conversion, with 64% selectivity, to >99% conversion to exclusively 1,4-NADH. Adding this same small amount of NRase to *non-bio-Au-Pt NPs* dramatically improved the selectivity from 0% to 96% 1,4-NADH (with 4% over-reduced product) with both conditions showing no remaining starting material (Table S4, compare entries 1 and 11). These experiments clearly demonstrate the effect of NRase in providing the required selectivity. To explore the stability of the *biohybrid NRase-Au@Pt NPs* under reaction conditions, the catalyst system was put through 3 cycles of re-use (Table S4, entries 12, 14 and 15). Although conversion dropped, likely in part due to difficulty in recovering the catalyst system at the small scale of these reactions, importantly, there was no loss in selectivity for 1,4-NADH, indicating that the NRase remains stable and in effective electronic communication with metal NPs.

Finally, the NPs with NRase were tested as an atom-efficient 1,4-NADH recycling catalyst for the enantioselective ketone reduction of 4'-chloroacetophenone using an alcohol dehydrogenase (Scheme 2). From a practical point, it is noteworthy to mention that the biohybrid NPs were made in batches, flash frozen in liquid N_2, and stored at -80 °C, before being slowly thawed (as per standard long-term storage procedures for handling enzymes) before use in these reactions. No aggregation or change in the UV-vis spectra was observed after thawing (Figure S31). High conversions, e.g. 84%, of the (*S*)-alcohol product were obtained, from analysing the reaction after 21 hours (higher conversions were achieved with longer reaction times, see Table S5 for more results). Importantly, no dechlorination was detected (by ^1H NMR or GC analysis) and chiral-GC analysis confirmed the (*S*)-enantiomer was formed selectively (≥99% e.e.). In comparison, commercial platinum or palladium on carbon catalysts often cause dehalogenation of organic substrates under hydrogenation conditions.[26] Thus, this demonstrates the advantage enzymatic biohybrid reactions can provide, over traditional chemical methods, in enabling the use of mild conditions – e.g. 25 °C and 1 bar H_2 pressure – to allow greater chemo- and enantio-selectivity.

In summary we have demonstrated how an isolated enzyme can be employed to synthesise Au NPs with relative ease, under mild conditions, and yielding high uniformity of NP size and shape, which can be further modified with a Pt shell. The reactivity of the NRase enzyme used to synthesise the metal NPs is retained in the final enzyme-metal NP hybrids, such that the composite catalysts exhibit properties of both the enzyme and metal. This is demonstrated in selective, H_2-driven recycling of 1,4-NADH, which is further coupled to an alcohol dehydrogenase, for enantioselective ketone reduction. This approach provides a blueprint for a new type of self-synthesised chemo-biocatalyst system which is likely to find wide-ranging applications in areas of biotechnology.

Acknowledgements

The authors gratefully acknowledge Miguel Ramirez for heterologous expression and purification of NRase (HoxFU) enzyme and Johnson Matthey, Cambridge, for supplying ADH-105 enzyme. M.L. has been supported by the EPSRC Centre for Doctoral Training in Inorganic Chemistry for Future Manufacturing (OxICFM, EP/S023828/1). The authors acknowledge the use of the characterisation facilities within the David Cockayne Centre for Electron Microscopy, Department of Materials, University of Oxford as well as the electron Physical Science Imaging Centre (ePSIC), Diamond Light Source, instrument E02 (MG32357). The authors kindly thank Caroline Paul, Delft University of Technology, for supplying samples of artificial cofactors. This project has been funded by the European Research Council (ERC-CoG- BiocatSusChem-819580, to K.A.V.).

Keywords: biocatalysis • biohybrid • chemoenzymatic • metal nanoparticle synthesis • nicotinamide cofactor regeneration

[1] R. Sardar, A. M. Funston, P. Mulvaney, R. W. Murray, *Langmuir* **2009**, *25*, 13840-13851.

[2] F. Viñes, J. R. B. Gomes, F. Illas, *Chem. Soc. Rev.* **2014**, *43*, 4922-4939.

[3] J. E. Ortiz-Castillo, R. C. Gallo-Villanueva, M. J. Madou, V. H. Perez-Gonzalez, *Coord. Chem. Rev.* **2020**, *425*, 213489.

[4] P. K. Jain, K. S. Lee, I. H. El-Sayed, M. A. El-Sayed, *J. Phys. Chem. B* **2006**, *110*, 7238-7248.

[5] J. Turkevich, P. C. Stevenson, J. Hillier, *Discuss. Faraday Soc.* **1951**, *11*, 55-75.

[6] N. G. Bastús, J. Comenge, V. Puntes, *Langmuir* **2011**, *27*, 11098-11105.

[7] K. An, G. A. Somorjai, *ChemCatChem* **2012**, *4*, 1512-1524.

[8] M. Brust, M. Walker, D. Bethell, D. J. Schiffrin, R. Whyman, *J. Chem. Soc., Chem. Commun.* **1994**, 801-802.

[9] Z. Wang, B. Tan, I. Hussain, N. Schaeffer, M. F. Wyatt, M. Brust, A. I. Cooper, *Langmuir* **2007**, *23*, 885-895.

[10] A. Guleria, H. Sachdeva, K. Saini, K. Gupta, J. Mathur, *Appl. Organomet. Chem.* **2022**, *36*, e6778.

[11] K. X. Lee, K. Shameli, Y. P. Yew, S.-Y. Teow, H. Jahangirian, R. Rafiee-Moghaddam, T. J. Webster, *Int. J. Nanomedicine* **2020**, *15*, 275-300.

[12] M. Sengani, A. M. Grumezescu, V. D. Rajeswari, *OpenNano* **2017**, *2*, 37-46.

[13] A. Rangnekar, T. K. Sarma, A. K. Singh, J. Deka, A. Ramesh, A. Chattopadhyay, *Langmuir* **2007**, *23*, 5700-5706.

[14] D. Scott, M. Toney, M. Muzikár, *J. Am. Chem. Soc.* **2008**, *130*, 865-874.

[15] J. Luo, L. Wang, D. Mott, P. N. Njoki, Y. Lin, T. He, Z. Xu, B. N. Wanjana, I. I. S. Lim, C.-J. Zhong, *Adv. Mater.* **2008**, *20*.

[16] C. M. Alder, J. D. Hayler, R. K. Henderson, A. M. Redman, L. Shukla, L. E. Shuster, H. F. Sneddon, *Green Chem.* **2016**, *18*, 3879-3890.

[17] M. Ledendecker, P. Paciok, W. T. Osowiecki, M. Pander, M. Heggen, D. Göhl, G. A. Kamat, A. Erbe, K. J. J. Mayrhofer, A. P. Alivisatos, *Commun. Chem.* **2022**, *5*, 71.

[18] A. Dorjgotov, Y. Jeon, J. Hwang, B. Ulziidelger, H. S. Kim, B. Han, Y.-G. Shul, *Electrochim. Acta* **2017**, *228*, 389-397.

[19] G. Zhang, H. Zheng, M. Shen, L. Wang, X. Wang, *J. Phys. Chem. Solids* **2015**, *81*, 79-87.

[20] L. Lauterbach, J. Liu, M. Horch, P. Hummel, A. Schwarze, M. Haumann, K. A. Vincent, O. Lenz, I. Zebger, *Eur. J. Inorg. Chem.* **2011**, *2011*, 1067-1079.

[21] R. Mertens, L. Greiner, E. C. D. van den Ban, H. B. C. M. Haaker, A. Liese, *J. Mol. Catal. B: Enzym.* **2003**, *24-25*, 39-52.

[22] H. A. Reeve, L. Lauterbach, O. Lenz, K. A. Vincent, *ChemCatChem* **2015**, *7*, 3480-3487.

[23] X. Wang, H. H. P. Yiu, *ACS Catal.* **2016**, *6*, 1880-1886.

[24] Y. Maenaka, T. Suenobu, S. Fukuzumi, *J. Am. Chem. Soc.* **2012**, *134*, 367-374.

[25] V. Köhler, Y. M. Wilson, M. Dürrenberger, D. Ghislieri, E. Churakova, T. Quinto, L. Knörr, D. Häussinger, F. Hollmann, N. J. Turner, T. R. Ward, *Nat. Chem.* **2013**, *5*, 93-99.

[26] X. Zhao, S. E. Cleary, C. Zor, N. Grobert, H. A. Reeve, K. A. Vincent, *Chem. Sci.* **2021**, *12*, 8105-8114.

[27] J. S. Rowbotham, H. A. Reeve, K. A. Vincent, *ACS Catal.* **2021**, *11*, 2596-2604.

[28] J. P. Adams, M. J. B. Brown, A. Diaz-Rodriguez, R. C. Lloyd, G.-D. Roiban, *Adv. Synth. Catal.* **2019**, *361*, 2421-2432.

[29] W. Haiss, N. T. K. Thanh, J. Aveyard, D. G. Fernig, *Anal. Chem.* **2007**, *79*, 4215-4221.

[30] S. K. Das, C. Dickinson, F. Lafir, D. F. Brougham, E. Marsili, *Green Chem.* **2012**, *14*, 1322-1334.

[31] G. Frens, *Nature Physical Science* **1973**, *241*, 20-22.
[32] W. Buckel, R. K. Thauer, *Biochim. Biophys. Acta - Bioenerg.* **2013**, *1827*, 94-113.
[33] H. A. Reeve, J. Nicholson, F. Altaf, T. H. Lonsdale, J. Preissler, L. Lauterbach, O. Lenz, S. Leimkühler, F. Hollmann, C. E. Paul, K. A. Vincent, *Chem. Commun.* **2022**, *58*, 10540-10543.
[34] A. Guarneri, A. H. Westphal, J. Leertouwer, J. Lunsonga, M. C. R. Franssen, D. J. Opperman, F. Hollmann, W. J. H. van Berkel, C. E. Paul, *ChemCatChem* **2020**, *12*, 1368-1375.
[35] H. Ataee-Esfahani, L. Wang, Y. Nemoto, Y. Yamauchi, *Chem. Mater.* **2010**, *22*, 6310-6318.

WILEY-VCH

Entry for the Table of Contents



Under mild conditions, small (<10 nm), spherical, monodisperse metal nanoparticles (NPs) can be synthesised using an NAD^+ reductase enzyme as reductant and stabilizer, forming Au NPs and Au@Pt (core-shell) NPs. The enzyme-Au@Pt NP hybrids demonstrated promising activity as a H_2-driven NADH cofactor recycling system, coupled with an alcohol dehydrogenase (ADH).

WILEY-VCH

Supporting Information
©Wiley-VCH 2021
69451 Weinheim, Germany

Controlled Biocatalytic Synthesis of a Metal Nanoparticle-Enzyme Hybrid: Demonstration for Catalytic H_2-driven NADH Recycling

Lucy B. F. Browne, Tim Sudmeier, Maya A. Landis, Christopher S. Allen, and Kylie A. Vincent*

Abstract: Here we demonstrate the preparation of enzyme-metal biohybrids of NAD^+ reductase with biocatalytically-synthesised small gold nanoparticles (NPs, <10 nm) and core-shell gold-platinum NPs for tandem catalysis. Despite the variety of methods available for NP synthesis, there remains a need for more sustainable strategies which also give precise control over the shape and size of the metal NPs for applications in catalysis, biomedical devices, and electronics. We demonstrate facile biosynthesis of spherical, highly uniform, gold NPs under mild conditions using an isolated enzyme moiety, an NAD^+ reductase, to reduce metal salts while oxidising a nicotinamide-containing cofactor. By subsequently introducing platinum salts, we show that core-shell Au@Pt NPs can then be formed. Catalytic function of these enzyme-Au@Pt NP hybrids was demonstrated for H_2-driven NADH recycling to support enantioselective ketone reduction by an NADH-dependent alcohol dehydrogenase.

DOI: 10.1002/anie.2021XXXXX

S.1 Experimental Procedures

S.1.1 General Reagents

All commercial reagents were used as received, without any further purification. NAD^+ and 1,4-NADH were purchased from Prozomix. Synthetic cofactors: 1-benzyl-1,4-dihydronicotinamide (BNAH) and 1-carbamoylmethyl-1,4-dihydronicotinamide (AmNAH) were received from Caroline Paul, Delft University of Technology. 4'-Chloroacetophenone was purchased from Alfa Aesar. Remaining reagents were purchased from Sigma-Aldrich. All aqueous solutions were prepared with deionized Milli-Q water (Millipore, ≥15 MΩcm).

S.1.2 General Method Considerations

To reduce any competing oxidation reactions, all reaction handling (including NP preparation procedures) was carried out in a glovebox, filled with a N_2 atmosphere. When handling metal salts including while preparing the NPs, care was taken to protect from exposure to light by covering in tinfoil (to eliminate any light-induced metal reduction). For "washing steps" used for removing small molecules from enzyme or NP solutions, 10 kDa Amicon ultra-0.5 centrifugal filter units (approximately 1 nm pore size, stated on Sigma-Aldrich website), purchased from Sigma-Aldrich were used. These were always washed with water prior to first use (by centrifuging at 12,000 rpm for 5 mins, x5) as recommended to remove residual glycerol found in the filters.

S.1.3 Enzymes

The NAD^+ reductase enzyme moiety, which we have abbreviated to "NRase", is the NAD^+ reducing/NADH oxidizing subunit (also known as HoxFU where HoxF: 66 kDa and HoxU: 26 kDa, PDB code: 5XF9) of a soluble hydrogenase from *Hydrogenophilus thermoluteolus* without the hydrogenase subunit. NRase was expressed heterologously in *E. coli.*, isolated and purified using standard protocols. Before use in NP preparation and NADH recycling reactions, NRase (from stock flash frozen at -80 °C and stored in 50 mM Tris-HCl pH 8 buffer) was washed with pH 8 water (NaOH added to adjust pH) using 10 kDa size exclusion filter to remove storage buffer salts (by centrifuging at 12,000 rpm for 10 mins, x3). The alcohol dehydrogenase (ADH-105) used for the ketone reduction was received in lypophilised form from Johnson Matthey, Cambridge. Stock solutions of ADH-105 were prepared in 5 mM potassium phosphate pH 8 buffer and washed using a 10 kDa size exclusion filter to remove any undesired smaller proteins/reductant molecules that may be present (by centrifuging at 12,000 rpm for 10 mins, x3). ADH-105 has previously been shown to be selective for 1,4-NADH cofactor and selective in the reduction of acetophenone for the (*S*)-enantiomer of 1-phenylethanol.[1]

S.1.4 Gold NP Preparation using NRase

Typical small-scale screening experiments were carried out by adding the following reagents, in order, to 1.5 mL plastic tubes (StarLabs): NRase (e.g. from a stock of 7.6 mg mL^{-1} in pH 8 water), pH 8 water (adjusting the amount of NRase and pH 8 water to obtain the desired NRase concentrations) followed by 1,4-NADH (1 mM final concentration in pH 8 water) and finally $HAuCl_4$ (from an aqueous stock solution with NaOH added to adjust to pH 8, 0.7 mM final concentration). Thus a 1: 1.4 molar ratio of Au^{3+}: NADH was used. The reaction solutions were left at ambient temperatures without any stirring/shaking. After the desired time (e.g. 16 h), the NPs were washed using a 10 kDa size exclusion filter (by centrifuging at 12,000 rpm for 10 mins, until the UV-vis of the filtrate indicated minimal remaining NADH/NAD^+ and gold salts). These could then be used directly in the NAD^+ reduction experiments or in combination with ADH for an enantioselective ketone reduction.

S.1.5 Gold-Platinum NP Preparation

A typical procedure followed a 2-step approach where gold NPs were first prepared using NRase (as described in **S.1.4**) then before any washing steps, more 1,4-NADH was added (0.8 mM in pH 8 water) and K_2PtCl_6 (0.38 mM final concentration in pH 8 water). Thus, using a 1: 2.1 molar ratio of Pt^{4+}: NADH for this step and a 1: 1.1 molar ratio of Au^{3+}: Pt^{4+}. Typically, this solution was left for 48 hours after the addition of NADH and K_2PtCl_6 in order to allow for maximum Pt reduction. After which the solution can be washed using the same procedure described in **S.1.4** to remove any excess metal salts and NADH/NAD^+.

S.1.6 Characterisation of NPs

UV-visible spectroscopy was used to monitor the NP formation *in situ* or at time points throughout the reaction. Transmission electron microscopy (TEM) imaging and analysis was then carried out on samples after the NPs had been washed to remove any residual reactants, to give information on particle shape and size distribution. Selected gold-platinum NP samples were also analysed by high-resolution scanning transmission electron microscopy (HR-STEM) with energy-dispersive x-ray (EDX) spectroscopy to give information on elemental composition of the particles.

S.1.6.1 UV-visible Spectroscopy

UV-visible spectroscopy was carried out using a Cary 60 UV-visible spectrophotometer (Agilent) using a plastic micro-cuvette (path length 1 cm). For monitoring reaction progress of NP formation, the reaction solution was added to the micro-cuvette and the spectra was recorded from 200 to 800 nm. The increase in absorbance across the 400-800 nm range indicated the presence of scattering caused by NPs. For gold NPs a surface plasmon resonance (SPR) peak with an absorbance maximum in the 500-550 nm range was clear indication that gold NPs were formed. The ratio of the absorbance at the SPR peak to the absorbance at 450 nm was used to estimate the average NP size.[2] To observe the NADH oxidation to NAD^+, small aliquots of the NP reaction solutions were diluted with pH 8 water by a factor of 10 (e.g. 10 µL reaction solution and 90 µL pH 8 water).

S.1.6.2 TEM Imaging

Dilute samples were dropcast onto copper grids (type: holey carbon 300 mesh Cu TEM grids, S147-3 from Agar Scientific) and dried under vacuum. TEM was performed using a JEOL-3000F microscope operated at 200 kV.

S.1.6.3 HR-STEM with EDX Analysis

Dilute samples were dropcast onto copper grids (type: holey carbon 300 mesh Cu TEM grids, S147-3 from Agar Scientific) and dried under vacuum. HR-STEM was performed using a JEOL ARM300F microscope operated at 300 kV and this was coupled to an EDX detector (Oxford Instruments XMAX 100 EDX detector). For further elemental mapping studies, HR-STEM was performed using a JEOL ARM200F microscope operated at 200 kV, coupled to EDX and EELS detectors (JEOL Centurio EDX detector and Gatan Quantum Dual EELS spectrometer).

S.1.7 Reaction Methods

The following reaction methods were used for investigating the selectivity and activity of gold-platinum NPs prepared using NRase (and compared to those prepared without NRase) for the application as H_2-driven NADH recycling catalysts.

S.1.7.1 Gold-Platinum NPs Catalysed NAD^+ Reduction

A typical small-scale procedure used a 550 µL total reaction volume inside a 600 µL sized plastic tube (StarLabs). A stock solution of 1.9 mM NAD^+ in 5 mM potassium phosphate pH 8 buffer was prepared. Then gold-platinum NP solutions (e.g. 160 µL) were added to plastic tubes followed by 90 µL of 5 mM potassium phosphate pH 8 buffer (or if adding extra NRase, then the required amount of NRase and the remaining volume of 5 mM potassium phosphate pH 8 buffer to make up to 90 µL). Then 300 µL of the 1.9 mM NAD^+ solution was added to each plastic tube, making a 1 mM concentration of NAD^+ in the reaction solutions. The lids of each plastic tube were pierced with a needle and placed inside a Büchi Tinyclave pressure vessel which was then filled with H_2 (to 2.5 bar and vented x3 and then filled to 1 bar). The pressure vessel was then placed on a Stuart® mini see-saw rocker set to 30 oscillations/min. For analysis of the reaction products, the procedure described in **S.1.8** was followed.

S.1.7.2 4'-Chloroacetophenone Reduction using NADH Recycling

A typical small-scale procedure used a 550 µL total reaction volume inside a 600 µL sized plastic tube (StarLabs). A stock solution of 1.9 mM NAD^+ in 5 mM potassium phosphate pH 8 buffer was prepared. Then gold-platinum NP solutions (e.g. 160 µL) were added to plastic tubes followed by NRase and 5 mM potassium phosphate pH 8 buffer (making up their

combined volume to 74.5 µL). Then 300 µL of the 1.9 mM NAD^+ solution was added to each plastic tube, making a 1 mM concentration of NAD^+ in the reaction solutions. Then 10 µL of an ADH-105 stock solution (24 mg mg mL^{-1} in 5 mM potassium phosphate pH 8 buffer) was added (making a 0.44 mg mL^{-1} ADH-105 concentration). Lastly 5.5 µL of a 0.5 M stock solution of was added (for example as a solution in acetonitrile) to make a 5 mM 4'-chloroacetophenone concentration with 1 vol% of the co-solvent in the reaction solution. The lids of each plastic tube were pierced with a needle and placed inside a Büchi Tinyclave pressure vessel which was then filled with H_2 (to 2.5 bar and vented x3 and then filled to 1 bar). The pressure vessel was then placed on a Stuart® mini see-saw rocker set to 30 oscillations/min. For analysis of the reaction products, the procedure described in **S.1.8** was followed.

S.1.8 Reaction Analysis

To confirm and quantify reaction products, ^{1}H NMR spectroscopy was used as the primary analytical technique. UV-visible spectroscopy was used to obtain more analysis from different time points across a NAD^+ reduction reaction, but ^{1}H NMR was required to confirm which NADH isomers were formed. A chiral-GC method was used for the confirmation of the enantioselectivity of the alcohol product from the 4'-chloroacetophenone reduction.

S.1.8.1 ^{1}H NMR Spectroscopy

After the desired reaction time, the reaction solution was added to a 10 kDa size exclusion filter and centrifuged for a total of 20 minutes at 12,000 rpm. The filtrate was then used for analysis and the residue in the filter (containing NPs and enzyme) could be re-used in a second reaction if desired. A total volume of 500 µL solution was prepared containing 400 µL of the filtered reaction solution and 100 µL of D_2O in a Norell® SelectSeries™ 5 mm 400 MHz NMR spectroscopy tube. All NMR spectra were obtained using a Bruker Advance III HD nanobay (400 MHz) instrument, a water suppression was applied and parameters used for acquiring NMR spectra are summarized in **Table S 1**. Data was processed using MestReNova. Manual rephasing was carried out when required followed by a Whittaker smoother baseline correction across the whole spectrum and a line broadening to improve signal to noise corresponding to 1.0 Hz. Signals were referenced against appropriate peaks such as acetonitrile (δ = 2.06 ppm).

Table S 1. NMR parameters used to acquire NAD^+ reduction and 4'-chloroacetophenone reduction product composition.

Experiment	^{1}H
RF pulse energy (MHz)	400.13
Temperature (K)	298
Number of scans	As required
Pulse width (µs)	14
Spectral width (Hz)	8000
Acquisition time (s)	4.09
Relaxation delay (s)	1.00

S.1.8.2 UV-visible Spectroscopy

UV-visible spectroscopy was carried out using a Cary 60 UV-visible spectrophotometer (Agilent) using a plastic micro-cuvette (path length 1 cm). To observe the NAD^+ reduction to NADH, small aliquots of the reaction solutions were diluted to make the initial NAD^+ concentration 0.1 mM. The increase in absorbance at 340 nm can be used as indication of the formation of NADH products. 1,4-NADH has absorbance maxima at 340 nm, however 1,6-NADH and 1,4-NADH also absorb at that wavelength (with their maxima at 345 nm and 395 nm respectively).[3] The observation of another peak around 290 nm indicated over-reduced NADH which was identified by ^{1}H NMR analysis.

S.1.8.3 Chiral-GC Method

After the desired reaction time, the reaction solution was added to a 10 kDa size exclusion filter and centrifuged for a total of 20 minutes at 12,000 rpm. The filtrate was then used for analysis. 50 µL of the filtrate was added to 800 µL EtOAc to extract the organic products. 600 µL of the EtOAc layer was removed, dried using Na_2SO_4, and added to a GC vial. The GC method was as described in **Table S 2**.

Table S 2. GC method conditions used for the enantiomeric excess (e.e.) determination of the reaction products from the reduction of 4'-chloroacetophenone.

Column	CP-Chirasil-Dex CB (Agilent), 25 m x 0.25 mm x 0.25 µm, fitted with a guard of 10 m undeactivated fused silica of the same diameter
Carrier	He (CP grade), 170 kPa (constant pressure)
Inlet temperature	200 °C
Injection conditions	Splitless with split flow 60 mL/min, splitless time 0.8 mins, purge 5 mL/min. Injection volume = 0.1 µL.
Detection	FID (H_2 = 35 mL/min, air = 350 mL/min, makeup N_2 = 40 mL/min, temp = 250 ℃)
Oven heating profile	Time (minutes) Temperature 0 – 5 Hold at 70 ℃ 5 – 14.5 Ramp to 165 ℃ at 10 ℃/min 14.5 – 15.2 Ramp to 200 ℃ at 50 ℃/min 15.2 – 20.2 Hold at 180 ℃ for 5 minutes
Compound retention times	Time (minutes) Compound 12.99 4'-Chloroacetophenone. 14.95 *(R)*-4'-Chloro-1-phenylethanol 15.10 (*S*)-4'-Chloro-1-phenylethanol

S.2 Results and Discussion

S.2.1 Enzyme Details

The NAD^+ reductase enzyme moiety (NRase) used in this work consists of the HoxFU subunits from *Hydrogenophilus thermoluteolus* soluble hydrogenase. The x-ray crystal structure of the whole soluble hydrogenase (PDB code: 5XF9)[4] determines there to be 4 unique protein chains: HoxF, HoxU, HoxY and HoxH (**Figure S 1**). The NRase subcomplex performs NAD^+ reduction/NADH oxidation while the HoxHY functions as a hydrogenase: active for H^+ reduction and H_2 oxidation. The hydrogenase moiety in intact soluble hydrogenases is found to be unstable over time,[5] while the NAD^+ reductase moiety has good stability. Thus, in this work we have prepared and isolated the NRase subcomplex and coupled it with a metal NP in place of the HoxHY subcomplex.

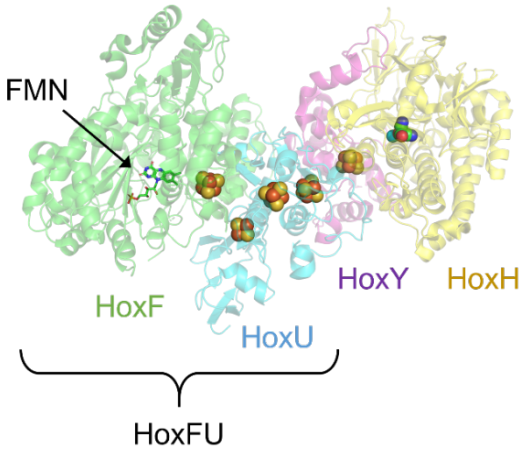


Figure S 1. Structure of NAD^+ reducing soluble hydrogenase (PDB: 5XF9) where the HoxFU subunit is what we have termed NRase in this work.

During NAD^+ reduction, 2 e^- need to be supplied to the FMN in the active site of NAD^+ reductase, via the FeS clusters. In the whole soluble hydrogenase these electrons will have originated from the hydrogenase subunit carrying out H_2 oxidation. In this work we have coupled a metal NP (specifically Au@Pt NPs), which carries out the H_2 oxidation, with the NRase subunit. In the NRase subunit, the configuration of amino acids surrounding the FMN in the active site only allows for the NAD^+/NADH to align itself in one configuration with respect to the FMN and thus causes the selectivity for the hydride transfer to occur at the 4-position of the pyridine ring. Therefore NAD^+ is reduced selectively to 1,4-NADH in the presence of the NAD^+ reductase enzyme (**Figure S 2**). The hydride will also only be transferred onto the *si* face of the NAD^+ therefore the reaction is also stereoselective which can be utilized in the presence of D_2O where the resulting product will be exclusively [4*S*-^{2}H]-NADH.[6] The whole reaction is reversible (the direction of the arrows drawn in **Figure S 2** can all be reversed). Thus, if no electrons are being supplied to the active site and there is 1,4-NADH present, NRase can oxidize NADH (by the hydride transferring onto FMN) and subsequently electrons are directed away from the active site, via the FeS clusters, to the surface of NRase.

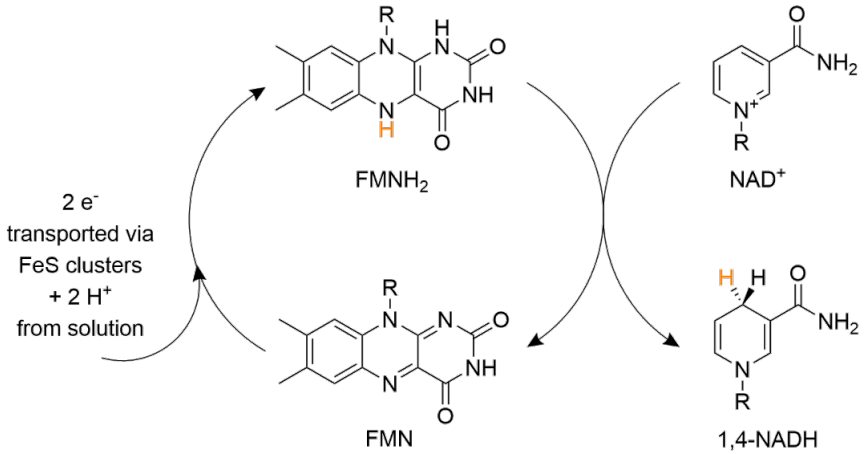


Figure S 2. Mechanism for NAD^+ reduction via hydride transfer from reduced FMN in active site of NRase. Arrows can be reversed for NADH oxidation, resulting in electrons directed towards surface of the NRase.

S.2.2 Redox Potentials

These redox potentials show that the oxidized cofactors have more negative reduction potentials than the metals, thus the reduced form of these cofactors can be used as sacrificial reductants to reduce Au(III) or Pt(IV).

Half-reaction	E°(vs SHE)/ V	Reference
$[AuCl_4]^- + 3e^- \rightleftharpoons Au_{(s)} + 4Cl^-$	1.00, (0.77 at pH 8)[a]	[7], [8]
$PtCl_6^{2-} + 2e^- \rightleftharpoons PtCl_4^{2-} + 2Cl^-$	0.726	[9]
$PtCl_4^{2-} + 2e^- \rightleftharpoons Pt_{(s)} + 4Cl^-$	0.758	[9]
$NAD^+ + 2e^- + H^+ \rightleftharpoons NADH$	-0.320	[10]
$NADP^+ + 2e^- + H^+ \rightleftharpoons NADPH$	-0.320	[10]
$BNA^+ + 2e^- + H^+ \rightleftharpoons BNAH$	-0.361	[11]
$AmNA^+ + 2e^- + H^+ \rightleftharpoons AmNAH$	-0.385	[11]

[a] This reference has measured a reduction potential of an aqueous solution of $HAuCl_4$ prepared at pH 8 of 0.53 V using a saturated calomel electrode (SCE). Solutions prepared at pH 6.2 and 2.9 were found to give reduction potentials of 0.59 V and 0.66 V respectively. At higher pH the speciation of the Au complexes are known to have a lower x number in $[AuCl_x(OH)_{4-x}]^-$ which gives rise to the lower reduction potentials.

S.2.3 Gold NP Synthesis UV-vis Spectra

The synthesis of gold NPs was tested with increasing amounts of NRase, as was discussed in the main text. **Figure S 3** shows the UV-vis spectra of all results from this experiment (including replicates which were omitted from Figure 1 for clarity). The replicates give very similar spectra after 16 h showing good reproducibility.

The trend of the blue-shift in the wavelength of the maxima of the surface plasmon resonance peak (λ_{max}) as the concentration of NRase is increased has been described in the main text. The other noticeable feature is there is an increase in the absorbance at the λ_{max} (from 0 to 0.8 mg mL^{-1} of NRase) followed by a decrease in absorbance at higher

NRase concentrations. The initial increase in absorbance is matched with a decrease in the λ_{max} which implies that the concentration of NPs increases. Thereafter, the decrease in absorbance cannot be assumed to be solely due to a decreasing NP concentration since the size of the NPs decreases and smaller NPs are known to have a smaller extinction coefficient.[12]

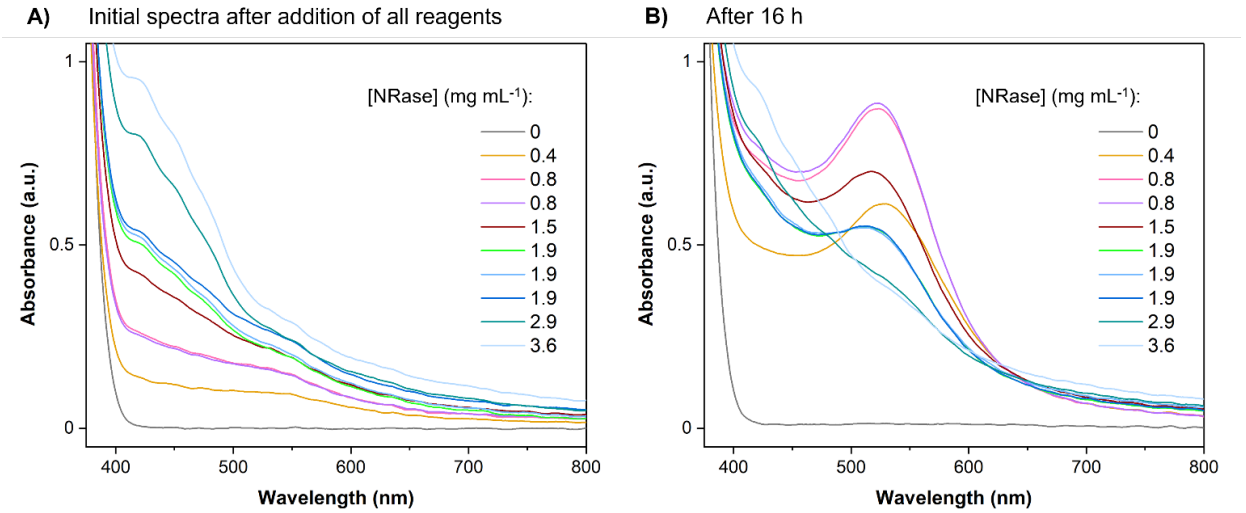


Figure S 3. Monitoring the synthesis of Au NPs using UV-vis. **A)** Spectra recorded after addition (within first 20 minutes) of all reagents: $HAuCl_4$, 1,4-NADH and NRase. The absorbance attributed to the NRase (strongest from 400-500 nm) becomes more pronounced as the NRase concentration is increased. **B)** Spectra of the same solutions recorded after 16 h (solutions in 1.5 mL plastic tubes at room temperature, no mixing).

S.2.4 Gold NP Size Calculation

The wavelength of the maxima of the surface plasmon resonance peak (λ_{max}) is often used as indication of the average NP size, with the broadness of the peak reflecting the NP uniformity (i.e. a broader peak has a large range in sizes of NPs). However, as the average NP size decreases, the environment around the NP becomes a more influential effect and thus using the λ_{max} alone would not give an accurate estimation of NP size. An improvement for estimating the NP size is described by W. Haiss et. al. and uses the absorbance at the surface plasmon resonance peak (A_{SPR}) and divides this by the absorbance at 450 nm (A_{450}).[2] The resulting ratio number is then used to estimate the average NP diameter using the equation:

$$d = exp\left(B_1 \frac{A_{SPR}}{A_{450}} - B_2\right)$$

where the experimentally determined fit parameters, B_1 = 3.00 and B_2 = 2.20 can be used. The authors determine there to be an approximately 11% standard deviation with this calculation method and do warn that it becomes less accurate for smaller NPs (< 10 nm). Thus, for these results, shown in **Table S 3**, where the NPs are calculated to be in the 2-5 nm range these should be considered an estimation which is more useful as a demonstration of the general trend of using higher NRase concentrations leading to smaller NPs than for giving highly accurate NP sizes. The TEM analysis is also used to confirm that this is a suitable estimate to make.

NPs below 2 nm become difficult to estimate their size since this is around the limit for NPs to give an absorbance in the UV-vis.[13] Thus, with the highest concentrations of NRase there may be very small Au NPs or nanoclusters (< 2 nm) which are not detected by UV-vis.

Table S 3. Analysis of the average NP size estimated from UV-vis spectra of reactions using different concentrations of NRase.

[NRase] (mg mL^{-1})	λ_{max} (nm)	A_{SPR} (a.u.)	A_{450} (a.u.)	A_{SPR} / A_{450}	d (nm)
0	-	-	-	-	-
0.4	530	0.61196	0.47158	1.29767	5.43578
0.8	524	0.87143	0.67868	1.28401	5.21750
0.8	523	0.88622	0.70076	1.26466	4.92337
1.5	516	0.70014	0.62897	1.11315	3.12507
1.9	513	0.55173	0.55247	0.99866	2.21664
1.9	514	0.54682	0.56275	0.97170	2.04438
1.9	513	0.55173	0.55432	0.99532	2.19454
2.9	-	-	-	-	-
3.6	-	-	-	-	-

S.2.5 Gold NP Size Distribution from TEM

After TEM images had been obtained, NP size analysis was carried out using ImageJ using the following protocol:

- Image threshold is adjusted to capture all NPs (**Figure S 4** and **Figure S 5**).
- NPs which can be seen in the image to be overlapping are removed so they do not skew the results, see **B**.
- NPs are analysed using ImageJ function.
- The size and circularity threshold are adjusted to only capture the NPs and not the background. For example, in the case of **Figure S 4**, size(nm^2): 1.70-Infinity and circularity: 0.10-1.00 were found to be good at capturing all the NPs while minimising the amount of background, see **C**.
- The area of each NP calculated by ImageJ is then used to calculate the diameter of each NP.
- The diameter data is then used in Origin to create statistical graphs (histogram or box plot) showing the range of NP diameters.

From these images, possible NPs of <1 nm were not included in the analysis since it was too difficult to distinguish between the background and these NPs. Thus, the first column in the size distribution histograms (**Figure S 6**) shows the number of particles between 1.0 to 1.5 nm size. The TEM analysis verifies the results acquired by UV-vis analysis – with the higher concentration of NRase leading to smaller sized NPs.

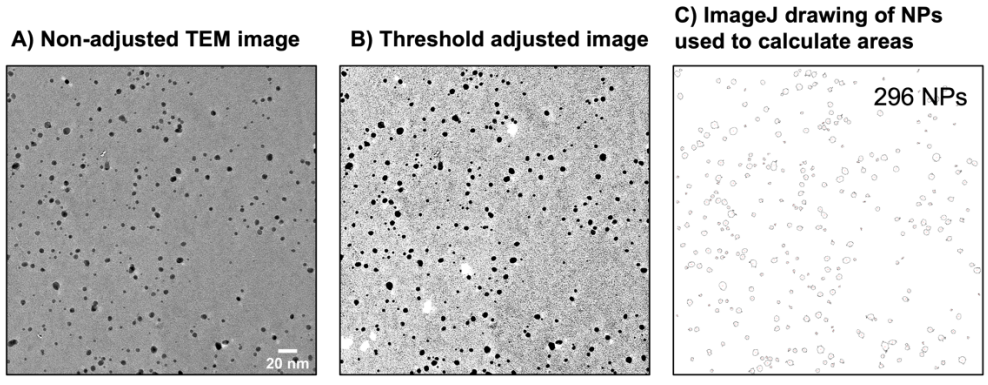


Figure S 4. TEM and NP size analysis for Au NPs made using 0.8 mg mL^{-1} NRase.

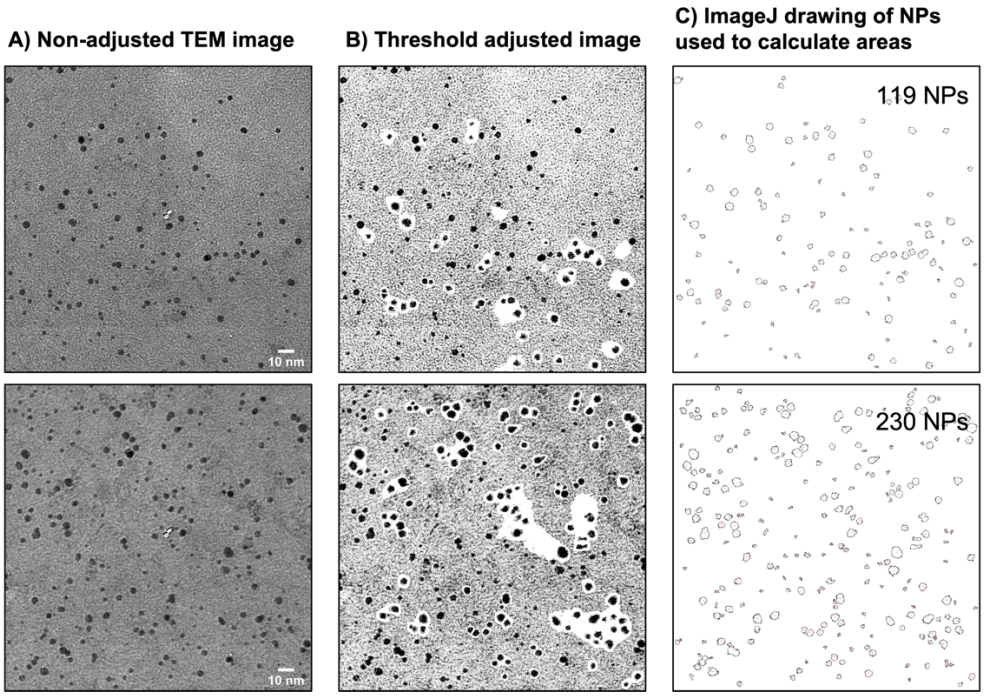


Figure S 5. TEM and NP size analysis for Au NPs made using 1.9 mg mL^{-1} NRase (the two images and subsequent analysis were combined to analyse a greater number of particles).

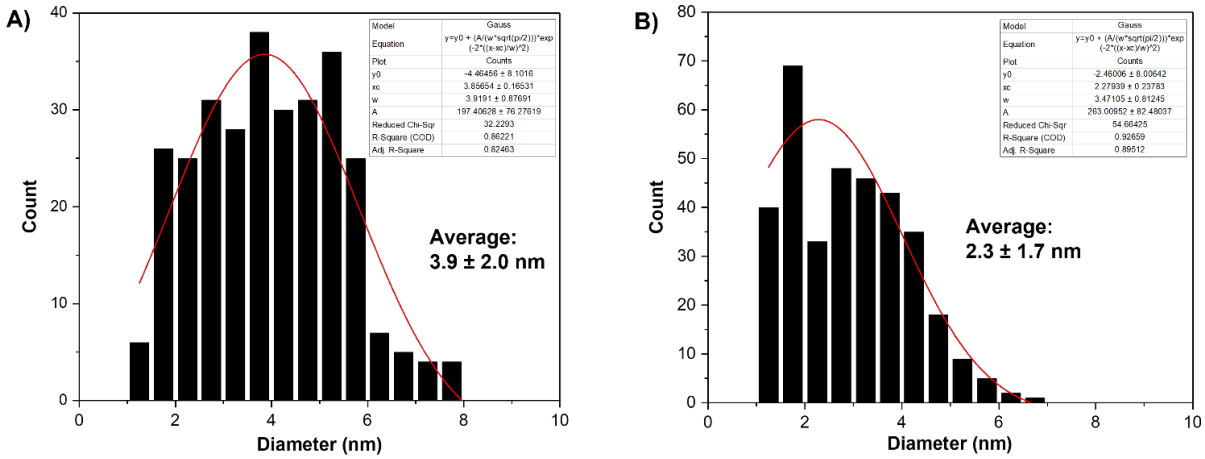


Figure S 6. Size distribution of Au NPs made using: **A)** 0.8 mg mL^{-1} and **B)** 1.9 mg mL^{-1} of NRase.

S.2.6 Gold NP Lattice Fringe Analysis

Good crystallinity of the Au NPs in the TEM images were observed. This allowed for lattice fringe analysis. **Figure S 7** shows the method used to estimate the d-spacing – in this example giving 0.283 nm as the measured lattice spacing which aligns with the interplanar distance expected for (111) plane of a *fcc* Au structure.[14] After Pt reduction has occurred the NPs are shown to retain their *fcc* crystallinity (**Figure S 8**).

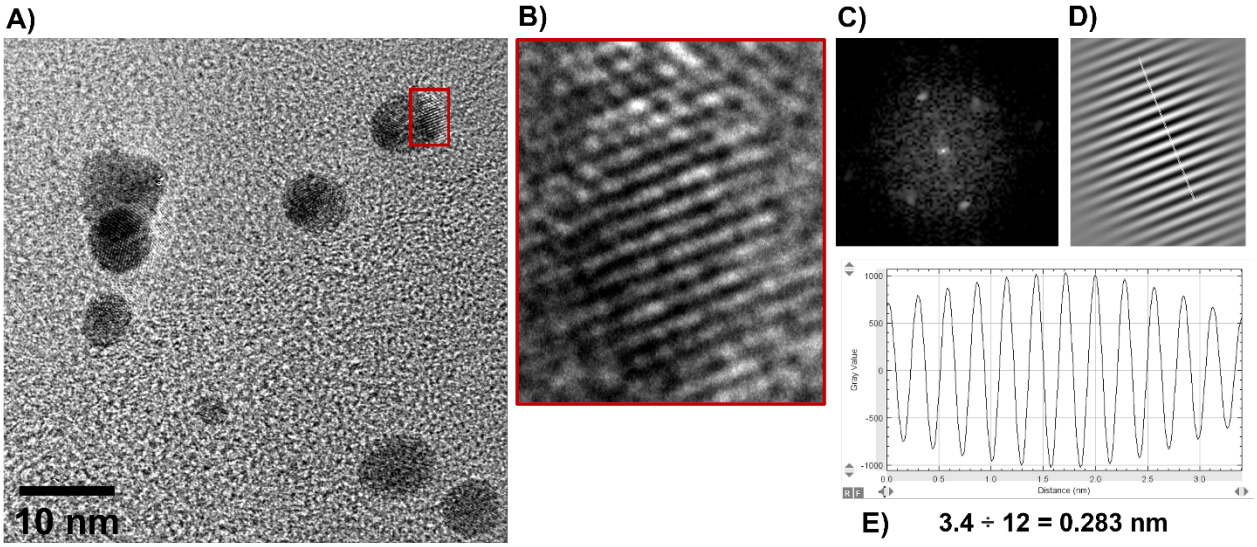


Figure S 7. Example of calculating the lattice spacing in Au NPs: these are *biohybrid NRase-Au NPs* (made using 0.8 mg mL^{-1} NRase). **A)** TEM image, red rectangle is area selected for the analysis. **B)** Zoomed-in section shown by the red rectangle in **A**. **C)** Fast Fourier transform (fft) of image **B**. **D)** Inverse fft with line drawn perpendicular to lattice fringes. **E)** Plot profile of line drawn in **D**, measuring the length of the line as 3.4 nm and there are 12 lattice fringes, therefore the average d-spacing across this line is 0.283 nm.

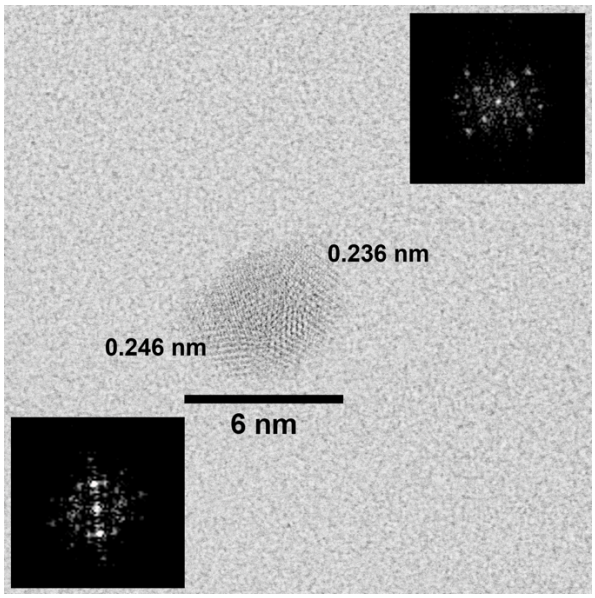


Figure S 8. HR-STEM BF image of *biohybrid NRase-Au@Pt NP* with insets of fast Fourier transform (fft) images showing lattice structure – spacing fitting with *fcc* lattice type. See **Figure S 16** for EDX analysis of the same NP.

S.2.7 Cofactor Studies

The native cofactor for the enzyme studied in this work, NRase, is 1,4-NADH. Another natural cofactor which is used by similar enzymes is 1,4-NADPH which only varies in the addition of a phosphate group (**Figure S 9** shows all the structures). Natural enzymes have evolved to be specific for either 1,4-NADH or 1,4-NADPH. There are a variety of non-natural cofactors, all containing the nicotinamide group, which can be made synthetically using a relatively simple and cheap method.[15-16] Two of these are used in this study – BNAH and AmNAH.

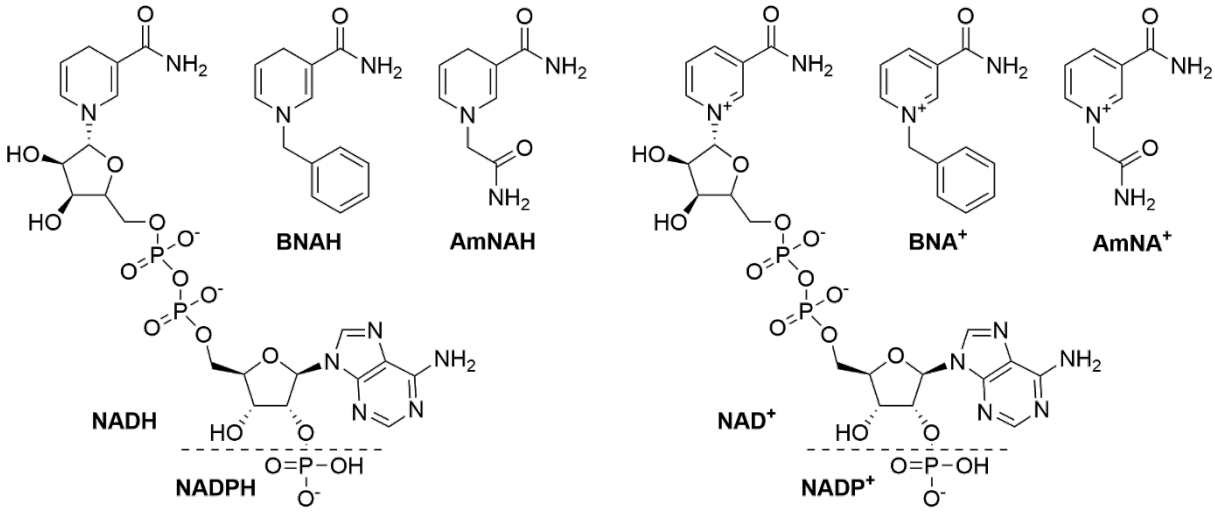


Figure S 9. Reduced and oxidised (left and right respectively) cofactor structures – the native cofactor for the NRase enzyme: NADH, the non-native NADPH and artificial cofactors: BNAH and AmNAH.

To confirm NRase causes the reduction of Au(III) and formation of Au NPs by oxidizing the supplied cofactor, 1,4-NADH, controls were carried out by using 1,4-NADPH instead of 1,4-NADH (**Figure S 10**). There is only a SPR peak for Au NPs in the UV-vis spectrum of the solution which contained $HAuCl_4$, NRase and 1,4-NADH. This indicates Au NP formation is catalysed by NRase by the hypothesised mechanism where NADH is oxidised at the buried active site (in which the specific nature of the configuration of amino acids surrounding the FMN does not allow for NADPH to undergo oxidation) and the resulting electrons can reduce the metal salt. The absorbance in the 400-600 nm region for the spectra of $HAuCl_4$, NRase and 1,4-NADPH is due to the absorbance from NRase.

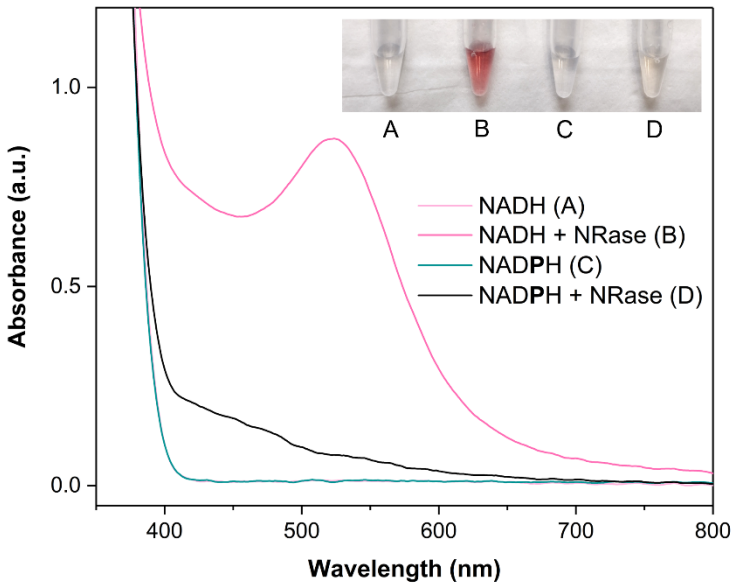


Figure S 10. UV-vis spectra of controls using the same conditions with either NADH or NADPH cofactor and in absence and presence of NRase. The inset shows a photograph of these solutions.

Next the artificial cofactors were tested and the results compared to NADH (**Figure S 11**). In the presence of the same concentration of NRase, the UV-vis spectra of the experiments using either NADH, BNAH or AmNAH, all have a similar λ_{max} (515 nm ± 1 nm) and a similar shape across 500-800 nm. Thus, indicating a similar size and shape distribution of Au NPs is made. This implies that the control of the NP morphology is directed by the NRase enzyme and not the cofactor. In the absence of NRase, while the UV-vis did not detect any Au NPs with NADH alone, there was significant absorbance across the 500-800 nm region when using BNAH or AmNAH cofactors. However the very broad nature of these absorbance peaks and the fact that precipitate was seen in these samples suggests these cofactors are able to reduce Au(III) but do not allow for size control or good stabilization of the resulting particles.

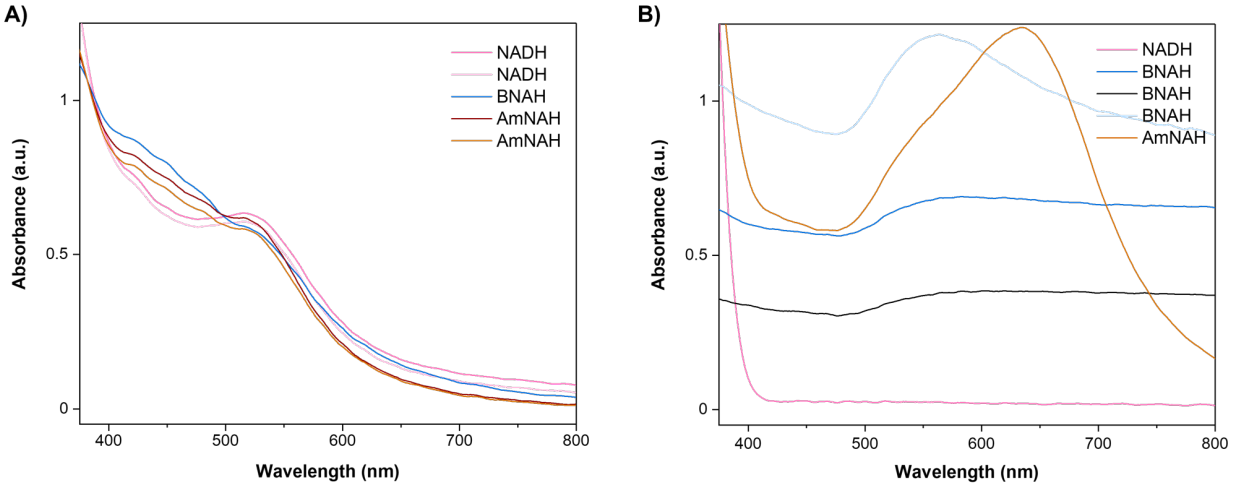


Figure S 11. UV-vis spectra of solutions containing a cofactor and $HAuCl_4$, after 16 h, **A)** in presence of NRase and **B)** in absence of NRase.

The TEM analysis confirmed the analysis made by UV-vis and showed the NPs made using NRase with NADH, BNAH or AmNAH were all spherical shaped NPs, under 10 nm in size (**Figure S 12**). The NPs prepared with BNAH without any NRase were seen to agglomerate and individual particles were seen to be irregular in shape and have a range of sizes.

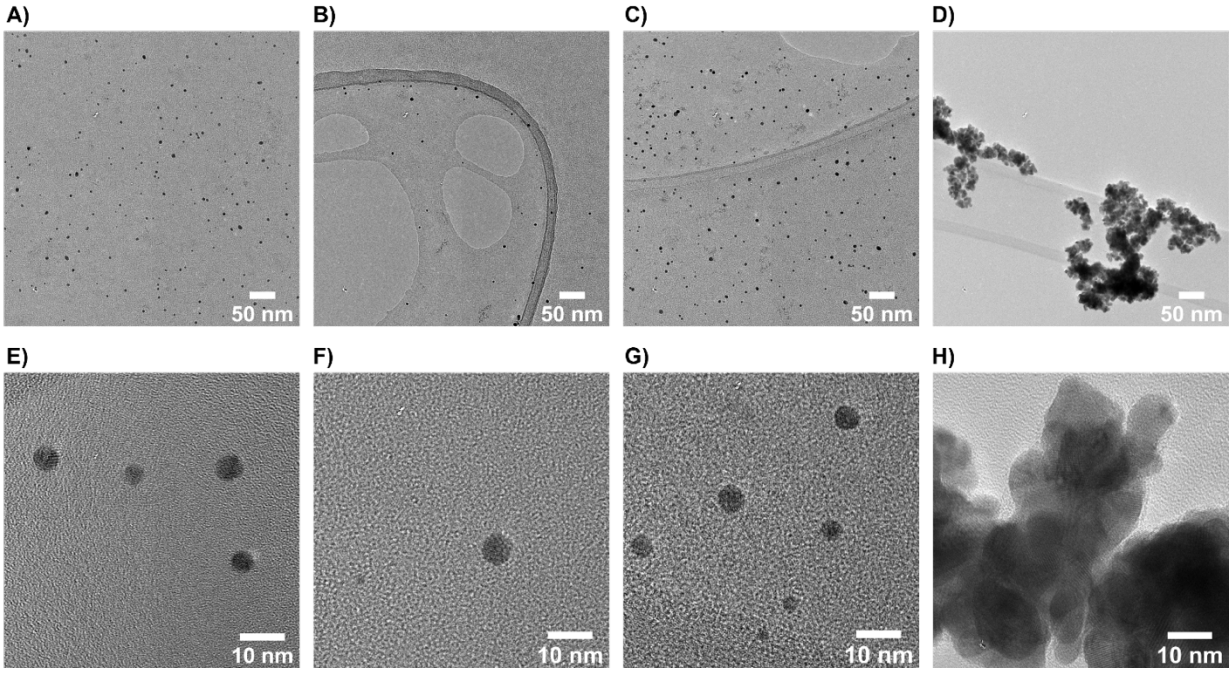


Figure S 12. TEM images from cofactor studies: **A)** & **E)** NADH with NRase, **B)** & **F)** BNAH with NRase, **C)** & **G)** AmNAH with NRase and **D)** & **H)** BNAH with no NRase. **A-D** lower magnification, **E-H** higher magnification.

The final experiment to verify that the whole NRase structure is required for achieving maximum NP size control and stability, involved testing FMN (the molecule where the hydride transfer occurs in the active site of NRase) and bovine serum albumin (BSA, a protein with no redox sites). The results using NADH as the cofactor (**Figure S 13**, **A**) showed only NRase could give good size control over the NPs, as indicated by the narrow SPR peak in the UV-vis spectrum. Whereas, replacing NRase for FMN (at approximately the same concentration) was found to, as expected, reduce Au(III) but with a very broad SPR peak indicating a large size/shape distribution of NPs. With FMN and BSA together there is an improvement in the shape of the absorbance spectrum compared to with FMN alone however much fewer NPs are formed thus BSA appears to limit the NP formation. BSA alone does not show any SPR absorbance confirming this is a suitable non-reactive protein to use as a control. The results using the artificial cofactor, BNAH, (**Figure S 13**, **B**) show a similar trend to the results with NADH. However, as it was shown earlier that BNAH alone can reduce Au(III) (**Figure S 11**, **B**), in the presence of BNAH and BSA Au NPs also formed. All the conditions tested do not give as good a size control as with NRase.

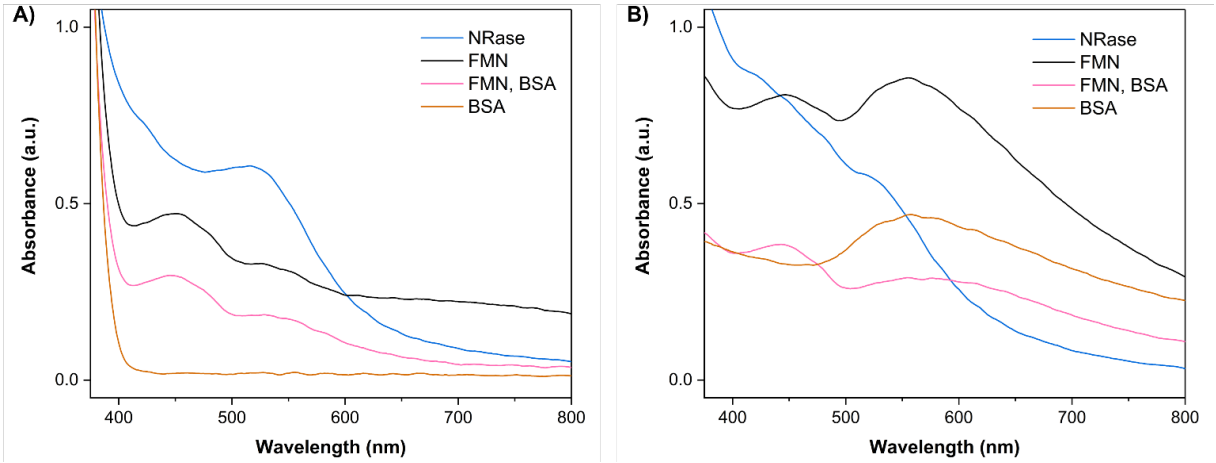


Figure S 13. UV-vis spectra of controls with FMN and/or BSA compared to NRase, after 16-17 h, **A)** with NADH cofactor and **B)** with BNAH cofactor.

S.2.8 Gold-Platinum NPs Size Distribution from TEM

The *biohybrid NRase-Au@Pt NPs* made by adding K_2PtCl_6 and NADH to a solution of already prepared Au NPs (made using NRase and NADH), were analysed by TEM. These were found to be quasi-spherical NPs of 6.4 ± 2.4 nm size (**Figure S 14**). The NPs prepared without NRase, when analysed by TEM, were found to contain a lot of large agglomerates and individual particles ranged in sizes – size distribution could not be accurately measured due to the overlapping nature of the NPs in the TEM images (**Figure S 15**).

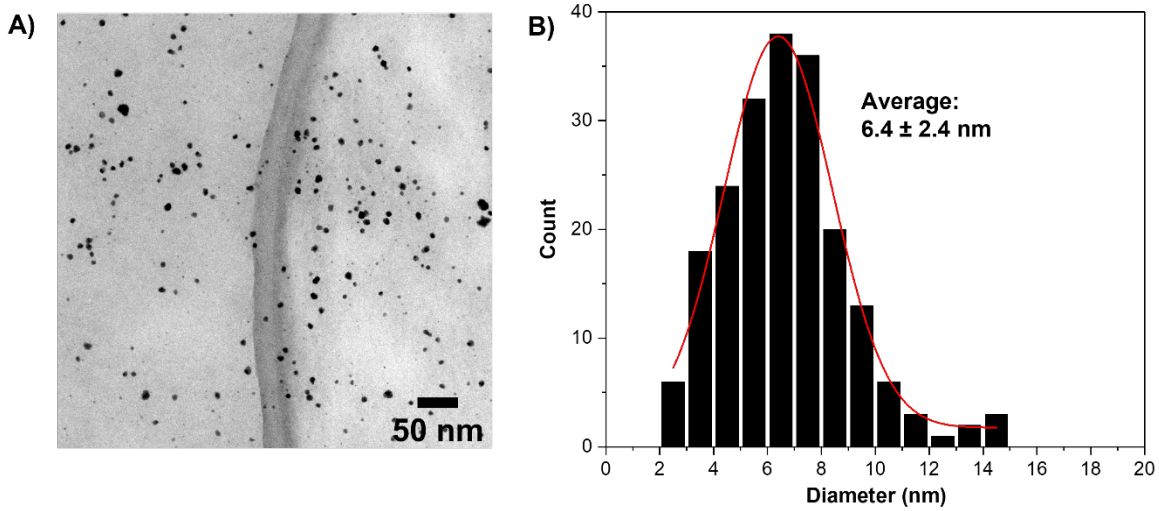


Figure S 14. Example of TEM analysis of *biohybrid NRase-Au@Pt NPs*, **A)** TEM image and **B)** NP size analysis (of 202 NPs, ignoring NPs smaller than 2 nm).

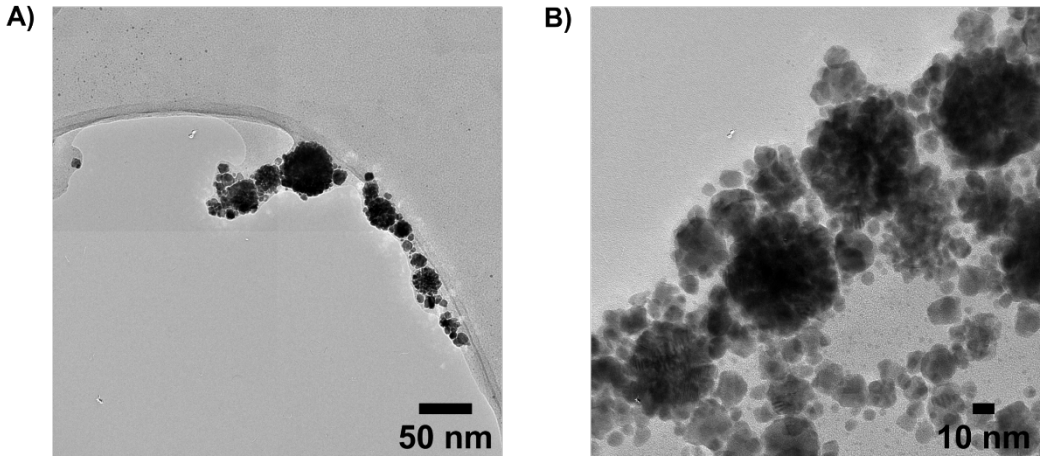


Figure S 15. TEM images of *non-bio-Au-Pt NPs* (Au-Pt NPs prepared without using NRase).

S.2.9 Gold-Platinum NPs HR-STEM-EDX Analysis

The following uncertainties should be taken into consideration when analysing these results: an EDX signal is always going to be somewhat delocalised due to the interaction volume of the electrons with the sample and the relatively large escape depth for x-rays and there may be some deformation of the nanoparticle under the beam. For the analysis the HR-STEM HAADF images of the corresponding NPs were used to measure the NP diameter and the position of the NP along the EDX line scan. The EDX line scan data was "smoothed" in Origin using a "Savitzky-Golay" method, with 20 pts of window and a polynomial order of 1. The shell thickness was estimated by using the distance from the edge of the NP (determined using the HAADF image, ± 0.1 nm) to the point at which the Au and Pt lines cross.

Thus, to calculate the core and shell thickness of the *biohybrid NRase-Au@Pt NPs* (made using NRase and the two-step procedure), the distances shown in **Figure S 16**, **A** were applied to the HR-STEM-EDX line scans shown in **Figure S 16**, **B** and **C** and therefore used to calculate the Au core diameter and Pt shell diameter. Using averages from the two line scans therefore calculated the Au core as 3.8 ± 0.1 nm and the Pt shell as 0.9 ± 0.4 nm.

The *non-bio-Au-Pt NPs* (made without NRase, with the same 2-step procedure), showed structures with more of an alloy composition or a Pt-core Au-layer and thin Pt-shell, as shown in **Figure S 17**, **A** and **B**. The *NRase-Au-Pt NPs,* prepared with NRase and with a 1-step procedure, also gave alloy structures and Pt-core Au-layer and thin Pt-shell structures such as those shown in **Figure S 17**, **C** and **D**.

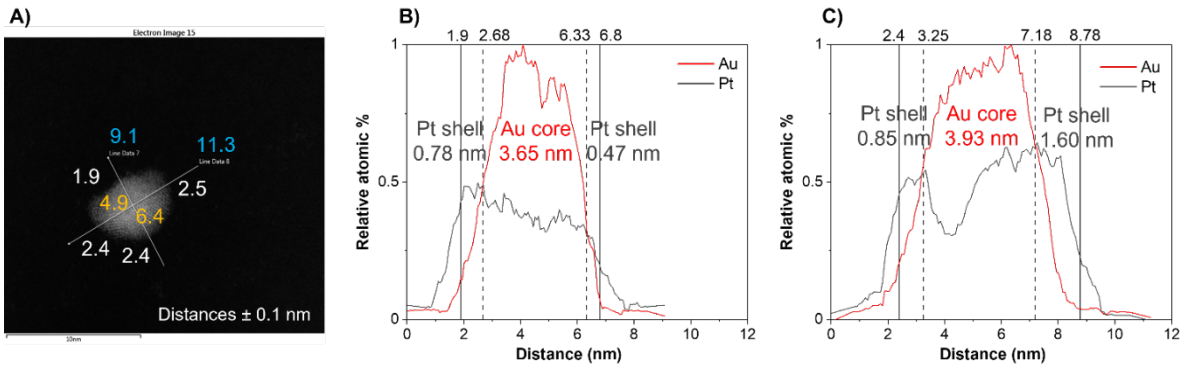


Figure S 16. EDX analysis of *biohybrid NRase-Au@Pt NP*, prepared using NRase and a two-step procedure: **A)** HR-STEM HAADF image of NP showing two line scans with distances measured using ImageJ (blue numbers are total length of line scan, yellow are diameter of NP across line scan and white are distance from start or end of line scan and edge of NP along line scan). **B)** HR-STEM-EDX line scan showing data converted to relative atomic % of detected Au and Pt along the line scan distance (of line data 7, 9.1 nm total, as labelled in **A**. **C)** HR-STEM-EDX line scan showing data converted to relative atomic % of detected Au and Pt along the line scan distance (of line data 8, 11.3 nm total, as labelled in **A**.

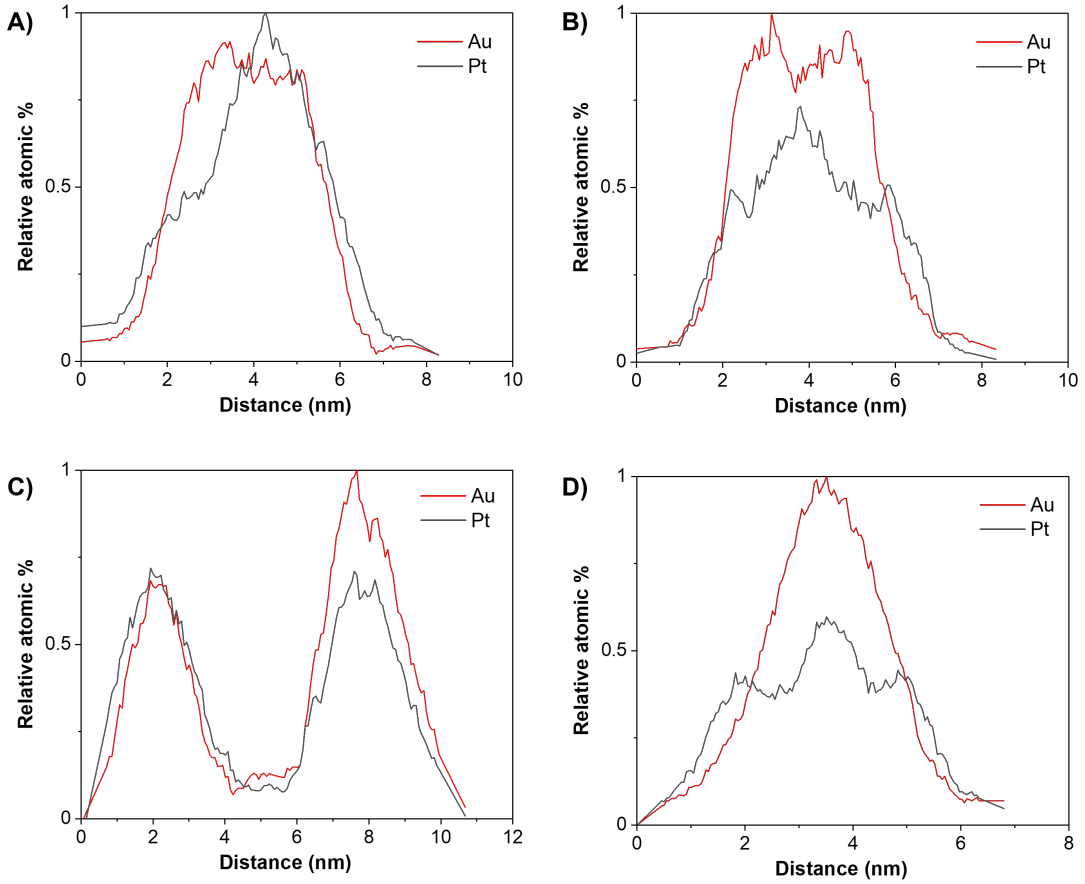


Figure S 17. EDX analysis of Au-Pt NPs: **A)** & **B)** examples of line scans from NPs prepared without NRase enzyme *(non-bio-Au-Pt NPs)*, **C)** & **D)** examples of line scans from NPs prepared with NRase enzyme and with a 1-step procedure (*NRase-Au-Pt NPs*).

S.2.10 1-Step Versus 2-Steps for Gold-Platinum NP Formation

A comparison of using a 1-step procedure, where the Au(III) and Pt(IV) are added at the same time, versus the original 2-step procedure where Au(III) is added first and Pt(IV) is added after an initial 16 hours, was carried out. The resulting UV-vis spectra (**Figure S 18**), after both procedures have allowed the metals to be reduced for a total of 64 hours, appear to be very similar between the different methods used. However, from the HR-STEM-EDX data (see **S.2.9**) the structures do appear different with there being evidence for Au@Pt core-shell structures after the 2-step procedure whereas the 1-step procedure seems to give a mixture of Pt-core Au-layer and thin Pt-shell structures as well as alloy structures. Most interesting to note is that without NRase no NPs form after the initial 16 h, when Au(III) and Pt(IV) are added in either a 1-step or 2-step procedure (**B** and **D**) but after more time NPs do start to form as observed by the broad absorbance from 400-800 nm at 48 and 64 h time points.

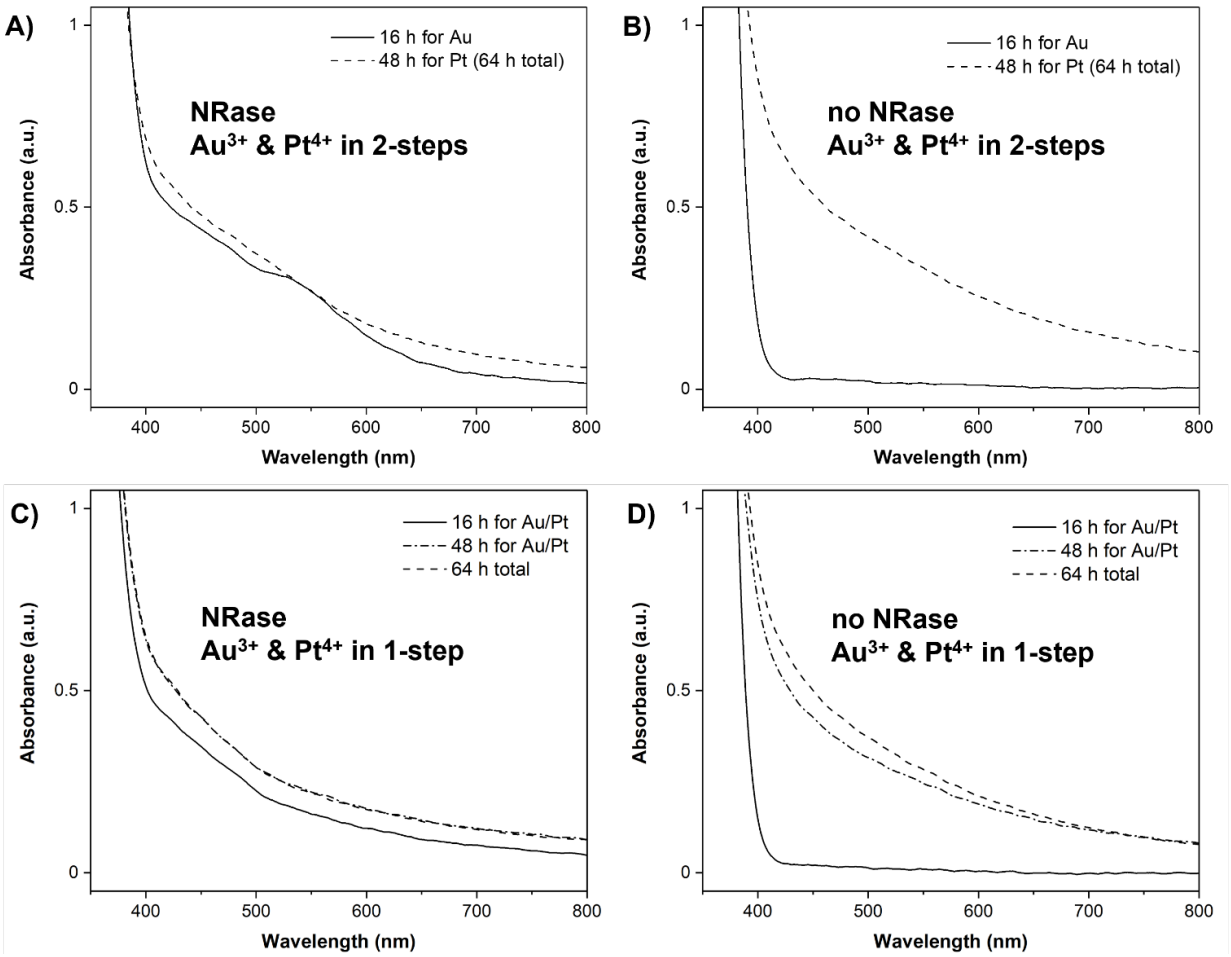


Figure S 18. UV-vis spectra recorded at different time points after $HAuCl_4$ and K_2PtCl_6 were either added in '2-steps' (with $HAuCl_4$ added first and K_2PtCl_6 after 16 h) or added at the same time, '1-step': **A)** 2-step addition with NRase present, **B)** 2-step addition with no NRase, **C)** 1-step addition with NRase present, **D)** 1-step addition with no NRase.

S.2.11 Control without Gold for Platinum NPs

A side-by-side experiment of four conditions in the absence and presence of gold and of NRase was carried out. The UV-vis spectra recorded at time points after K_2PtCl_6 and NADH were added are shown in **Figure S 19**. The very low absorbance seen in the spectra of the 'no Au' solutions (**C** and **D**) suggests only low concentration of Pt NPs were formed.

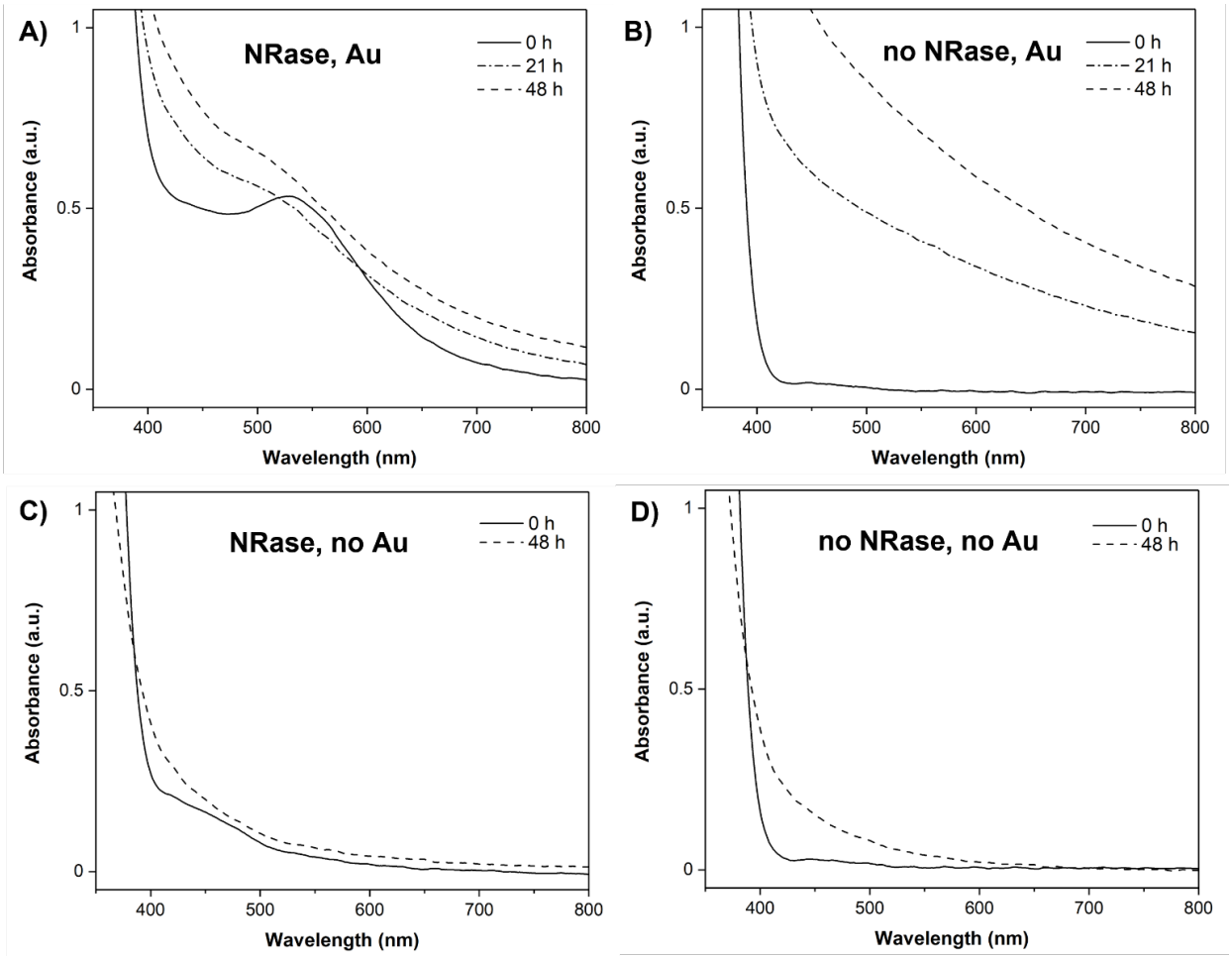


Figure S 19. UV-vis spectra recorded at different time points after K_2PtCl_6 and NADH were added to a solution which either contained: **A)** Au NPs made using NRase and NADH, **B)** no NRase but a solution of "aged Au salts and NADH", **C)** NRase but no Au, or **D)** no NRase and no Au. The "aged Au salts and NADH" solution means the same amount of $HAuCl_4$ and NADH as were used to make the Au NPs in **A** had been left under the same conditions (16 h, at room temperature).

S.2.12 Comparison of Using Different Ratios of Pt(IV) to Au(III)

The effect of varying the ratio of Pt(IV) to Au(III) on the synthesis of Au-Pt NPs was tested by either using a slight excess of Au or a slight excess of Pt (**Figure S 20**). These tests were carried out using the '2-step' procedure where Au(III) is added first and Pt(IV) is added after an initial 16 hours. The difference between the results is most apparent for the conditions with no NRase where the absorbance is much larger for the sample using an excess of Pt – see **B** compared to **D**. The difference is more difficult to detect by UV-vis in the case of the conditions where NRase was present – **A** and **C**.

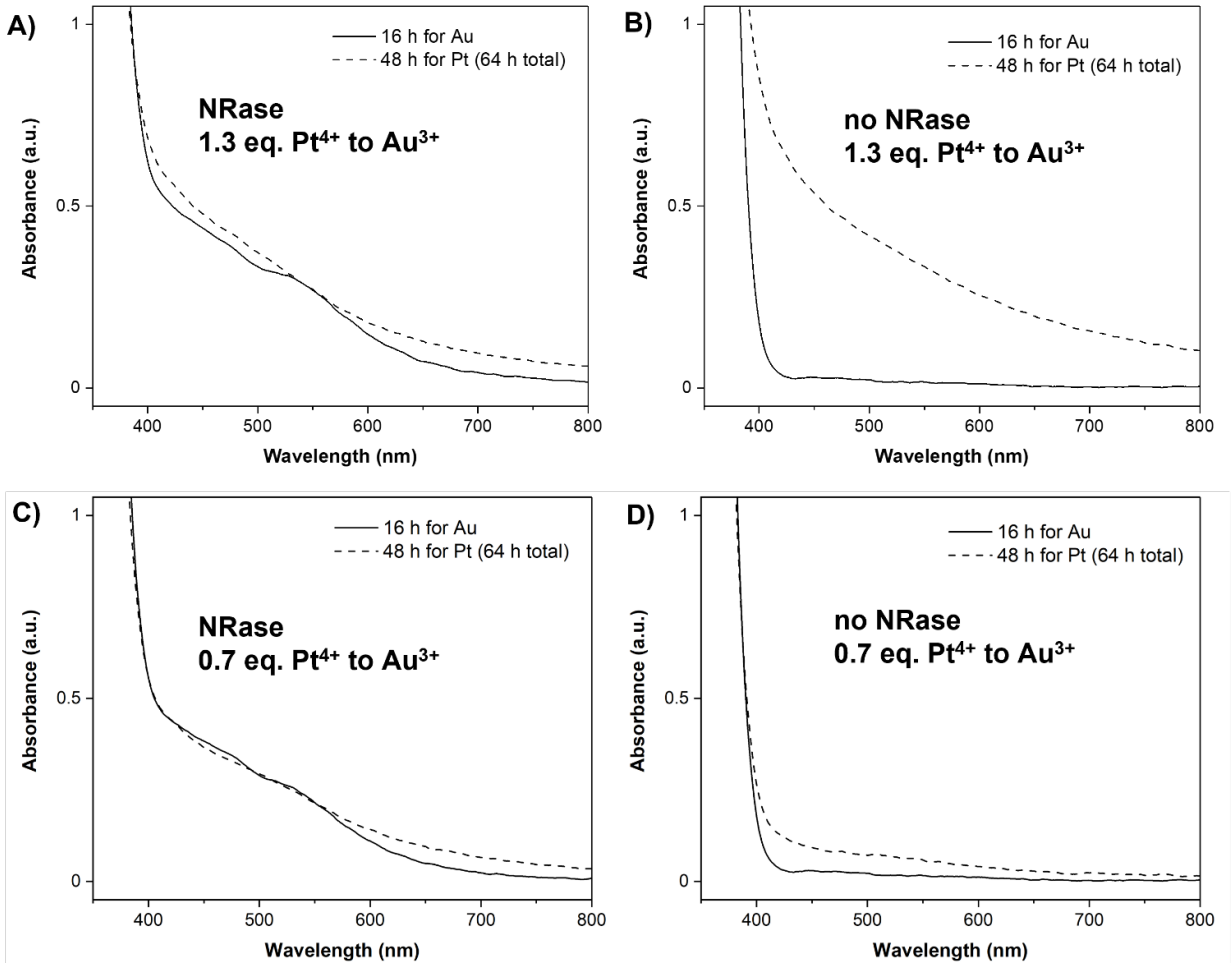


Figure S 20. UV-vis spectra recorded after 16 h from which $HAuCl_4$ and NADH were added together, followed by the addition of different amounts of K_2PtCl_6 and NADH, '16 h for Au', and then after leaving for a further 48 h, '48 h for Pt (64 h total)'. **A)** an excess, 1.3 molar equivalents, of Pt^{4+} to Au^{3+} was used, with NRase present, **B)** same conditions as **A** without NRase, **C)** 0.7 molar equivalents, of Pt^{4+} to Au^{3+} was used, with NRase present, **D)** same conditions as **C** without NRase.

S.2.13 Monitoring the Rate of Au NP Formation

The 16-hour reaction time used for testing different conditions in the synthesis of Au NPs was used to make sure each synthesis had reached completion. However as was seen by the colour change of the solutions, most were probably completed in a much shorter time. To investigate this, an experiment was performed by in situ monitoring of the reaction solution by UV-vis, recording spectra every 30 minutes (**Figure S 21**). From 0 to 1 hour, a fast initial rate of NP formation is observed by the increase at 509 nm (which was the final SPR λ_{max}) which is followed by a slower period where the absorbance at 509 nm decreases by 18%. This decrease in absorbance may be related to the FMN in the active site of NRase becoming reduced to $FMNH_2$ once there are no more metal salts for $FMNH_2$ to reduce by itself being oxidized. FMN has an absorbance peak with λ_{max} at 445 nm which decreases as is it reduced to $FMNH_2$.[17]

Another factor worth mentioning that has not been investigated thus far is the effect of stirring as all the NP synthesizes have been carried out without any stirring. Thus, the rate of NP formation is likely to be increased by introducing stirring.

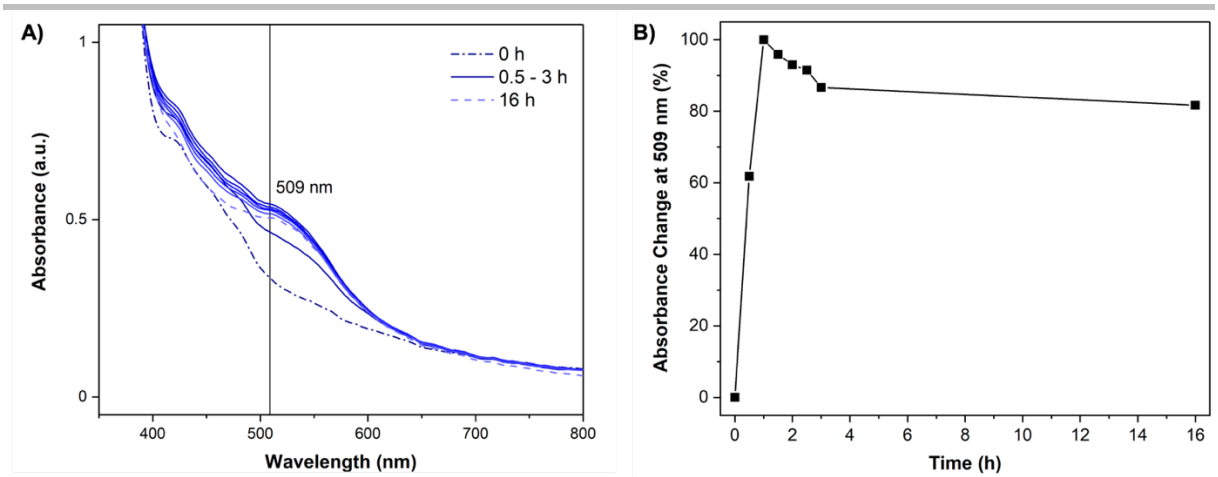


Figure S 21. Monitoring the synthesis of Au NPs using UV-vis spectrometry. **A)** UV-vis spectrum recorded immediately after addition of all reagents: $HAuCl_4$, 1,4-NADH and NRase (0 h) and then subsequent spectra recorded every 30 mins for 3 h, then a final spectrum recorded after 16 h. The formation of Au NPs is apparent within 30 minutes and at 1 h the SPR peak becomes more defined with the peak maximum at 509 nm. **B)** Plot of the absorbance change at the λ_{max} (509 nm) over time, with respect to the maximum absorbance at 509 nm which was recorded at 1 h.

S.2.14 NAD^+ Reduction Studies

The reduction of NAD^+ can lead to different products depending on the catalyst and conditions used. As described in the main text, 1,4-NADH is the only bioactive cofactor out of the possible products, shown in **Figure S 22**. Therefore, it is important to study the selectivity for 1,4-NADH.

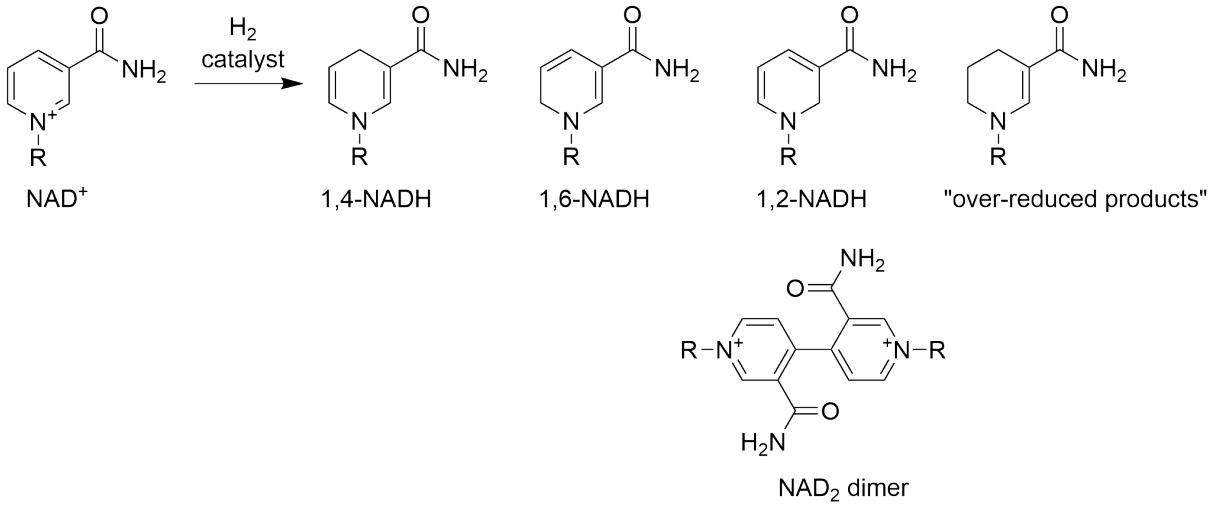


Figure S 22. NAD^+ reduction and potential products (R = adenosine diphosphoribose).

For NAD^+ reduction using H_2 and Au-Pt NPs, the following conditions were tested: the amount of NRase used in the NP synthesis, the ratio of Au^{3+} to Pt^{4+} used in the NP synthesis, whether the Au^{3+} and Pt^{4+} salts were added at the same time or not ('1-step' versus '2-step'), as well as adding more NRase after the NP synthesis for the NAD^+ reduction. A few recycling tests were also attempted. All results, with analysis after a reaction time of 21 h, are shown in **Table S 4**.

The results from entries 1-7 and -10 show that as the amount of NRase in the NP synthesis is increased, there is an increase in selectivity for 1,4-NADH, while the conversion decreases. Entries 7 and 8 show that using a slight excess of Pt compared to Au is better for conversion of NAD^+ than an excess of Au to Pt. Entries 7 and 9 show that using the '1-step' procedure for making Au-Pt NPs may be detrimental for achieving conversion of NAD^+. Adding more NRase after the NP synthesis gave improvement in results with all batches of NPs tested (comparing entry 1 with 11, entry 3 with 12 and entries 4-5 with 13). The amount of NRase added to these preformed NPs was less than used in the NP synthesis (e.g. 0.54 mg mL^{-1} NRase in NP syn. equates to 0.16 mg mL^{-1} once added to a solution of NAD^+, while the concentration of extra NRase added to this solution is 0.07 mg mL^{-1}). Thus, suggesting some of the NRase after the Au-Pt NP synthesis is no longer in an active form, perhaps due to being involved in the stabilisation of the NPs.

The preliminary studies of recycling the *biohybrid NRase-Au@Pt NPs* were carried out by filtering the organic reaction products through a size exclusion membrane (10 kDa, 1 nm pore size) and thus reusing the NPs and enzyme left behind in the filter for a second and subsequently a third reaction. The results (entries 12, 14 and 15) suggested the enzyme remained active, with no loss in selectivity across a total of 63 hours. There was however loss in total conversion – likely due to a non-optimized recycling procedure where some NPs and enzyme may be lost between reactions, on the membrane filter. Further studies are needed to assess the recyclability of these NPs for repeated batch or flow systems.

Table S 4. Results from H_2-driven, NAD^+ reduction studies using *non-bio-Au-Pt NPs, NRase-Au-Pt NPs* and *biohybrid NRase-Au@Pt NPs*, prepared with different NRase concentrations.[a]

Entry	NP synthesis conditions:			[NRase] in NAD^+ reaction (mg mL^{-1}):		Selectivity for 1,4-NADH (%)[c]	Conversion of NAD^+ (%)[d]
	NP batch[b]	[NRase] in total NP syn. (mg mL^{-1})	Au^{3+}: Pt^{4+} molar ratio	Introduced during NP syn.	Added after NP syn.		
1	1a	0	1: 1.1	0	0	0	>99
2	1b	0.20	1: 1.1	0.06	0	17	>99
3	2b	0.54	1: 1.1	0.16	0	64	88
4	2c	0.81	1: 1.1	0.24	0	74	33
5	2c	0.81	1: 1.1	0.24	0	73	37
6	3b	1.88	1: 1.1	0.55	0	>99	20
7	4b	1.60	1: 1.3	0.47	0	>99	41
8	4c	1.60	1: 0.7	0.47	0	N/A	0
9	4d	1.60	1: 1.3[e]	0.47	0	N/A	0
10	4e	3.19	1: 1.3	0.93	0	N/A	0
11	1a	0	1: 1.1	0	0.07	96	>99
12	2b	0.54	1: 1.1	0.16	0.07	>99	>99
13	2c	0.81	1: 1.1	0.24	0.07	>99	>99
14[f]	2b	0.54	1: 1.1	0.16	0.07	>99	68
15[g]	2b	0.54	1: 1.1	0.16	0.07	>99	40

[a] Reaction conditions follow **S.1.7.1**. Analysis after reaction time of 21 h. [b] Different batches of NPs (number and letter referring to experiment no. and sample no. respectively: "a" indicates no NRase used). [c] Selectivity is measured by the content of 1,4-NADH as a percentage out of the total reaction products, as analysed by ^{1}H NMR spectroscopy. [d] Conversion measures the consumption of NAD^+ starting material, as analysed by ^{1}H NMR spectroscopy. [e] Au^{3+} and Pt^{4+} salts added together at same time, using the '1-step' procedure. [f] Recycled NPs/enzyme study: after first reaction (entry 12), reaction solution filtered with 10 kDa size exclusion filter and new NAD^+ solution added. [g] Recycled NPs/enzyme study: after second reaction (entry 14), reaction solution filtered with 10 kDa size exclusion filter and new NAD^+ solution added.

In analysis by ^{1}H NMR, the 5.0 to 10.0 ppm spectral region is useful for quantifying reaction products (**Figure S 23**). As NAD^+ is reduced, the nicotinamide ring loses its aromaticity thus there is the disappearance of the peaks at high ppm (8.2, 8.8, 9.1 and 9.3 ppm) and the appearance of a single new peak in this region, at 6.9 ppm, indicates the 1,4-NADH isomer has been made. If there are other peaks in the 6.8 to 7.4 ppm region this indicates other NADH isomers, i.e. 1,6-NADH and 1,2-NADH, are present.

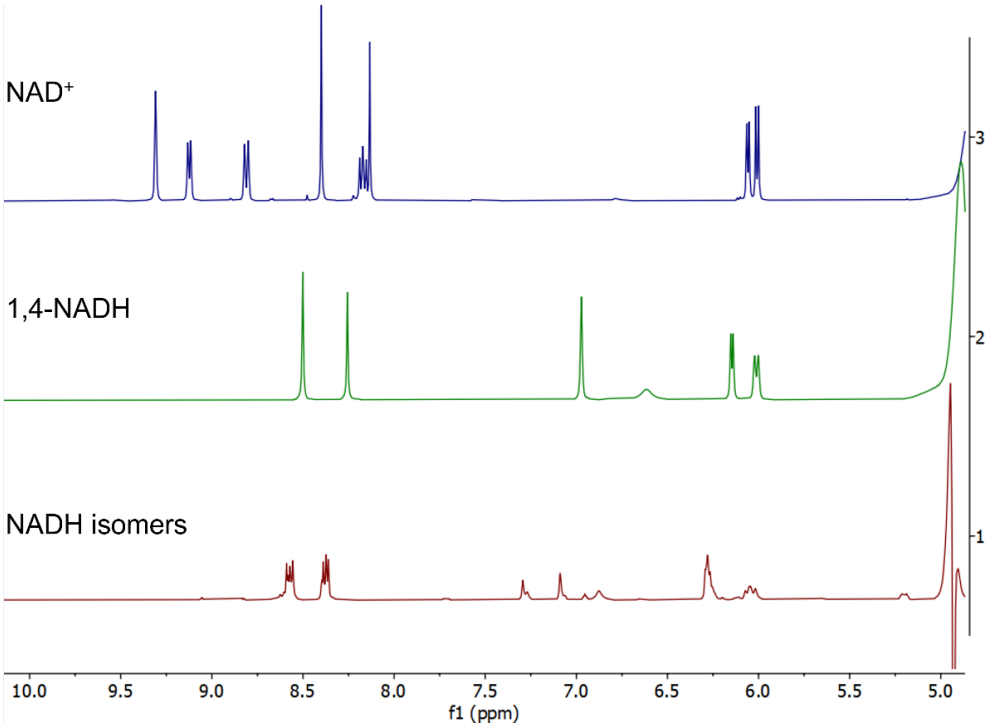


Figure S 23. ^{1}H NMR spectra (20% D_2O in aqueous 5 mM potassium phosphate pH 8) of standards of NAD^+ and 1,4-NADH and a mixture of other NADH isomers made by reacting NAD^+ with $NaBH_4$.

As well as other NADH isomers, in the reactions with the *non-bio-Au-Pt NPs* there is evidence for over-reduced products (i.e. further reduction of the nicotinamide ring). This can be seen by the peaks at 2.8 to 3.4 ppm indicating saturated bonds (**Figure S 24**).

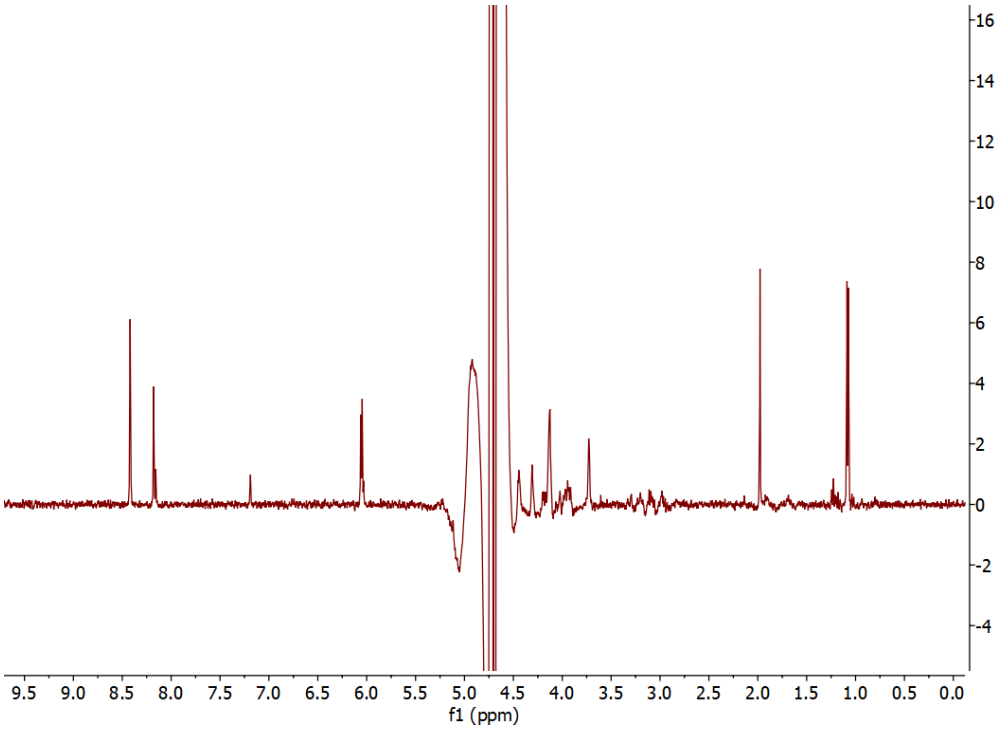


Figure S 24. ^{1}H NMR spectra (20% D_2O in aqueous 5 mM potassium phosphate pH 8) of example from NAD^+ reduction reaction using *non-bio-Au-Pt NPs* without any NRase (**Table S 4**, entry 1) giving no selectivity for 1,4-NADH and instead giving over-reduced products (as evidenced by the peaks at 2.8-3.4 ppm).

When NRase (in high enough concentration) is included in the NAD^+ reduction reactions, the ^1H NMR spectra show complete selectivity for 1,4-NADH isomer such as in the example shown in **Figure S 25**.

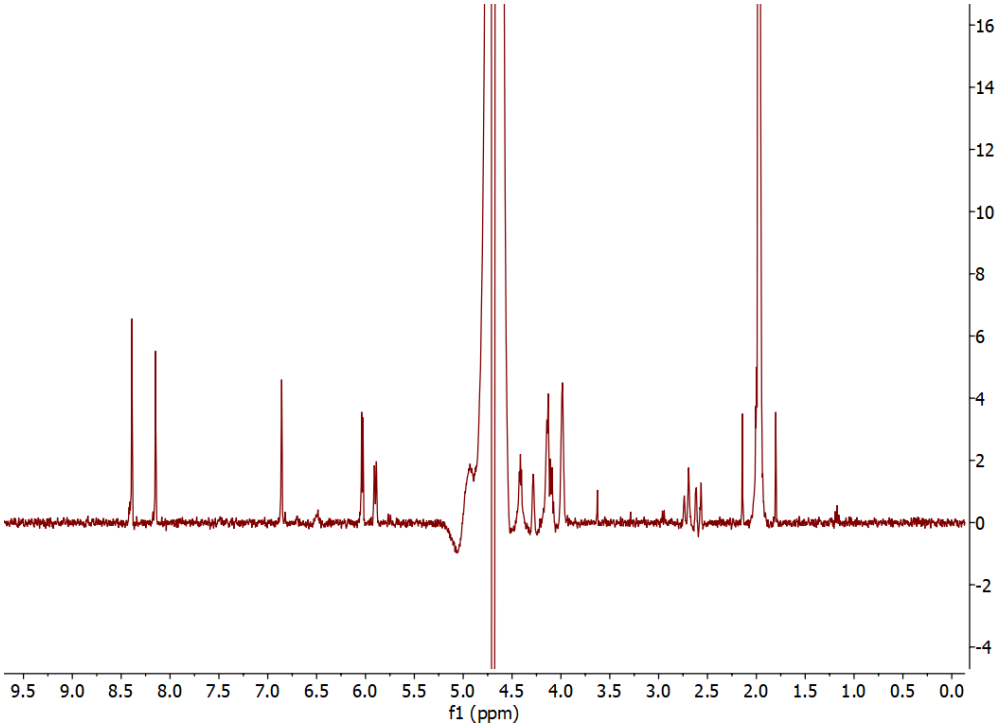


Figure S 25. ^1H NMR spectra (20% D_2O in aqueous 5 mM potassium phosphate pH 8) of example from NAD^+ reduction reaction using *biohybrid NRase-Au@Pt NPs* (**Table S 4**, entry 13) where conditions were selective for 1,4-NADH (with complete conversion of NAD^+).

S.2.15 4'-Chloroacetophenone Reduction

The results displayed in **Table S 5** are from reactions comparing reaction conditions and the type of NPs that were used. The initial conditions tested were based on those from previous work in the group where a NADH dehydrogenase was coupled with a Pd/C catalyst.[18] After long reaction times, the conversion was moderate but not high (entries 1-2), thus since sulfur containing molecules are known to often coordinate strongly to metal NPs, the tris buffer and DMSO co-solvent was exchanged for no buffer (unbuffered water instead) and acetonitrile as the co-solvent to solubilize 4'-chloroacetophenone in solution. This change in conditions allowed for 91-98% conversion of product (entries 3-4). Due to the acidic nature of NAD^+ these reaction solutions were around pH 6 which may not be optimal for recycling the catalyst as pH 6 is also around the electrostatic potential (pI) of NRase meaning NRase can cause aggregation of the NPs by weakening stabilization forces. Indeed, after attempting to recycle the catalyst from these reactions, only very low conversion (<10%) was obtained. Therefore, a low concentration of a non-coordinating buffer was introduced, 3.5 mM of pH 8 potassium phosphate, which was enough to keep the pH at pH 8 (with 1 mM NAD^+ concentration). Shorter reaction times were also focused on.

As expected from the NAD^+ reduction experiments, without adding extra NRase, the conversions were significantly lower (entries 5-6). Increasing the amount of NRase added did not significantly increase the conversion (entries 8-9). However, it was later found that increasing the amount of metal NPs present did significantly increase the conversion such that high conversion (entries 11-13) could be obtained within the 21-hour reaction length.

Reactions were also tested with ethanol instead of acetonitrile as the co-solvent. However as can be observed by the reaction without any NPs or NRase (but still with ADH), 1 vol% ethanol gave 22% product (entry 16). In this case ADH is oxidising ethanol while reducing NAD^+ and thus subsequently allowing it to reduce 4'-chloroacetophenone using the generated 1,4-NADH. There is therefore a build-up of ethanal which is not recycled. It is a useful comparison to the results with NPs and NRase which therefore shows that the biohybrid NRase-NP system can provide faster reaction rates than the ethanol system.

Pt NPs prepared without Au (which only formed in low concentrations under the synthesis conditions) were also tested by adding much higher volumes of the synthesis solution – to try to reach a similar concentration as the Au-Pt NPs

prepared under the same conditions. The Pt NPs prepared without NRase gave only a slightly higher conversion than the control without NPs (entries 15-16). The Pt NPs prepared in the presence of NRase gave 64% conversion (entry 14) however the *biohybrid NRase-Au@Pt NPs* gave 95% (entry 13) under the same conditions and with using less of the synthesis solution. Therefore these experiments confirm that using Au to catalyse Pt(IV) reduction is beneficial for the application of the resulting NPs.

Reaction optimisation has not been carried out thus far, therefore the catalytic activity values (TTN, TOF and TN) displayed in the table should only be considered as an initial starting point and not as fully optimised rates for this reaction and catalyst system which is beyond the scope of this communication.

Table S 5. Results from 4'-chloroacetophenone reduction studies using Au-Pt NPs and NRase to recycle 1,4-NADH which is required by ADH to carry out the enantioselective reduction of the ketone to (*S*)-4'-chloro-1-phenylethanol.[a]

Entry	NP synthesis conditions:			Reduction reaction conditions:				Time (h)	Product (%)[e]	NRase TTN[f]	NRase TOF (h^{-1})[f]	NAD^+ TN[g]
	NP batch[b]	[NRase] in NP syn. (mg mL^{-1})	Au^{3+}: Pt^{4+} molar ratio	[NRase] introduced during NP syn. (mg mL^{-1})	[NRase] added after NP syn. (mg mL^{-1})	Au, Pt mol%[c]	Buffer and cosolvent conditions[d]					
1[h]	5b	0.85	1: 1.3	0.25	0.36	2.0, 2.6	A	64	41	309	5	2.1
2[h]	5a	0	1: 1.3	0	0.36	2.0, 2.6	A	64	20	256	4	1.0
3	5b	0.85	1: 1.3	0.25	0.36	2.0, 2.6	B[i]	64	>99	747	12	5.0
4	5a	0	1: 1.3	0	0.36	2.0, 2.6	B[i]	64	88	1124	18	4.4
5	2b	0.54	1: 1.1	0.16	0	2.0, 2.2	C	21	4	115	5	0.2
6	5a	0	1: 1.3	0	0	2.0, 2.6	C	21	2	N/A	N/A	0.1
7	none	N/A	N/A	N/A	N/A	N/A	C	21	0	N/A	N/A	0.0
8	2b	0.54	1: 1.1	0.16	0.36	2.0, 2.2	C	21	18	159	8	0.9
9	2b	0.54	1: 1.1	0.16	0.51	2.0, 2.2	C	21	22	151	7	1.1
10	5a	0	1: 1.3	0	0.36	2.0, 2.6	C[j][k]	21	25	319	15	1.3
11	5a	0	1: 1.3	0	0.36	4.0, 5.2	C[j]	21	84	1073	51	4.2
12	5a	0	1: 1.3	0	0.36	2.0, 2.6	C[j]	21	33	422	20	1.7
13	2b	0.54	1: 1.1	0.32	0.36	4.0, 4.4	D	21	95	643	31	4.8
14	5b*	0.85	0: 1	0.48	0.36	0, 7.8	D	21	64	350	17	3.2
15	5a*	0	0: 1	0	0.36	0, 7.8	D	21	29	371	18	1.5
16	none	N/A	N/A	N/A	N/A	N/A	D	21	22[l]	N/A	N/A	1.1

[a] Reaction procedure as described in **S.1.7.2**. Conditions, unless otherwise stated: NAD^+ (1 mM), 4'-chloroacetophenone (5 mM), ADH-105 (0.44 mg mL^{-1}), H_2 (1 bar), room temperature (20-25 °C). [b] Different batches of NPs (number and letter referring to experiment no. and sample no. respectively: "a" indicates no NRase used and * has no Au). [c] Mol% calculated from concentration of Au^{3+} and Pt^{4+} used in the NP synthesis and adjusted to reflect concentration in the reaction solution relative to 5 mM concentration of 4'-chloroacetophenone. [d] A: tris-HCl (50 mM, pH 8), DMSO (1 vol%), B: no buffer (pH 6), acetonitrile (1 vol%), C: potassium phosphate (3.5 mM, pH 8), acetonitrile (1 vol%) and D: potassium phosphate (3.5 mM, pH 8), ethanol (1 vol%). All other conditions are kept the same, unless otherwise stated, as follows: NAD^+ (1 mM), 4'-chloroacetophenone (5 mM), ADH-105 (0.44 mg mL^{-1}), H_2 (1 bar), room temperature (20-25 °C). [e] Conversion was calculated using ^1H NMR spectroscopy by using a calibration curve of known concentrations of mixed 4'-chloroacetophenone and (*S*)-4'-chloro-1-phenylethanol and using the ratio between their absolute integrations at 7.90-8.05 ppm and 7.30-7.50 ppm respectively (see **Figure S 27**). Chiral-GC was also used to confirm some of the conversions and to determine the enantioselectivity of the product (see **Figure S 30**). [f] NRase total turnover number (mol of 4'-chloro-1-phenylethanol per mol of NRase) and NRase turnover frequency (mol of 4'-chloro-1-phenylethanol per mol of NRase per hour) using total mol of NRase in reaction (i.e. NRase introduced during NP synthesis + NRase added after NP synthesis) and mol of product determined from analysis at end of reaction therefore TOF only an approximation. [g] NAD^+ turnover number (mol of 4'-chloro-1-phenylethanol per mol of NAD^+). [h] A higher

amount of ADH-105 was used (0.87 mg mL^{-1}). However, under these same conditions, using NP batch 5b, with 0.44 mg mL^{-1} ADH-105 the conversion was similar (44%). [i] These conditions led to low conversions (<10%) when recycling the catalyst. [j] These were carried out using 2.5 bar H_2. [k] The same conditions at 1 bar H_2 gave a similar conversion (20%). [l] This product is formed since ADH has oxidised the ethanol (present as a cosolvent) while reducing NAD^+ to NADH which it can then re-oxidise while reducing 4'-chloroacetophenone.

S.2.16 4'-Chloroacetophenone Reduction Analysis

^{1}H NMR spectroscopy was used as the main method for analysis of the 4'-chloroacetophenone reduction reactions, with the peaks in the 7.3 to 8.1 ppm region used to calculate the conversion (**Figure S 26**, **Figure S 28**, **Figure S 27**).

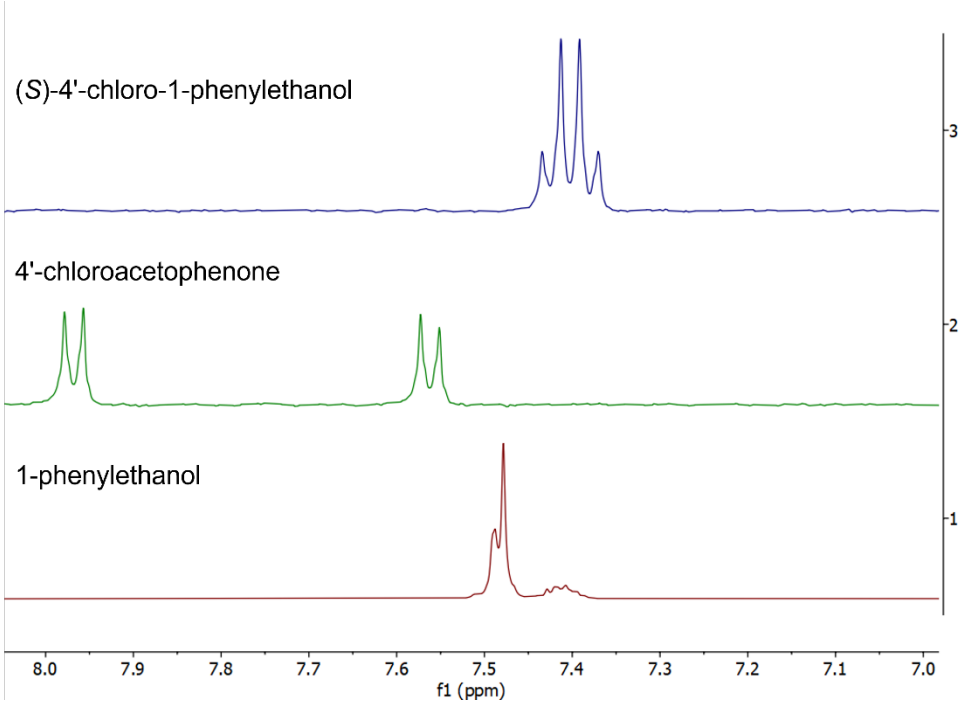


Figure S 26. ^{1}H NMR spectra (20% D_2O in aqueous 5 mM potassium phosphate pH 8) of standards of product, starting material and dechlorinated product (top to bottom spectra respectively).

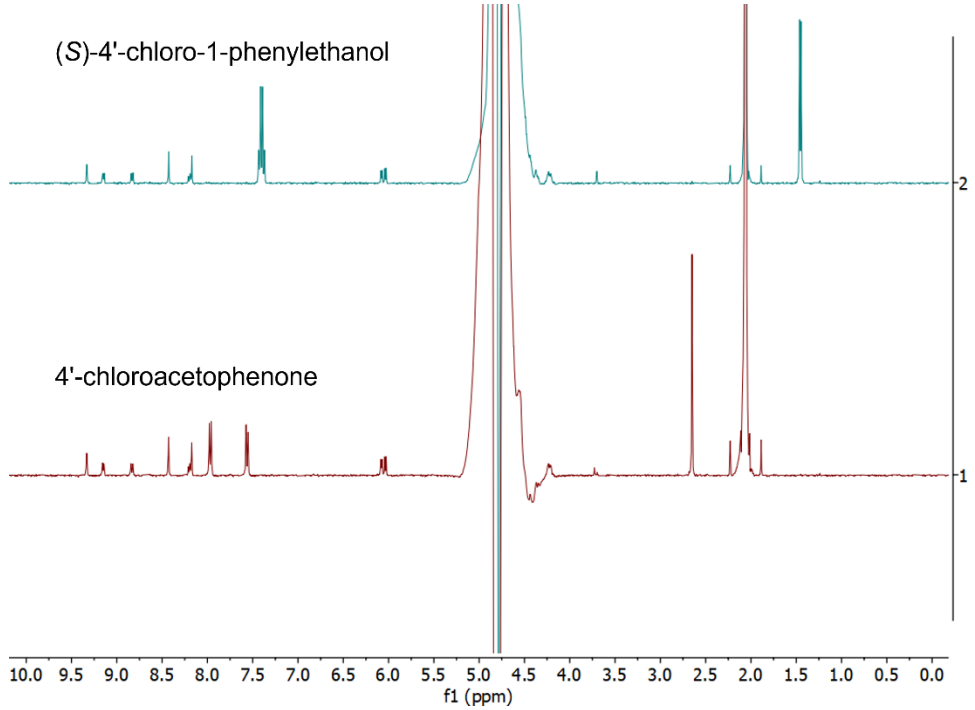


Figure S 28. ^{1}H NMR spectra (20% D_2O in aqueous 5 mM potassium phosphate pH 8) of standards of product and starting material in aqueous solutions (with 1 vol% acetonitrile) also containing 1 mM NAD^+.

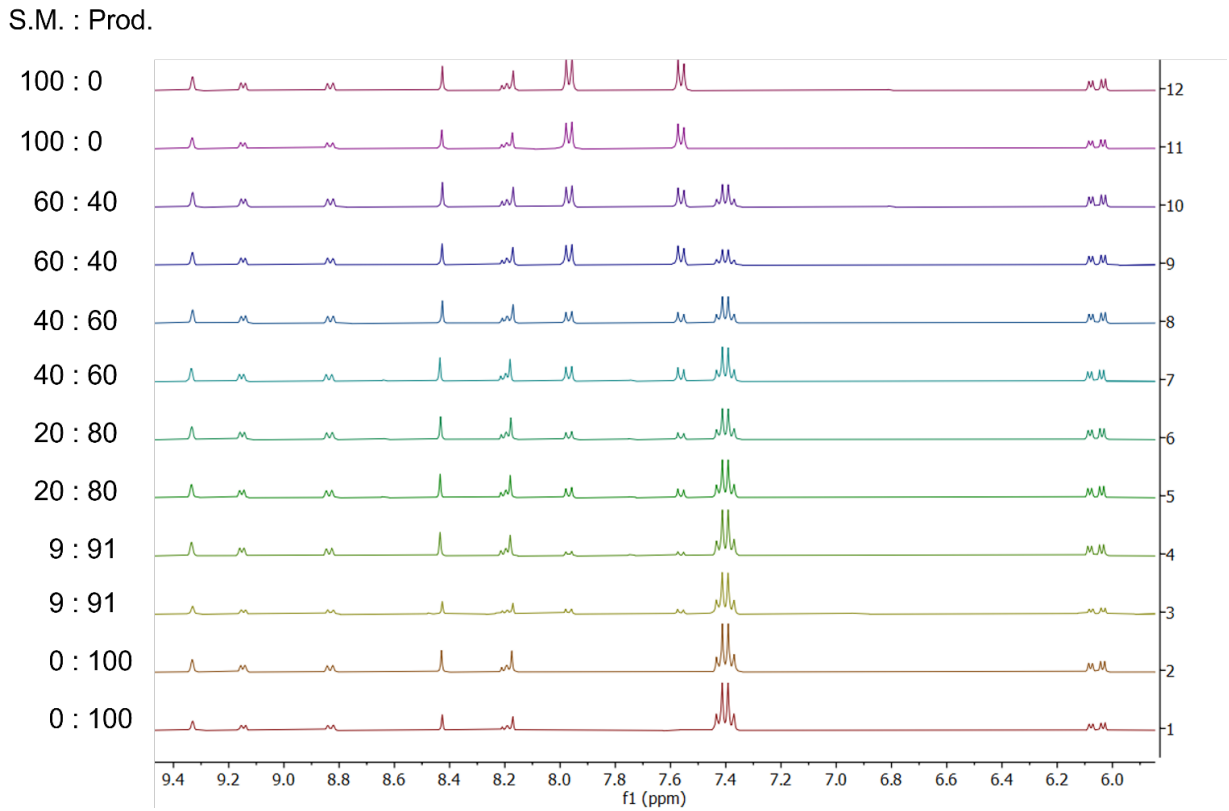


Figure S 27. ^{1}H NMR spectra (for calibration curve, showing 6.0 to 9.4 ppm region) of different ratios of starting material and product in aqueous solutions (with 1 vol% acetonitrile) also containing 1 mM NAD^+.

No dechlorinated products were observed in the ^{1}H NMR spectra of reactions. **Figure S 29** shows an example of a reaction result which had >99% product and <1% starting material remaining and no sign of a peak around 7.50 ppm which would indicate the presence of 1-phenylethanol.

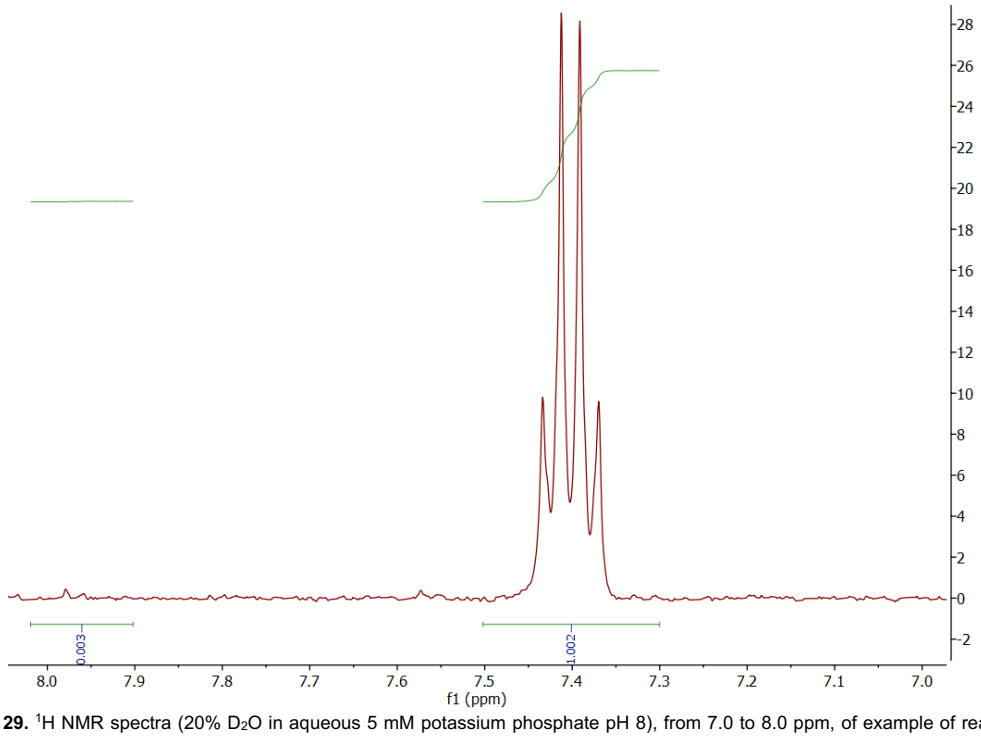


Figure S 29. ^{1}H NMR spectra (20% D_2O in aqueous 5 mM potassium phosphate pH 8), from 7.0 to 8.0 ppm, of example of reaction results (entry 3, >99% product). No dechlorinated product (1-phenylethanol) observed.

Chiral-GC analysis was also performed for selected samples to determine the enantioselectivity of the reaction (**Figure S 30**). The reaction conversion from the GC analysis correlated well with the NMR conversion results (up to 2% difference between the results).

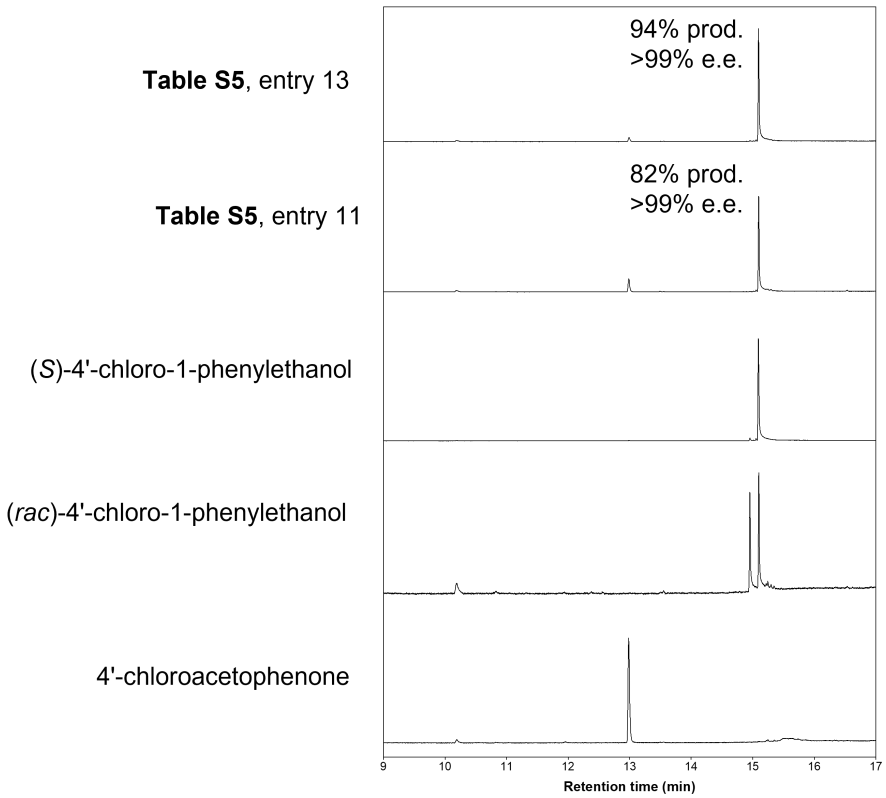


Figure S 30. Examples of chiral-GC results from reactions in **Table S 5** with the starting material and product standards. Standard for 4'-chloroacetophenone (available as 98% purity) and (*S*)-4'-chloro-1-phenylethanol (available as 95% purity) were purchased from Alfa Aesar and Sigma Aldrich respectively and diluted in ethyl acetate before injection. The racemic product standard was prepared by mixing 4'-chloroacetophenone with $NaBH_4$ in water. For each GC analysis, a 50 µL aliquot of the reaction filtrate or product standard was mixed with 800 µL EtOAc, then 600 µL of the separated EtOAc layer was removed and dried over Na_2SO_4.

S.2.17 Stability of NPs

As the NPs were prepared in batches to be used in the 4'-chloroacetophenone reduction, these were frozen after the NP synthesis (by flash freezing at -80 °C) and thawed slowly before use in reactions. The NPs were also "washed" using a size exclusion filter (10 kDa molecular weight cutoff, by centrifuging at 12,000 rpm for 10 mins) to remove any remaining metal salts. The UV-vis spectra after these stages are shown in **Figure S 31** and demonstrate the stability of the NPs to the freeze/thawing and to washing under centrifugal force; there is no noticeable change in the spectra after the freeze/thawing step, after washing there is some loss of absorbance which may have been due to some loss of NPs stuck to the filter but there is crucially no significant appearance of aggregated NPs.

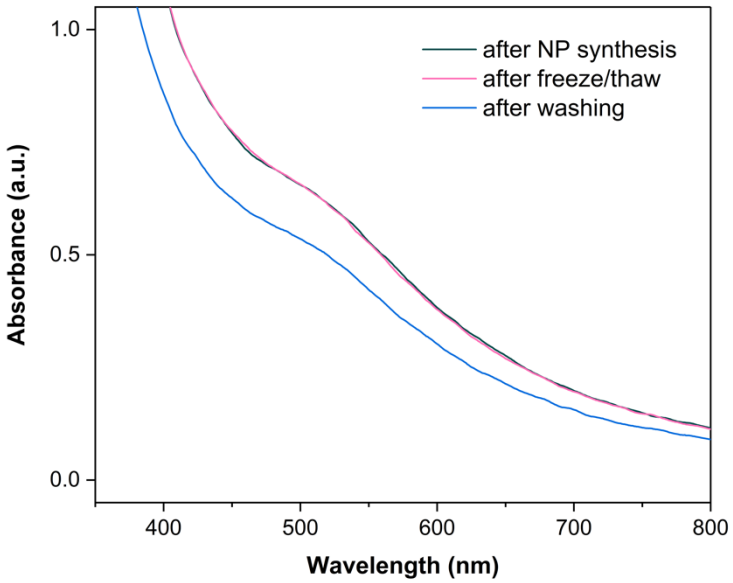


Figure S 31. UV-vis spectra of sample of *biohybrid NRase-Au@Pt NPs* recorded after the NP synthesis step, then after freezing at -80 °C and thawing and then after "washing" these NPs using a size exclusion filter.

S.3 References

[1] H. A. Reeve, L. Lauterbach, O. Lenz, K. A. Vincent, *ChemCatChem* **2015**, *7*, 3480-3487.
[2] W. Haiss, N. T. K. Thanh, J. Aveyard, D. G. Fernig, *Anal. Chem.* **2007**, *79*, 4215-4221.
[3] H. Jaegfeldt, *J. Electroanal. Chem. Interf. Electrochem.* **1981**, *128*, 355-370.
[4] Y. Shomura, M. Taketa, H. Nakashima, H. Tai, H. Nakagawa, Y. Ikeda, M. Ishii, Y. Igarashi, H. Nishihara, K.-S. Yoon, S. Ogo, S. Hirota, Y. Higuchi, *Science* **2017**, *357*, 928-932.
[5] L. Lauterbach, J. Liu, M. Horch, P. Hummel, A. Schwarze, M. Haumann, K. A. Vincent, O. Lenz, I. Zebger, *Eur. J. Inorg. Chem.* **2011**, *2011*, 1067-1079.
[6] J. S. Rowbotham, H. A. Reeve, K. A. Vincent, *ACS Catal.* **2021**, *11*, 2596-2604.
[7] I. V. Mironov, E. V. Makotchenko, *J. Solution Chem.* **2009**, *38*, 725-737.
[8] S. Wang, K. Qian, X. Bi, W. Huang, *J. Phys. Chem. C* **2009**, *113*, 6505-6510.
[9] A. J. Bard, L. R. Faulkner, *Electrochemical Methods: Fundamentals and Applications, 2nd Edition*, Wiley, **2001**.
[10] C. Greening, F. H. Ahmed, A. E. Mohamed, B. M. Lee, G. Pandey, A. C. Warden, C. Scott, J. G. Oakeshott, M. C. Taylor, C. J. Jackson, *Microbiol Mol Biol Rev* **2016**, *80*, 451-493.
[11] J. Drenth, G. Yang, C. E. Paul, M. W. Fraaije, *ACS Catal.* **2021**, *11*, 11561-11569.
[12] X. Liu, M. Atwater, J. Wang, Q. Huo, *Colloids Surf. B: Biointerfaces* **2007**, *58*, 3-7.
[13] V. Amendola, R. Pilot, M. Frasconi, O. M. Maragò, M. A. Iatì, *J. Phys.: Condens. Matter* **2017**, *29*, 203002.

[14] P.-A. Buffat, M. Flüeli, R. Spycher, P. Stadelmann, J.-P. Borel, *Faraday Discuss.* **1991**, *92*, 173-187.
[15] C. E. Paul, I. W. C. E. Arends, F. Hollmann, *ACS Catal.* **2014**, *4*, 788-797.
[16] A. Guarneri, A. H. Westphal, J. Leertouwer, J. Lunsonga, M. C. R. Franssen, D. J. Opperman, F. Hollmann, W. J. H. van Berkel, C. E. Paul, *ChemCatChem* **2020**, *12*, 1368-1375.
[17] S. Joseph Srinivasan, S. E. Cleary, M. A. Ramirez, H. A. Reeve, C. E. Paul, K. A. Vincent, *Angew. Chem. Int. Ed.* **2021**, *60*, 13824-13828.
[18] X. Zhao, S. E. Cleary, C. Zor, N. Grobert, H. A. Reeve, K. A. Vincent, *Chem. Sci.* **2021**, *12*, 8105-8114.

S.4 Author Contributions

Lucy B. F. Browne carried out the experimental work and formal analysis and wrote the majority of the original draft of this manuscript. Tim Sudmeier and Kylie A. Vincent advised on initial project ideas and experimental work. Maya A. Landis performed the TEM imaging. Christopher S. Allen performed the HR-STEM and EDX spectroscopy. All authors reviewed the manuscript. K. A. Vincent acquired funding to support this work.

Chapter 4. H_2-Driven Riboflavin Recycling

4.1. Introduction

This chapter investigates another H_2-driven cofactor recycling system for use in biocatalysis. Instead of NAD^+ reduction that was tested in *Chapter 3*, flavin reduction is tested here with use of a hydrogenase enzyme. Specifically, expanding on previous work which showed a robust Hyd1 enzyme could be used for FMN or FAD reduction (as discussed in *Chapter 1*, **1.5.**),[1] the cheaper cofactor, riboflavin was tested using this system. As well as demonstrating H_2-driven riboflavin reduction, riboflavin was accepted by commercial ene-reductase enzymes therefore enabling selective alkene reduction reactions to be carried using this atom-efficient cofactor recycling system.

[1] S. Joseph Srinivasan, S. E. Cleary, M. A. Ramirez, H. A. Reeve, C. E. Paul, K. A. Vincent, *Angew. Chem. Int. Ed.* **2021**, *60*, 13824-13828.

4.2. Paper 2: Riboflavin with H_2-Driven or Electrochemical Recycling is a Cheap Cofactor System for Supporting Biocatalytic Alkene Reduction

The manuscript and corresponding supporting information are presented on the following pages as a final draft ready for submission to a journal. I carried out the experimental work relating to the H_2-driven riboflavin recycling while the rest of the experimental work was carried out by other members of the Vincent group: Charlotte C. Hancox carried out the electrochemical recycling studies, Sofia M. Helin carried out the studies in flow and Peter M. T. Todd carried out the K_M studies. I was the main contributor for preparing the original draft ready for submission.

Riboflavin with H_2-Driven or Electrochemical Recycling is a Cheap Cofactor System for Supporting Biocatalytic Alkene Reduction

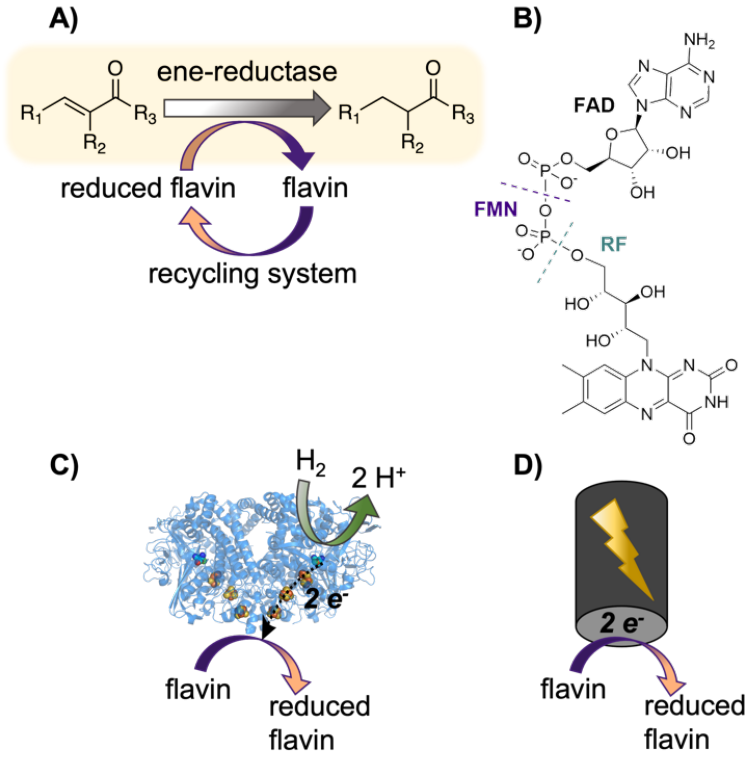
Lucy B. F. Browne, Charlotte C. Hancox, Sofia M. Helin, Peter M. T. Todd, Kylie A. Vincent*

Abstract: We show that the cheap organic cofactor riboflavin provides a cheap and atom-efficient source of reducing equivalents to sustain biocatalytic alkene reductions by ene-reductase enzymes, when coupled with a H_2-driven or electrochemical recycling system. We employ the robust NiFe hydrogenase, *Escherichia coli* Hyd1, for H_2-driven riboflavin reduction, and also show scope for unmediated electrochemical recycling of reduced riboflavin at a simple carbon electrode. We show that H_2-driven reduction of riboflavin can be extended to continuous flow with a packed bed reactor comprising Hyd1 immobilised on a carbon support. These findings demonstrate scope for replacing the expensive nicotinamide cofactors, NADH or NADPH, with riboflavin for applications of ene-reductases in biotechnology in either batch or continuous flow, and in electrosynthesis.

Introduction

It is well-established that flavin mononucleotide (FMN) in its reduced hydroquinone form ($FMNH_2$) is able to replace the expensive nicotinamide cofactor, NADH, as a source of reducing equivalents for 'old yellow enzyme' (OYE)-type ene-reductase enzymes which catalyse the reduction of a variety of activated alkene compounds (Scheme 1A).[1-4] Reduced flavin has been recycled during applications in biotechnology by stoichiometric reduction using artificial cofactor analogues such as BNAH (1-benzyl-1,4-dihydronicotinamide), by photoreduction or by direct electrochemical reduction.[2, 5-9] Observations that FMN can also be reduced by nickel-iron (NiFe) hydrogenase enzymes (Scheme 1C) have opened up opportunities for H_2-driven biocatalysis.[1, 4, 10] Electrons released during H_2 oxidation at the

active site of robust NiFe hydrogenase 1 (Hyd1) from *Escherichia coli (E. coli)* are channelled to the surface of the protein via an iron-sulfur cluster relay, where they become available for the reduction of non-native substrates such as flavins.[1] Coupling hydrogenase with ene-reductase or nitro reductase in the presence of H_2 and FMN provides a platform for more sustainable biocatalytic alkene reductions or nitro reductions, respectively, compared to the standard way of operating these enzymes with NAD(P)H recycled by the carbon-intensive glucose dehydrogenase/glucose cofactor recycling system.[11]



Scheme 1. A) Biocatalytic selective C=C reduction using an ene-reductase and flavin recycling system. B) Flavin chemical structures (RF: riboflavin, smallest flavin with the ribitol chain ending in OH, FMN: flavin mononucleotide, same structure as RF with a phosphate group at the end of the ribitol and FAD: flavin adenine dinucleotide, an adenine is joined via a ribose and phosphate to the FMN structure). C) H_2-driven reduction of flavins can be carried out using hydrogenase (Hyd1) enzyme. D) Flavins can be electrochemically reduced.

It has also been shown that the Hyd1 from *E. coli* gives good activity for the reduction of flavin adenine dinucleotide (FAD).[1] Herein we show that the scope of Hyd1 for flavin reductions can be further extended to riboflavin (RF) which is significantly cheaper than FMN and FAD and which is already produced at >9000 tonne per annum scale, by fermentation, as the nutritional supplement vitamin B2.[12] RF has a similar reduction potential to FMN, around -0.2 V vs SHE, as well as similar structure, differing only in the exclusion of a phosphate group (Scheme 1B,

S.2.1 for reported reduction potentials and cost comparisons).[13-14] RF has been demonstrated as a source of reducing equivalents for ene-reductases using a light-driven recycling system, where light excites oxidised RF into an electronic excited state which can accept electrons from an organic sacrificial reductant ethylenediaminetetraacetic acid.[2] In this study, we establish scope for application of Hyd1 to enable atom-efficient H_2-driven recycling system of RF (Scheme 1C) for supplying ene-reductase enzymes, and we also explore feasibility for an unmediated electrochemical recycling system at a carbon electrode (Scheme 1D).

The growing application of biocatalysis in selective chemical transformations has led to interest in translation of batch processes into continuous flow in packed bed reactors. There are a number of examples of flow processes which unite NAD(P)H dependent catalysis with a cofactor recycling system such as formate dehydrogenase/formate.[15-16] Hyd1 is readily immobilised on a carbon support, and has been exploited in flow as part of an NADH recycling cascade for NADH-dependent biocatalysis.[17] In this study, we also explored whether immobilised Hyd1 on carbon (Hyd1/C) packed into a flow cartridge can be used for H_2-driven RF reduction which would underpin extension of the use of this cost-efficient cofactor to flow processes. Together, these findings set the scene for riboflavin as a cheap cofactor for biotechnology in batch as well as in continuous flow.

Results and Discussion

Demonstration of RF Recycling by Hyd1 and Applicability as Reductant for Ene-Reductases

First, we performed activity assays to investigate whether Hyd1 can reduce RF and to compare the rate to FMN reduction by Hyd1. Hyd1 was added to a cuvette containing a H_2-saturated solution of flavin and the cuvette headspace (sealed using a Suba-seal®) was kept under a flow of H_2 gas during the assays. For both FMN and RF, spectral changes in the UV-visible region indicate reduction of the flavin, with clear isosbestic points indicative of clean

reduction to the hydroquinone form of the respective flavin (Figure 1A-B).[14] The initial activities (moles of flavin per minute per mole enzyme) for reduction of FMN and RF by Hyd1/H_2 were very similar within the small experimental error range calculated from a duplicate of the experiment with RF.

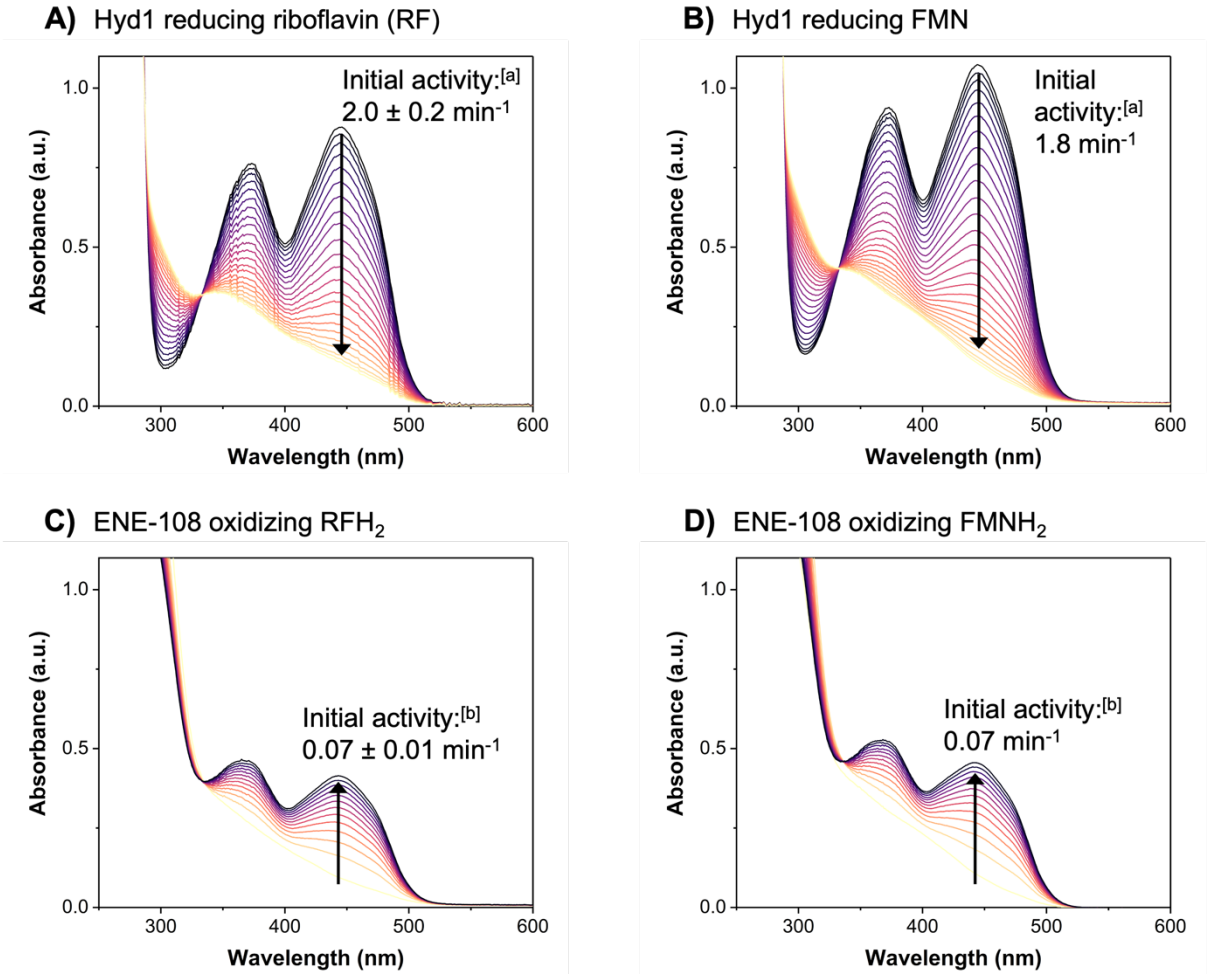


Figure 1. Testing RF as a cheaper alternative to FMN as a biological cofactor, where Hyd1, under H_2, can reduce the flavin cofactor, and subsequently the reduced cofactor can be used by an ene-reductase for the biocatalytic selective reduction of an alkene to alkane. UV-vis spectra (showing scans recorded every 5 mins) of flavin solutions containing: Hyd1/H_2 with, A) RF, B) FMN, or ene-reductase (ENE-108) with alkene substrate (4-phenyl-3-buten-2-one) with, C) RFH_2, D) $FMNH_2$. [a] Hyd1 initial activity: mol flavin per minute per mol Hyd1. [b] ENE-108 initial activity: mol flavin per minute per mol ENE-108. See methods section for assay procedures.

Encouraged by this result, we then used Hyd1/H_2 to prepare samples of reduced RF and FMN, followed by removing the Hyd-1, and mixing the reduced flavin with the commercial ene-reductase enzyme ENE-108 from Johnson Matthey, and an alkene substrate, 4-phenyl-3-buten-2-one, **1** (Figure 1C-D). Pleasingly, initial activity values were identical for ENE-108 fed

with reduced RF or with reduced FMN (i.e. the value for FMN matched with the average value from duplicate assays run for RF) showing that ENE-108 can take up electrons effectively from reduced RF.

It is also useful to compare the reaction rates for the reduction and oxidation steps: here ENE-108 was found to give a lower rate for oxidation of reduced flavin coupled to alkene reduction, compared to Hyd1-catalysed flavin reduction, suggesting that when combining the two systems, a significant excess of ENE-108 to Hyd1 must be used so that the reaction is not severely rate limited by the alkene reduction step. We also carried out activity assays under the same conditions to measure the rate of NADH oxidation by ENE-108 or ENE-103. The results gave initial activities of 1.7 ± 0.3 min^{-1} for each ene-reductase, from assays carried out in triplicate (see S.2.4). This rate is 13-25 times faster than was observed with reduced RF or FMN. This is not surprising since NADH is the native cofactor for these enzymes and the conditions may not be fully optimised in the case of the RF reduction.

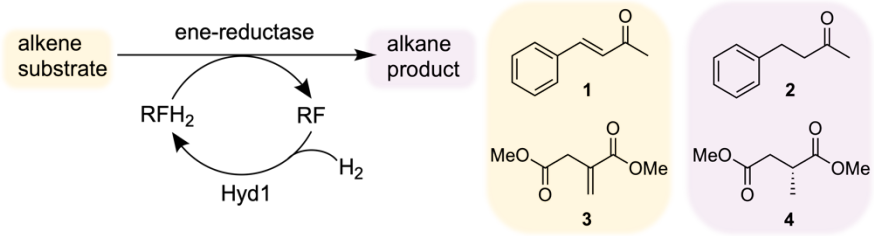
Additionally, to investigate suitable RF concentrations for the combined Hyd1/ene-reductase reactions, assays measuring the initial rate of RF reduction (with Hyd1 and H_2) were carried out for a series of RF concentrations, from 0 to 0.3 mM. The solubility of RF in an aqueous solution is significantly lower than FMN, with the limit around 0.3 mM for RF. These assays showed the initial rate increased linearly until around 0.1 mM RF, with a smaller increase up to 0.2 mM where activity levels off (see S.2.2 for assay results and comparison to assays run with FMN and FAD).

Ene-Reductase with Hyd1/H_2 Recycling of Reduced RF

Next the H_2-driven RF recycling using Hyd1 was coupled with ene-reductase for selective alkene reduction (Table 1). These reactions were all carried out using 1 bar H_2, with multiple reactions ran simultaneously in plastic tubes inside a pressure vessel (details for reaction set-up and conditions can be found in the methods section). The alkene reduction was initially investigated using substrate **1**, for the selective reduction of the C=C bond over the C=O bond

to give 4-phenyl-2-butanone, **2**, as determined by GC analysis, comparing to reference standards. A 0.1 mM concentration of RF was chosen for the initial reactions since this was indicated to provide suitable activities by the assays discussed earlier. Two commercial ene-reductases were compared for their activity with substate **1**; ENE-108 gave approximately 3 times higher conversion after 24 h than ENE-103 and 1.5 times higher initial TOF, measured after 2 hours (Table 1, entries 1 and 2). A similarly faster rate with ENE-108 was measured in UV-vis activity assays, monitoring the rate of re-oxidation of reduced RF, in the presence of **1** (see S.2.3). When the reaction using ENE-108 was intensified by increasing the substrate concentration from 1 to 10 mM while also increasing the enzyme concentrations, it was found to be necessary to increase the RF concentration from 0.1 to 0.2 mM to maintain complete conversion to **2** in 24 hours (Table 1, entries 3 and 4).

Table 1. H_2-driven RF recycling for the biocatalytic reduction of **1** or **3**.[a]



Entry	[Hyd1] (mg mL^{-1})	ENE-	[ENE] (mg mL^{-1})	Alkene	[Alkene] (mM)	[RF] (mM)	Conv. (%)[b]	*e.e.* (%)[c]	Hyd1 TOF [min^{-1}][d]	Hyd1 TTN[e]	RF TN[e]
1[f]	0.05	103	0.5	**1**	1	0.1	29 ± 14	n/a	1.0 ± 0.2	620 ± 308	2.9 ± 1.4
2[f]	0.05	108	0.5	**1**	1	0.1	99	n/a	1.5	2114	9.9
3	0.5	108	5	**1**	10	0.1	36	n/a	1.6	769	35.9
4	0.5	108	5	**1**	10	0.2	>99 ± <1	n/a	2.6 ± 0.1	2138 ± 0.5	49.9 ± <0.1
5	0.5	108	10	**1**	20	0.2	60 (66)[g]	n/a	4.7	2563	59.8
6	0.05	108	0.5	**3**	1	0.1	32 (55)[g]	>99	0.6	689	3.2
7	0.5	108	10	**3**	20	0.2	66 ± 13 (96 ± 5)[h]	>99	2.2 ± 0.5	2817 ± 546 (4104 ± 224)[h]	65.7 ± 12.7 (95.8 ± 5.2)[h]

[a] Reaction conditions: RF (0.1 or 0.2 mM), Hyd-1 (0.05 or 0.5 mg mL^{-1}), ene-reductase (0.5 to 10 mg mL^{-1}), 4-phenyl-3-buten-2-one, **1**, or dimethyl itaconate, **3**, in DMSO (1 vol%), pH 7, 50 mM potassium phosphate, H_2 (1 bar), room temperature (20-25 °C). See methods section for reaction procedures. [b] GC conversion to **2** or **4** at 24 h. [c] Enantioselectivity for (*R*)-enantiomer of **4** calculated from chiral-GC analysis at final reaction time point. [d] Hyd1 turnover frequency (mol **2** or **4** per mol Hyd1 per minute) calculated after 2 h. [e] Hyd1 total turnover number (mol **2** or **4** per mol Hyd1) and RF turnover number (mol **2** or **4** per mol RF) calculated after 24 h. [f]

Acetonitrile (1 vol%) co-solvent used instead of DMSO. [g] GC conversion to **2** or **4** at 44 h. [h] These results in brackets were an average of three experiments: two measured at 44 h and one at 48 h.

Entry 5 of Table 1 shows the results of an experiment using ENE-108, in which the concentration of substrate **1** was further increased to 20 mM, and the ENE-108 concentration was doubled, while keeping the concentration of Hyd1 the same as in entry 4 where the substrate concentration was 10 mM. An increase in the initial TOF measured at 2 h suggests that the reaction rate was limited by the ene-reductase in entry 4. Despite the faster initial TOF, the conversion appeared to slow over time, reaching 60% after 24 h and showing only a small increase to 66% after 44 h (Table 1, entry 5). To investigate a hypothesis that product inhibition might be affecting the activity of the enzymes over time, assays were carried out to study the effect of **1** and **2** on Hyd1. First, the reduction rate of RF was measured, using Hyd1 under H_2, after adding specific amounts of **1** or **2** (see S.2.5). These assays were then repeated on the same samples after 24 h incubation periods. There was no significant difference between the rates obtained in any of these assays (and compared to the control which had no DMSO, **1** or **2**), showing that Hyd1 is not affected by the alkene substrate or build-up of **2** even in reactions at high concentration. Therefore, product inhibition is more likely occurring at the ene-reductase than at Hyd1.

Another substrate was then tested using the H_2-driven RF recycling system with ENE-108: dimethyl itaconate, **3**, which upon reduction of the C=C bond gives rise to a chiral product, dimethyl methylsuccinate, **4**. Chiral-GC analysis showed ENE-108 was enantioselective (>99% *e.e.*) for the (*R*)-enantiomer of **4**. An initial test at 1 mM of **3**, under the same conditions as used for **1**, found ENE-108 was less active for this substrate, with the reaction having a lower initial TOF value (measured after 2 h) and lower conversion after 24 h (Table 1, entry 6 compared to entry 2). However interestingly, under conditions in which 20 mM of **3** was introduced, it was possible to achieve 96 ± 5 % conversion after 44-48 h, thereby giving a Hyd1 TTN value of 4104 ± 224 and RF TN of 95.8 ± 5.2 (Table 1, entry 7). This again suggests there is product inhibition by **2** in the reduction of **1** but no product inhibition (or to a much

lesser extent) for reduction of **3**. For these two substrates, reasonable total turnover numbers and RF turnover numbers were reached, demonstrating the feasibility of using RF as a cofactor with ene-reductases.

Translation of Hyd1/H_2 Recycling of RF into a Packed Bed Flow Column

Having established successful RF reduction in batch, flow biocatalysis was next investigated in a packed bed reactor, with Hyd1 (pre-activated with H_2 overnight) immobilised on activated charcoal. The catalyst was packed into a column with inert glass beads as extra packing material. The reaction mixture contained RF (0.1 mM, in pH 7, 100 mM potassium phosphate buffer) and was first purged with N_2 to remove trace O_2 which would cause re-oxidation of RF in the reactor. A H_2 gas feed at < 1 bar pressure was mixed into the reaction solution feed prior to the column (Figure 2A). The effluent was pumped through an in-line UV-visible cuvette, with spectra collected at 30-minute intervals (each spectrum corresponding to 3.5 reactor volumes) to measure the concentration of oxidised RF remaining (Figure 2B and C).

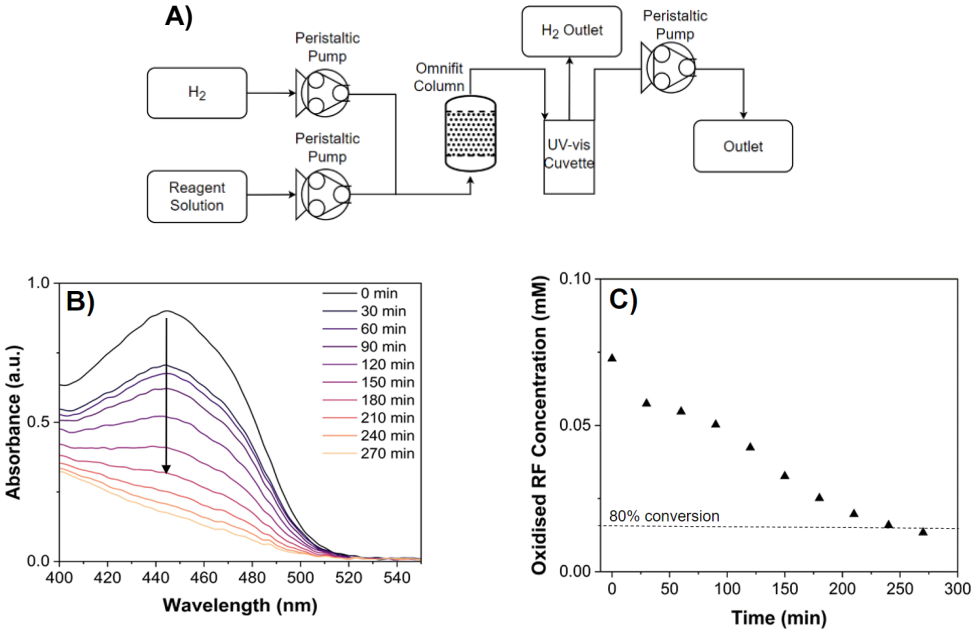


Figure 2. Single pass biocatalytic RF reduction in continuous flow at room temperature, using 0.2 mL min^{-1} liquid and 3 mL min^{-1} H_2 gas flow. RF (0.1 mM) was reduced by pre-immobilised Hyd1 on activated charcoal (0.2 mg Hyd1 on 2.2 mg activated charcoal) in pH 7, 100 mM potassium phosphate buffer, over 270 mins. A) Diagram of flow set-up including commercial Diba Omnifit column and inline UV-vis. B) Inline UV-vis data at 30-minute intervals

showing reduction of oxidised RF (absorbance decrease at 444 nm) over time. C) Concentration time graph of plot B, showing change in oxidised riboflavin concentration over time.

The single pass conversion increased up to 82% after running the reactor for almost 5 hours, suggesting that this system is suitable for future flow applications of RF recycling, provided that an anaerobic environment is used. The initial lag phase shown in Figure 2C could be due to trace residual O_2 in the packed bed or equilibration of the reactor.

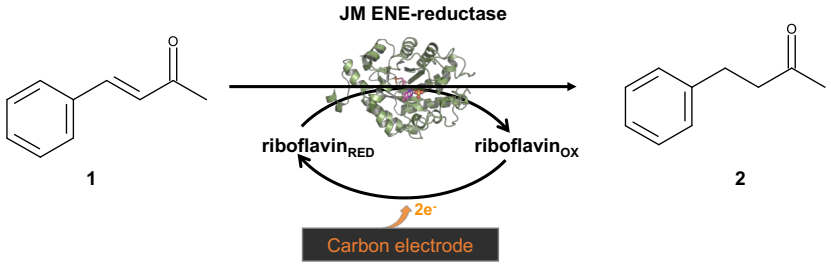
Demonstration of Ene-Reductase with Electrochemical Recycling of Reduced RF

Electrochemical reduction of RF at a pyrolytic graphite 'edge' electrode shows a reversible response indicative of both surface-adsorbed and solution species under diffusion control, consistent with a degree of pi-stacking of RF on the carbon surface (see Figure S 7). To determine whether a bulk solution of RF could be reduced at mild potential at a high surface area carbon felt electrode, a fixed potential of -0.356 V vs SHE was applied to a carbon felt electrode in contact with a 10 mL, stirred solution of 0.1 mM RF (see section S.2.8 for details). Aliquots (200 µL) were removed at 5-minute intervals for UV-visible spectrophotometric analysis and subsequently returned to the electrochemical cell. Spectra showed that RF was fully reduced within 20 minutes, consistent with the measure of charge passed from integration of the current-time trace (see Figure S 8).

Encouraged by this, electrosynthesis experiments were then performed to investigate whether electrochemically-reduced RF retained its biological activity for supply of reducing equivalents to ene-reductase (see Methods). In an initial test (Table 2, entry 1), the electrochemical cell solution contained 1 mM of substrate **1**, RF (0.1 mM), ENE-108 (0.5 mg mL^{-1}) and 10 vol% DMSO as a cosolvent in aqueous buffer. The electrode was poised at 0.40 V vs SHE. The concentration of product, **2**, was determined by GC analysis after a 24-hour reaction period, comparing to reference standards. Integration of the current over time was used to determine the charge passed, and hence a Faradaic efficiency (moles of product **2** per 2 moles of electrons consumed). The reaction conditions were intensified by increasing concentration of **1** to 5 mM and 10 mM (entries 2 and 3 in Table 2) with the RF concentration kept at 0.1 mM.

After 24 hours, the conversion was similar in entries 1-3, despite the increase in substrate concentration, but Faradaic efficiency increased with substrate concentration.

Table 2. Electrochemical-driven RF recycling for the biocatalytic reduction of **1**.[a]



Entry	[ENE-108] (mg mL^{-1})	[**1**] (mM)	[RF] (mM)	Reaction time (h)	GC Conv. (%)[b]	Faradaic efficiency (%)[c]
1	0.5	1	0.1	24	60	79
2[d]	0.5	5	0.1	24	68	96
3	0.5	10	0.1	24	58	~100
4[e]	0.5	10	0.1	120	>99	~100
5[f]	0.5	20	0.1	3	63	86

[a] Unless otherwise stated the reaction conditions were as follows: RF (0.1 mM), ene-reductase, ENE-108, (0.5 mg mL^{-1}), 4-phenyl-3-buten-2-one, **1**, in DMSO (10 vol%), pH 7, 50 mM potassium phosphate, room temperature (20-25 °C), fixed potential -0.40 V vs SHE, stirred continuously (400 rpm). See methods section and section S.2.8 for procedure. [b] GC conversion to **2**. [c] Faradaic efficiency: GC conversion per 2 e$^-$ equivalents passed. [d] A lower electrode potential of -0.42 V vs SHE was used. [e] Dosing experiment adding substrate **1** at hourly intervals: starting at 2 mM with 2% DMSO up to 10 mM with 10% DMSO. [f] Performed in electrochemical flow cell with a carbon felt working electrode (4 mm x 5 mm), ENE-108 (1.0 mg mL^{-1}), **1** (20 mM), DMSO (30 vol%).

A dosing experiment was then performed (Table 2, entry 4) where initially a 2 mM concentration of **1** was added with 2 vol% DMSO and then over the next 48 hours the concentration of **1** was increased up to 10 mM (in 2 mM increments) which gave a final concentration of 10 vol% DMSO. This reaction was left to run for 120 hours and achieved >99% conversion of **1** to **2**, with 100% Faradaic efficiency.

Flow Electrochemistry for Recycling of Reduced RF to Drive Alkene Reduction

One of the possible limiting factors affecting conversion in the electrochemical cell was stirring inefficiencies. To overcome this issue the reaction was performed in continuous flow using a home-built electrochemical flow cell machined from polyether ether ketone (PEEK) (Figure 3A shows a diagram of the set-up, full details in S.2.9). A 12.7 mL reaction solution comprising **1** (20 mM), RF (0.1 mM) and ENE-108 (1.0 mg mL^{-1}) was recirculated continuously through the electrochemical flow cell (internal cell volume, 180 µL) whilst a potential of -0.40 V vs SHE was applied to the 5x10 mm^2 carbon felt working electrode. Figure 3B shows the current-time trace (left-hand axis). Integrating the current/time curve gives the charge passed which was used to calculate the 2 e^- equivalents passed at each time point (right-hand axis). Determination of conversion to **2** by GC after approximately 3 hours gave a Faradaic efficiency of 86% (Table 2, entry 5).

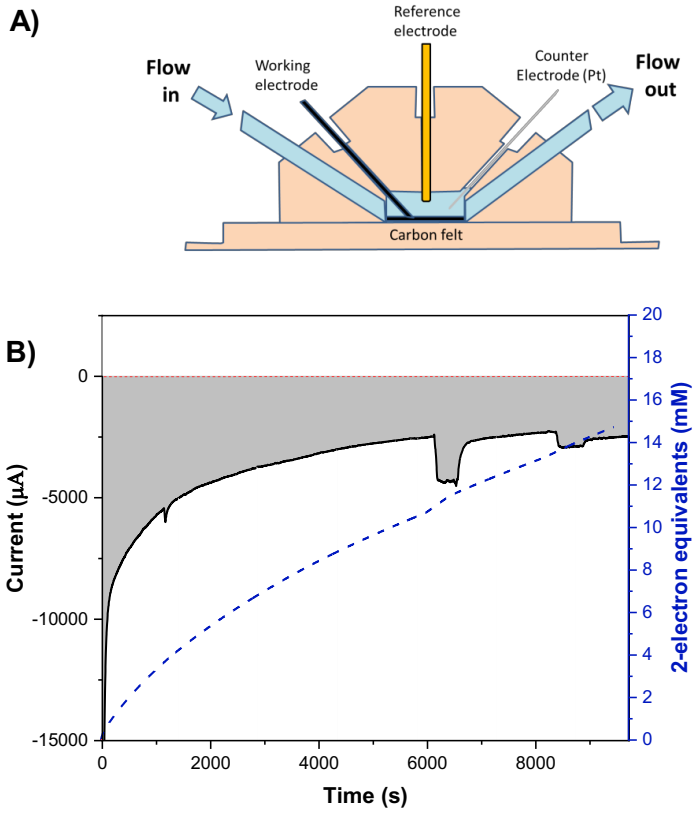


Figure 3. Electrochemical RF recycling coupled with ene-reductase in a flow cell. A) Diagram of home-built electrochemical flow cell. B) Current-time trace (left hand axis) during reduction of 12.7 mL of substrate **1** (20 mM) performed in continuous flow using RF (0.1 mM), and ENE-108 (1.0 mg mL^{-1}) with the working electrode poised at

-0.40 V vs SHE. Area of shaded region shows the area integrated to calculate the charge passed which was used to calculate the '2 e^- equivalents' (mM, blue, right-hand axis).

Conclusion

We have demonstrated that the cheap flavin cofactor, riboflavin, vitamin B2, can be reduced readily by Hyd1 under mild H_2 conditions. In its reduced form, riboflavin serves as an effective source of reducing equivalents for commercial OYE-type ene-reductases, ENE-103 and ENE-108, with a total turnover number for Hyd1 of approximately 4000 and RF cofactor turnover number of about 100 measured in these demonstration reactions. We also show that H_2-driven reduction of RF can be translated into a flow hydrogenation reactor by immobilising Hyd1 on a carbon support, with single-pass conversion of 82% to reduced RF. Electrochemical reduction of RF is also shown as a viable approach for recycling the reduced flavin cofactor, without the need for an additional enzyme. This shows that electricity could serve as a clean source of electrons for driving flavin-dependent biocatalysis. Together these findings establish RF as a cost-effective cofactor for applied biotechnology.

Methods

General Reagents and Enzymes

Most commercial reagents were purchased from Merck and used as received, without any further purification. The exceptions were dimethyl itaconate and dimethyl (*R*)-(+)-methylsuccinate which were purchased from Fluorochem and ChemCruz respectively. All aqueous solutions were prepared with deionised Milli-Q water (Millipore, 18 MΩcm). *E. coli* Hyd1, was prepared following published procedures.[10] Molecular weight for over-expressed *E. coli* Hyd1 is 107 kDa per monomer (PDB: 4GD3, without cytochrome). The ene-reductases (ENE-103 and ENE-108, molecular weight: 37,780 and 37,460 Da respectively) used for the alkene reduction were received in lypophilised form from Johnson Matthey, Cambridge, and used without further purification.

General Method Considerations

To reduce any competing oxidation reactions, all reaction handling, including UV-vis assays, was carried out in a glovebox, filled with a N_2 atmosphere (O_2 < 5 ppm). When handling aqueous flavin solutions (FMN, FAD or RF), including while the alkene reduction reaction was carried out, aluminium foil was used to cover solutions to protect from photodecomposition.[18] Before Hyd1 was used in UV-vis activity assays or in alkene reduction reactions with ene-reductase, the Hyd1 was firstly "pre-activated" under H_2. A typical procedure for this involved pipetting the desired amount into a 0.5 mL plastic tube (StarLabs), piercing the lid of the plastic tube with a needle and putting inside a Büchi Tinyclave pressure vessel which was then filled with H_2 (to 2.5 bar and vented x3 and then filled to 1 bar) and left for 16-20 h.

Flavin Reduction UV-Vis Activity Assay

Assays were performed using a Cary 60 UV-visible spectrophotometer (Agilent) and a quartz cuvette (1 cm path length). A Peltier accessory was used to control the temperature of the cuvette which was set to 25 °C for all assays. The settings on the Scan software were set to record a spectrum from 800 to 200 nm every 30 seconds during an assay. A background spectrum using pH 7, 50 mM potassium phosphate was recorded before beginning the experiment. A 0.103 mM solution of flavin (FMN or RF) in pH 7, 50 mM potassium phosphate was prepared and 880 µL of this solution was added to the quartz UV-vis cuvette. A Suba-seal® was used to seal the UV-vis cuvette and two needles were added through the top of the Suba-seal®. A H_2 gas line and an outlet line were attached to the needles and the inlet needle was moved below the surface of the flavin solution to sparge the solution with H_2 for a minimum of 15 minutes. Meanwhile pH 7, 50 mM potassium phosphate buffer was used to make the volume of the Hyd1 solution up to 20 µL (thus making the flavin concentration in each assay experiment as 0.1 mM and Hyd1 concentration as 0.05 mg mL^{-1}). After the sparging of the flavin solution was complete, both needles were lifted out of the solution so they were now in

the cuvette headspace. The UV-vis was set to start scanning every 30 seconds before the Hyd1 solution was added to the cuvette, using a needle and syringe to do so, using 200 µL of flavin solution to aid transfer. The flavin reduction rate was then measured by the decrease in absorbance over time, using the data from the linear section of the graph. Molar adsorption coefficients used to calculate Hyd1 initial activity values: 11.0 mM^{-1} cm^{-1} at 444 nm for RF,[19] and 12.5 mM cm^{-1} at 445 nm for FMN.[14]

Oxidation of Reduced-Flavin UV-Vis Activity Assay

The same UV-vis settings as detailed for the flavin reduction activity assays were used. Reduced-flavin solutions were prepared as per the conditions in flavin reduction activity assays (does not need to be carried out in a UV-vis cuvette, can also prepare multiple solutions at the same time by preparing in StarLabs 0.5 mL plastic tubes which are then put under H_2). After reducing the flavin, the Hyd1 enzyme was removed using a 50 kDa size exclusion filter (centrifuging at 12,000 rpm for 10 minutes). The filtered reduced-flavin solution was then added to the quartz cuvette for the UV-vis assay. A stock solution of ene-reductase was prepared in pH 7, 50 mM potassium phosphate (45 mg mL^{-1}). The alkene substrate 4-phenyl-3-buten-2-one, **1**, (as a 100 mM stock solution in DMSO) was added to the solution (making a 1 mM assay concentration with 1 vol% DMSO) and mixed thoroughly using a pipette. The ene-reductase was added (making a 0.5 mg mL^{-1} assay concentration) and the solution was mixed using a pipette. The reduced-flavin oxidation rate was then measured by the increase in absorbance, at 444 nm or 445 nm for RF or FMN respectively, over time, using the data from the linear section of the graph.

Alkene Reduction using Ene-Reductase and Hyd1/H_2 Recycling of Reduced RF

A 0.124 mM solution of RF in pH 7, 50 mM potassium phosphate was prepared and sparged with H_2 for 15 minutes minimum. If extra buffer was needed to make the desired total Hyd1

concentrations, then that was added to the plastic tubes containing "pre-activated" Hyd1. Then 350 µL of H_2-saturated RF (making a 0.1 mM reaction concentration or initial stock concentration adapted to make 0.2 mM) was added and the plastic tubes were placed back into a Büchi Tinyclave pressure vessel, filled with H_2 (to 2.5 bar, vented x3, and then filled to 1 bar) and then placed on a Stuart® mini see-saw rocker set to 30 oscillations/min. Typically, the reactions were left for 1 to 1.5 h before the vessel was vented and ene-reductase (from a stock solution prepared in pH 7, 50 mM potassium phosphate) followed by alkene (in acetonitrile or DMSO) were added to the plastic tubes, and solutions mixed using a pipette. These were then put back into a Büchi Tinyclave pressure vessel, filled with H_2 (to 2.5 bar, vented x3, and then filled to 1 bar) and placed back on the rocker set to 30 oscillations/min. The reactions were analysed by GC (as detailed in S.1.1 in the Supporting Information).

Flow Set-up for Hyd1/H_2 Recycling of RF

Mesh 100 activated charcoal and 1 mm inert glass beads were purchased from Merck. For the immobilised catalyst, 0.2 mg Hyd1 was immobilised on 2.2 mg activated charcoal suspended in 200 µL pH 7, 100 mM potassium phosphate buffer by leaving for 1 hour at 4 °C. The catalyst was separated by centrifugation at 12,000 g for 2 minutes, then the supernatant was removed and analysed via UV-vis. This showed a very small absorbance (0.027 a.u.) at 280 nm indicative of protein absorption, suggesting that 98.5% of the enzyme had been successfully immobilised. The catalyst was activated in an anaerobic glovebox overnight under 3 mL min^{-1} H_2 flow and was then packed into an Omnifit column (Diba) with 2 g glass beads for additional column packing. The column was charged with reaction solution purged with N_2 containing 0.1 mM RF in pH 7, 100 mM potassium phosphate buffer. The reaction was run single-pass at room temperature and pressure, with 3 mL min^{-1} H_2 and 0.2 mL min^{-1} liquid flow rate used to push the RF solution through the packed bed using 3 SF-10 peristaltic pumps (Vapourtec) with chemically resistant PEEK fittings (Figure 2A). An S200 UV-vis spectrophotometer (OceanStar) was used in line to monitor column effluent.

Electrochemical Reduction of RF and Coupling to Ene-Reductase

Electrochemical work was all carried out in an anaerobic glove box under N_2 (5 ppm O_2), with glass cells wrapped in aluminium foil to exclude the possibility of photochemical side reactions involving RF. A three-electrode set-up was used in all cases. Bulk reduction of RF (see also section S.2.8) was carried out in a stirred glass cell using a PalmSens4 potentiostat and the associated PSTrace software. The working electrode was carbon felt, the reference was a Saturated Calomel Electrode (SCE), and the Pt wire counter electrode was contained in KCl solution and separated from the main cell by a frit. Potentials (E) were converted to volts (V) vs the Standard Hydrogen Electrode (SHE) using the conversion $E_{SHE} = E_{SCE} + 0.242$ V. An electrochemical flow experiment was carried out using an Autolab PGStat30 potentiostat and the associated Nova 1.1 software, again using a carbon felt working electrode and separated Pt counter electrode, within a home-built cell (Figure 3A, and see also section S.2.9). In this case the reference electrode was a leak-free Ag/AgCl electrode (PalmSens BV Netherlands), and potentials were corrected to V vs SHE by comparison of the reference electrode potential to a SCE and application of the appropriate conversion.

Acknowledgements

We are grateful to Dr Stephen Carr for his assistance in preparing and isolating E. coli hydrogenase 1 (Hyd1), and to Dr Beatriz Dominguez and Dr Sarah Montgomery at Johnson Matthey (Cambridge, U.K.) for providing the ene-reductase enzymes (ENE-103 and ENE-108). This project has been funded by the European Research Council (ERC-CoG-BiocatSusChem-819580) to K.A.V. which provided studentship support to L.B.F.B. and P.M.T.T. We are also grateful for studentship support from the BBSRC Interdisciplinary Bioscience Doctoral Training Partnership (DTP) to S.M.H., and an iCASE award with Johnson Matthey through the BBSRC DTP to C.C.H.

Keywords: biocatalysis • bioelectrochemistry • continuous flow • hydrogenase • riboflavin

References

[1] S. Joseph Srinivasan, S. E. Cleary, M. A. Ramirez, H. A. Reeve, C. E. Paul, K. A. Vincent, *Angew. Chem. Int. Ed.* **2021**, *60*, 13824-13828.

[2] M. M. Grau, J. C. van der Toorn, L. G. Otten, P. Macheroux, A. Taglieber, F. E. Zilly, I. W. C. E. Arends, F. Hollmann, *Adv. Synth. Catal.* **2009**, *351*, 3279-3286.

[3] W. Zhang, F. Hollmann, *Chem. Commun.* **2018**, *54*, 7281-7289.

[4] A. Al-Shameri, S. J. P. Willot, C. E. Paul, F. Hollmann, L. Lauterbach, *Chem. Commun.* **2020**, *56*, 9667-9670.

[5] M. Ismail, L. Schroeder, M. Frese, T. Kottke, F. Hollmann, C. E. Paul, N. Sewald, *ACS Catal.* **2019**, *9*, 1389-1395.

[6] F. Hollmann, A. Taglieber, F. Schulz, M. T. Reetz, *Angew. Chem. Int. Ed.* **2007**, *46*, 2903-2906.

[7] A. Taglieber, F. Schulz, F. Hollmann, M. Rusek, M. T. Reetz, *ChemBioChem* **2008**, *9*, 565-572.

[8] V. Massey, M. Stankovich, P. Hemmerich, *Biochemistry* **1978**, *17*, 1-8.

[9] F. Hollmann, K. Hofstetter, T. Habicher, B. Hauer, A. Schmid, *J. Am. Chem. Soc.* **2005**, *127*, 6540-6541.

[10] M. A. Ramirez, S. Joseph Srinivasan, S. E. Cleary, P. M. T. Todd, H. A. Reeve, K. A. Vincent, *Frontiers in Catalysis* **2022**, *2*.

[11] H. S. Toogood, N. S. Scrutton, *ACS Catal* **2019**, *8*, 3532-3549.

[12] S. K. Schwechheimer, E. Y. Park, J. L. Revuelta, J. Becker, C. Wittmann, *Appl. Microbiol. Biotechnol.* **2016**, *100*, 2107-2119.

[13] C. Greening, F. H. Ahmed, A. E. Mohamed, B. M. Lee, G. Pandey, A. C. Warden, C. Scott, J. G. Oakeshott, M. C. Taylor, C. J. Jackson, *Microbiol Mol Biol Rev* **2016**, *80*, 451-493.

[14] P. Macheroux, *Methods in molecular biology (Clifton, N.J.)* **1999**, *131*, 1-7.

[15] B. Poznansky, L. A. Thompson, S. A. Warren, H. A. Reeve, K. A. Vincent, *Organic Process Research & Development* **2020**, *24*, 2281-2287.

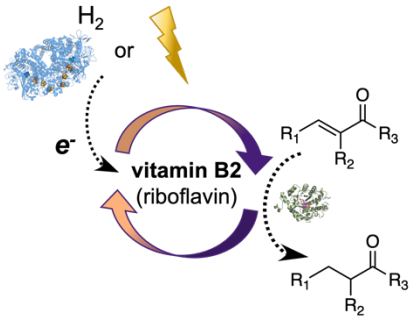
[16] Q. Chen, Y. Wang, G. Luo, *ChemSusChem* **2023**, *16*, e202201654.

[17] C. Zor, H. A. Reeve, J. Quinson, L. A. Thompson, T. H. Lonsdale, F. Dillon, N. Grobert, K. A. Vincent, *Chem. Commun.* **2017**, *53*, 9839-9841.

[18] W. Holzer, J. Shirdel, P. Zirak, A. Penzkofer, P. Hegemann, R. Deutzmann, E. Hochmuth, *Chem. Phys.* **2005**, *308*, 69-78.

[19] M. I. Gutiérrez, S. M. Fernández, W. A. Massad, N. A. García, *Redox Report* **2006**, *11*, 153-158.

Entry for the Table of Contents



Riboflavin, also known as vitamin B2, can substitute for NADH as electron donor to alkene ('ene') reductase enzymes, offering an economical cofactor system when coupled with hydrogenase for dihydrogen-driven recycling, or with a carbon electrode for electrochemical recycling.

Supporting Information

S.1 Experimental Procedures

S.1.1 GC-FID Method for Alkene Reduction Analysis

50 µL of the reaction solution was added to 200 µL EtOAc to extract the organic products (vortexed for 30 s to mix, then allowed to settle for 2 mins). 150 µL of the EtOAc layer was removed, dried using Na_2SO_4 and centrifuged at 12,000 rpm for 3 mins to precipitate the Na_2SO_4. The dried sample was then added to a GC vial. The GC method was as described in **Table S 1**.

Table S 1. GC method conditions used for the determination of reaction conversion for the reduction of 4-phenyl-3-buten-2-one (**1**) to 4-phenyl-2-butanone (**2**) and dimethyl itaconate (**3**) to dimethyl methylsuccinate (**4**).

Column	CP-Cyclosil-B (Agilent), 30 m x 0.25 mm x 0.25 µm, fitted with a guard of 10 m undeactivated fused silica of the same diameter
Carrier	H_2, 3 mL/min (constant flow rate)
Inlet temperature	250 °C
Injection conditions	Split flow 75 mL/min, split ratio 25, purge 5 mL/min. Injection volume = 1 µL
Detection	FID (H_2 = 35 mL/min, air = 350 mL/min, makeup N_2 = 40 mL/min, temp = 250 ℃)
Oven heating profile	Time (minutes) Temperature 0 – 2 Hold at 70℃ 2 – 18.25 Ramp to 200 ℃ at 8 ℃/min 18.25 – 34 Hold at 200 ℃ for 15.75 minutes
Compound retention times	Time (minutes) Compound 11.26 4-Phenyl-2-butanone, **2** 13.48 4-Phenyl-3-buten-2-one, **1** 7.08 Dimethyl (*R*)-(+)-methylsuccinate, **4** 7.15 Dimethyl (*S*)-(-)-methylsuccinate, **4** 7.89 Dimethyl itaconate, **3**

S.2 Results and Discussion

S.2.1 Flavin Comparisons

As mentioned in the main text the structure of RF only differs to the structure of FMN by the exclusion of a terminal phosphate group (instead the ribitol chain ends with a hydroxy group). FAD is a bulkier flavin with the addition of an adenine joined via a ribose group. The structures displayed in **Figure S 1** show that these structural differences occur at the other end of the molecule to the part of the molecule which undergoes reduction during a flavin-dependent biocatalytic reaction. Thus, it is logical that the standard reduction potentials for the two-electron reduction of the isoalloxazine ring is in a similar range for all three flavins, as has been found experimentally (**Table S 2**). The cost estimates, in **Table S 2**, give an idea about the order of magnitude of savings that could be obtained from switching from using FMN or FAD to RF for a biocatalytic process (where the enzyme accepts RF as its cofactor).

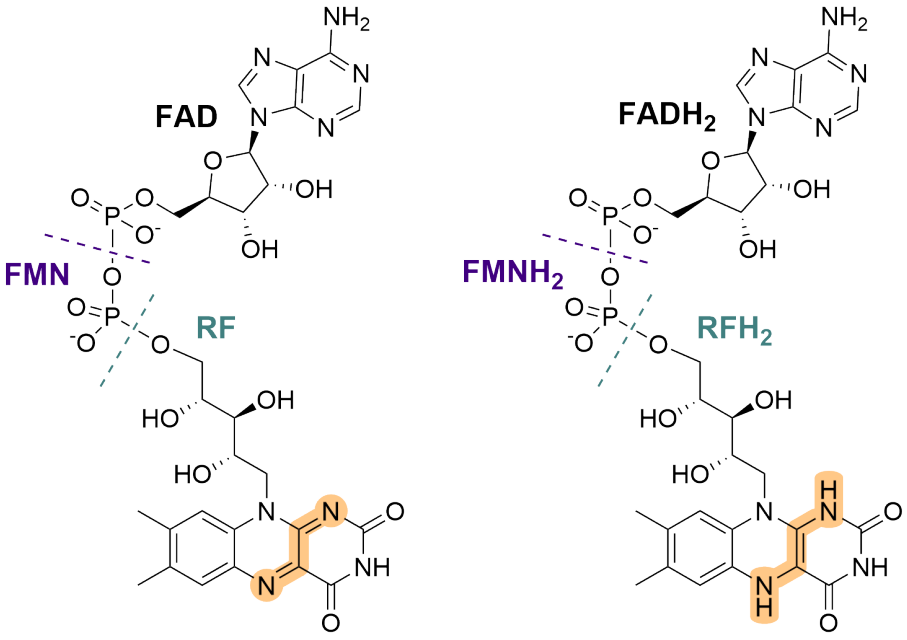


Figure S 1. Oxidised and reduced (left and right respectively) flavin structures, orange highlighted bonds show where the reduction occurs.

Table S 2. Comparison of flavins, showing their standard reduction potentials and cost estimates.

Flavin	Standard Reduction Potential (mV)	Cost Estimate[a]	
		As Available	Per Gram
RF	-210,[1] -208,[2] -190[3]	£749 per 1 kg	£0.75 (MW: 376.36)
FMN	-190,[1] -216[2]	£196 per 50 g	£3.92 (MW: 478.33)
FAD	-220,[1] -220[3]	£615 per 1 g	£615 (MW: 829.51)

[a] Cost estimate from Sigma-Aldrich with lowest price (and pack size) available (searched on 2nd Oct 2023). Costs are per weight, but molecular weights (MW) are given in brackets.

S.2.2 Kinetic Studies for the Initial Rate of Flavin Reduction by Hyd1

UV-vis assays for the initial rate of flavin reduction using Hyd1 under H_2 were carried out using different concentrations of flavin (**Figure S 2**). The apparent Michaelis Menten constant (K_M) for each flavin estimated from these data are:

K_M for FMN (1.0-1.5 mM), FAD (0.5-1.0 mM) and RF (0.08-0.10 mM)

Due to poor solubility for RF above about 0.25 mM, the 0.3 mM data point was not included in the fitting.

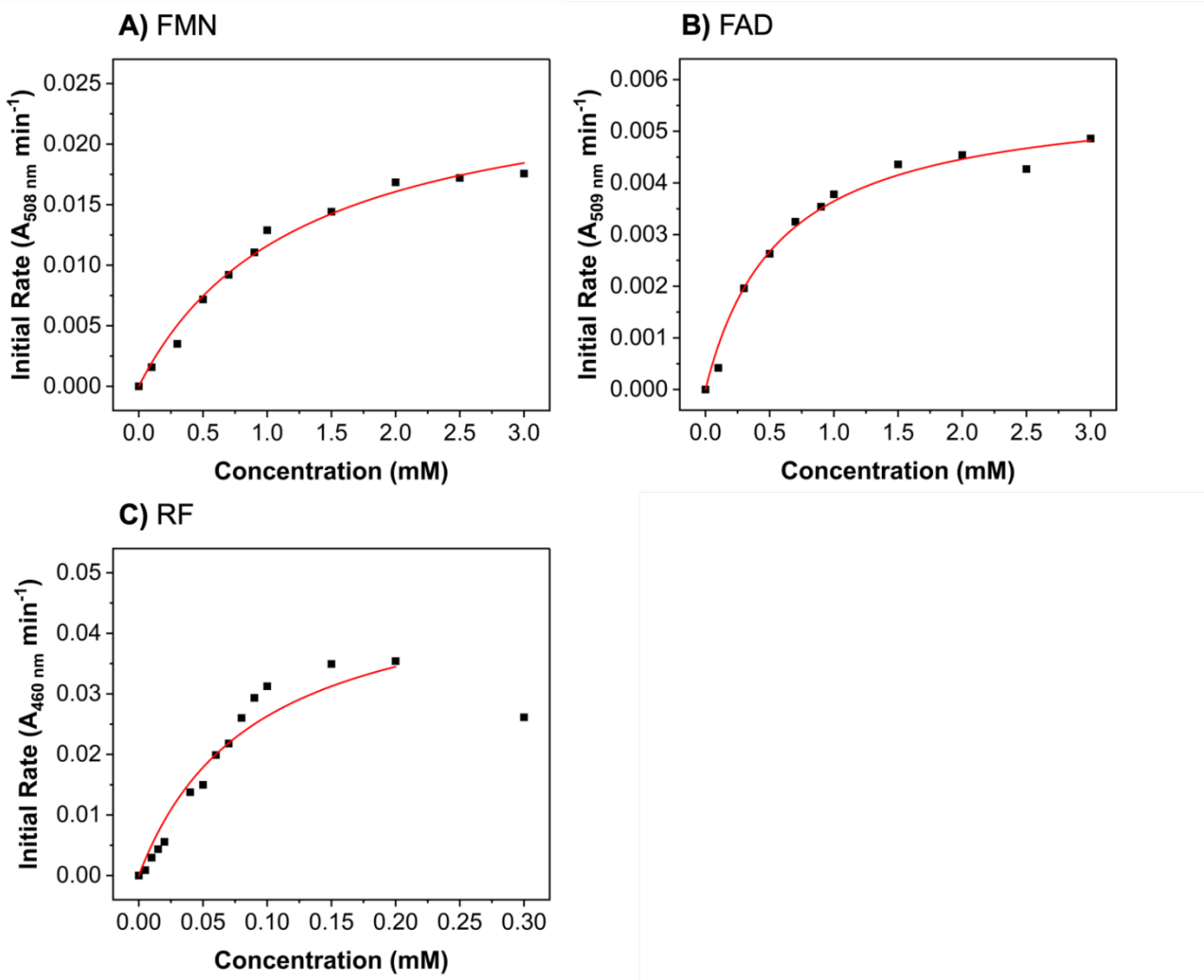


Figure S 2. Michaelis-Menten style plots of the initial rates for flavin reduction by Hyd1 at different flavin concentrations.

S.2.3 Reduced Flavin Activity Comparison of Ene-Reductases

UV-vis assays were carried out to test whether there was any rate difference observed between the oxidation of reduced RF or reduced FMN using either ENE-103 or ENE-108. Example UV-vis traces are shown in **Figure S 3**. These assays, as discussed in the main text, showed there was very little difference between the rate of oxidation of the two flavins while using ENE-108 (**Table S 3**, entries 1-3). Upon further assays it was found that for ENE-103 the rate of oxidation for reduced FMN was approximately 1.5 times faster than for reduced-RF (entries 5-7). These assays also revealed the activity comparison of ENE-108 versus ENE-103; it was found that for the oxidation of reduced RF, in the presence of 4-phenyl-3-buten-2-one, ENE-108 could provide an approximately 3 times faster rate than ENE-103 (entries 6-8 and assay examples shown in **Figure S 3**).

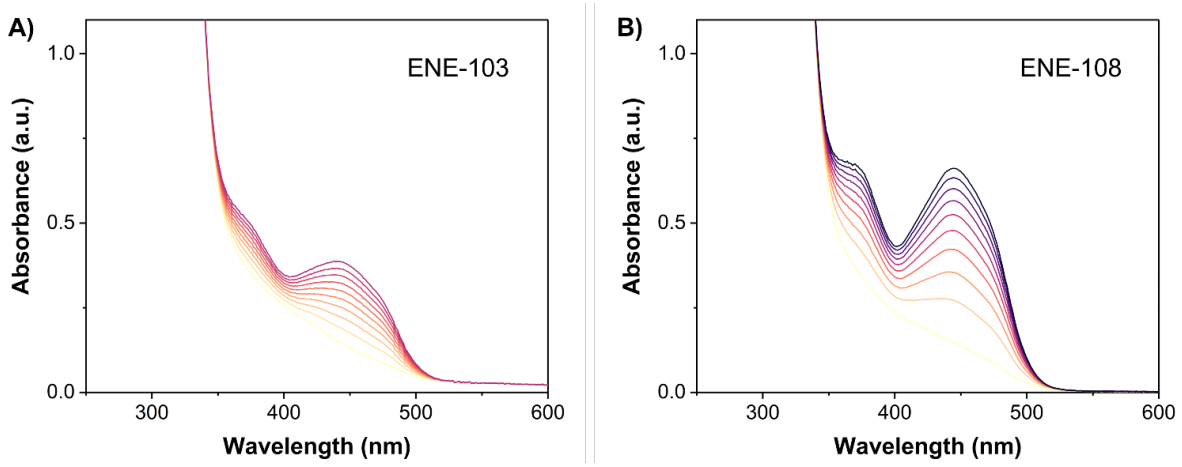


Figure S 3. UV-vis assays of the oxidation of reduced RF (RFH_2) by ene-reductase: **A)** ENE-103 and **B)** ENE-108. UV-vis spectra show scans recorded every 5 mins up to 45 mins, with assays carried out using the procedure described in the methods section of the main text and the following conditions: RFH_2 (0.1 mM), ene-reductase (0.5 mg mL^{-1}), 4-phenyl-3-buten-2-one, **1**, (1 mM) in DMSO (1 vol%), pH 7, 50 mM potassium phosphate, 25 °C.

Table S 3. Results from testing the oxidation rate of reduced flavin by an ene-reductase, using a UV-vis assay procedure.[a]

Entry	Reduced flavin	ENE-	Max. linear rate (a.u. min^{-1})[b]	Initial activity (mol reduced-flavin/min/mol ENE)[c]	Average activity (min^{-1})[d]	S.D. (±)[d]
1	RFH_2	108	0.01093	0.074	0.0659	0.009
2	$FMNH_2$	108	0.01122	0.067		
3	RFH_2	108	0.00843	0.057		
4	$FMNH_2$	103	0.00423	0.026		
Adapted procedure used:[e]						
5	$FMNH_2$	103	0.01194	0.072		
6	RFH_2	103	0.00717	0.049	0.0455	0.004
7	RFH_2	103	0.00608	0.042		
8	RFH_2	108	0.01960	0.133		
9	$FMNH_2$	108	0.02123	0.127		

[a] The procedure used was as described in the methods section of the main text with the following conditions: reduced flavin (0.1 mM), ene-reductase (0.5 mg mL^{-1}), 4-phenyl-3-buten-2-one, **1**, (1 mM) in DMSO (1 vol%), pH 7, 50 mM potassium phosphate, 25 °C. [b] The maximum linear rate for the increase in absorbance at the λ_{max} of the flavin. [c] Ene-reductase initial activity calculated using molar adsorption coefficients for RF (at 444 nm, 11.0 mM^{-1} cm^{-1}) and for FMN (at 445 nm, 12.5 mM cm^{-1}) and molar weights of 37,460 Da and 37,780 Da for ENE-108 and ENE-103 respectively. [d] Average and standard deviation for duplicate experiments (as highlighted by the green rows). [e] In entries 5-9, 4-phenyl-3-buten-2-one, **1**, was added to the reduced flavin solution and thoroughly mixed before the ene-reductase was added (in comparison, in entries 1-4, the ene-reductase was added before **1**).

S.2.4 NADH Activity Comparison of Ene-Reductases

To keep the conditions comparable to the reduced flavin assays in **S.2.3**, the tail of the 340 nm absorbance peak for NADH was observed at 380 nm to measure the rate of NADH oxidation (examples of assays shown in **Figure S 4**). A separate calibration curve (of various concentrations of NADH with 1 mM of 4-phenyl-3-buten-2-one) was created to ensure that we were able to determine the absorbance change for NADH against the backdrop of the absorbance of the alkene which was at 10-fold higher concentration compared to the cofactor.

UV-vis assays were carried out to test whether there was any rate difference observed between the oxidation of NADH to NAD^+ between ENE-103 or ENE-108. This could be compared to the reduced flavin assays to determine the difference in activity with RF compared to NADH as the enzyme cofactor. As shown below in **Table S 4**, the ENE-103 and

ENE-108 had similar activities with NADH as the cofactor, which was approximately 30 times the activity observed using RF as the cofactor.

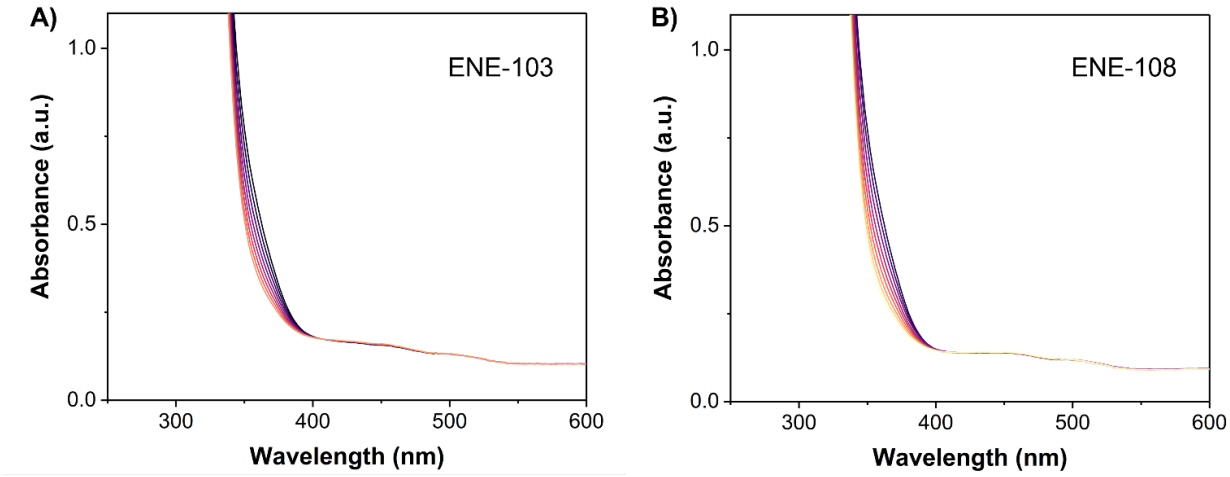


Figure S 4. UV-vis assays of the oxidation of NADH by ene-reductase: **A)** ENE-103 and **B)** ENE-108. UV-vis spectra show scans recorded every 30 s up to 10 mins. Conditions of assay were kept the same as for flavin oxidations where possible: NADH (0.1 mM), ene-reductase (0.5 mg mL^{-1}), 4-phenyl-3-buten-2-one, **1**, (1 mM) in DMSO (1 vol%), pH 7, 50 mM potassium phosphate, 25 °C.

Table S 4. Results from testing the oxidation rate of NADH by an ene-reductase, using a UV-vis assay procedure.[a]

Entry	ENE-	Initial activity (mol NADH/min/mol ENE)[b]	Average activity (min^{-1})[c]	S.D. (±)[c]
1	103	1.618		
2	103	1.466	1.718	0.26
3	103	2.071		
4	108	2.158		
5	108	1.525	1.741	0.30
6	108	1.539		

[a] The procedure used was as described in the methods section of the main text with the following conditions: NADH (0.1 mM), ene-reductase (0.5 mg mL^{-1}), 4-phenyl-3-buten-2-one, **1**, (1 mM) in DMSO (1 vol%), pH 7, 50 mM potassium phosphate, 25 °C. [b] Ene-reductase initial activity calculated using calibration curve and absorbance at 380 nm and molar weights of 37,460 Da and 37,780 Da for ENE-108 and ENE-103 respectively. [c] Average and standard deviation for triplicate experiments.

S.2.5 Riboflavin Reduction Inhibition Tests

Since it was found that in attempts to reduce 4-phenyl-3-buten-2-one, **1**, at 20 mM, the reaction rate significantly slowed over time, with 60% conversion after 24 h and an increase only to 66% after 44 h, it was investigated whether this was due to any inhibition of the RF reduction rate caused by the presence of organic molecules (**1**, **2** or DMSO). Therefore, these organics were added to solutions of Hyd1 in RF and the RF reduction rate was measured initially and after "incubating" overnight under H_2. The order in which the assays were carried out is the order of the entries in **Table S 5** (same order on both days). A duplicate of the same conditions was carried out (entries 1 and 3) which indicates the minimum experimental error as ± 0.16 min^{-1} for the initial activity. Despite all results giving a lower initial activity on day 2 than day 1, the values are not significantly lower. The results for the control without DMSO and alkene in DMSO gave very similar results to each other on both days (entries 4 and 5). Overall, the results suggest there is no inhibition caused by the organics on the RF reduction rate.

Table S 5. Results from UV-vis assays testing the effect of "incubating" Hyd1 with the alkene starting material or alkane product from the reduction of 4-phenyl-3-buten-2-one, **1**.

Entry	Conditions[a]	Rate of absorbance decrease at 444 nm on day 1 (a.u. min^{-1})	Initial activity of Hyd1 on day 1 (min^{-1})	Rate of absorbance decrease at 444 nm on day 2 (a.u. min^{-1})	Initial activity of Hyd1 on day 2 (min^{-1})	Difference between activity on day 2 and day 1 (min^{-1})
1	alkane in DMSO[b]	0.01345	2.59	0.01141	2.20	-0.39
2	DMSO	0.01395	2.69	0.01036	1.99	-0.70
3	alkane in DMSO[b]	0.01463	2.82	0.01110	2.14	-0.68
4	no DMSO (control)	0.01417	2.73	0.01390	2.68	-0.05
5	alkene in DMSO[c]	0.01415	2.72	0.0140	2.69	-0.03

[a] All entries were carried out using the following conditions and the procedure as described in the methods section of the main text: "incubating" conditions: Hyd1 (0.1 mg mL^{-1}), RF (0.1 mM), alkane/alkene in DMSO (5 mM, 1 vol%). Assay conditions: Hyd1 (0.05 mg mL^{-1}), RF (0.1 mM), RFH_2 (0.05 mM), alkane/alkene in DMSO (2.5 mM, 0.5 vol%) [b] 4-phenyl-2-butanone, **2** [c] 4-phenyl-3-buten-2-one, **1**.

S.2.6 Example GC Data

GC analysis, using the method described in **S.1.1**, was used to calculate reaction conversion, which was also used for calculating TOF, TTN and TN. Starting material and product standards as well as some example reaction GC traces are shown in **Figure S 5** for the alkene reduction of 4-phenyl-3-buten-2-one.

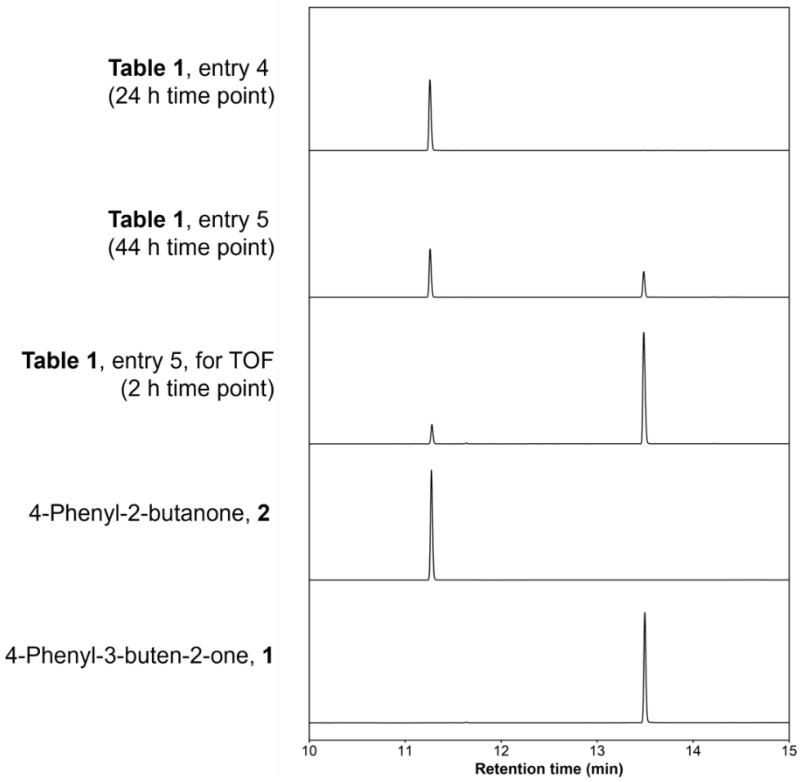


Figure S 5. Examples of GC results from reactions in **Table 1** of main text with the starting material and product standards. Standard for 4-phenyl-3-buten-2-one, **1**, (available as 99% purity) and 4-phenyl-2-butanone, **2**, (available as 98% purity) were purchased from Sigma Aldrich and diluted in ethyl acetate before injection.

For the alkene reduction of dimethyl itaconate, the product is chiral. The two enantiomers of the product are able to be separated on the chiral-GC column used (see **S.1.1** for details) as shown in **Figure S 6**. In all reaction samples, the reaction appeared to give >99% e.e. of the (*R*)-enantiomer as shown in the examples in **Figure S 6**.

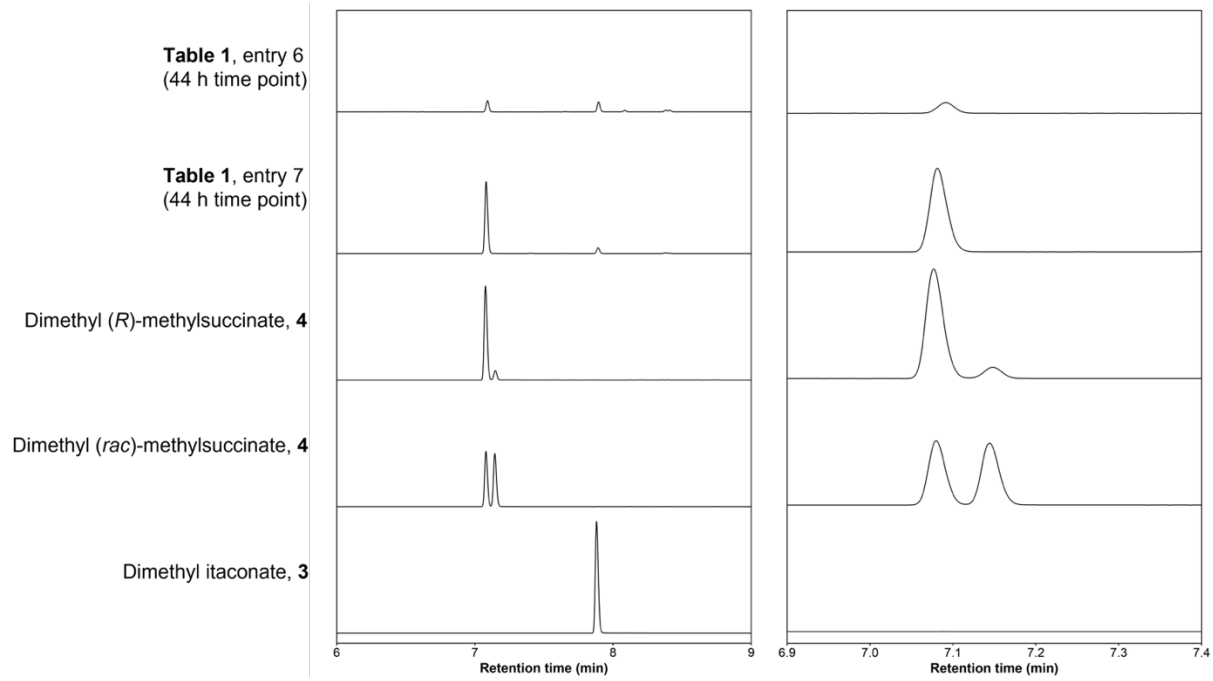


Figure S 6. Examples of chiral-GC results from reactions in **Table 1** of main text with the starting material and product standards. Standard for dimethyl itaconate, **3**, (available as 98% purity), dimethyl (*rac*)-methylsuccinate, **4**, (available as 98% purity) and dimethyl (*R*)-(+)-methylsuccinate, **4**, (available as 99% purity) were purchased from Fluorochem, Sigma Aldrich and ChemCruz respectively and diluted in ethyl acetate before injection.

S.2.7 Cyclic Voltammetry of RF

Electrochemical experiments were carried out inside a glovebox with an inert N_2 atmosphere (O_2 < 5 ppm) and recorded using a PalmSens4 potentiostat and the associated PSTrace software. The reference electrode (RE) was a saturated calomel electrode (SCE, PalmSens BV Netherlands) and the counter electrode (CE) was a coiled Pt wire inside a fritted glass tube that had been filled with KCl solution; this was to avoid any O_2 evolved at the CE contaminating the experiment. Recorded potential was converted to Volts (V) vs Standard Hydrogen Electrode (SHE). Electrolyte for all measurements was 50 mM potassium phosphate buffer, pH 7 that had been purged with nitrogen for 24 hours prior to use to exclude any O_2.

Cyclic voltammetry was used to confirm the potential of RF reduction (**Figure S 7**), with the electrochemical cell covered in aluminium foil to exclude light. The working electrode (WE) was a pyrolytic graphite 'edge' (PGE) disc electrode with a planar graphite surface of 0.03 cm^2 encased in epoxy resin. Before use the PGE surface was polished with 800 grit sandpaper

and rinsed with MilliQ water. The cell contained 7 mL buffer with 0.1 mM RF. The voltammogram shows evidence of some adsorption of RF onto the electrode surface overlaid with a diffusion-controlled response.

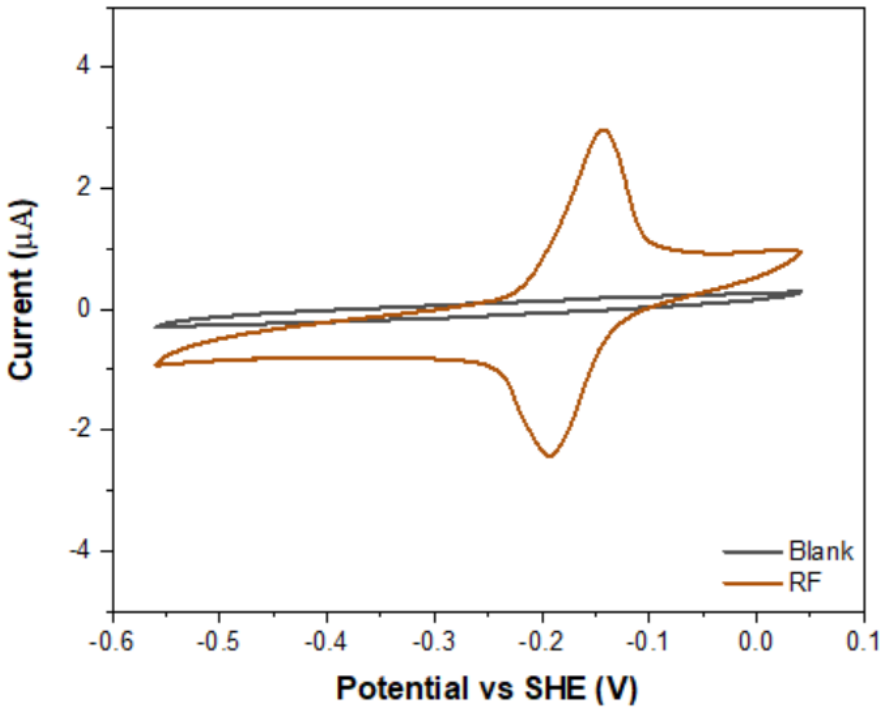


Figure S 7. Cyclic voltammograms of RF, (orange trace) with blank carbon electrode (black trace) performed at a stationary electrode.

S.2.8 Electrochemical Reduction of Riboflavin

Bulk electrochemical reduction of RF was carried out using a PalmSens4 potentiostat and the associated PSTrace software. The working electrode (WE) was a strip of carbon felt (10 mm x 30 mm). The stirred electrochemical cell contained 10 mL of riboflavin solution (0.1 mM) that had been prepared using degassed pH 7, 50 mM potassium phosphate buffer.

A chronoamperometry experiment was performed by poising the electrode at -0.356 V vs SHE. Aliquots (200 µL) of solution were removed from the cell at 300 s intervals (as indicated by the coloured stars **Figure S 8A**) for UV-vis analysis (corresponding spectra shown in **Figure S 8B**) and were subsequently returned to the electrochemical cell.

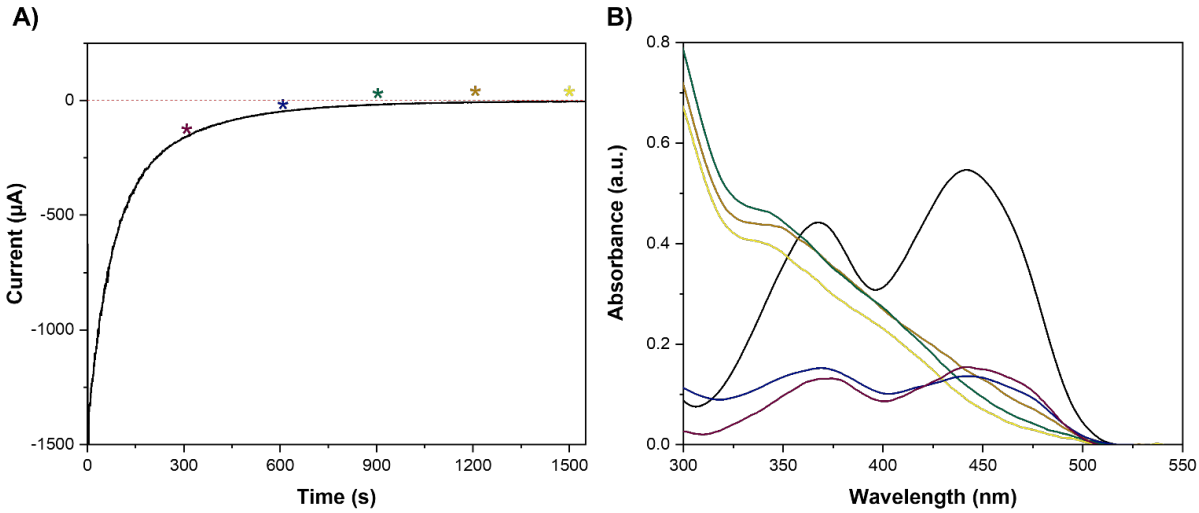


Figure S 8. Electrochemical reduction of 0.1 mM riboflavin, showing: **A)** the chronoamperometry trace, recorded by poising the electrode at -0.356 V vs SHE and **B)** the UV-Vis spectra of scans taken of aliquots removed from the electrochemical cell at regular intervals, at the points shown by the stars on the chronoamperometry trace. The electrochemical cell was covered in aluminium foil to exclude light.

S.2.9 Electrochemical Reduction of RF coupled to Ene-Reductase in Flow

Electrochemical flow experiments were recorded using an Autolab PGStat30 potentiostat and the associated Nova 1.1 software. The reference electrode (RE) was a leak-free Ag/AgCl electrode (PalmSens BV Netherlands) and counter electrode (CE) was Pt wire inside a fritted tube that had been filled with KCl, to avoid any O_2 evolved at the CE contaminating the experiment. Recorded potential was converted to V vs SHE. The electrolyte for all measurements was pH 7, 50 mM potassium phosphate buffer purged with N_2 for 24 hours before use.

An example GC trace from the flow set-up is shown below in **Figure S 9,** with accompanying product and reactant standards. The sample shown was taken after 3 hours.

Flow experiments were carried out using a home-built PEEK electrochemical flow cell (**Figure 3A** of the main text shows a diagram of the set-up). The working electrode (WE) consists of a square of carbon felt (4 mm x 5 mm) placed inside the cell with a glassy carbon rod in contact with the carbon felt inserted through one of the holes in the cell. The internal dimensions of the flow cell give a total volume of 180 µL. The reaction mixture flows into the cell through an inlet and over the WE where the reaction takes place; the solution is then pumped out of the

outlet. For this experiment, the solution was circulated continuously throughout the experiment from a 10 mL glass reservoir. The overall volume of reaction mixture was 12.7 mL of 20 mM 4-phenyl-3-buten-2-one with 30% DMSO as cosolvent made up in buffer. The solution also contained 0.1 mM riboflavin and 1.0 mg mL^{-1} ENE-108.

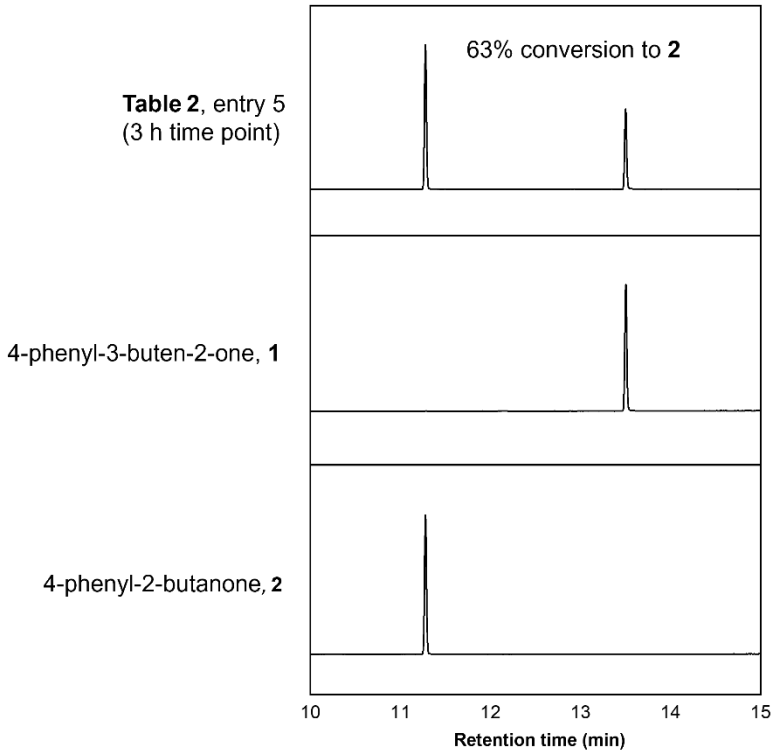


Figure S 9. GC trace from entry 5 of **Table 2** in main text with the GC traces for starting material and product standards. Standard for 4-phenyl-3-buten-2-one, **1**, (available as 99% purity) and 4-phenyl-2-butanone, **2**, (available as 98% purity) were purchased from Sigma Aldrich and diluted in ethyl acetate before injection.

S.3 References

[1] C. Greening, F. H. Ahmed, A. E. Mohamed, B. M. Lee, G. Pandey, A. C. Warden, C. Scott, J. G. Oakeshott, M. C. Taylor, C. J. Jackson, *Microbiology and Molecular Biology Reviews* **2016**, *80*, 451.

[2] Z. Shi, J. M. Zachara, L. Shi, Z. Wang, D. A. Moore, D. W. Kennedy, J. K. Fredrickson, *Environmental Science & Technology* **2012**, *46*, 11644-11652.

[3] A. H. Pakiari, M. Salarhaji, T. Abdollahi, M. Safapour, *J. Mol. Model.* **2021**, *27*, 96.

S.4 Author Contributions

LBFB performed activity assays for Hyd1 and ene-reductases with RF and demonstrated operation of ene-reductase with Hyd1/H2 driven RF recycling. CCH demonstrated electrochemically-driven RF recycling with ene-reductase. SMH performed activity assays for ene-reductase with NADH for comparison to RF assays, and demonstrated RF reduction in flow. PMTT performed the measurements of effective KM of Hyd1 for flavins. All authors contributed to data analysis and presentation. LBFB wrote the original draft; SMH and KAV led manuscript editing with contribution from CCH and LBFB. KAV acquired funding.

Chapter 5. Biocatalytic Synthesis of Metal Nanoparticles, using *Hydrogenase*, and Application of Resulting Biohybrids

5.1. Introduction

This chapter returns to the theme of the synthesis of metal nanoparticles using a biocatalytic approach. Instead of using NAD^+ reductase with NADH (or analogous synthetic cofactors) that was described in *Chapter 3*, this chapter investigates using a hydrogenase enzyme under H_2 as the reductants for Au^{3+} reduction. Hyd1, the same enzyme used in *Chapter 4* for riboflavin reduction, was used for this purpose. The advantage of this method, employing H_2 as the sacrificial electron source, means there is no need to separate out any by-products from the synthesised metal NPs. The resulting biohybrids were also tested for their effect on the rate of riboflavin reduction compared to the rate at which the enzyme alone can reduce riboflavin. Factors effecting the catalytic rate were investigated, including conditions for the synthesis of the NPs: the ratio of Hyd1: Au^{3+} used and the length of time "aging" the Au^{3+} salt solution before using it in the synthesis were identified as key factors which changed the appearance of the UV-vis spectra of the samples and led to differences in rate observed. The conditions using the biohybrid catalyst which were found to give a significantly enhanced rate of riboflavin reduction were then employed to demonstrate an increased rate of selective reduction of an alkene to alkane using an ene-reductase enzyme relying on the supply of reduced riboflavin.

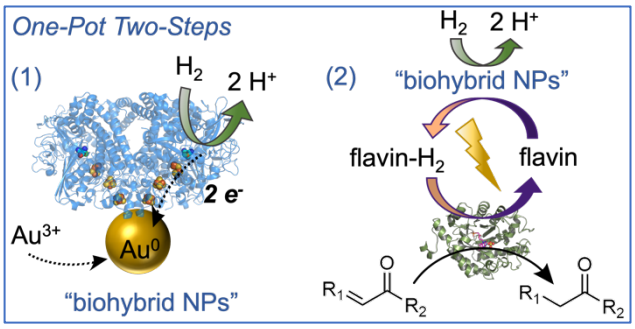
5.2. Paper 3: Using Low Pressure H_2 with Hydrogenase for the Synthesis of Enzyme-Gold Nanoparticle Biohybrids; Demonstrating their Catalytic Rate Enhancement in Ene-Reductase Biocatalysis

The manuscript and corresponding supporting information are presented on the following pages as a final draft ready for submission to a journal. I carried out all the experimental work and analysis presented. Maya A. Landis carried out the TEM. Tim Sudmeier and Kylie A. Vincent advised on initial project ideas. I wrote the majority of the manuscript as presented.

Using Low Pressure H_2 with Hydrogenase for the Synthesis of Enzyme-Gold Nanoparticle Biohybrids; Demonstrating their Catalytic Rate Enhancement in Ene-Reductase Biocatalysis

Lucy B. F. Browne, Tim Sudmeier, Maya A. Landis, and Kylie A. Vincent*

Abstract: Using hydrogen at atmospheric pressure as a reductant improves the sustainability for the synthesis of gold nanoparticles (NPs) compared to the commonly used energy-intensive or harsh-chemical routes. Gold NPs are widely applied in the biomedical industry, electronics, and catalysis, hence the continuing interest in developments for their synthesis. Here we show how we can utilise the high activity of a hydrogenase enzyme for H_2 oxidation to provide electrons for reduction of Au^{3+} to Au^0. The hydrogenase also acts as a stabiliser to the thereby synthesised Au NPs through electrostatic interactions thus creating well-stabilised and uniform, small, spherical NPs (e.g. 6.5 ± 2.5 nm as analysed by TEM). These resulting biohybrids NPs were found to have 8-10 times faster turnover frequencies for the reduction of riboflavin (than the hydrogenase could give alone). Encouragingly, this also translated to faster rates of selective alkene reduction when tested as a H_2-driven riboflavin recycling catalyst with a flavin-dependent ene-reductase. Overall, we demonstrate a one-pot, two-step process, using H_2 as the electron source, for the synthesis of Au NPs followed by the rate-enhanced biocatalytic alkene reduction.



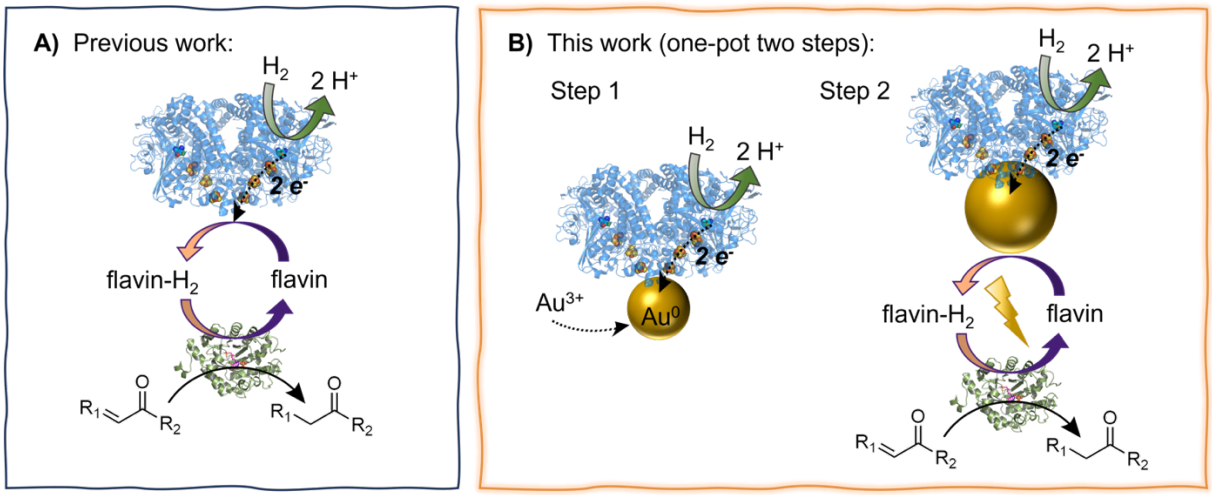
Keywords: biocatalysis • biohybrid • chemoenzymatic • ene reductase • flavin cofactor regeneration • gold nanoparticle catalysis • hydrogenase • metal nanoparticle synthesis

Introduction

Reduction by H_2 is a long-established convenient means to synthesise Pd or Pt nanoparticles (NPs),[1] but the lack of reactivity of Au with H_2 has precluded this for Au.[2] Here we show how the hydrogenase enzyme can be used to enable H_2 reduction of Au^{3+} salts under mild conditions to generate small Au NPs and further, how this creates a hybrid enzyme-metal NP catalyst capable of hydrogenating flavins for onward use in biocatalysis.

Biocatalysis has inherent advantages over other more traditional catalysis options in providing very selective and thus waste-minimising routes to pharmaceutical intermediates. However, there are still many factors which limit the widespread use of enzymes in industrial applications. These include the narrow substrate scope typical of native enzymes, which efforts in protein engineering can often improve, or the need for expensive cofactors.[3] To overcome the latter, cofactor recycling strategies have been investigated by many in the field and have led to the successful scale-up of biocatalytic steps in the manufacturing of pharmaceuticals.[4] A commonly employed method for recycling redox cofactors such as NAD(P)H or reduced flavin involves a second enzyme which uses a sacrificial reductant to reduce the oxidised biological cofactor, resulting in a build-up of a carbon-containing by-product.[5] Therefore, strategies to minimise this waste are still required.

There has been increasing interest in use of hydrogenase enzymes to enable H_2 to be used as an atom-efficient reductant for driving biocatalysis,[6-7] including a recycling system for reduced flavin, in which hydrogenase transfers electrons from H_2 to flavin (**Scheme 1 A**).[8-10] This has been demonstrated for alkene reduction reactions using ene-reductases where the flavin cofactor supplying reducing equivalents can be either flavin mononucleotide (FMN) or flavin adenine dinucleotide (FAD).[8-9] For application in biotechnology, an attractive hydrogenase is the [NiFe]-hydrogenase 1 from *E. coli*, known as “Hyd1”: it is O_2-tolerant, while many other hydrogenases (NiFe as well as FeFe enzymes) will inactivate in the presence of low concentrations of O_2,[11] and can be produced in *E. coli* using a moderate over-expression system.[10]



Scheme 1. A) H_2-driven recycling of flavins was demonstrated using Hyd1 (Pymol protein in blue) coupled to an ene-reductase (Pymol protein in green) for selective alkene reduction.[8] **B)** In this work, Hyd1 is used to reduce Au^{3+} and make Au NPs (step 1) and then the resulting biohybrid Au NPs are used, under the flavin reducing conditions where it is found that increased catalytic rates are observed (step 2).

There has also been recent interest in exploring chemo-bio hybrid catalysts, including systems that employ metal sites in a protein scaffold (artificial metalloenzymes) or use metal NPs alongside enzymes for cascade/tandem catalysis.[12-16] We have shown that the directed electron flow from an isolated NAD^+ reductase enzyme can be harnessed to provide electrons from NADH to reduce metal salts and control NP growth on the enzyme surface to achieve highly uniform NPs.[17] The present study was inspired by these findings, to address the question of H_2-driven reduction of Au salts to generate Au NPs and the application of these in biocatalysis. We looked at making gold NPs using Hyd1, by utilising the high H_2 oxidation activity of Hyd1 whereby the released electrons can be used to reduce Au^{3+} to Au^0. The Hyd1 can then also be thought of as a stabiliser to the resulting Au NPs, through electrostatic interactions – stopping them from aggregating in solution (**Scheme 1 B**, step 1).

Since one of the first Au NP synthesis, reported in 1951 by Turkevich et. al.,[18] there have been many variations to this chemical synthesis procedure, which often use high temperatures and/or harsh reagents.[19-20] More recent ongoing efforts in the field of Au NP synthesis have been directed towards improving the sustainability, with the majority of published work making use of plant extracts as the source of reductant/stabilisers.[21-23] While these methods provide a green source for the reagents there can often be drawbacks such as limited control over

size and shape of the NPs due to the complex and often difficult-to-analyse composition of chemicals found in the plant extracts.[21, 24-25] This lack of control limits their use in applications where high NP uniformity is required, such as in biomedical devices or in catalysis. Most of these methods involving plant-based reductants report relatively large NPs (>10 nm) which are less suitable for catalysis applications due to the lower number of, highest catalytically active, low-coordination surface atoms.[26-27]

One option explored for more controlled synthesis of metal NPs exploits biological catalytic processes. There have been a number of studies using bacterial whole cells to reduce metals, mostly for Pd NPs.[28] One of the first examples used the sulfate-reducing bacterium, *Desulfovibrio desulfuricans*, to reduce Pd^{2+} to Pd^0 in the presence of pyruvate, formate or H_2 as electron donors.[29] In this study, several control tests were performed: including pre-incubating the cells in Cu^{2+}, a known hydrogenase inhibitor,[30-31] in which no Pd reduction was observed to occur, leading the authors to conclude that hydrogenase enzymes were strongly implicated for carrying out the reduction. A later study confirmed the involvement of hydrogenase in the synthesis of Pd NPs, by using *E. coli* mutants lacking genes to express hydrogenase, where only mutants with Hyd1 or another hydrogenase, Hyd2, had comparable activity for Pd reduction to the wildtype.[32] These studies along with the finding that Hyd1 is known to have a H_2 oxidation onset potential of -0.36 $\pm$ 0.01 V vs SHE (pH 7, 1 bar H_2),[33] forms the basis for our hypothesis that Hyd1, as an isolated enzyme, should be able to reduce Au^{3+} to Au^0, which has a reduction potential of +0.80 V vs SHE at pH 7 (extrapolated from electrochemical measurements at pH 8.0 and pH 6.2).[34] We show the feasibility of this approach by demonstrating synthesis of gold NPs using an atmospheric pressure of H_2 and the enzyme Hyd1.

We were also interested in finding out whether Hyd1 remains active after the NP synthesis and whether the resulting biohybrids (subsequently referred to as Hyd1-Au NPs) exhibit any enhanced properties due to the presence of both metal NP and enzyme. We show that the Hyd1-Au NPs can significantly accelerate the rate of flavin reduction compared to Hyd1 alone

(**Scheme 1 B**, step 2). It is hypothesised that this can be attributed to the increase in electronic surface area which the NPs provide. Thus, this work showcases an example where a biohybrid (of metal NP and enzyme) improves the reaction rate of a biocatalytic process.

Results and Discussion

Preliminary studies found that FMN can be replaced by the cheaper cofactor, riboflavin (RF) in studies using Hyd1 and ene-reductase, and hence we chose to focus on using RF in this work. **Figure 1 A** shows the result of a UV-visible spectrophotometric activity assay used to determine the rate of reduction of RF by Hyd1 under H_2. The Hyd1 enzyme is "pre-activated under H_2" before use to ensure the enzyme is in its active state, so there is no lag-phase at the start of the reaction.[8, 35] The RF solution is also pre-sparged with H_2. The reaction is started by addition of Hyd1 to the RF solution (kept under a constant flow of H_2 at atmospheric pressure), and a steady decrease is observed in the absorbance peaks at 370 and 444 nm which are associated with oxidised RF, indicating the cofactor is becoming reduced. The experiment was then repeated with Au^{3+} added to solution in the form of $HAuCl_4$, pre-dissolved in pH 7, 50 mM potassium phosphate buffer, as shown in **Figure 1 B.** In this case, after addition of Hyd1, a small volume of the Au^{3+} solution was immediately added. As seen in **Figure 1 B** and **C**, there are two distinct reaction phases. **1.** An initial phase where there is no significant change in the RF peaks, but there is the appearance and growth of an absorbance peak between 500-800 nm which is indicative of Au NP surface plasmon resonance (SPR) and thus shows the formation of Au NPs.[36] **2.** A phase where RF reduction then occurs very rapidly (around 8 times faster than without Au present).

Next it was investigated whether the accelerated RF reduction observed in the presence of Au NPs translates to a faster alkene reduction when coupling the H_2-driven RF recycling with an ene-reductase. This was initially investigated using the substrate 4-phenyl-3-buten-2-one, **1**, for the selective C=C (over C=O) reduction to 4-phenyl-2-butanone, **2**. It was first checked whether all the reagents could be added at the same time, i.e. Au^{3+}, Hyd1 and RF as well as the ene-reductase and alkene substrate. In this case, Au NPs were formed, and RF was

reduced, however there was a low conversion of **1**, indicating the ene-reductase was inactivated during the Au NP formation (see **S.2.1** for details). Therefore, a one-pot, two-step procedure was used: firstly, the Au^{3+} and RF were allowed to be reduced by Hyd1 under H_2 for an hour to ensure complete reduction, before the ene-reductase and **1** were added and the reactions were put back under 1 bar H_2 to enable catalytic recycling of reduced RF to support alkene reduction by the ene-reductase (the two steps are as shown in **Figure 2 A** and **B**, respectively). It should be noted that for both steps, the reaction samples were covered in foil to minimise the exposure to light since flavins can be photoexcited by visible light which can lead to their decomposition over time.[37]

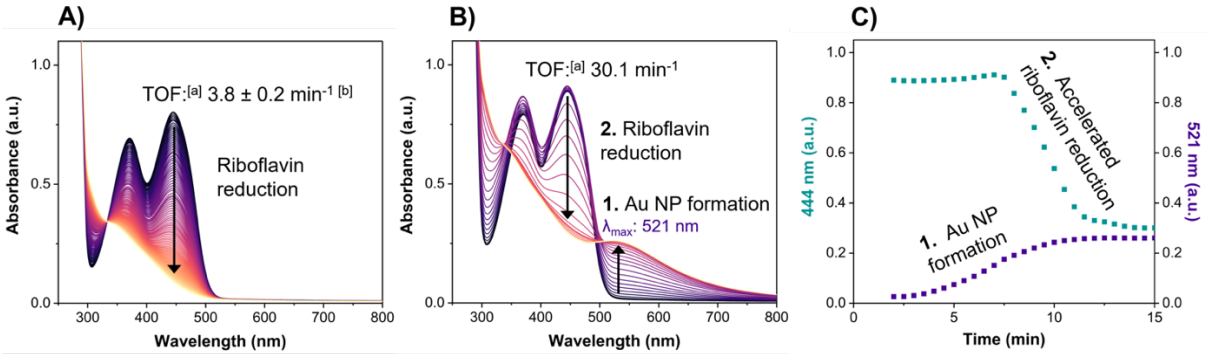


Figure 1. Riboflavin (RF) reduction in absence and presence of Au. UV-vis spectra (showing scans recorded every 30 s) of RF solutions, pre-sparged with H_2 then assay under flow of H_2 over headspace, containing: **A)** Hyd1, **B)** Hyd1 and $HAuCl_4$ – where Au NP formation is followed by an accelerated RF reduction compared to just Hyd1 alone, as in **A**. **C)** Absorbances, from **B**, corresponding to RF concentration and Au NP concentration, 444 nm and 521 nm (the wavelength of the SPR maximum, λ_{max}) respectively, displayed over time. [a] Hyd1 turnover frequency (TOF): mol RF per mol Hyd1 per minute calculated using the molar adsorption coefficient (11.0 mM^{-1} cm^{-1}) at 444 nm.[38] [b] The TOF shown is an average with standard deviation of assays performed in triplicate. Reaction conditions: RF (0.1 mM), Hyd1 (0.05 mg mL^{-1}), ± $HAuCl_4$ (0.125 mM), pH 7, 50 mM potassium phosphate, H_2, 25 °C. See **S.1.4** for the reaction procedure.

This two-step procedure was employed to investigate the effect of the ratio of Hyd1 to Au^{3+} used in the Au NP synthesis step. Since Hyd1 is known to exist in solution as a homodimer, with one active site in each identical unit, we refer here to the concentration of the Hyd1 dimer. Ratios of Hyd1 dimer: Au^{3+} between 1: 100 to 1: 1050 were investigated. The resulting UV-vis spectra recorded after 1 hour are displayed in **Figure 2 A**. As expected, the overall absorbance increased with increasing amounts of Au^{3+} in the reaction mixture, since scattering increases with increased amount of Au^0.[39] At 1: 100, no significant peak is observed,

indicating < 2 nm sized NPs,[39] whereas a slight peak appears in the spectrum of solution at 1: 200 ratio. Upon further increase of Au^{3+}, to a 1: 550 ratio (solid blue line) the peak is more defined, with a narrow peak shape and low absorbance at high wavelengths, indicating a uniform NP size distribution. The NP synthesis was repeated at the 1: 550 ratio (compare the two solid blue lines in **Figure 2 A**), and the similarity in peak shape shows good consistency between batches.

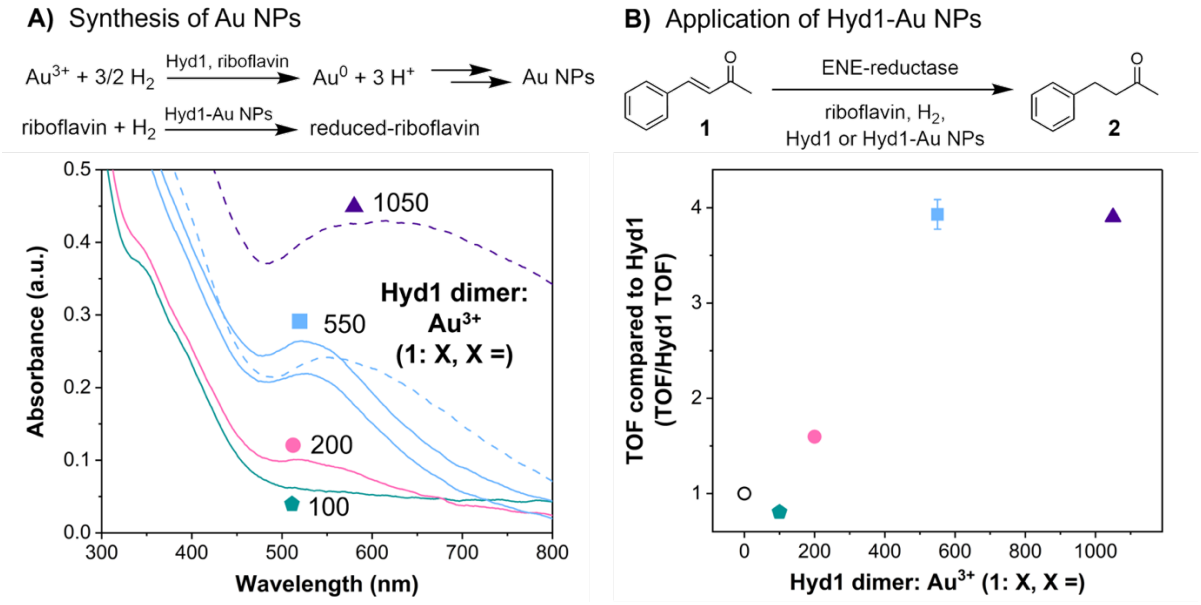


Figure 2. Investigating the effect of different ratios of Hyd1 to Au^{3+}. **A)** UV-vis spectra recorded after 1 hour, when Au NP formation was complete, in solutions initially containing different concentrations of $HAuCl_4$ but same concentration of Hyd1. Solid and dashed lines correspond to results from using Au^{3+} solution that was "aged" or freshly prepared, respectively. Reaction conditions: RF (0.1 mM), Hyd1 (0.05 mg mL^{-1}), $HAuCl_4$ (0.025 mM to 0.25 mM), pH 7, 50 mM potassium phosphate, H_2, 20-25 °C. **B)** Initial turnover frequency (TOF) calculated from GC analysis from reaction sampling after 2 h for the formation of alkane product and compared to the TOF from a side-by-side experiment containing only Hyd1 (no Au). Reaction conditions: same as in **A** with addition of: ene-reductase: ENE-103 (0.5 mg mL^{-1}), 4-phenyl-3-buten-2-one, **1**, (1 mM), acetonitrile (1 vol%). See **S.1.5** and **S.1.7** for reaction procedures.

Variation was observed, however, when the age of the Au^{3+} solution differed: the results indicated by solid lines used a Au^{3+} solution that was prepared 1-2 hours before use, whereas the dashed lines in **Figure 2 A** show results from using a freshly prepared Au^{3+} solution (i.e. within 1 hour). The blue dashed line (also at 1: 550 ratio) shows a significantly broader peak, suggesting less uniform NPs. At 1: 1050 ratio, using a freshly prepared Au^{3+} solution, this peak is again very broad. From further investigation into the effect of the length of time "aging" the Au^{3+} solution, it was found that increasing the "aging" time gave narrower SPR peaks (tested

up to 73 hours, see **S.2.2**). Therefore, for subsequent experiments the Au^{3+} solution was prepared at least 16 hours before use. Other studies have implied a slow change in Au^{3+} speciation in aqueous solution over several days and hence it may be inhomogeneity of Au^{3+} species present initially which leads to a less controlled NP synthesis.[34]

The Hyd1-Au NPs (from **Figure 2 A**) were then tested alongside reactions with just Hyd1 (no Au) as the RF recycling system for the reduction of alkene substrate, **1**, by a commercial ene-reductase (ENE-103). With Hyd1 alone as the RF recycling system, initial turnover frequency (TOF) values of 1.0 ± 0.2 min^{-1} were observed for conversion of **1** to **2**, measured after the first 2 hours. TOF values obtained using Hyd1-Au NPs as the RF recycling system, prepared with the different Hyd1 dimer: Au^{3+} ratios, were next compared to the system with Hyd1 alone (shown graphically in **Figure 2 B**). Increasing the ratio of Hyd1 dimer: Au^{3+} from 1: 100 to 1: 550 gave an increase in both the initial TOF, measured after 2 hours, and conversion after 24 hours (**Figure 2 B** and **S.2.4** for conversion results). Despite the peak shape difference in the UV-vis spectra for the solid and dashed blue lines, these NPs were found to give similar TOF results, with a small standard deviation as indicated by the error bar in **Figure 2 B**. The result using a 1: 1050 ratio was also within the error bar found at 1: 550, therefore there appears to be a plateau beyond which adding more Au^{3+} does not improve the results (this could be due to another factor, such as the alkene reduction carried out by the ene-reductase, becoming rate limiting). Therefore, for subsequent reactions, 1: 550 was selected as a suitable ratio of Hyd1 dimer: Au^{3+}.

In the series of samples shown in **Figure 2 A**, the Hyd1 quantity is kept constant and hence the number of nucleation sites for NPs remains constant as we increase the Au^{3+}, which is expected to lead to successively larger Au NPs. **Figure 2 B** shows a trend of increased TOF with increasing Au^{3+}, up to the 1: 550 ratio of Hyd1 dimer: Au^{3+}. A hypothesis for this trend is that Au NPs in electronic contact with Hyd1 provide the main site where RF is reduced. At the 1: 100 ratio, the TOF was lower than the TOF without any Au NPs present (Hyd1 alone). At this ratio, the Hyd1-Au NPs (of < 2 nm NP size) would give an exposed “redox-active” surface

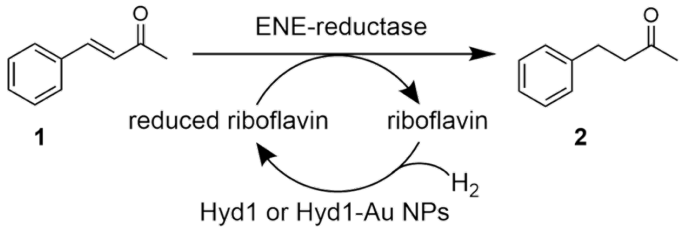
area where RF can be reduced which has similar or smaller size to the "redox-active" area around the terminal iron-sulfur electron-relay cluster on the Hyd1 enzyme itself. Using Pymol, and analysing the crystallographic protein structure, PDB 4GD3, the surface area of Hyd1 from which electrons can be transferred can be estimated to be 15 nm^2 which is equivalent to the surface area of a 1.1 nm sized "naked" Au NP, see **S.2.3** for details. As the NP size is increased, this "redox active" surface area will increase, and would account for the increase in RF rate observed in the presence of Au NPs (from the 1: 200 ratio onwards). For reference the planar isoalloxazine fragment of RF, which is expected to interact with the NP surface during electron transfer,[40] is approximately 1 nm in diameter (3 nm^2 surface area).

Thus, using a 1: 550 ratio, the increased TOF in the alkene reduction reaction in the presence of Au NPs, meant that instead of 29 ± 14% product obtained after 24 hours with Hyd1 alone as RF recycling system, 65 ± 22% could be obtained under the same conditions, with Hyd1-Au NPs (**Table 1**, entries 1-2). During these initial screening experiments, the ene-reductase ENE-103 was used. To check that this increased rate with Au NPs was not exclusive to one enzyme, experiments were then carried out using ENE-108. This enzyme was found to be more active for substrate **1**, thus improving the results for the reactions with Hyd1 alone and with Hyd1-Au NPs (**Table 1**, comparing entries 1-2 with 3-4). For the reactions with Hyd1 for RF recycling, near-complete conversion of **1** (1 mM) was achieved after 24 hours, so the initial Hyd1 TOF over 2 hours was used to compare to the reaction with Au^{3+} added, which showed a significant rate enhancement with the inclusion of Au NPs again (**Table 1**, comparing entries 3 and 4).

Upon increasing the substrate concentration to 10 mM, the RF concentration was increased to 0.2 mM, thereby maintaining complete conversion of **1** to **2** within 24 hours (**Table 1**, entries 5-6). For the Au containing reactions, the effect of a 10-fold increase in Hyd1 and Au^{3+} concentrations was examined, keeping the ratio of Hyd1 dimer: Au^{3+} as 1: 550 (**Table 1**, entry 7). This led to formation of a much higher concentration of Au NPs, with absorbance too high to measure by UV-vis without diluting. These Hyd1-Au NPs gave a slightly faster TOF, leading

to 96% product measured at 18 hours, compared to a reaction under the same conditions without Au, which gave 87% product at the same time point (see **S.2.4** for time point analysis). These results did not therefore show as significant a difference between Hyd1 and Hyd1-Au NPs as was observed for reactions at 1 mM substrate concentration. It is possible that increased Hyd1 and Au^{3+} concentrations led to faster, but less controlled, NP synthesis. Therefore, conditions more similar to those used in **Table 1**, entries 1-4 were used for the Au NP synthesis step, followed by adding more Hyd1 for RF recycling in the alkene reduction step, to make the total Hyd1 concentration the same as used in the comparison without Au (i.e. 0.1 mg mL^{-1} Hyd1, 0.25 mM Au^{3+} and 0.2 mM RF for the Au NP synthesis, followed by adding an extra 0.4 mg mL^{-1} Hyd1). These NP synthesis conditions were therefore only 2 times more concentrated than the conditions used at the 1 mM substrate scale (since 0.2 mM RF was used, 2 times keeps the molar ratios the same, i.e. a Hyd1 dimer: Au^{3+}: RF ratio of 1: 550: 450). These results were similar to the ones using 1.25 mM Au^{3+}, with again a slight advantage in the reaction being complete a few hours before the reaction with just Hyd1 (**S.2.4**). This suggests that under these conditions the reaction rate is not limited by the RF recycling system and more likely by the ene-reductase. Therefore, to test this, at 20 mM substrate concentration, the Hyd1 concentration was kept the same as was used at 10 mM, while the ENE-108 concentration was increased by 2 times (**Table 1**, entries 8-9). This gave higher TOF values measured at 2 hours (**Table 1**, entries 8-9), confirming ENE-108 was rate limiting during the 10 mM reactions (**Table 1**, entries 6-7). Under these conditions, at 20 mM, the reaction without Au was not able to reach full conversion, with 60% product after 24 h and 66% after 44 hours (**Table 1**, entry 8). Meanwhile the reaction which used 0.25 mM Au^{3+} gave 95% product after 24 hours (**Table 1**, entry 9). Thus, once more a significant improvement is seen in the results with Hyd1-Au NPs compared to Hyd1 alone.

Table 1. H_2-driven RF recycling for the biocatalytic reduction of **1**.[a]



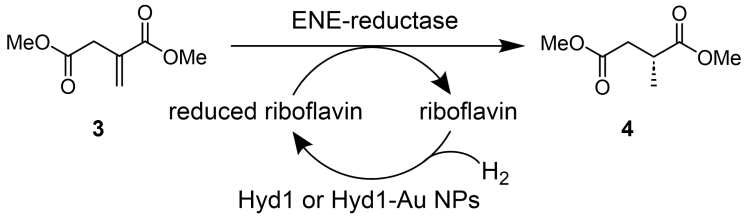
Entry	RF Recycling Catalyst	[Au] (mM)	ENE-	[**1**] (mM)	[RF] (mM)	Conv. (%)[b]	Hyd1 TOF [min^{-1}][c]	Hyd1 TTN[d]	RF TN[d]
1	Hyd1	0	103	1	0.1	29 ± 14	1.0 ± 0.2	620 ± 308	2.9 ± 1.4
2	Hyd1-Au NPs	0.125	103	1	0.1	65 ± 22	2.9 ± 0.8	1401 ± 463	6.5 ± 2.2
3	Hyd1	0	108	1	0.1	99	1.5	2114	9.9
4	Hyd1-Au NPs	0.125	108	1	0.1	>99	7.4	2132	10.0
5[e]	Hyd1	0	108	10	0.1	36	1.6	769	35.9
6[e]	Hyd1	0	108	10	0.2	>99 ± <1	2.6 ± 0.1	2138 ± 0.6	49.9 ± <0.1
7[e]	Hyd1-Au NPs	1.25	108	10	0.2	>99	3.6	2142	50.0
8[f]	Hyd1	0	108	20	0.2	60 (66)[g]	4.7	2563	59.8
9[f]	Hyd1-Au NPs	0.25	108	20	0.2	95 (>99)[g]	4.2	4049	94.5

[a] Reaction conditions: RF (0.1 or 0.2 mM), Hyd1 (0.05 mg mL^{-1}), Au concentration as indicated by [Au], relating to the Au^{3+} concentration used in the Au NP synthesis step, ene-reductase (0.5 mg mL^{-1}), 4-phenyl-3-buten-2-one, **1**, in acetonitrile (1 vol%), pH 7, 50 mM potassium phosphate, H_2 (1 bar), room temperature (20-25 °C). See **S.1.7** for reaction procedures. [b] GC conversion to **2** at 24 h. [c] Hyd1 turnover frequency (mol **2** per mol Hyd1 per minute) calculated after 2 h. [d] Hyd1 total turnover number (mol **2** per mol Hyd1) and RF turnover number (mol **2** per mol RF) calculated after 24 h. [e] DMSO (1 vol%) co-solvent used instead of acetonitrile. Enzyme concentrations increased: Hyd1 (0.5 mg mL^{-1}) and ene-reductase (5 mg mL^{-1}). [f] DMSO (1 vol%) co-solvent used instead of acetonitrile. Enzyme concentrations increased: Hyd1 (0.5 mg mL^{-1}) and ene-reductase (10 mg mL^{-1}). [g] GC conversion to **2** at 44 h.

To verify that the accelerating effect of the Hyd1-Au NPs was not a unique case for this substrate, reactions were then performed on another substrate: dimethyl itaconate, **3**, which upon reduction of the C=C bond by ene-reductase leads to a chiral product, dimethyl methylsuccinate, **4** (**Table 2**). ENE-108 was used in these reactions and in all cases, whether in the absence or presence of Au NPs, the reaction was enantioselective (>99% *e.e.*) for the (*R*)-enantiomer of **4**. Initial tests at 1 mM of **3**, again showed higher TOF and higher conversion (obtained after 24 and 44 hours) for the reaction containing Hyd1-Au NPs as the RF recycling catalyst, compared to the reaction with just Hyd1 (**Table 2**, entries 1-2). When increasing the

substrate concentration to 20 mM of **3**, similar results were seen in the reactions using 0.5 mg mL^{-1} Hyd1, in the absence and presence of Au NPs (**Table 2**, entries 3-4). However, in a reaction where the Hyd1 concentration was decreased to 0.1 mg mL^{-1} (by using the same method to prepare NPs as in **Table 2**, entry 4 but without adding extra Hyd1 after the NP synthesis), an approximate doubling of the TOF and TTN was observed (**Table 2**, entry 5). Addition of excess Hyd1 may partially block the "redox active" surface of the Au NPs, leaving less area for RF reduction. This hypothesis was verified by UV-vis assays measuring the RF reduction rate for samples of Hyd1-Au NPs with different amounts of Hyd1 added after the NP synthesis, and then "incubated" for 16 hours, before starting the assays (see **S.2.5** for results). Samples with no Au were also tested alongside. When using Hyd1-Au NPs with no extra Hyd1 added, the TOF was significantly higher than for all other conditions tested. Adding extra Hyd1 to these Hyd1-Au NPs caused a dramatic decrease in the TOF: giving a more similar TOF to those obtained under the conditions without any Au (at the same Hyd1 concentration), consistent with the observation from the alkene reduction reactions. Thus, there appear to be many factors which need to be carefully controlled to give fully optimised results, including the "free" NP surface area which has been identified as a key factor.

Table 2. H_2-driven RF recycling for the biocatalytic enantioselective reduction of **3**.[a]



Entry	RF Recycling Catalyst	[Hyd1] (mg mL^{-1})	[Au] (mM)	[**3**] (mM)	[RF] (mM)	Conv. (%)[b]	*e.e.* (%)[c]	Hyd1 TOF [min^{-1}][d]	Hyd1 TTN[e]	RF TN[e]
1	Hyd1	0.05	0	1	0.1	32 (55)	>99	0.6	689	3.2
2	Hyd1-Au NPs	0.05	0.125	1	0.1	98 (>99)	>99	4.4	2107	9.8
3	Hyd1	0.5	0	20	0.2	66 ± 13 (96 ± 5)[f]	>99	2.2 ± 0.5	2817 ± 546	65.7 ± 12.7
4	Hyd1-Au NPs	0.5	0.25	20	0.2	69 ± 5 (>99 ± 3)	>99	2.5 ± 0.6	2938 ± 222	68.6 ± 5.2
5	Hyd1-Au NPs	0.1	0.25	20	0.2	31 (57)[g]	>99	6.1	6555	30.6

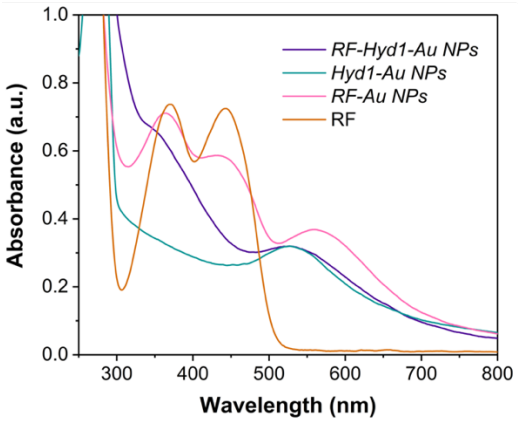
[a] Reaction conditions: RF (0.1 or 0.2 mM), Hyd1 (0.05 to 0.1 mg mL^{-1}), Au concentration as indicated by [Au], relating to the Au^{3+} concentration used in the Au NP synthesis step, ene-reductase, ENE-108, (0.5 and 10 mg mL^{-1} for 1 and 20 mM of **3** respectively), dimethyl itaconate, **3**, in DMSO (1 vol%), pH 7, 50 mM potassium phosphate, H_2 (1 bar), room temperature (20-25 °C). See **S.1.7** for reaction procedures. [b] GC conversion to **2** at 24 h (and 44 h in brackets). [c] Enantioselectivity for (*R*)-enantiomer of **4** calculated from chiral-GC analysis at final reaction time point. [d] Hyd1 turnover frequency (mol **3** per mol Hyd1 per minute) calculated after 2 h. [e] Hyd1 total turnover number (mol **3** per mol Hyd1) and RF turnover number (mol **3** per mol RF) calculated after 24 h. [f] This conversion in brackets is an average of three experiments: two measured at 44 h and one at 48 h. [g] This conversion in brackets was measured at 48 h.

Controls of conditions without RF or Hyd1 were tested for Au NP formation. Without RF, the formation of Au NPs with Hyd1 and H_2 was significantly slower, e.g. taking approximately 8 hours compared to under 30 mins (see **S.2.6**). Once the UV-vis spectra stopped changing, indicating Au NP formation was complete, these spectra show very similar absorbance from 500-800 nm (**Figure 3 A**), indicating similar size and size-distribution of NPs are made with Hyd1 in the absence or presence of RF, hereafter specified as *Hyd1-Au NPs* or *RF-Hyd1-Au NPs* respectively. The *Hyd1-Au NPs* were estimated from their UV-vis spectra to have an average NP size of 4.7 ± 0.5 nm (method detailed in **S.2.7**). The spectra for the RF-containing reactions cannot be used to estimate NP size by this method since RF also contributes to the absorbance at 450 nm. TEM analysis of *Hyd1-Au NPs* and *RF-Hyd1-Au NPs* found NPs of size: 6.5 ± 2.5 nm and 4.0 ± 2.1 nm respectively (**S.2.8**), consistent with the range estimated

from the UV-vis spectra. The hydrodynamic diameter (measured by DLS) of *Hyd1-Au NPs* and *RF-Hyd1-Au NPs* gave 18.6 ± 2.4 nm and 22.6 ± 5.5 nm (**S.2.9**) hence the diameter of the layer around the Au NP is 12.1 ± 2.2 nm and 18.6 ± 2.8 nm respectively (by subtracting the TEM sizes). Since the Hyd1 can be calculated to have a mass-equivalent spherical diameter of 7.8 nm, it suggests that in the case of *Hyd1-Au NPs,* the metal NPs may have an incomplete "shell" of Hyd1 around them, i.e. some of surface may also have loosely coordinating buffer molecules etc. (see **S.2.9** for calculations). For *RF-Hyd1-Au NPs* there could also be an incomplete shell of Hyd1 with RF molecules also adsorbed on the Au NP surface.[40] Zeta potential analysis on these samples suggest the *Hyd1-Au NPs* may be slightly more stable than the *RF-Hyd1-Au NPs* (-34 ± 4 mV vs. -27 ± 4 mV), but with both being around the value usually quoted for "stable particles" (-30 mV).[41]

Interestingly, without Hyd1, with just RF under H_2, Au NPs also formed, albeit at a slower rate than under the conditions where Hyd1 and RF were both present. These will be referred to as *RF-Au NPs*. The higher λ_{max} for the SPR peak (560 nm instead of 527 nm), in the UV-vis spectra shown in **Figure 3 A**, indicates the presence of larger NPs than the NPs made in the presence of Hyd1. TEM analysis was found to corroborate with the UV-vis (**S.2.8**). Attempts to analyse *RF-Au NPs* by DLS found these were too unstable and quickly formed large aggregates under the DLS conditions.

A) UV-vis spectra after 20 h under H_2[a]



B) Results from coupling H_2-driven RF reduction to alkene reduction[b]

Entry	RF Recycling Catalyst	Addition after NP synthesis	Conv. (%)[c]	Hyd1 TOF [min^{-1}][d]
1	*RF-Hyd1-Au NPs*	-	>99	7.1
2	*Hyd1-Au NPs*	- (no RF)	2	<0.1
3	*Hyd1-Au NPs*	+ RF[e]	>99	6.3
4	*RF-Au NPs*	-	2	n/a
5	*RF-Au NPs*	+ Hyd1	58	1.9
6	none (RF)	n/a	1	n/a
7	Hyd1[f]	n/a	73 ± 9	2.0 ± 0.4

Figure 3. Comparing synthesis of Au NPs in absence/presence of RF and Hyd1 and the effect on alkene reduction. **A)** UV-vis spectra after Au NP synthesis step where conditions testing absence of one or more reagents were tested alongside each other, keeping all other conditions the same. **B)** Testing the NPs from the different NP synthesis conditions for their H_2-driven RF reduction activity coupled with an ene-reductase carrying out the reduction of 4-phenyl-3-buten-2-one, **1**. [a] Reaction conditions: RF (0.1 mM), Hyd1 (0.05 mg mL-1), $HAuCl_4$ (0.125 mM), pH 7, 50 mM potassium phosphate, H_2 (1 bar), room temperature (20-25 °C) and reaction procedure as in **S.1.5** or **S.1.6**. Duplicate experiments under each condition were carried out (shown in **S.2.6**). [b] Reaction conditions: same as in **A** with addition of: ENE-108 (0.5 mg mL^{-1}), 4-phenyl-3-buten-2-one, **1**, (1 mM), DMSO (1 vol%). See **S.1.7** for reaction procedures. [c] GC conversion to **2** at 20 h. [d] Hyd1 turnover frequency (mol **2** per mol Hyd1 per minute) calculated after 2 h. [e] After the NP synthesis, the solution was added to a 10 kDa size exclusion filter to concentrate (by centrifuging) before H_2-sparged RF solution was added to the Hyd1-Au NPs collected in the filter. [f] This reaction, which was carried out in triplicate, contained no NPs, with just Hyd1 acting as the RF recycling system, keeping the rest of the conditions the same as the other reactions.

Further controls shown in **S.2.10** confirm Au must be able to activate H_2 itself, but in the absence of Hyd1, RF is required for the NP formation: since Au NPs do not form in an aqueous pH 7 solution of $HAuCl_4$ under H_2, nor by just mixing a solution of $HAuCl_4$ and RF without H_2 (**S.2.10**). In a recent study it was shown that Au NPs (of around 37 nm in size) could be made with trimethyl chitosan under 3 bar H_2 where it is proposed that Au^{3+} forms a complex with the trimethyl chitosan which then catalyses the reduction reaction of H_2 with Au^{3+} to Au^0.[42] Therefore, a similar mechanism could be occurring in the presence of RF and H_2.

After the NP synthesis step, ene-reductase and **1** were added to these reaction solutions. The *Hyd1-Au NPs* without RF present gave negligible conversion, however upon addition of RF they gave almost the same result as *RF-Hyd1-Au NPs* (**Figure 3 B**, entries 1-3). Since a filtration step was used to concentrate these *Hyd1-Au NPs* (for **Figure 3 B**, entry 3) before adding RF to achieve the same concentration as in the other reactions, this also shows that the enhanced catalytic activity is unlikely due to any soluble Au(I) species which may be

present as these would have been removed at the filtration stage. The *RF-Au NPs* showed negligible activity without any Hyd1 (**Figure 3 B**, entry 4) – thus confirming both Hyd1 and RF are needed for the alkene reduction. Upon addition of Hyd1 to *RF-Au NPs*, significantly lower TOF and conversion was achieved compared to *RF-Hyd1-Au NPs* or *Hyd1-Au NPs* (**Figure 3 B**, entry 5 vs. 1 and 3). This reaction gave similar results to reactions with just Hyd1 (**Figure 3 B**, entry 7). In summary, for the Au NP synthesis, the presence of Hyd1 is key to controlling the NP size and forming highly active biohybrid catalysts, while the presence of RF helps to increase the rate at which the NPs are formed but does not significantly affect the activity of the biohybrids. However, for the alkene reduction, carried out by the ene-reductase, reduced RF must be present for the reaction to proceed.

Conclusions

We initially tested the effect of Au^{3+} on the RF reduction rate in the presence of Hyd1 and H_2, this led to our discovery that the TOF was up to 8-10 times faster than with Hyd1 enzyme alone for RF recycling. UV-vis and TEM analysis confirmed that Au NPs were made *in situ* with the Au^{3+} reduction dominating initially before the RF was quickly reduced. Controls performed without Hyd1 or with Hyd1 added after Au NP formation (which was observed with just RF under H_2) confirmed this rate-enhancement was exclusive to the biohybrids formed in the presence of Hyd1. H_2-driven RF recycling was then demonstrated with these biohybrids with two commercial ene-reductases and two alkene substrates. Improved reaction rates for the alkene reduction were observed with the biohybrids and the enantioselectivity in the case of a substrate with a chiral product was not lowered by the presence of Au NPs.

In conclusion, this work has presented two important findings; 1) hydrogenase (specifically, *E. coli* NiFe Hyd1 was tested here), by oxidising H_2, can be used to make Au NPs under a mild H_2 pressure, and 2) the resulting biohybrid Au NPs can boost the H_2-driven flavin reduction rate for Hyd1, leading to faster, yet still highly selective, biocatalytic reductions, when coupled to a flavin-dependent enzyme. We hope this encourages others to explore the potential for rate enhancement using biohybrids in other areas of biocatalysis.

Associated Content

Supporting Information: complete experimental procedures; NP characterisation techniques including TEM images, DLS and zeta potential analysis as well as additional UV-visible spectra; examples of GC traces; additional experimental results: testing a one-step procedure, investigating "aging" time for Au^{3+} solution, more results from investigating changing the Au^{3+} concentration, RF reduction assays with Hyd1-Au NPs with additional Hyd1 added and further controls.

Author Information

Corresponding Author

Kylie A. Vincent - Department of Chemistry, University of Oxford, Inorganic Chemistry Laboratory, South Parks Rd, Oxford, OX1 3QR (United Kingdom)

E-mail: kylie.vincent@chem.ox.ac.uk

Authors

Lucy B. F. Browne - Department of Chemistry, University of Oxford, Inorganic Chemistry Laboratory, South Parks Rd, Oxford, OX1 3QR (United Kingdom)

Tim Sudmeier - Department of Chemistry, University of Oxford, Inorganic Chemistry Laboratory, South Parks Rd, Oxford, OX1 3QR (United Kingdom)

Maya A. Landis - Department of Chemistry, University of Oxford, Inorganic Chemistry Laboratory, South Parks Rd, Oxford, OX1 3QR (United Kingdom)

Author Contributions

Lucy B. F. Browne carried out the experimental work and formal analysis and wrote the majority of the original draft of this manuscript. Tim Sudmeier and Kylie A. Vincent advised on initial project ideas and experimental work. Maya A. Landis performed the TEM imaging. All authors reviewed the manuscript. K. A. Vincent acquired funding to support this work.

Acknowledgements

We gratefully thank Dr Stephen Carr for his assistance in preparing and isolating *E. coli* hydrogenase 1 (Hyd1) and Johnson Matthey, (Cambridge, U.K.) for providing the ene-reductase enzymes. M.L. has been supported by the EPSRC Centre for Doctoral Training in Inorganic Chemistry for Future Manufacturing (OxICFM, EP/S023828/1). The authors acknowledge the use of the characterization facilities within the David Cockayne Centre for Electron Microscopy, Department of Materials, University of Oxford. This project has been funded by the European Research Council (ERC-CoG-BiocatSusChem-819580) awarded to K.A.V.

References

[1] L. D. Rampino, F. F. Nord, *J. Am. Chem. Soc.* **1941**, *63*, 2745-2749.
[2] A. Henglein, *J. Phys. Chem. B* **2000**, *104*, 6683-6685.
[3] S. P. France, R. D. Lewis, C. A. Martinez, *JACS Au* **2023**.
[4] C. Egan-Morriss, R. L. Kimber, N. A. Powell, J. R. Lloyd, *Nanoscale Adv.* **2022**, *4*, 654-679.
[5] F. Hollmann, D. J. Opperman, C. E. Paul, *Angew. Chem. Int. Ed.* **2021**, *60*, 5644-5665.
[6] H. A. Reeve, J. Nicholson, F. Altaf, T. H. Lonsdale, J. Preissler, L. Lauterbach, O. Lenz, S. Leimkühler, F. Hollmann, C. E. Paul, K. A. Vincent, *Chem. Commun.* **2022**, *58*, 10540-10543.
[7] B. Poznansky, S. E. Cleary, L. A. Thompson, H. A. Reeve, K. A. Vincent, *Front. Chem. Eng.* **2021**, *3*.
[8] S. Joseph Srinivasan, S. E. Cleary, M. A. Ramirez, H. A. Reeve, C. E. Paul, K. A. Vincent, *Angew. Chem. Int. Ed.* **2021**, *60*, 13824-13828.
[9] A. Al-Shameri, S. J. P. Willot, C. E. Paul, F. Hollmann, L. Lauterbach, *Chem. Commun.* **2020**, *56*, 9667-9670.
[10] M. A. Ramirez, S. Joseph Srinivasan, S. E. Cleary, P. M. T. Todd, H. A. Reeve, K. A. Vincent, *Frontiers in Catalysis* **2022**, *2*.
[11] K. A. Vincent, A. Parkin, O. Lenz, S. P. J. Albracht, J. C. Fontecilla-Camps, R. Cammack, B. Friedrich, F. A. Armstrong, *J. Am. Chem. Soc.* **2005**, *127*, 18179-18189.
[12] S. J. Freakley, S. Kochius, J. van Marwijk, C. Fenner, R. J. Lewis, K. Baldenius, S. S. Marais, D. J. Opperman, S. T. L. Harrison, M. Alcalde, M. S. Smit, G. J. Hutchings, *Nature Communications* **2019**, *10*, 4178.
[13] H. R. de Barros, L. Y. Tanaka, R. T. P. da Silva, J. Santiago-Arcos, S. I. C. de Torresi, F. López-Gallego, *Particle & Particle Systems Characterization* **2021**, *38*, 2100136.
[14] L. Zhang, G. Morello, S. B. Carr, F. A. Armstrong, *J. Am. Chem. Soc.* **2020**, *142*, 12699-12707.
[15] X. Zhao, S. E. Cleary, C. Zor, N. Grobert, H. A. Reeve, K. A. Vincent, *Chem. Sci.* **2021**, *12*, 8105-8114.
[16] A. G. Jarvis, *Curr. Opin. Chem. Biol.* **2020**, *58*, 63-71.
[17] L. B. F. Browne, T. Sudmeier, M. A. Landis, C. S. Allen, K. A. Vincent, *Angew. Chem. Int. Ed.* **2024**, e202404024.
[18] J. Turkevich, P. C. Stevenson, J. Hillier, *Discuss. Faraday Soc.* **1951**, *11*, 55-75.
[19] N. G. Bastús, J. Comenge, V. Puntes, *Langmuir* **2011**, *27*, 11098-11105.

[20] Z. Wang, B. Tan, I. Hussain, N. Schaeffer, M. F. Wyatt, M. Brust, A. I. Cooper, *Langmuir* **2007**, *23*, 885-895.
[21] A. Guleria, H. Sachdeva, K. Saini, K. Gupta, J. Mathur, *Appl. Organomet. Chem.* **2022**, *36*, e6778.
[22] M. Sengani, A. M. Grumezescu, V. D. Rajeswari, *OpenNano* **2017**, *2*, 37-46.
[23] M. Kumari, S. Pandey, V. P. Giri, C. S. Nautiyal, A. Mishra, *Environmental Nanotechnology, Monitoring & Management* **2023**, *20*, 100895.
[24] M. A. R. Khan, M. S. Al Mamun, M. A. Habib, A. B. M. N. Islam, M. Mahiuddin, K. M. R. Karim, J. Naime, P. Saha, S. K. Dey, M. H. Ara, *Results in Chemistry* **2022**, *4*, 100478.
[25] K. X. Lee, K. Shameli, Y. P. Yew, S.-Y. Teow, H. Jahangirian, R. Rafiee-Moghaddam, T. J. Webster, *Int. J. Nanomedicine* **2020**, *15*, 275-300.
[26] I. V. Yudanov, R. Sahnoun, K. M. Neyman, N. Rösch, J. Hoffmann, S. Schauermann, V. Johánek, H. Unterhalt, G. Rupprechter, J. Libuda, H.-J. Freund, *J. Phys. Chem. B* **2003**, *107*, 255-264.
[27] M. Haruta, M. Daté, *Applied Catalysis A: General* **2001**, *222*, 427-437.
[28] N. Joudeh, A. Saragliadis, G. Koster, P. Mikheenko, D. Linke, *Frontiers in Nanotechnology* **2022**, *4*.
[29] R. Lloyd Jon, P. Yong, E. Macaskie Lynne, *Appl. Environ. Microbiol.* **1998**, *64*, 4607-4609.
[30] V. M. Fernandez, M. L. Rua, P. Reyes, R. Cammack, E. C. Hatchikian, *Eur. J. Biochem.* **1989**, *185*, 449-454.
[31] R. M. Fitz, H. Cypionka, *Arch. Microbiol.* **1991**, *155*, 444-448.
[32] K. Deplanche, I. Caldelari, I. P. Mikheenko, F. Sargent, L. E. Macaskie, *Microbiology* **2010**, *156*, 2630-2640.
[33] B. J. Murphy, F. Sargent, F. A. Armstrong, *Energy & Environmental Science* **2014**, *7*, 1426-1433.
[34] S. Wang, K. Qian, X. Bi, W. Huang, *J. Phys. Chem. C* **2009**, *113*, 6505-6510.
[35] M. J. Lukey, A. Parkin, M. M. Roessler, B. J. Murphy, J. Harmer, T. Palmer, F. Sargent, F. A. Armstrong, *J. Biol. Chem.* **2010**, *285*, 3928-3938.
[36] W. Haiss, N. T. K. Thanh, J. Aveyard, D. G. Fernig, *Anal. Chem.* **2007**, *79*, 4215-4221.
[37] A. Taglieber, F. Schulz, F. Hollmann, M. Rusek, M. T. Reetz, *ChemBioChem* **2008**, *9*, 565-572.
[38] M. I. Gutiérrez, S. M. Fernández, W. A. Massad, N. A. García, *Redox Report* **2006**, *11*, 153-158.
[39] V. Amendola, R. Pilot, M. Frasconi, O. M. Maragò, M. A. Iatì, *J. Phys.: Condens. Matter* **2017**, *29*, 203002.
[40] B. R. A. Junior, F. L. F. Soares, J. A. Ardila, L. G. C. Durango, M. R. Forim, R. L. Carneiro, *Spectrochimica Acta Part A: Molecular and Biomolecular Spectroscopy* **2018**, *188*, 589-595.
[41] A. Carone, S. Emilsson, P. Mariani, A. Désert, S. Parola, *Nanoscale Adv.* **2023**, *5*, 2017-2026.
[42] Y. A. Alli, O. Ejeromedoghene, P. O. Oladoye, A. Bamisaye, F. O. Oladoyinbo, S. Adewuyi, H. Anuar, S. Thomas, *Kuwait Journal of Science* **2024**, *51*, 100162.

Supporting Information

S.1 Experimental Procedures

S.1.1 General Reagents

Most commercial reagents were purchased from Sigma-Aldrich and used as received, without any further purification. The exceptions were dimethyl itaconate and dimethyl (*R*)-(+)-methylsuccinate which were purchased from Fluorochem and ChemCruz respectively. All aqueous solutions were prepared with deionised Milli-Q water (Millipore, ≥15 MΩcm).

S.1.2 General Method Considerations

To reduce any competing oxidation reactions, all reaction handling (including metal nanoparticle, NP, preparation procedures) was carried out in a glovebox, filled with a N_2 atmosphere. When handling metal salts including while preparing the NPs, care was taken to protect from exposure to light by covering in tinfoil (to eliminate any light-induced metal reduction). Also, while handling aqueous flavin solutions, flavin mononucleotide or riboflavin (FMN or RF respectively), including while the alkene reduction reaction was carried out, foil was used to cover solutions to protect from photodecomposition.[1]

S.1.3 Enzymes

The hydrogenase enzyme known as Hyd1 was prepared by over-expression in *E. coli.* and purified by standard protocols, following published procedures.[2] The ene-reductases (ENE-103 and ENE-108) used for the alkene reduction were received in lypophilised form from Johnson Matthey, Cambridge, and used without further purification.

S.1.4 Flavin Reduction UV-vis Assay Procedure

These assays were carried out inside a glovebox using a Cary 60 UV-visible spectrophotometer (Agilent) and a quartz cuvette (path length 1 cm). A Peltier accessory was used to control the temperature of the cuvette which was set to 25 °C for all assays. The settings on the Scan software were set to record a spectrum from 800 to 200 nm every 30 seconds during an assay. A background spectrum using pH 7, 50 mM potassium phosphate was recorded before beginning the experiment. A 0.3 mM solution of flavin (FMN or RF) in pH 7, 50 mM potassium phosphate was initially prepared and used to prepare a 0.103 mM solution. 880 µL of this solution was then added to a quartz UV-vis cuvette. A suba-seal was used to seal the UV-vis cuvette and two needles were added through the top of the suba-seal in order to have an inlet and outlet for H_2 gas. A H_2 gas line and an outlet line were attached and the inlet needle was moved below the surface of the flavin solution in order to sparge the solution with H_2 for a minimum of 15 minutes. Meanwhile pH 7, 50 mM potassium phosphate buffer was used to make the volume of the Hyd1 solution up to 20 uL (thus making the flavin concentration in each assay experiment as 0.1 mM). The Hyd1 was “pre-activated” before this stage, i.e. an aliquot containing the amount of Hyd1 desired to be used per assay (e.g. 0.05 mg mL^{-1} assay concentration) was put under H_2 (1 bar) for 16-20 hours. After the sparging of the flavin solution was complete, both needles were lifted out of the solution so they were now in the cuvette headspace. The UV-vis was set to start scanning every 30 seconds before the Hyd1 solution was added to the cuvette, using a needle and syringe to do so, using 200 µL of flavin solution to aid transfer. The flavin reduction rate was then measured by the decrease in absorbance, at 444 nm or 445 nm for RF or FMN respectively, over time, using the data from the linear section of the graph.

For assays in the presence of Au, the same procedure was followed except with the addition of a $HAuCl_4$ solution (dissolved in pH 7, 50 mM potassium phosphate) following the addition of Hyd1 to the cuvette.

S.1.5 Gold NP Preparation using Hyd1 and Riboflavin

Hyd1 was firstly "pre-activated" by pipetting the desired amount into a 0.5 mL plastic tube (StarLabs), piercing the lid of the plastic tube with a needle and putting inside a Büchi Tinyclave pressure vessel which was then filled with H_2 (to 2.5 bar and vented x3 and then filled to 1 bar) and left for 16-20 h. A solution of $HAuCl_4$ in pH 7, 50 mM potassium phosphate (4.25 mM) was made at least 16 h before use (to allow the Au species to equilibrate at pH 7). A 0.3 mM solution of RF in pH 7, 50 mM potassium phosphate was initially prepared and used to prepare a 0.124 mM solution. This solution was sparged with H_2 for 15 minutes minimum. Then the following was added, in order, to the pierced 0.5 mL plastic tube containing "pre-activated" Hyd1: any extra buffer that may be needed to obtain the desired Hyd1 concentration, 350 µL of H_2-saturated RF (making a 0.1 mM reaction concentration) and the desired amount of pre-equilibrated $HAuCl_4$ solution (i.e. 12.5 uL for 0.125 mM). The plastic tubes can then be placed back into a Büchi Tinyclave pressure vessel, filled with H_2 (to 2.5 bar and vented x3 and then filled to 1 bar) and then placed on a Stuart® mini see-saw rocker set to 30 oscillations/min. The pressure vessel was wrapped in tinfoil to protect the RF from photodecomposition. Typically, the reactions were left for 1.5 h before the vessel was vented and the samples were analysed by UV-vis.

S.1.6 Gold NP Preparation Controls without Hyd1 or Riboflavin

Controls without Hyd1 were carried out by following the same procedure as in **S.1.5** with the exception of substituting Hyd1 for the same volume of pH 7, 50 mM potassium phosphate buffer. To prepare Au NPs without RF, the same procedure as in **S.1.5** was used, replacing RF with pH 7, 50 mM potassium phosphate buffer which had been sparged with H_2 for 15 minutes minimum.

S.1.7 Alkene Reduction Standard Procedure

Typically, the same procedure as is described in **S.1.5** was followed to initially prepare Hyd1-Au NPs (usually also containing a side-by-side reaction without Au: but where Hyd1 will reduce RF). Then the ene-reductase (from a stock solution prepared in pH 7, 50 mM potassium phosphate) followed by the alkene substrate (in acetonitrile or DMSO) were added to the plastic tubes, and solutions mixed using a pipette. These were then put back into a Büchi Tinyclave pressure vessel, filled with H_2 (to 2.5 bar and vented x3 and then filled to 1 bar) and then placed on a Stuart® mini see-saw rocker set to 30 oscillations/min. The pressure vessel was wrapped in tinfoil to protect the RF from photodecomposition. Typically, the reactions were analysed by GC using 50 µL of reaction solution removed from reactions inside a glovebox (to stop any reduced RF from re-oxidizing) at various time points, before the vessel was re-sealed and re-filled with H_2.

S.1.8 Characterisation of NPs

UV-visible spectroscopy was used to monitor the NP formation *in situ* or at time points throughout the reaction. Transmission electron microscopy (TEM) imaging and analysis was then carried out on selected samples, to give information on Au NP shape and size distribution. DLS and zeta potential measurements were also carried out on selected samples to find out the hydrodynamic diameter of the enzyme-Au NP biohybrids as well as their zeta potential (indicating stability).

S.1.8.1 UV-visible Spectroscopy

UV-visible spectroscopy was carried out using a Cary 60 UV-visible spectrophotometer (Agilent) using a plastic micro-cuvette (path length 1 cm). For monitoring reaction progress of NP formation, the reaction solution was added to the micro-cuvette and the spectra was

recorded from 200 to 800 nm. The increase in absorbance across the 400-800 nm range indicated the presence of scattering caused by NPs. For gold NPs a surface plasmon resonance peak with an absorbance maximum in the 500-550 nm range was clear indication that gold NPs were formed. The ratio of the absorbance at the surface plasmon resonance peak to the absorbance at 450 nm was used to estimate the average NP size (only for NPs in absence of flavin which has a strong absorbance around 450 nm).[3]

S.1.8.2 TEM Imaging

Dilute samples were dropcast onto copper grids (type: holey carbon 300 mesh Cu TEM grids, S147-3 from Agar Scientific) and dried under vacuum. TEM was performed using a JEOL ARM-200F microscope operated at 200 kV.

S.1.8.3 DLS and Zeta Potential Measurements

DLS and zeta potential measurements were carried out using a Malvern Panalytical Zetasizer with a disposable folded capillary cell (DTS1070). The ZS XPLORER 2.1.0.15 software (from Malvern Panalytical) was used with the settings as given in **Table S 1** for successive DLS and zeta potential measurements on diluted aqueous samples. Milli-Q water and samples were filtered using a disposable filter with 0.45 µm pore size (Cytiva Whatman™ Puradisc™ 13 mm) before adding to the cell.

Table S 1. Settings used for DLS and zeta potential measurements.

Material	Colloidal gold: Refractive Index: 0.18, Absorption: 3.433 or Protein: Refractive Index: 1.45, Absorption: 0.001
Dispersant	Water: Refractive Index: 1.33, F(ka) model: Smoluchowski
Measurement	25.0 °C, 30 s equilibration time
Data Processing	General purpose analysis model
Advanced Settings	Attenuation: Automatic, Measurement process: Automatic (10-100 runs), Use pause after sub runs: No, Voltage selection: Automatic, Pause between repeats: 60 s

S.1.9 GC-FID Method for Alkene Reduction Analysis

50 µL of the reaction solution was added to 200 µL EtOAc to extract the organic products (vortexed for 30 s to mix, then allowed to settle for 2 mins). 150 µL of the EtOAc layer was removed, dried using Na_2SO_4 and centrifuged at 12,000 rpm for 3 mins to precipitate the Na_2SO_4. The dried sample was then added to a GC vial. The GC method was as described in **Table S 2**.

Table S 2. GC method conditions used for the determination of reaction conversion for the reduction of 4-phenyl-3-buten-2-one (**1**) to 4-phenyl-2-butanone (**2**) and dimethyl itaconate (**3**) to dimethyl methylsuccinate (**4**).

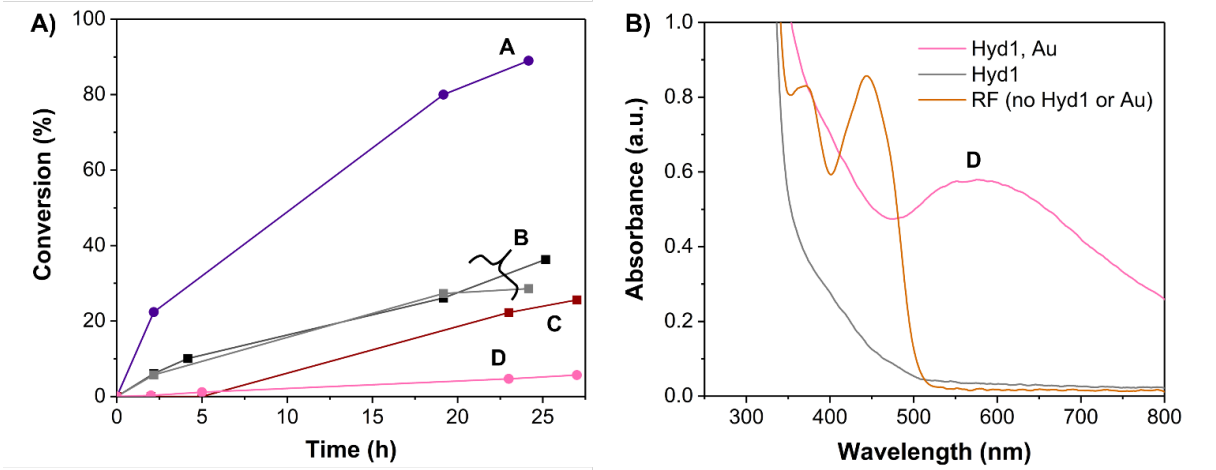
Column	CP-Cyclosil-B (Agilent), 30 m x 0.25 mm x 0.25 µm, fitted with a guard of 10 m undeactivated fused silica of the same diameter
Carrier	H_2, 3 mL/min (constant flow rate)
Inlet temperature	250 °C
Injection conditions	Split flow 75 mL/min, split ratio 25, purge 5 mL/min. Injection volume = 1 µL.
Detection	FID (H_2 = 35 mL/min, air = 350 mL/min, makeup N_2 = 40 mL/min, temp = 250 ℃)
Oven heating profile	Time (minutes) Temperature 0 – 2 Hold at 70 ℃ 2 – 18.25 Ramp to 200 ℃ at 8 ℃/min 18.25 – 34 Hold at 200 ℃ for 15.75 minutes
Compound retention times	Time (minutes) Compound 11.26 4-Phenyl-2-butanone, **2** 13.48 4-Phenyl-3-buten-2-one, **1** 7.08 Dimethyl (*R*)-(+)-methylsuccinate, **4** 7.15 Dimethyl (*S*)-(-)-methylsuccinate, **4** 7.89 Dimethyl itaconate, **3**

S.2 Results and Discussion

S.2.1 Testing Using a One-Step Procedure

To check whether it was necessary to carry out the Au NP synthesis and alkene reduction as a one-pot, two-step process instead of one combined step, all reagents were added at the same time and samples were removed at time points for GC analysis. Compared to reactions carried out using a one-pot, two-step process, there was very little conversion to the alkane product in the reaction where Au^{3+} salts were added at the same time as the ene-reductase (ENE-103) and alkene substrate (**Figure S 1 A**). Au NPs were observed to form on a similar time scale as in the first step of the two-step procedure and the UV-vis recorded after 23 h showed a broad surface plasmon peak indicating a range of NP sizes were present and that RF had been reduced (**Figure S 1 B**). Therefore, in the case of adding all reagents at the

same time, the ene-reductase was inhibited and thus it was concluded that it was necessary to use a one-pot, two-step process.



Conditions:

A Hyd1, RF, Au^{3+} under H_2 for 1 h before ENE and alkene added
B Hyd1, RF, under H_2 for 1 h before ENE and alkene added
C Hyd1, RF, ENE and alkene added at same time
D Hyd1, RF, Au^{3+}, ENE and alkene added at same time

Figure S 1. Testing using a one-step procedure where Au^{3+} is added at the same time as the ene-reductase and alkene substrate (in comparison to allowing Au^{3+} reduction to occur first before the alkene reduction). **A)** Reaction time points showing conversion of alkene (4-phenyl-3-buten-2-one) to alkane (4-phenyl-2-butanone) as measured by GC. **B)** UV-vis spectra of the reactions where all reagents were added at the same time, recorded after 23 h.

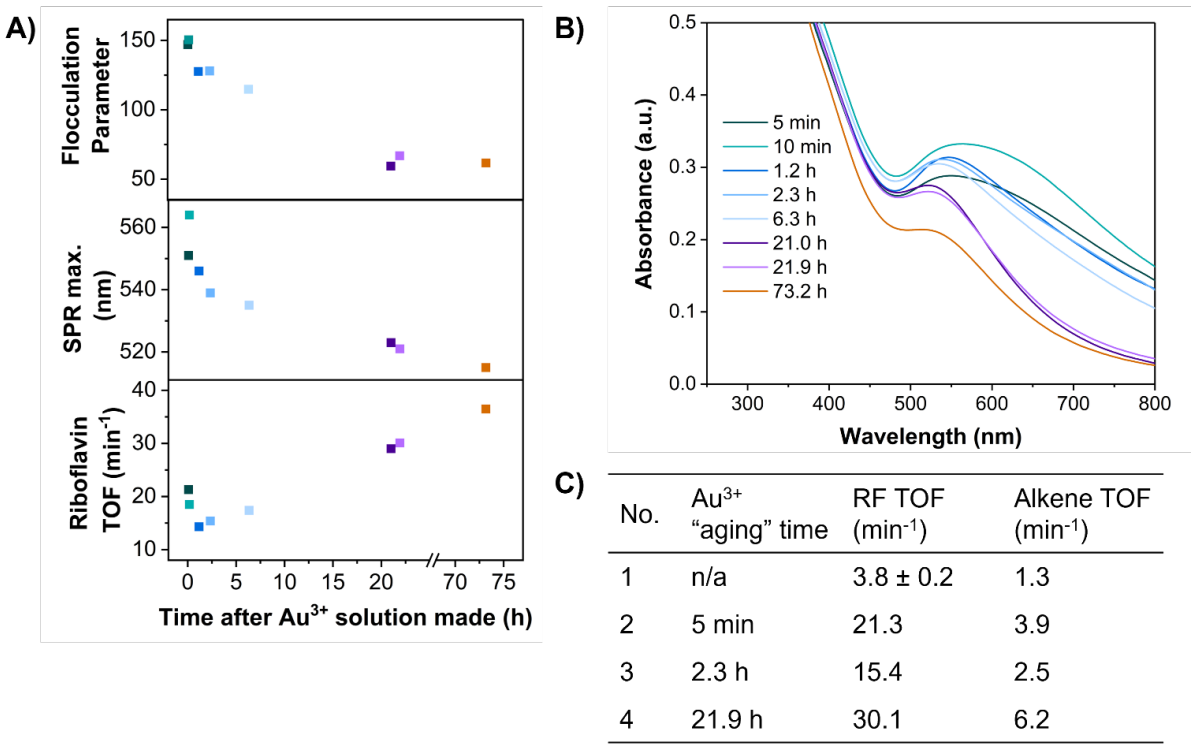
S.2.2 Testing the Effect of "Aging" Au^{3+} in pH 7 Buffer

In initial experiments some variability in the UV-vis spectra of resulting Au NPs was observed; it was noticed that using $HAuCl_4$ solutions which had been prepared at different time lengths before use were giving different results, therefore this was investigated more closely. The results from UV-vis assays of these solutions are summarized in **Figure S 2 A** where the procedure described in **S.1.4** was used. It was found that for a freshly prepared solution (i.e. under an hour), the UV-vis spectra gave a very broad SPR peak and a high SPR maximum, signalling larger NPs with a broad size distribution (**Figure S 2 B**). As the age of the Au^{3+} solution increased the SPR maxima was found to decrease and with a decreasing flocculation parameter (indicating smaller and narrower size distribution of NPs).

Interestingly the RF TOF is relatively high at the beginning, then after a few hours it is slower and then after many hours the TOF becomes very high, therefore there must be a few different factors affecting the TOF (i.e. size of NPs and surface coverage of the NPs by Hyd1).

Testing these same *RF-Hyd1-Au NPs* for their TOF of alkene substrate showed the same trend as the RF TOF (**Figure S 2 C**). The values for alkene TOF are all between 3-6 times lower than their respective RF TOF which suggests, under these conditions, the RF reduction rate is not the limiting factor for the rate of alkene reduction (the concentration of ENE-108 may be rate limiting in this case).

These results provide more evidence, along with the results described in the main text, **Figure 2**, that it is best to use an "aged" Au^{3+} solution, to achieve greatest NP uniformity and activity.



C)

No.	Au^{3+} "aging" time	RF TOF (min^{-1})	Alkene TOF (min^{-1})
1	n/a	3.8 ± 0.2	1.3
2	5 min	21.3	3.9
3	2.3 h	15.4	2.5
4	21.9 h	30.1	6.2

Figure S 2. Results from investigating the effect of "aging" $HAuCl_4$ salts in pH 7, 50 mM potassium phosphate buffer before use in the synthesis of Au NPs. **A)** Results measured from UV-vis analysis of using a Au^{3+} solution aged for different lengths of time before being added to a solution of RF and Hyd1, under H_2. **B)** UV-vis spectra of the samples after Au NP formation stopped (no further change in the UV-vis spectra). **C)** Comparison of time allowed for "aging" of $HAuCl_4$ in buffer with the RF TOF (measured from UV-vis assay) and alkene TOF (measured from reaction at 2 h time point by GC analysis). No. 1 is the comparison of Hyd1, without any Au, under the same conditions.

S.2.3 Surface Area Comparison of Hyd1, Au NP and Riboflavin

Figure S 3 illustrates the size comparisons of Hyd1, Au NP and RF, showing an example with a Au NP of 6.5 nm diameter where Hyd1 is larger than the NP. There is likely to be more than one Hyd1 molecule interacting with the NP surface however since there will also be repulsion between Hyd1 molecules, there is also likely to be some areas of the NP surface that are "free" from Hyd1 and will either have loosely coordinating buffer molecules or RF (in the case of *RF-Hyd1-Au NPs*). The "redox active" surface area of Hyd1 has been estimated using the crystallographic structure of Hyd1 (PDB: 4GD3) by measuring the distance across two planes within which electrons are able to transfer from the terminal iron-sulfur electron-relay clusters to the surface of the protein, using a maximum distance from iron-sulfur cluster to protein surface as 1.4 nm which is the maximum distance known for electron transfer in redox proteins.[4] The measured distances are shown in **Figure S 3**.

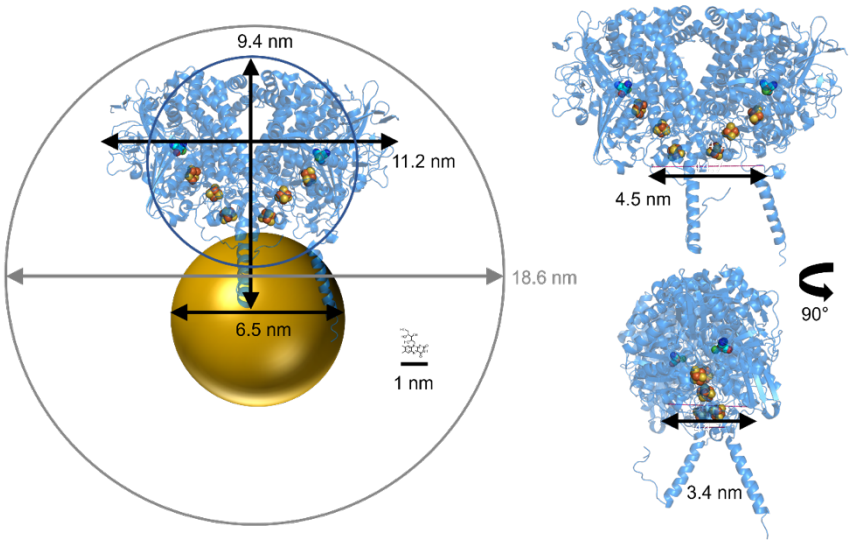


Figure S 3. Left: To scale image showing Hyd1 (blue protein structure, Pymol PDB code: 4GD3), a Au NP (with 6.5 nm diameter) and a RF molecule (1 nm diameter across the isoalloxazine fragment). The mass equivalent spherical size of Hyd1 is shown by the blue circle (7.8 nm in diameter) and the grey circle depicts the hydrodynamic diameter which was measured for a sample of *Hyd1-Au NPs*. Right: Images of Hyd1 showing measured distances (on Pymol) used to estimate the contact area of Hyd1 (15 nm^2).

Calculations shown in **Table S 3** can be used firstly to estimate the number of Hyd1 molecules per Au NP found in a solution of a certain size of NPs and Hyd1: Au atom ratio (assuming all Au^{3+} have been reduced to Au^0, resulting in all the Au atoms found in the Au NPs). A theoretical

maximum number of Hyd1 per Au NPs can also be calculated based on the size of the NPs and the surface area of Hyd1 that is expected to experience interaction with the NP surface. These values can be compared and thus in all the examples in the table the number of Hyd1 molecules expected experimentally is lower than the maximum for complete coverage of the NP by Hyd1. The percentage of NP surface coverage by Hyd1 is also of interest to note: a high value indicates there is a lower amount of "free" metal NP surface. The Gaussian curvature of a sphere is another value which may give indication of NP activity (a value closer to zero indicates a flatter surface; generally, a higher curvature gives higher catalytic activity due to a greater number of edge sites). However, it has become clear from the experiments described that there are many competing factors affecting the activity of the enzyme-metal biohybrid NPs.

Table S 3. Calculations to estimate NP surface area and NP surface area coverage by Hyd1 and curvature constant for different sized NPs.

Diameter of NP (nm)	1.1	4.0	6.5	9.0	2.0
V of sphere (nm^3)	1	34	144	382	4
V of Au unit cell (nm^3)	0.068	0.068	0.068	0.068	0.068
No. of unit cells per NP	10	494	2118	5622	62
No. of atoms per FCC unit cell	4	4	4	4	4
No. of atoms of Au per NP	41	1974	8471	22486	247
Hyd1 dimer: Au atom ratio used (1: X)[a]	550	550	550	550	100
No. of Hyd1 per Au NP	<1	4	15	41	2
Surface area of sphere (nm^2)	15	201	531	1018	50
Surface area of Hyd1 contact (nm^2)	15	15	15	15	15
Max. no. of Hyd1 per Au NP[b]	1	13	35	68	3
Surface area of Hyd1 contact per NP (nm^2)	1	54	231	613	37
Percentage of NP surface coverage by Hyd1 (%)	7	27	44	60	74
Radius of sphere	1	2	3	5	1
Gaussian curvature of sphere	3.31	0.25	0.09	0.05	1.00

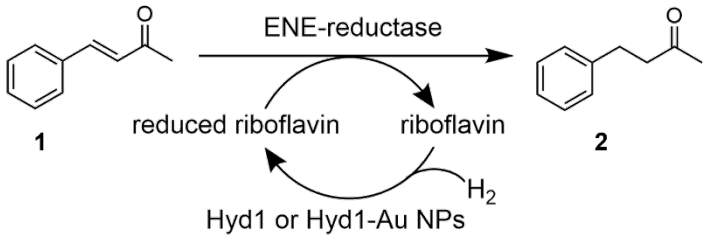
[a] This ratio uses the molecular weight of the dimeric protein: 214.29 kDa. [b] This is a theoretical maximum value ignoring electrostatic repulsion between Hyd1 molecules (therefore true value will be lower).

S.2.4 Investigating Effects of Conditions on the Rate of Reduction of 4-Phenyl-3-buten-2-one

Some initial tests for the H_2-driven RF reduction coupled to an alkene reduction step were carried out using different concentrations of Au with Hyd1 (in the form of preformed Hyd1-Au NPs as discussed in the main text). A significantly higher conversion to alkane product was measured after 24 h from tests using 0.125 or 0.25 mM Au^{3+} concentration in the NP synthesis than was seen in the tests using just Hyd1 or at the lower concentrations of Au^{3+} (**Table S 4**, entries 4-5 compared to 1-3). Faster initial Hyd1 TOF was also observed in these reactions from time points after 2 h and due to the higher conversions higher Hyd1 TTN and RF TN values were also achieved. From this data the conditions using 0.25 mM Au^{3+} concentration

appear to give the best results, however in that experiment the test with 0.125 mM Au^{3+} gave 97% conversion after 24 h, with a similar TOF after 2 h. Therefore, conditions using 0.125 mM Au^{3+} were used for subsequent tests; this relates to an approximate Hyd1 dimer: Au^{3+} ratio of 1: 550.

Table S 4. Initial tests investigating the effect of Au^{3+} concentration used for the synthesis of Hyd1-Au NPs on the rate of biocatalytic reduction of **1**.[a]



Entry	RF Recycling Catalyst	[Au] (mM)	Conv. (%)[b]	Hyd1 TOF [min^{-1}][c]	Hyd1 TTN[d]	RF TN[d]
1	Hyd1	0	29 ± 14	1.0 ± 0.2	620 ± 308	2.9 ± 1.4
2	Hyd1-Au NPs	0.025	37	0.6	799	3.7
3	Hyd1-Au NPs	0.05	38	1.2	812	3.8
4	Hyd1-Au NPs	0.125	65 ± 22	2.9 ± 0.8	1401 ± 463	6.5 ± 2.2
5	Hyd1-Au NPs	0.25	89	4.0	1907	8.8

[a] Reaction conditions: RF (0.1 mM), Hyd1 (0.05 mg mL^{-1}), ENE-reductase, ENE-103, (0.5 mg mL^{-1}), 4-phenyl-3-buten-2-one, **1**, (1 mM) in acetonitrile (1 vol%), pH 7, 50 mM potassium phosphate, H_2 (1 bar), room temperature (20-25 °C). See **S.1.7** for reaction procedures. [b] GC conversion to **2** at 24 h. [c] Hyd1 turnover frequency (mol **2** per mol Hyd1 per minute) calculated after 2 h. [d] Hyd1 total turnover number (mol **2** per mol Hyd1) and RF turnover number (mol **2** per mol RF) calculated after 24 h.

Upon increasing the substrate concentration of 4-phenyl-3-buten-2-one from the initial tests at 1 mM, to 10 and 20 mM, the conditions were optimized in order to achieve full conversion of product in approximately 24 hours. **Figure S 4 A** shows some of these conditions tested and the conversion over time. Thus, under the conditions where 0.5 mg mL^{-1} Hyd1 was used, whether or not in the presence of Au NPs, full conversion can be achieved at 10 mM substrate concentration. In comparison, at 20 mM, even with increasing the ENE-108 concentration by 2 times, the reaction with Hyd1 alone cannot achieve high conversion and the reaction

significantly slows over time. However, in the presence of Au, the reaction rate remains fast over time and 95% conversion was achieved at the 24-hour time point (>99% at a 44-hour time point). The UV-vis spectra for the *RF-Hyd1-Au NPs* used in these reactions (using the 0.25 mM Au^{3+} conditions) indicate the NPs are small with a narrow size distribution, due to the relatively low λ_{max} and the narrow shape of the SPR peak (**Figure S 4 B**).

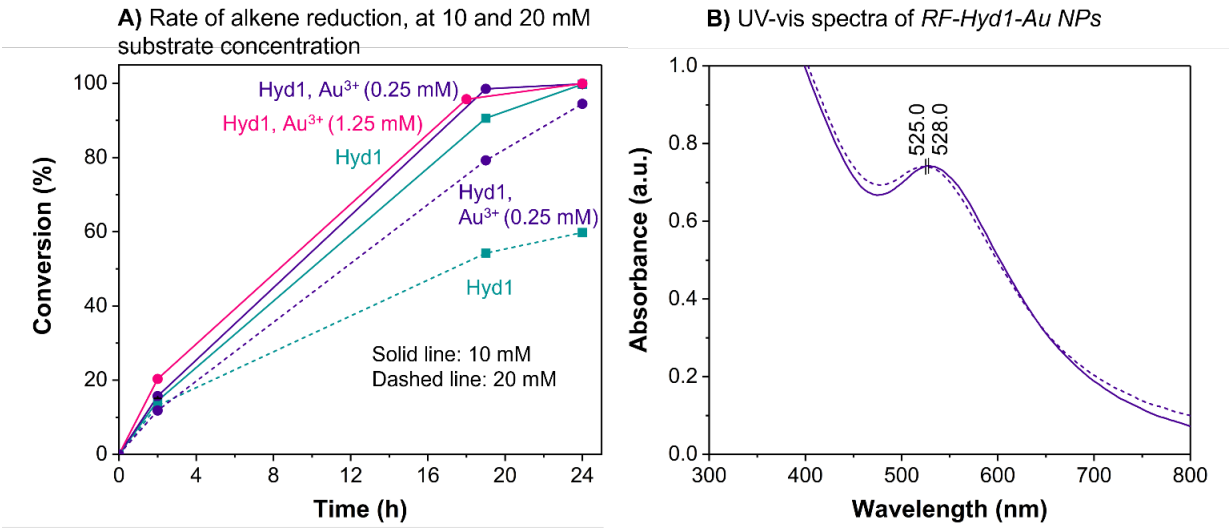


Figure S 4. Comparison of effect of conditions used on the rate of alkene reduction of 4-phenyl-3-buten-2-one substrate. Reaction conditions: RF (0.2 mM), Hyd1 (0.5 mg mL^{-1}), $HAuCl_4$ (0.25 mM or 1.25 mM), ENE-108 (5 or 10 mg mL^{-1} for 10 or 20 mM substrate concentration respectively), 4-phenyl-3-buten-2-one (10 or 20 mM), DMSO (1 vol%), pH 7, 50 mM potassium phosphate, H_2, 25 °C. See **0** for reaction procedures. Conversion time points for conditions using Hyd1 and 10 mM substrate concentration are averages from triplicate experiments where standard deviations are ± <1.

S.2.5 Investigating Riboflavin Reduction Rate for Hyd1-Au NPs with Extra Hyd1 Added

The effect of a higher concentration of Hyd1 molecules on the surface of Au NPs was tested, using Au NPs prepared under the same conditions (so they have the same size/morphology) and with adding extra Hyd1 after the Au NP synthesis. The rate of RF reduction was therefore tested for these samples after the extra Hyd1 had 16 h to incubate with the already-prepared Au NPs (in the form of *RF-Hyd1-Au NPs*). The rate of RF reduction was also tested for samples with no Au but with the same concentration of Hyd1 (incubated in solutions of RF). The rate of the decrease in absorbance at 444 nm (corresponding to RF reduction) was significantly faster for the sample of *RF-Hyd1-Au NPs* where no extra Hyd1 was added (**Figure S 5 A**) than the samples where an extra 0.1 or 0.2 mg mL^{-1} Hyd1 was added (the concentration of

Hyd1 in the Au NP synthesis step was 0.1 mg mL^{-1}). The resulting TOF for *RF-Hyd1-Au NPs* with no extra Hyd1 was approximately 7x higher than the next fastest, *RF-Hyd1-Au NPs* with 0.1 mg mL^{-1} Hyd1 added (**Figure S 5 B**). The TOF became almost the same as the sample without Au (at the same Hyd1 concentration) when 0.2 mg mL^{-1} Hyd1 was added thus suggesting at this concentration the Au NP surface was fully covered by Hyd1.

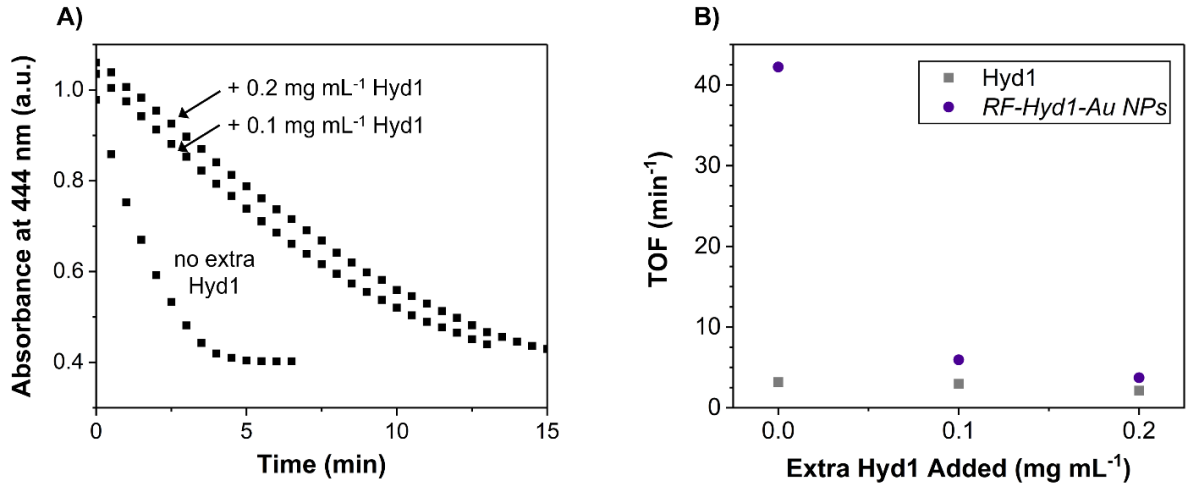


Figure S 5. Results measured from UV-vis assays of RF reduction using Hyd1 or *RF-Hyd1-Au NPs* which had then been incubated with extra Hyd1 for 16 h (using standard procedure as described in **S.1.4** for carrying out the assays). **A)** Absorbance rates for the decrease in absorbance at 444 nm corresponding to the reduction of RF for a sample of *RF-Hyd1-Au NPs* which either had no extra Hyd1 added, 0.1 or 0.2 mg mL^{-1} Hyd1. **B)** The results from the UV-vis assays displayed as the TOF (mole of RF per mole of Hyd1 per minute) calculated using the final concentration of Hyd1 in the assay (i.e. summing initial and extra amount added).

S.2.6 Riboflavin Effect on Rate of Au NP Formation with Hyd1

Monitoring the rate of Au NP formation was carried out by recording UV-vis spectra of solutions containing different reagents at time points throughout a reaction (**Figure S 6**). The initial spectra ("0 h") was recorded after all reagents were added. In the case of the solution containing Hyd1, RF, Au^{3+} and H_2 (**A**) the initial spectra already indicated Au NPs were formed; therefore, these were made in approximately 10 minutes. The spectra at later time points showed the RF was reduced (before the 2.5 h time point) and with no significant further increase in the SPR peak absorbance suggesting the NP formation was mostly complete by the initial time point. In comparison, for the solution with the same conditions but without RF

(**B**), no significant NP formation was seen until the 2.5 h time point and it required at least 5.5 h for the NP formation to be mostly complete (probably requiring a few more hours, i.e. 8 h total, for NP formation to stop). In the case of the control without Hyd1 (**C**), the NP formation rate is slower than in the presence of both Hyd1 and RF (**A**), with it requiring between 2.5 to 5.5 hours for complete NP formation. Up to this time it does not appear that RF has been reduced at all however beyond this time (when the NPs formation has stopped), it does appear that some RF reduction may have occurred (with the RF absorbance peaks being lower at the 20 h time point). The control with only RF under H_2 (**D**) shows that over time the RF absorbance peaks get smaller but have not decreased as much as in **C**, thus the decrease in **C** must relate to some reduction of RF. However, this reduction rate is very slow and therefore not useful as a RF recycling catalyst in combination with an ene-reductase for an alkene reduction; these *RF-Au NPs* gave negligible product formation when tested alongside *RF-Hyd1-Au NPs* and *Hyd1-Au NPs* (results discussed in main text and shown in **Figure 3 B**).

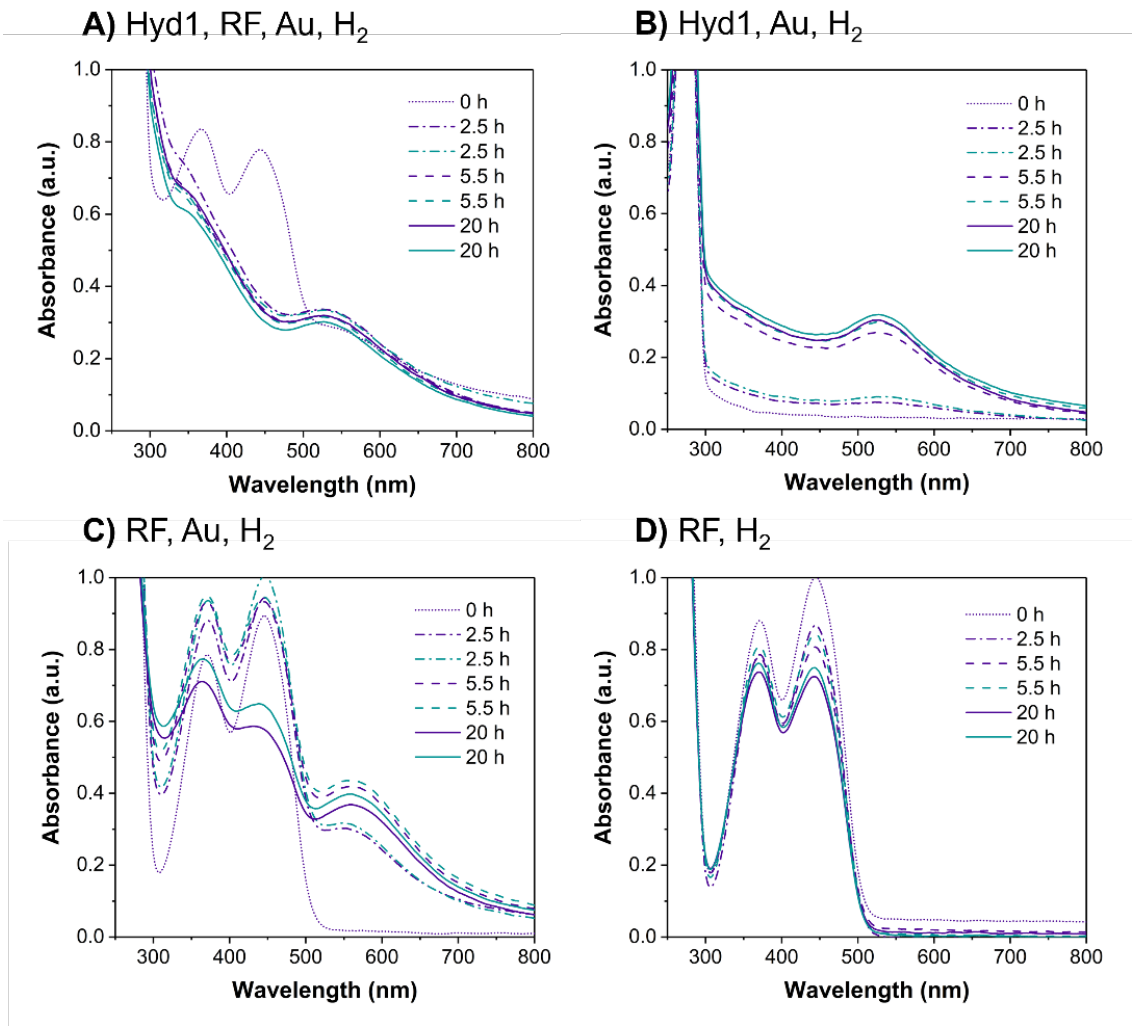


Figure S 6. Comparison of Au NP formation rate under different conditions, showing UV-vis spectra recorded at different time points (times are ± 30 mins) during the reaction (with reactions carried out in duplicates). All solutions of RF, or pH 7, 50 mM potassium phosphate buffer in the case of **B,** were sparged with H_2 before being added to other reagents. Hyd1 was also "pre-activated" under H_2 before use (under 1 bar H_2 for 16-18 h).

S.2.7 Estimating Gold NP Size from UV-vis

The wavelength of the maxima of the surface plasmon resonance peak (λ_{max}) is often used as indication of the average NP size, with the broadness of the peak reflecting the NP uniformity (i.e. a broader peak has a large range in sizes of NPs). However, as the average NP size decreases, the environment around the NP becomes a more influential effect and thus using the λ_{max} alone would not give an accurate estimation of NP size. An improvement for estimating the NP size is described by W. Haiss et. al. and uses the absorbance at the surface plasmon resonance peak (A_{SPR}) and divides this by the absorbance at 450 nm (A_{450}).[3] The resulting ratio number is then used to estimate the average NP diameter using the equation:

$$d = exp\left(B_1 \frac{A_{SPR}}{A_{450}} - B_2\right)$$

where the experimentally determined fit parameters, B_1 = 3.00 and B_2 = 2.20 can be used. The authors determine there to be an approximately 11% standard deviation with this calculation method and do warn that it becomes less accurate for smaller NPs (< 10 nm). Thus, for these results, shown in **Table S 5**, where the NPs are calculated to be in the < 10 nm range these should be considered an estimation. TEM analysis is also used to confirm that this is a suitable estimate to make. NPs below 2 nm become difficult to estimate their size since this is around the limit for NPs to give an absorbance in the UV-vis.[5]

Table S 5. Analysis of the average Au NP size estimated from UV-vis spectra of duplicate reactions (using just Hyd1 and H_2, no RF present) shown in **Figure S 6**.

Entry	λ_{max} (nm)	A_{SPR} (a.u.)	A_{450} (a.u.)	A_{SPR} / A_{450}	d (nm)
1	527.0	0.303905	0.247938	1.225727	4.38 ± 0.48
2	527.0	0.319435	0.264433	1.207999	4.15 ± 0.46

S.2.8 TEM Analysis of Gold NPs

TEM was used to compare the size and shapes of the Au NPs made in the presence and absence of Hyd1 and RF. Images from the same magnification of the 3 types of Au NPs (**Figure S 7**) suggest that the *RF-Hyd1-Au NPs* are the smallest on average, with spherical or slightly elliptical shapes while the *Hyd1-Au NPs* appear to be slightly larger, also with spherical or slightly elliptical shapes. Whereas the *RF-Au NPs* are significantly larger with some more triangular and elliptical NPs.

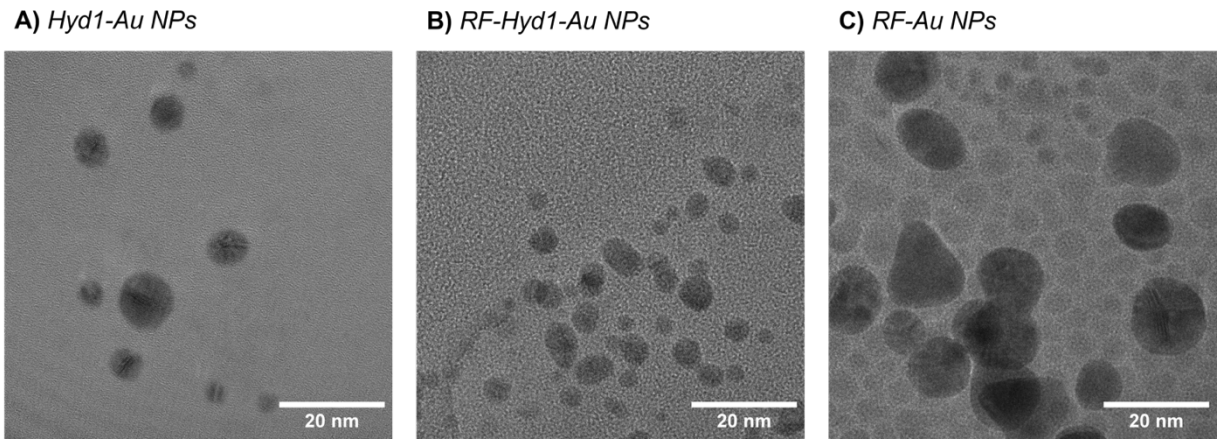


Figure S 7. TEM images all at 50 k magnification of samples of Au NPs made under the same conditions, testing the effect of the presence of Hyd1 and RF.

More TEM images were analysed to obtain an estimated average NP size and size distribution. For the sample of *Hyd1-Au NPs* these were generally quite sparse on the grid thus 3 images were combined to obtain a size distribution from analysis of 70 NPs (**Figure S 8**). Any overlapping NPs were excluded from the analysis leaving behind the NPs which had clearly defined edges as shown in **D** and **E**. For the sample of *RF-Hyd1-Au NPs* there appeared to be a much greater number of NPs on the grid therefore 603 NPs, from 2 images, were included in the size analysis (**Figure S 9**). Finally for *RF-Au NPs* the analysis was difficult because there appeared to be layers of NPs on top of each other and there were a lot of overlapping NPs (**Figure S 10**). The size distribution curve was made from measuring only 12 NPs therefore should not be interpreted as highly accurate. Overall, the TEM analysis can be summarized as *RF-Hyd1-Au NPs* having an average size of 4.0 ± 2.1 nm, *Hyd1-Au NPs* having an average size of 6.5 ± 2.5 nm and *RF-Au NPs* with an estimated average size of 14.1 ± 0.3 nm (from high to low accuracy).

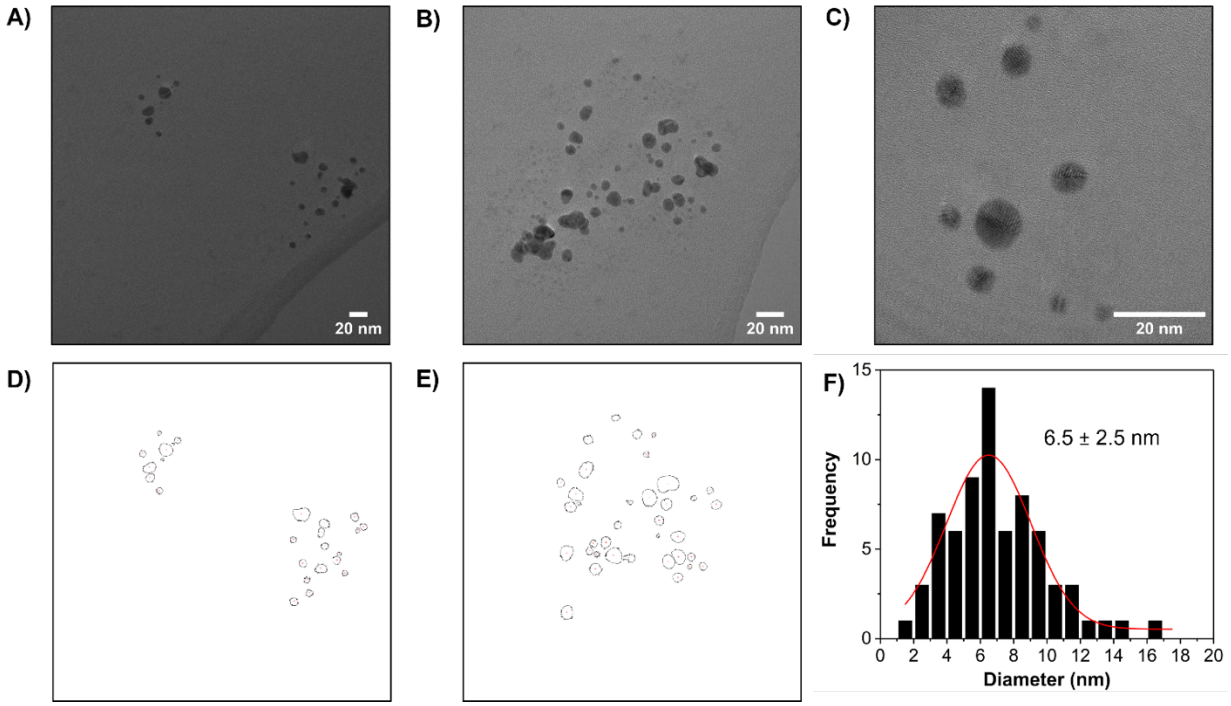


Figure S 8. TEM size analysis for a *Hyd1-Au NP* sample. TEM images **A**, **B**, **C** (10 k, 15 k and 50 k magnification respectively), were used for the analysis which was done using ImageJ to detect the NP sizes as shown in **D** and **E** to calculate the size distribution as shown in **F** (Gaussian fit curve in red).

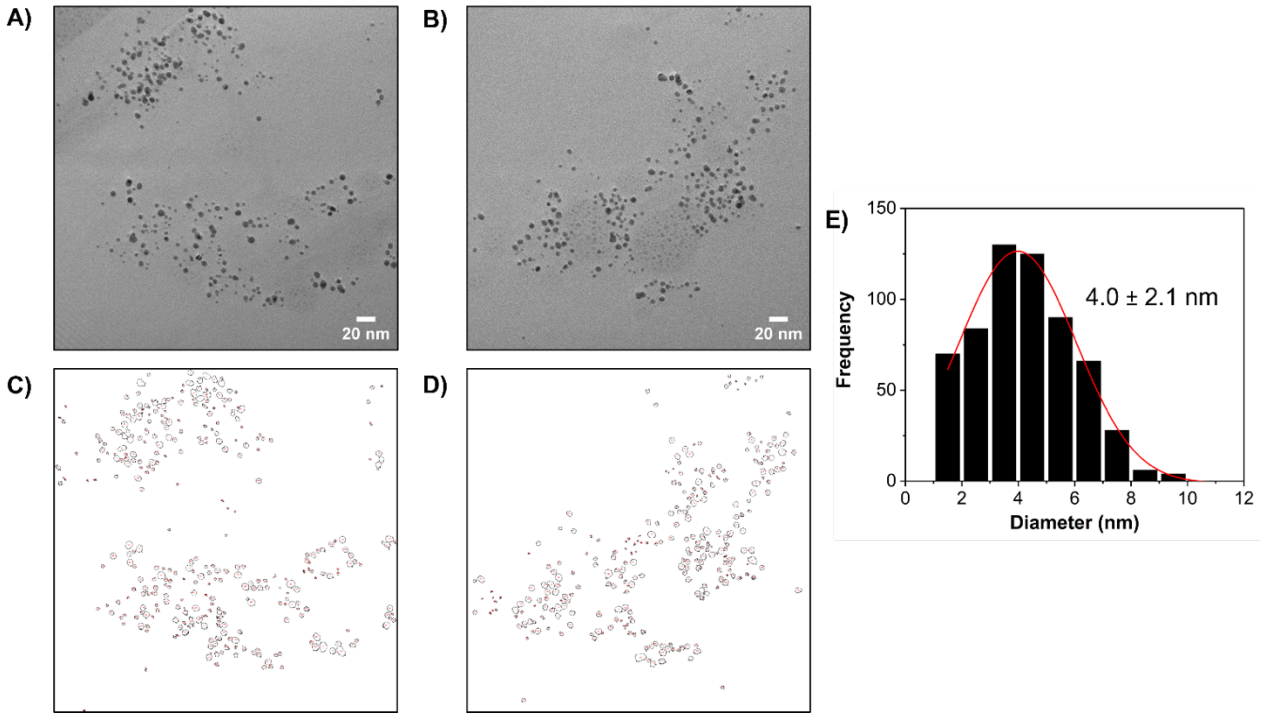


Figure S 9. TEM size analysis for a *RF-Hyd1-Au NP* sample. TEM images **A** and **B** (10 k magnification) were used for the analysis which was done using ImageJ to detect the NP sizes as shown in **C** and **D** to calculate the size distribution as shown in **E** (Gaussian fit curve in red).

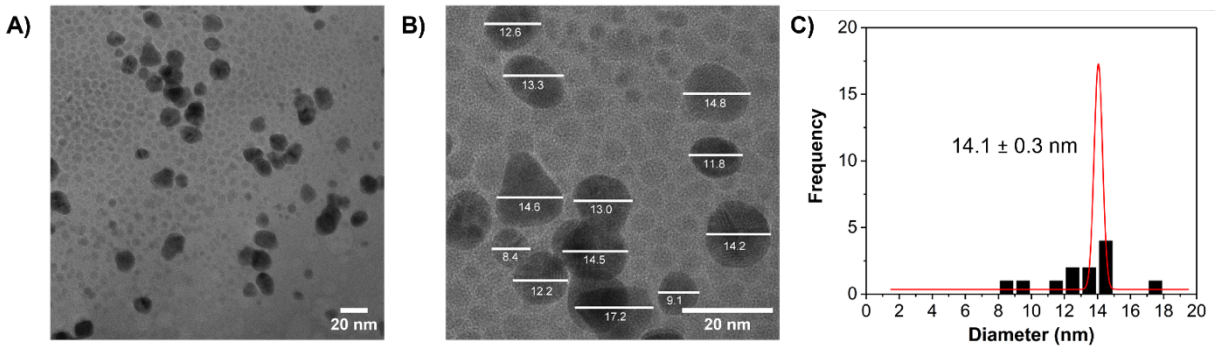


Figure S 10. TEM size analysis for a *RF-Au NP* sample. **A** shows a TEM image (15 k magnification) where there are many overlapping NPs. **B** shows a TEM image (50 k magnification) which was used to measure the NP diameters and **C** shows the size distribution of these NPs (Gaussian fit curve in red) – only 12 individual NPs therefore should only be used as a demonstration of the types of NP sizes made using only RF under H_2 (not an accurate size distribution of the whole sample).

S.2.9 DLS and Zeta Potential Analysis

To further characterize the NPs, DLS and zeta potential analysis was carried out (**Figure S 11** and **Table S 6**). The Hyd1 batch that was used for the synthesis of *Hyd1-Au NPs* and *RF-Hyd1-Au NPs* was also analysed. The mass equivalent spherical diameter of this Hyd1 (using molecular weight of dimeric protein: 214.29 kDa) can be calculated as 7.8 nm.[6] The hydrodynamic diameter measured was almost double that (14.4 ± 2.4 nm) indicating a large layer of surrounding buffer/detergent molecules. The *Hyd1-Au NPs* were measured to have an average hydrodynamic diameter of 18.6 ± 2.4 nm and the *RF-Hyd1-Au NPs* as 22.6 ± 5.5 nm. These samples had been analysed by TEM thus subtracting the size of the Au NP cores leaves an outer layer of sizes 12.1 ± 2.2 nm and 18.6 ± 2.8 nm for the *Hyd1-Au NPs* and *RF-Hyd1-Au NPs* respectively. To have a complete layer of Hyd1 surrounding the NPs this layer would need to be a minimum of 15.6 nm in size (but most likely higher due to other interacting molecules around). Thus, particularly in the case of the *Hyd1-Au NPs*, it seems likely that there is an incomplete "shell" of Hyd1 around the metal NPs. The calculations in **Table S 3** also add to this claim, since based on the number of Hyd1 molecules that are present in the solution of *Hyd1-Au NPs* (of 6.5 ± 2.5 nm size), if they are spread equally between the Au NPs, the percentage of the surface of the NPs covered by Hyd1 will be between 27-60%.

The zeta potential analysis of these samples revealed the *Hyd1-Au NPs* to have a slightly lower zeta potential than the *RF-Hyd1-Au NPs*, thus indicating higher stability.

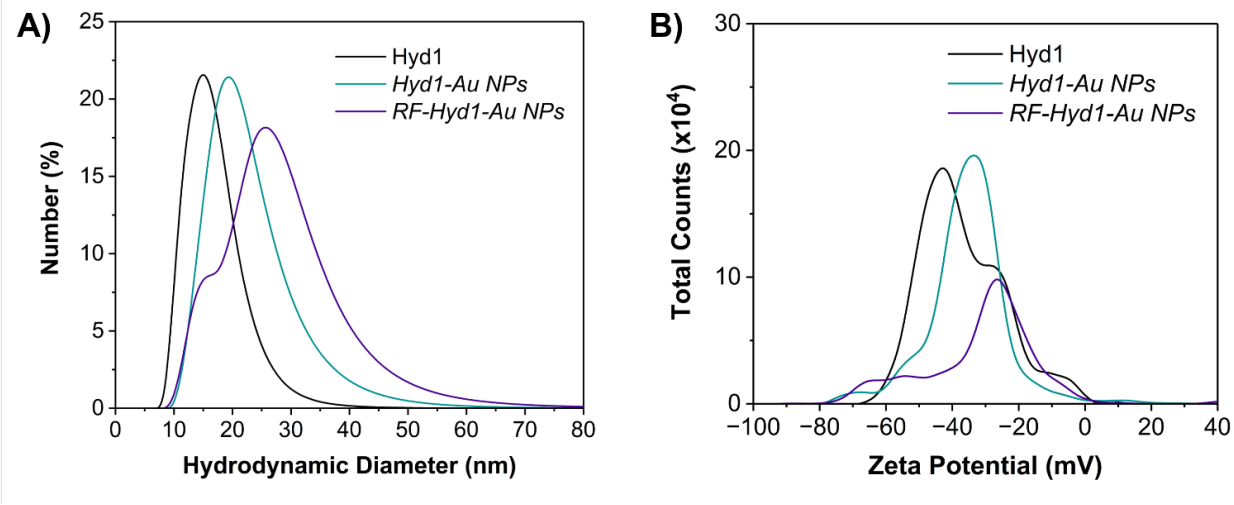


Figure S 11. Hydrodynamic diameters and zeta potentials of Hyd1, *Hyd1-Au NPs* and *RF-Hyd1-Au NPs*. **A**) Averaged hydrodynamic spectra of 5-6 scans. **B**) Averaged zeta potential spectra of 5-6 scans (all carried out at pH 7).

Table S 6. Summary of NP characterisation from UV-vis, TEM and DLS/Zetasizer.

Entry	NP Type	Average Au NP Size, nm (from UV-vis)	Average Au NP Size, nm (from TEM)	Hydrodynamic Diameter, nm (from DLS)	Zeta Potential, mV (from Zetasizer)
1	*RF-Hyd1-Au NPs*	n/a[a]	4.0 ± 2.1	22.6 ± 5.5	-27 ± 4
2	*Hyd1-Au NPs*	4.7 ± 0.5	6.5 ± 2.5	18.6 ± 2.4	-34 ± 4
3	*RF-Au NPs*	n/a	14.1 ± 0.3[b]	>100[c]	n/a

[a] Cannot estimate an average NP size due to the absorbance from RF around 450 nm however the SPR λ_{max} is at 518 nm for this sample which is lower than was measured for sample no. 2 which had a SPR λ_{max} at 531 nm. Therefore, indicating these NPs will be smaller than those in no. 2. [b] Only an estimate since too few NPs analysed. [c] Very large sizes measured but sample quickly formed large agglomerates therefore not stable under DLS conditions.

S.2.10 Controls for Au NP Formation

A number of controls were carried out where reagents were excluded from reaction conditions. The UV-vis spectra recorded for these are shown in **Figure S 12** with the conditions and results in **Table S 7**. NPs were therefore only observed in the experiments which contained Hyd1 and H_2, or RF and H_2 (entries 1, 2 and 4). Complete reduction of RF was only observed in the presence of Hyd1 and H_2 (entries 1 and 7). Therefore, despite there being Au NP formation in the presence of RF and H_2, Au NPs alone cannot reduce RF (or at least not under the same conditions and time frame as in the presence of Hyd1).

Table S 7. Summary of control experiments carried out.

Entry	$HAuCl_4$	RF	Hyd1	H_2	Au NPs?[a]	Complete reduction of RF?[b]
1	+	+	+	+	✓	✓
2	+	+	-	+	✓	×
3	+	+	-	-	×	×
4	+	-	+	+	✓	n/a
5	+	-	-	+	×	n/a
6	+	+	+[c]	+	×	×
7	-	+	+	+	n/a	✓

+ indicates presences, - indicates absence of reagent. [a] The presence of Au NPs was detected using UV-vis by a SPR peak in the 500-800 nm region (✓or × for whether this peak was observed). [b] Complete reduction of RF was monitored by the decrease of two peaks at 370 and 445 nm in the UV-vis spectra. [c] This Hyd1 was boiled before use (to heat-denature).

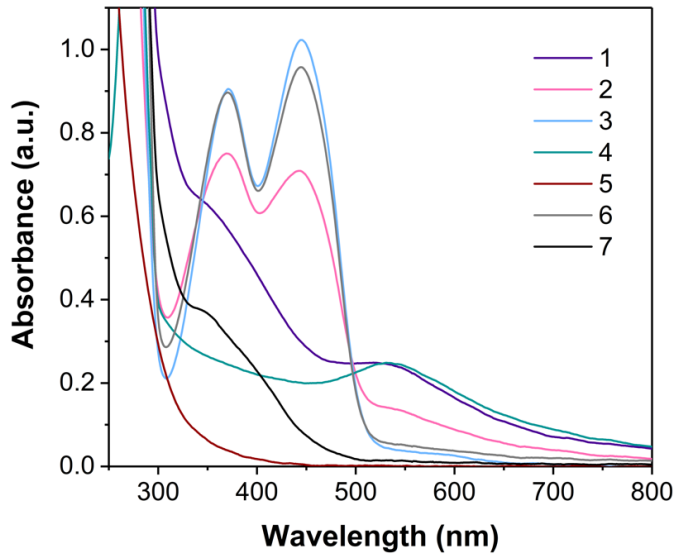


Figure S 12. UV-vis spectra of controls, with numbers referring to entries in **Table S 7**. All spectra recorded after 17-20 h.

S.2.11 Example GC Data

GC analysis was used to calculate reaction conversion, which was also used for calculating TOF, TTN and TN. Starting material and product standards as well as some example reaction GC traces are shown in **Figure S 13** for the alkene reduction of 4-phenyl-3-buten-2-one.

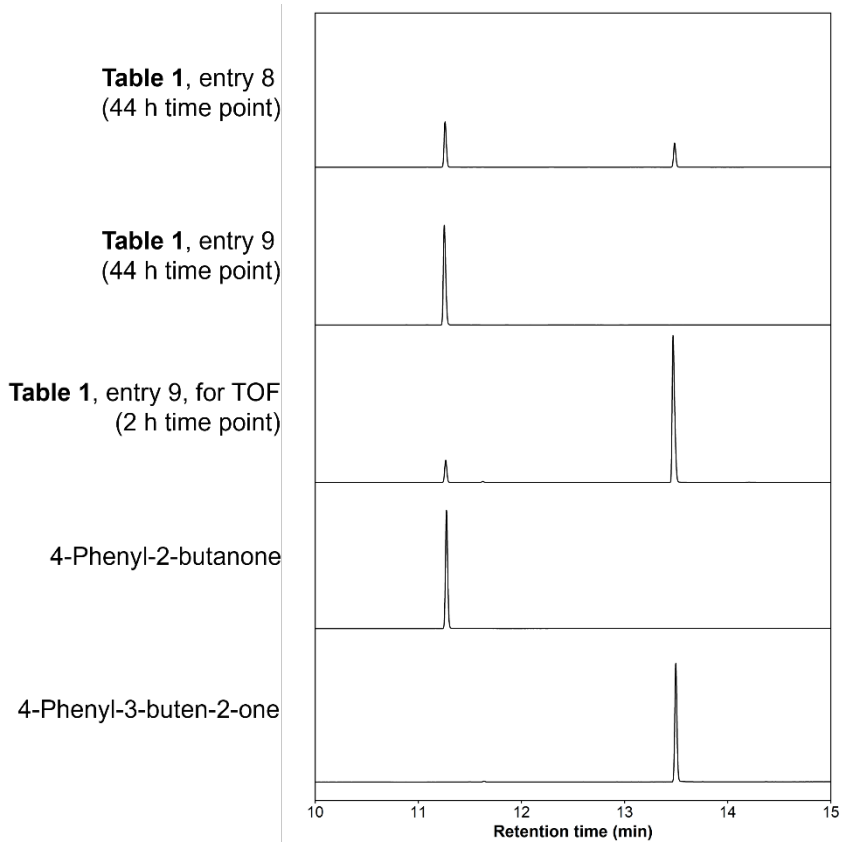


Figure S 13. Examples of GC results from reactions in **Table 1** of main text with the starting material and product standards. Standard for 4-phenyl-3-buten-2-one (available as 99% purity) and 4-phenyl-2-butanone (available as 98% purity) were purchased from Sigma Aldrich and diluted in ethyl acetate before injection.

For the alkene reduction of dimethyl itaconate, the product is chiral. The two enantiomers of the product are able to be separated on the chiral-GC column used (see **S.1.9** for details) as shown in **Figure S 14**. In all reaction samples, the reaction appeared to give >99% e.e. of the (*R*)-enantiomer as shown in the examples in **Figure S 14**.

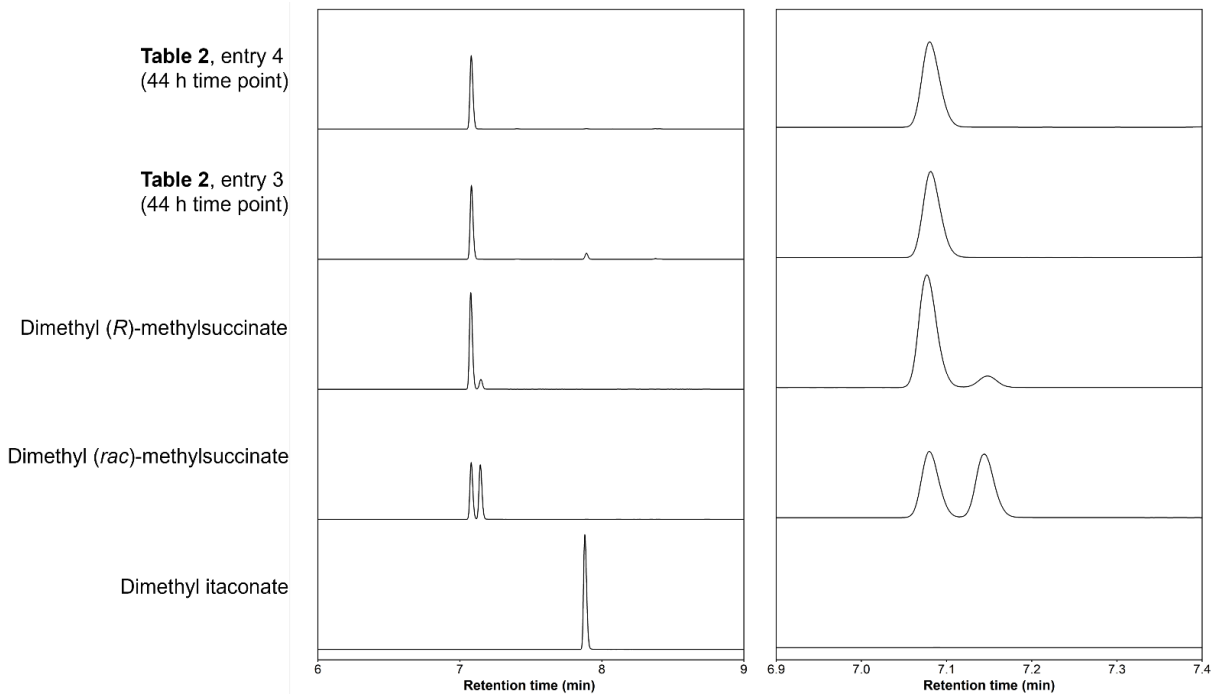


Figure S 14. Examples of chiral-GC results from reactions in **Table 2** of main text with the starting material and product standards. Standard for dimethyl itaconate (available as 98% purity), dimethyl (*rac*)-methylsuccinate (available as 98% purity) and dimethyl (*R*)-(+)-methylsuccinate (available as 99% purity) were purchased from Fluorochem, Sigma Aldrich and ChemCruz respectively and diluted in ethyl acetate before injection.

S.3 References

[1] W. Holzer, J. Shirdel, P. Zirak, A. Penzkofer, P. Hegemann, R. Deutzmann, E. Hochmuth, *Chem. Phys.* **2005**, *308*, 69-78.
[2] M. A. Ramirez, S. Joseph Srinivasan, S. E. Cleary, P. M. T. Todd, H. A. Reeve, K. A. Vincent, *Frontiers in Catalysis* **2022**, *2*.
[3] W. Haiss, N. T. K. Thanh, J. Aveyard, D. G. Fernig, *Anal. Chem.* **2007**, *79*, 4215-4221.
[4] C. C. Page, C. C. Moser, X. Chen, P. L. Dutton, *Nature* **1999**, *402*, 47-52.
[5] V. Amendola, R. Pilot, M. Frasconi, O. M. Maragò, M. A. Iatì, *J. Phys.: Condens. Matter* **2017**, *29*, 203002.
[6] E. Buxbaum, in *Biophysical Chemistry of Proteins: An Introduction to Laboratory Methods* (Ed.: E. Buxbaum), Springer US, Boston, MA, **2011**, pp. 237-249.

Chapter 6. Biocatalytic Synthesis of Supported Metal NPs and their Potential Applications

6.1. Introduction

In contrast to the previous chapters, this chapter discusses the synthesis and potential applications of metal NPs on a heterogeneous support. These can be thought as more akin to the types of heterogeneous catalysts, such as palladium on carbon (Pd/C), that are used in large-scale industrial chemical manufacturing. The inherent advantages of these types of catalysts are their ease of separation from reaction products and for catalyst recycling. They also provide an easier transition from a batch to a "flow" process – where liquid/gas reagents can be passed through a solid catalyst. A continuous flow process can also link multiple supported catalysts together therefore creating a cascade where individual intermediates do not need to be isolated.[1] There are however downsides which can be experienced with using a supported catalyst, especially when integrating enzymes since these can often exhibit a loss in activity when immobilised onto a support or enzyme leaching issues can arise.[1] Despite this, it is still considered worth investigating due to the advantageous recycling properties, potential improvements in long-term enzyme stability,[2] as well as even potentially providing new reactivities: this was revealed in other research carried out in the Vincent group where immobilising Hyd1 onto a carbon support allowed this catalyst to reduce nitro groups of various substrates, to amines (in contrast to Hyd1 in the absence of any support which gave no activity).[3] The general strategy used here was to firstly immobilise the enzyme onto the support, then to carry out the metal reduction, aiming to synthesise enzyme-directed, uniform metal NPs that are anchored onto the support.

6.2. Synthesis of Supported Metal NPs

6.2.1. Initial Work

This work was mostly carried out by Hazel Rycroft, a master's student in the group, whose project I helped to supervise. Her project began with investigating supporting Hyd1 onto C_{60}, where C_{60} would act as a molecular support on which planar substrates present in reaction

mixture may be less likely to adsorb to than larger carbon particle-based supports. A C_{60} molecule is 0.70 ± 0.05 nm in diameter[4] while the average "BP2000" (Black Pearls® 2000, by Cabot) particle – commercial, commonly-used, spherical carbon particles – is 13-16 nm in diameter.[5] Unfortunately, it appeared that the process of attempting to immobilise Hyd1 onto C_{60} in an aqueous solution was detrimental to the activity of Hyd1. However interestingly if the C_{60} was firstly sonicated in isopropanol instead of water, before adding the Hyd1 to adsorb, the Hyd1 retained its activity. In this case the resulting hybrid catalyst is made up in 40 vol% isopropanol (60 vol% water). Despite the activity retention of Hyd1, this amount of solvent may cause a loss in activity of other enzymes which this system would be desired to be coupled with, e.g. ene-reductases which require a flavin cofactor recycling system which Hyd1 has been shown to be able to provide.[6] However the vol% of isopropanol was not fully investigated nor was a screening of other solvent systems therefore there is still promise that Hyd1 immobilised on C_{60} could be an effective support for use in biocatalytic processes.

Hazel's project then moved onto immobilising Hyd1 onto BP2000. This has been a well-used strategy by others in the group to achieve the immobilisation of multiple enzymes on a conductive support, e.g. where electrons from the oxidation of H_2 by Hyd1 can be passed through the support and to a second enzyme such as an NAD^+ reductase that can use the electrons for the reduction of NAD^+ to NADH which is then used by a third enzyme such as an alcohol dehydrogenase for an enantioselective ketone reduction.[7] Following the same principle it was hypothesised that metals (with positive enough reduction potential) would be able to be reduced by the electrons passed through the support, leading to the formation of NPs on the support. This was tested for Au and Cu.

6.2.2. General Procedure for Synthesis of Supported NPs

Firstly, a suspension of BP2000 (20 mg mL^{-1}) in water or buffer was sonicated for 1 hour, to break up any aggregated particles and allow maximum surface area. Then Hyd1 was immobilised onto BP2000 by adding the desired amount of BP2000 suspension into plastic tubes already containing Hyd1 solutions, mixing, and then allowing the Hyd1 to adsorb onto

the BP2000 while leaving on an ice-block, for 1 hour. After this the samples were centrifuged (at 12,000 rpm for 3 minutes), the supernatants were removed, and the carbon material was resuspended in water or buffer. Metal salts were dissolved in water and adjusted to pH 8 with 3 M NaOH. Then the metal salt solutions were added, mixing thoroughly after the addition, before the samples were added to a pressure vessel which was then put under 1 bar H_2 and left for 18 hours. After which time, the samples were centrifuged (at 12,000 rpm for 3 minutes), supernatant removed, and the carbon material was resuspended in water or buffer (this step was repeated 3 times to remove any excess metal salts).

Since carbon particles have a strong absorbance, UV-vis spectroscopy cannot be used to determine if NPs are formed; instead, CV, XRD, XPS and TEM analysis were used.

6.2.3. Analysis of Au Supported NPs

For Au, the successful synthesis of Au NPs using Hyd1 and H_2, without carbon, had already been demonstrated (as discussed in *Chapter 5*), therefore it would have been unexpected if NPs were not formed. However, it was also interesting to investigate whether the presence of the support had any effect on the size and shapes of the NPs which formed.

After following the procedure described in **6.2.2** where a solution of $HAuCl_4$ was added to the immobilised Hyd1 on BP2000, using Hyd1: Au^{3+} ratios of 1: 50 and 1: 500, the resulting material was tested by CV. Alongside the synthesis involving Hyd1, controls without Hyd1 were also tested (i.e. Au^{3+} was added to BP2000, under H_2). Thus, the CV scans for material with and without Hyd1 were compared (**Figure 6. 1. A**, before sonicating scans). These showed that in the presence of Hyd1 a significantly larger current was observed (for both concentrations of Au^{3+} tested) – at the potential for Au_2O_3 reduction, around +0.65 V vs SHE, (which forms during the oxidising direction of the CV scan).[8]

These samples were then sonicated, centrifuged and supernatant removed and retested by CV to test how well “stuck on” the Au was. At this stage it was not possible to determine if the Au was present as Au^0 or Au^{x+} ions therefore this would help to indicate whether Hyd1 had an

influence over the Au species present. The CVs for the sample with Hyd1 did not change after sonicating whereas there was complete loss of the Au reduction peak in the CV after sonicating the sample with BP2000 alone (**Figure 6. 1. A** compared to **B** respectively). This indicates Hyd1 has played a role in attaching Au to the surface (and is a promising sign for the robustness of the material, with no loss of Au after sonicating). To confirm the presence of Au NPs, XRD and TEM were subsequently used.

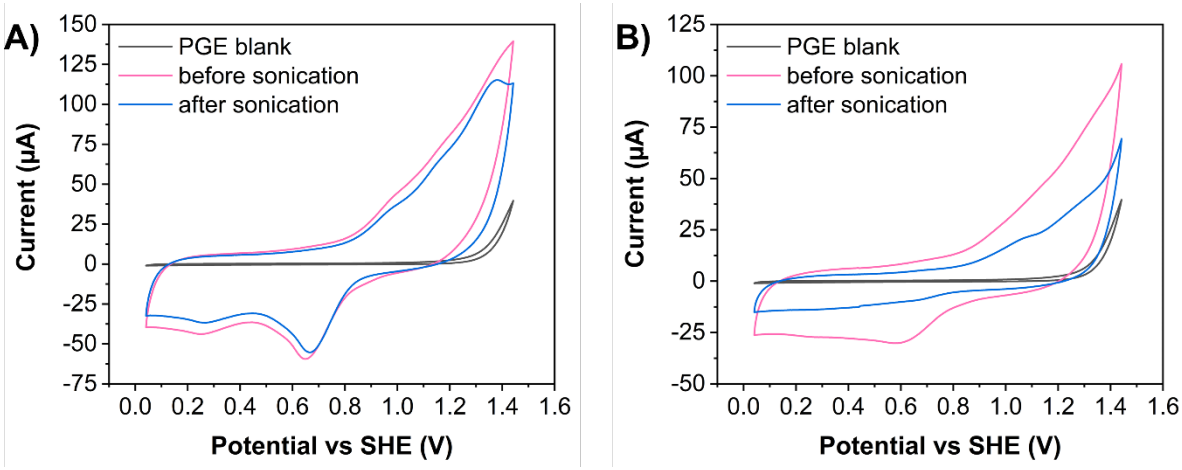


Figure 6. 1. CVs showing effect of sonicating samples prepared with Au^{3+} and BP2000, under H_2, with **A)** Hyd1 and **B)** no Hyd1. CVs recorded at pH 8 (50 mM Tris buffer), using a stationary graphite electrode, under a N_2 atmosphere, 25 °C, scan rate: 30 mV/s, scanning direction from high to low (and reverse), showing second scan of experiment.

The sample with Hyd1, showed the presence of crystalline Au in the XRD trace, compared to ICSD reference code: 01-071-4614 (**Figure 6. 2.**). The sample at the same concentration of Au^{3+} but with no Hyd1, showed significantly lower intensity of XRD reflections, thus indicating Hyd1 was able to reduce more Au than the conditions used without Hyd1.

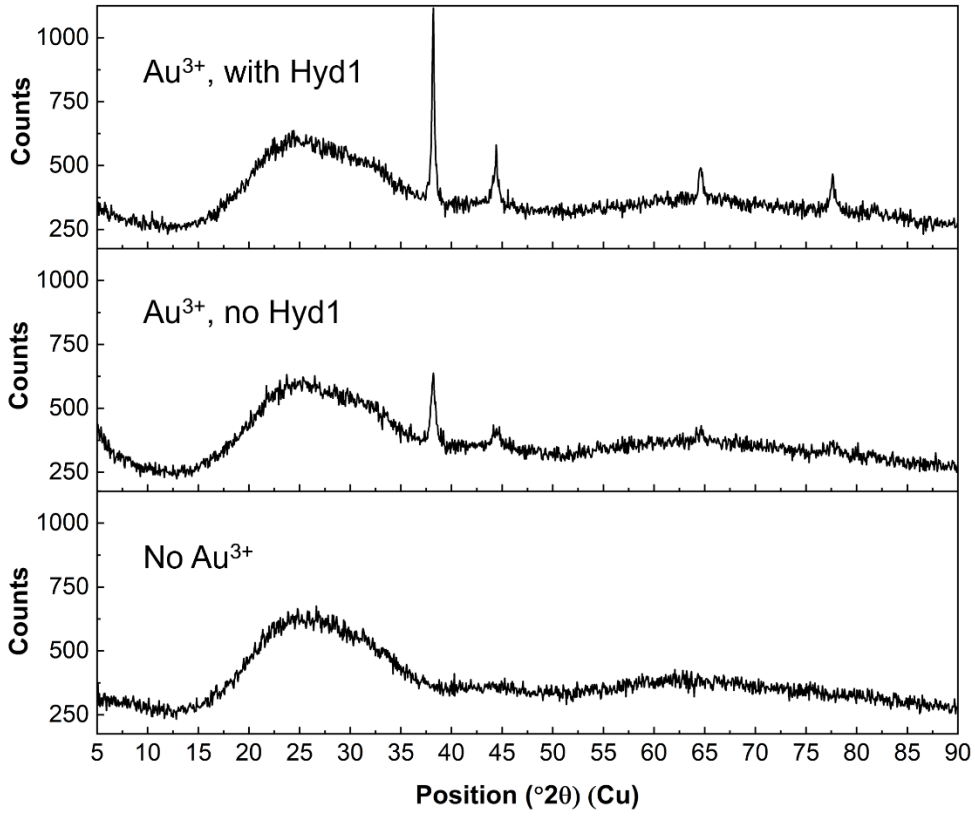


Figure 6. 2. XRD patterns for samples prepared using Au^{3+} on BP2000 in the absence and presence of Hyd1 and comparison of BP2000 with no Au^{3+}.

TEM then provided information on the nature of the Au^0 species present, i.e. whether Au^0 atoms were distributed throughout the samples or in the form of NPs. TEM was carried out for samples prepared under the four different conditions: two concentrations of Au^{3+} and in the absence and presence of Hyd1 (**Figure 6. 3.**). TEM images of samples using the highest initial concentration of Au^{3+} showed spherical NPs were present on the carbon surface in both the absence and presence of Hyd1. A significantly higher concentration of NPs was seen however for the sample with Hyd1 (corroborating with the CV and XRD analysis). The NPs were all quasi-spherical and under 10 nm in diameter, in the 3-10 nm size range. Similar sizes were seen in the comparison without Hyd1. For the samples using the lower initial concentration of Au^{3+} the number of NPs was, as expected, significantly lower but were similar in size to the highest Au^{3+} concentration samples.

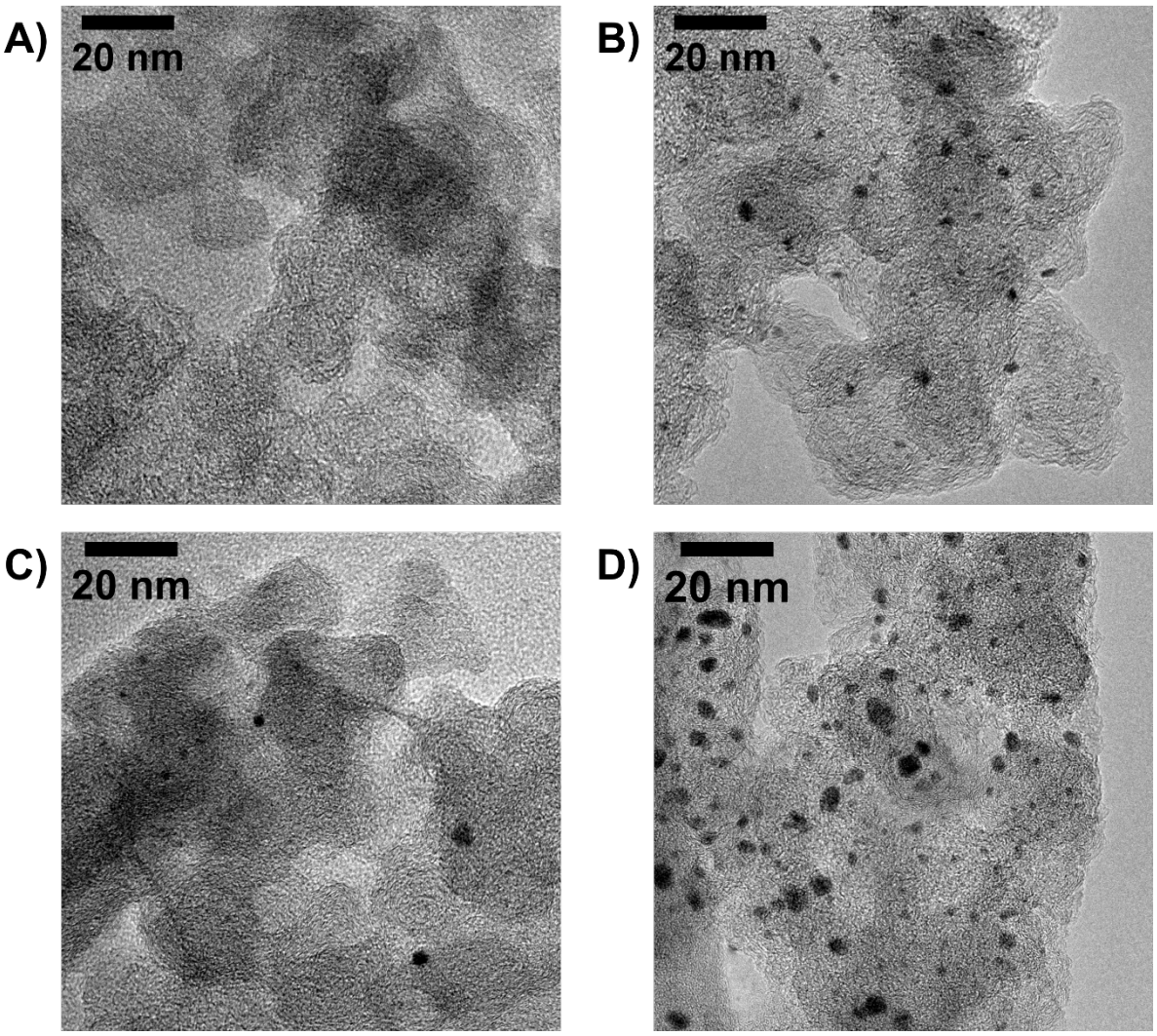


Figure 6. 3. TEM images for samples prepared using Au^{3+} on BP2000, with two different Au^{3+} concentrations, with **A)** no Hyd1 (same Au^{3+} concentration as in 1: 50), **B)** Hyd1, 1: 50, **C)** no Hyd1 (same Au^{3+} concentration as in 1: 500), **D)** Hyd1, 1: 500. TEM performed by Dr Michal Klosowski.

Thus, this analysis showed that Hyd1 immobilised onto BP2000 was able to catalyse the reduction of Au^{3+} to Au^0 and form well-dispersed small, quasi-spherical Au NPs which were stabilised onto the carbon support (these will be referred to as Hyd1-Au/C). The presence of the support did not appear to significantly alter the size or shape of the Au NPs by comparing to those formed by Hyd1 under H_2 without a support present (results from *Chapter 5*).

6.2.4. Analysis of Cu Supported NPs

In contrast to Au, attempts to synthesize Cu NPs using Hyd1 and H_2 (without any support present) had not been successful. Testing the activity of Hyd1 in the presence of $Cu(II)Cl_2$

found a correlation with increasing concentration of $Cu(II)Cl_2$ and decreasing activity. Thus, it appears Hyd1 is inhibited by Cu^{2+}. It has already been shown for another [NiFe] hydrogenase, from *Desulfovibrio gigas*, that Cu^{2+} (via reduction to Cu^{+}) causes destruction of the Fe-S clusters, as evidenced by a loss of signals in ESR spectra.[9] Thus it is unsurprising that this was also found for Hyd1. It was therefore wondered whether a carbon support would help to stop Hyd1 being inhibited by Cu^{2+} by allowing the Cu^{2+} to be reduced away from contact with the Fe-S clusters.

As was done for Au, two initial concentrations of Cu^{2+} were tested, each in the absence and presence of Hyd1 (again following the procedure described in **6.2.2**, with $CuCl_2$). The four different samples were then tested by CV (**Figure 6. 4.**). In all samples, two oxidation and corresponding reduction peaks were present matching with the Cu^{2+}/Cu^{+} and Cu^{2+}/Cu^{0} potentials. The ratios of these peaks gave some insight into the Cu species present in the samples. For the highest concentration of Cu sample with Hyd1, the Cu^{0} to Cu^{2+} oxidation peak was significantly larger than the Cu^{+} to Cu^{2+} peak (**Figure 6. 4. A**). Whereas for the sample with the same initial Cu^{2+} concentration without Hyd1, the Cu^{+} to Cu^{2+} peak was larger than the Cu^{0} to Cu^{2+} peak. At the lower initial Cu^{2+} concentration, the Cu^{+} to Cu^{2+} oxidation peak is non-existent in the sample with Hyd1, with only the oxidation peak corresponding to Cu^{0} present, whereas without Hyd1 the Cu^{+} to Cu^{2+} oxidation peak is still present (**Figure 6. 4. B**). This all gives evidence that Hyd1 has reduced a higher amount of Cu^{2+} to Cu^{0} than samples on just BP2000.

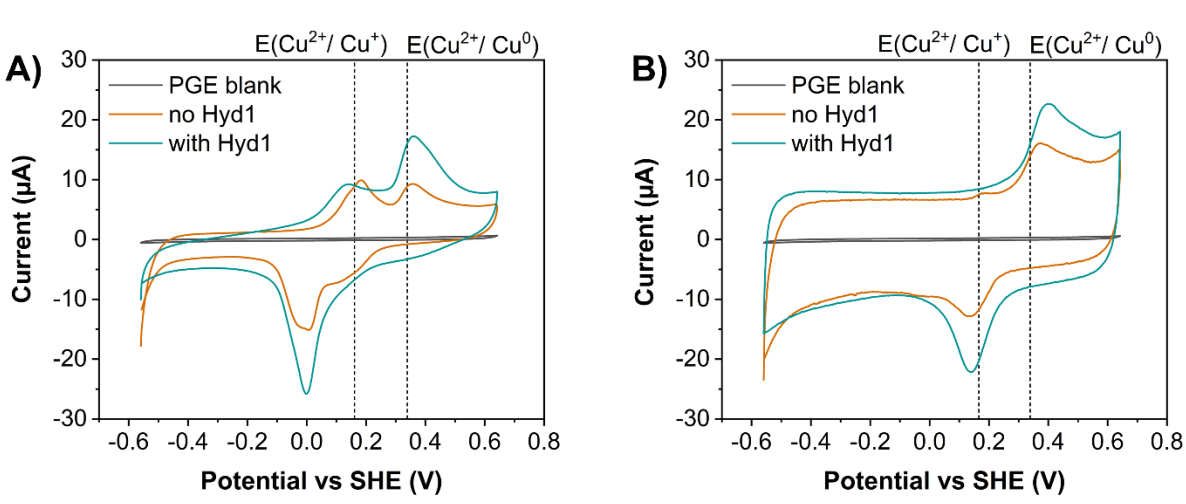


Figure 6. 4. CVs of samples prepared with Cu^{2+} and BP2000, under H_2, with and without Hyd1, at two different Cu^{2+} concentrations, where Hyd1: Cu^{2+} ratio was **A)** 1: 500, and **B)** 1: 50. CVs recorded at pH 7 (100 mM NaPi buffer), using a stationary graphite electrode, under a N_2 atmosphere, 25 °C, scan rate: 30 mV/s, scanning direction from high to low (and reverse), showing second scan of experiment.

Next, as was carried out for Au, the samples were sonicated, supernatant removed, and samples retested by CV. In this case changes in the ratio of the two oxidation peaks were compared before and after sonicating. The ratio of the peaks in the CV for the sample with Hyd1 remained unchanged after sonicating (**Figure 6. 5. A**), again suggesting Hyd1 is involved with stabilising the metal onto the carbon support. For the sample without Hyd1 the oxidation peak for the Cu^{+} ions was diminished, relative to the Cu^{0} peak, after sonicating (**Figure 6. 5. B**) which fits with the hypothesis that loosely bound ions would be more easily removed from the surface.

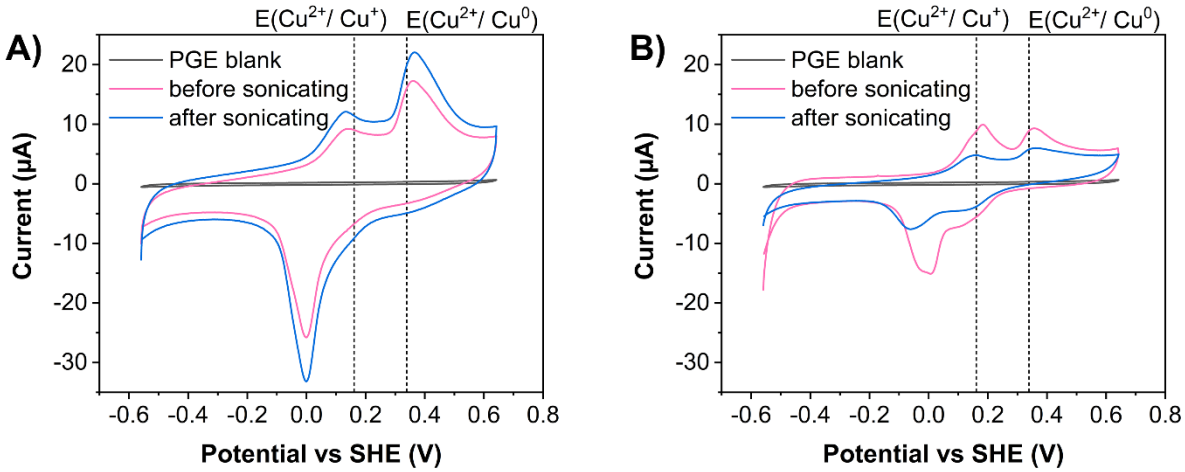


Figure 6. 5. CVs showing effect of sonicating samples prepared with Cu^{2+} and BP2000, under H_2, with **A)** Hyd1 and **B)** no Hyd1. CVs recorded at pH 7 (100 mM NaPi buffer), using a stationary graphite electrode, under a N_2 atmosphere, 25 °C, scan rate: 30 mV/s, scanning direction from high to low (and reverse), showing second scan of experiment.

These samples were then attempted to be analysed by XRD, however no XRD reflections were observed (either too low a concentration or too small sizes of crystalline material – reflections are too broad to be detected with NPs below 3 nm).[10] Therefore, XPS was used to determine the Cu content of the samples which had been sonicated before analysis. The results showed a higher concentration of Cu was found in the sample with Hyd1 (**Figure 6. 6. B** and **Table 6. 1.**), reflecting the results observed in the CV studies. Also, notably, the presence of nitrogen was detected in this sample (**Figure 6. 6. C** and **Table 6. 1.**), verifying that Hyd1 also remains attached to the carbon after sonicating.

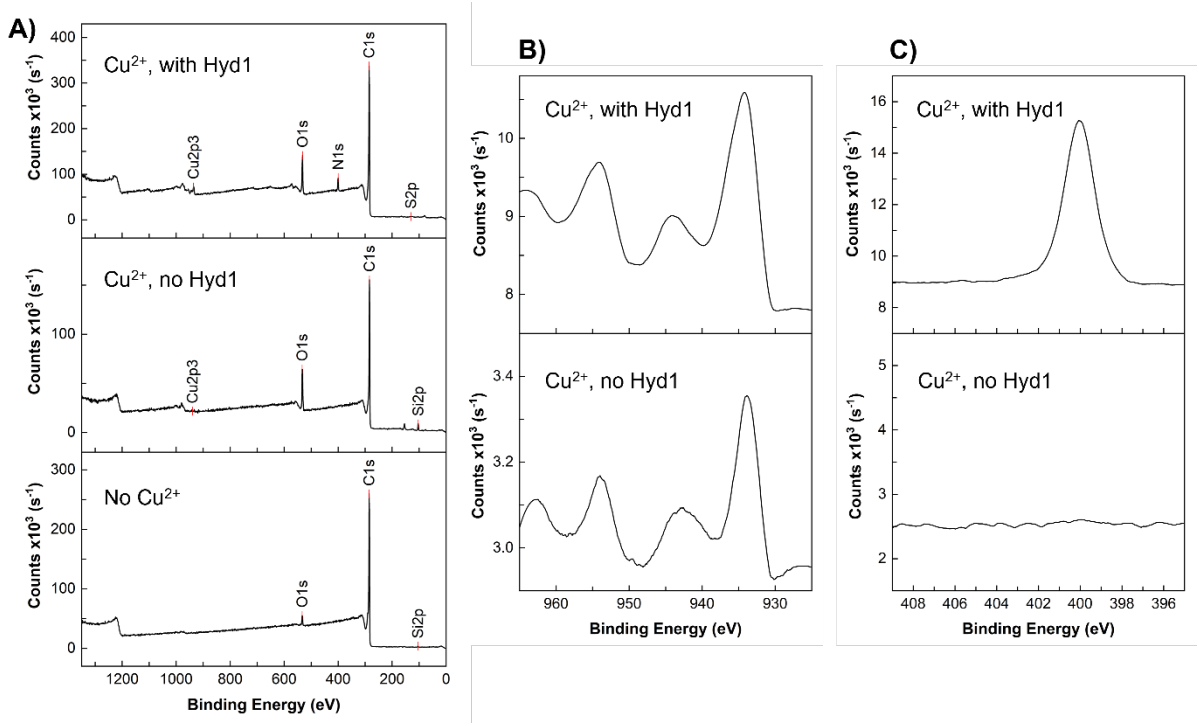


Figure 6. 6. XPS data for samples prepared using Cu^{2+} on BP2000 in the absence and presence of Hyd1 and comparison of BP2000 with no Cu^{2+}. **A)** XPS survey scans: 7 scans, 1 m 35.3 a, 200 µm, Constant Analyser Energy (CAE) 200.0, 1.00 eV. **B)** XPS Cu2p scans: 25 scans, 8 m 21.3 s, 200 µm, CAE 50.0, 0.10 eV. **C)** XPS N1s scan: 15 scans, 2 m 15.8 s, CAE 50.0, 0.10 eV.

Table 6. 1. Atomic percentage for samples prepared using Cu^{2+} on BP2000 in the absence and presence of Hyd1 (of samples using Hyd1: Cu^{2+} ratio of 1: 500) and comparison of BP2000 alone (no Cu^{2+}).[a]

Orbital	**Concentration (atomic %)**		
	No Cu^{2+}	**Cu^{2+}, no Hyd1**	**Cu^{2+}, with Hyd1**
C1s	96.9	84.8	85.1
O1s	2.6	11.2	9.3
N1s	0	0	4.4
S 2p	0.5	3.9	0.7
Cu2p3	0	0.1	1.0
S2p	0	0	0.2

[a] Samples were dropcast onto silicon wafers (hence the presence of Si in all results). XPS data were collected and analysed by Dr Phil Holdway.

Finally, TEM was carried out; for these Cu samples no NPs could be observed (**Figure 6. 7.**).

Therefore, despite the evidence for Cu^0 formation, from CV and XPS, the atoms must either

be individually scattered across the surface or in very small nanoclusters that are too small to detect by TEM (< 1 nm).

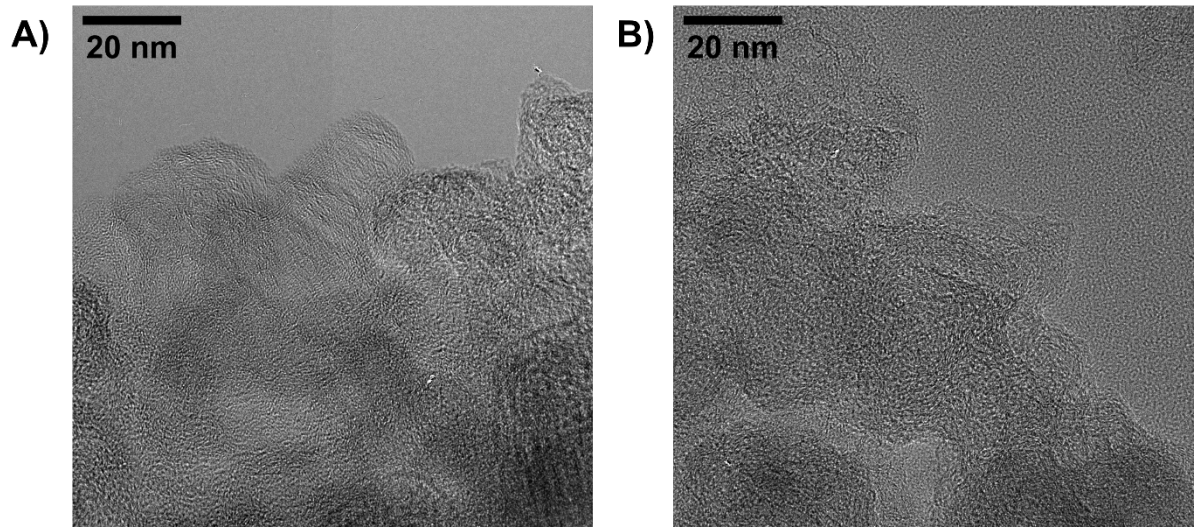


Figure 6. 7. TEM images for samples prepared using Cu^{2+} on BP2000, with **A)** no Hyd1, and, **B)** Hyd1 (of samples using Hyd1: Cu^{2+} ratio of 1: 500). TEM performed by Maya Landis.

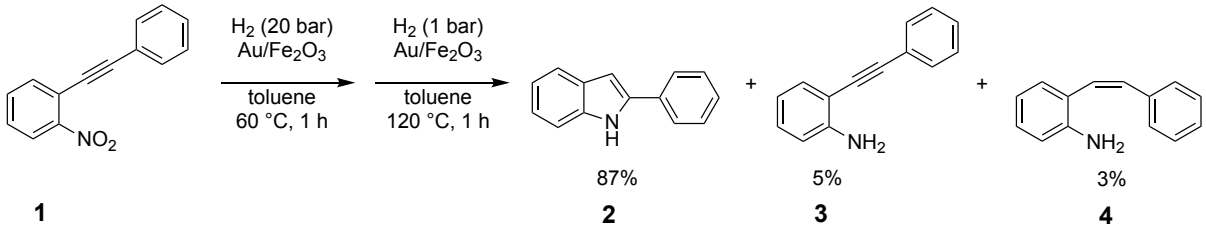
Thus, Hyd1 is likely still to be experiencing the inhibition effect of Cu^{2+} since the results were very different from the samples prepared using the same conditions but with Au^{3+}; the CVs showed there was still unreduced Cu^{2+} ions present in the sample with highest Cu concentration and there were no NPs observed during TEM.

6.3. Application of Supported Metal NPs

6.3.1. Indole Synthesis Background

Since it was shown to be possible to form supported Au NPs using Hyd1 immobilised on BP2000 under H_2, as discussed in **6.2.3**, it was desired to demonstrate their application as a catalyst in a chemical transformation. The reduction and cyclisation of 1-nitro-2-(2-phenylethynyl)benzene, **1**, to 2-phenylindole, **2**, was chosen to be investigated since it would test whether the Hyd1 enzyme and Au NPs were able to carry out separate steps of the reaction in a cascade fashion. The one-pot synthesis of indoles from (2-nitroaryl)alkynes,

including substrate **1**, was shown to be catalysed using supported Au NPs under hydrogenation conditions.[11] Indoles are a common chemical fragment of an API (active pharmaceutical ingredient) and thus their selective synthesis is highly sought.[12] The Au NP catalysed option is an attractive approach since it could allow for a selective reduction of a nitro group (over an alkyne) and is cheaper than other stoichiometric reagents such as In–HI (involving the expensive metal indium).[13] After a series of tests using different conditions with supported Au NPs, the authors reported optimised conditions, where over-reduction by-products were minimised, and high conversion was achieved using a one-pot two-step process (**Scheme 6. 1.**). The first step involved a high pressure of H_2 (20 bar), at 60 °C, to afford a high conversion to the amine intermediate (**3**), followed by a venting of the reaction vessel to 1 bar H_2 and an increase in temperature to 120 °C, to encourage the intramolecular cyclisation from amine intermediate **3** to indole **2** to occur. The reaction was carried out in toluene and the use of high pressure and 120 °C (which is above the boiling point of toluene) means that these conditions cannot be considered as "green".



Scheme 6. 1. Optimised one-pot two-step process using supported Au NP catalyst for the reduction and cyclisation of 1-nitro-2-(2-phenylethynyl)benzene, **1**, to 2-phenylindole, **2**.[11]

6.3.2. Investigating the Synthesis of Indoles using Hyd1-Au/C

Thus, it was hypothesised that Hyd1-Au/C (synthesis and characterisation discussed in **6.2.2** and **6.2.3**) could provide a route from **1** to **2** under milder conditions. As mentioned earlier Hyd1 immobilised on carbon has already been shown to reduce aromatic nitro groups to aromatic amines.[3] This was carried out in aqueous conditions and 1 bar H_2. Therefore, with the addition of Au NPs, it was speculated whether the reaction could proceed via the aromatic

amine intermediate **3** and then to indole product **2**, all under 1 bar H_2. To check whether the nitro group of **1** has a reduction potential in the range accessible by the Hyd1/C catalyst (i.e. above around -0.296 V vs. SHE which is the measured H_2 onset potential of Hyd1 at pH 6, 25 °C, 1 bar H_2),[3] a solution of **1** was added to an electrochemical cell and CV was performed (following procedure as described in **2.1.2**). This showed the reduction of **1** began before the H_2 onset potential for Hyd1: at approximately -0.167 V vs. SHE at pH 6 at 25 °C (**Figure 6. 8.**). As expected at higher pH this shifts to a lower potential: -0.217 V vs. SHE at pH 8 (**Figure 6. 9.**) which is still above the H_2 onset potential for Hyd1: approximated to -0.376 V vs. SHE (80 mV lower than pH 6).[14] This therefore shows that at both pH 6 and pH 8 the reduction of **1** is thermodynamically feasible by the oxidation of H_2 with Hyd1.

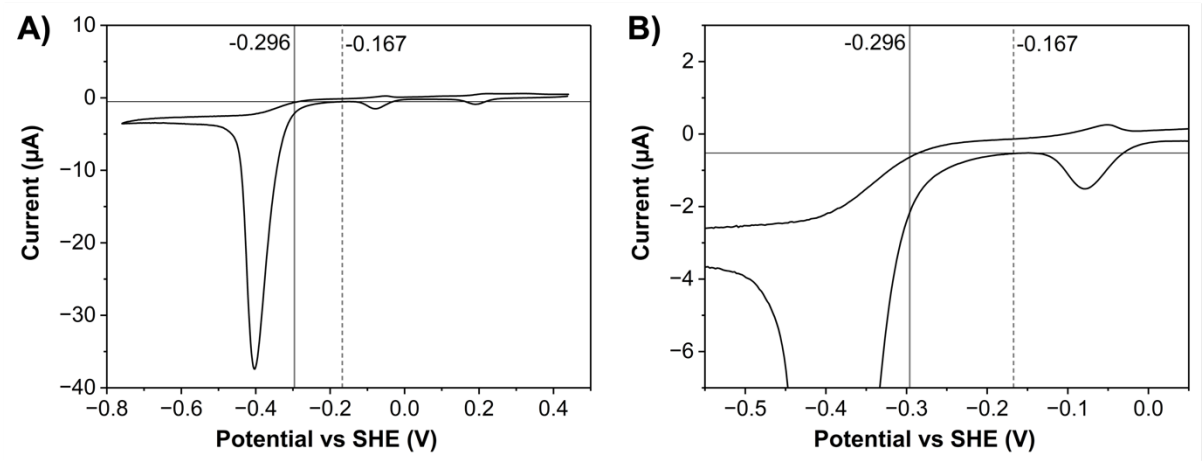


Figure 6. 8. CV of **1** at pH 6 (1 mM of **1**, in pH 6, 100 mM NaPi, 10 vol% acetonitrile). Using a graphite electrode, rotating at 3000 rpm, under a N_2 atmosphere, 25 °C, scan rate: 10 mV/s, scanning direction from high to low (and reverse). **A)** First CV scan of experiment, showing whole range measured. **B)** Close up section showing where the onset reduction potential for **1** is measured as (dashed line). Solid grey line is the measured H_2 onset potential for Hyd1/C.

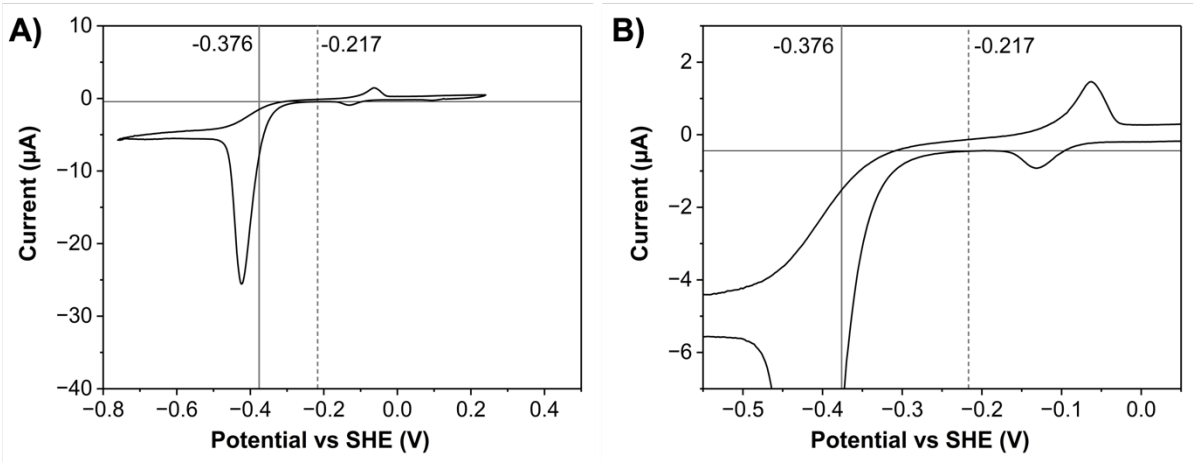


Figure 6. 9. CV of **1** at pH 8 (1 mM of **1**, in pH 8, 100 mM KPi, 10 vol% acetonitrile). Using a graphite electrode, rotating at 3000 rpm, under a N_2 atmosphere, 25 °C, scan rate: 10 mV/s, scanning direction from high to low (and reverse). **A)** First CV scan of experiment, showing whole range measured. **B)** Close up section showing where the onset reduction potential for **1** is measured as (dashed line). Solid grey line is the measured H_2 onset potential for Hyd1/C.

CVs using a stationary working electrode were also carried out for **1** in pH 6 and pH 8 solutions (**Figure 6. 10.**). Here intermediate redox features can be more easily observed after the first scan has been completed. At both pH conditions, a reversible reduction and oxidation couple can be seen at higher potential than the largest reduction peak observed in the first scan. This can be considered as corresponding to a 2-electron oxidation of hydroxylamine intermediate to nitroso and the reverse reduction. A smaller difference between the potentials for the peak centre of the oxidation and reduction indicates a greater reversibility function; however any difference around 30 mV is commonly considered to be electrochemically reversible for a two electron transfer (60/number of transferred electrons),[15] therefore at both pH 6 and 8 the nitroso to hydroxylamine reduction is reversible. Overall, this suggests that the 6-electron reduction of **1** is likely to go via the 4-electron reduction to hydroxylamine intermediate (and subsequent 2-electron reduction to amine) which can be looked out for in the ^{1}H NMR spectra of reaction samples. Due to the symmetrical shape of the reduction peaks, differing from that of a standard diffusion-controlled tailing peak, this suggests this compound has a high affinity for the electrode surface and has therefore become very quickly adsorbed to the electrode.

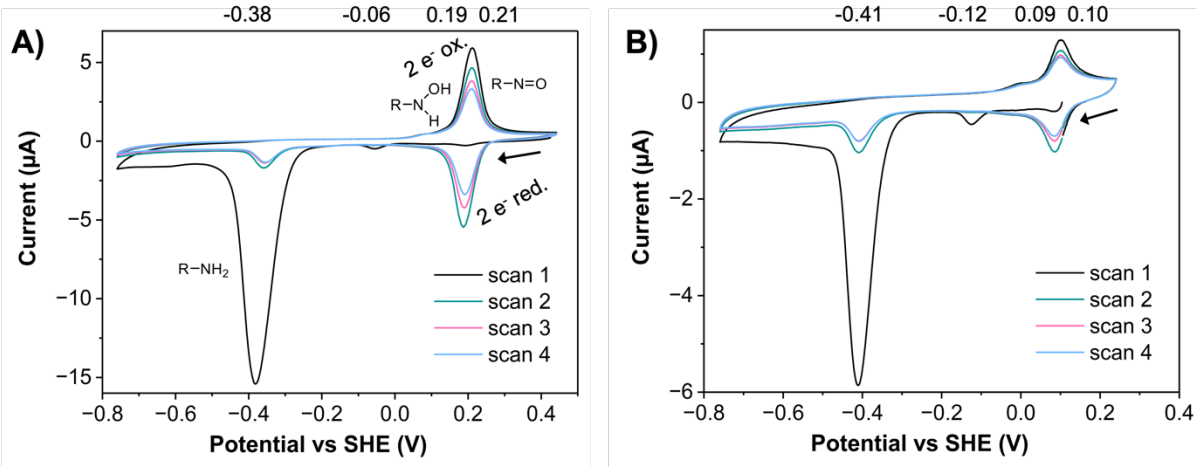


Figure 6. 10. CV of **1**, using a stationary graphite electrode, in **A)** pH 6 and **B)** pH 8 (same solutions as in **Figure 6. 8.** and **Figure 6. 9.** respectively), under a N_2 atmosphere, 25 °C, scan rate: 10 mV/s, scanning direction from high to low, as indicted by the arrow (and reverse). Numbers above graphs refer to the potential of the redox features directly below. The small reduction peak observed at -0.06 and -0.12 V vs. SHE corresponds to an unknown impurity present in the crude starting material (estimated to have 84% purity by ^{1}H NMR).

The reaction for the reduction and cyclisation of **1** to **2**, under H_2, was carried out with side-by-side reactions containing Hyd1-Au/C, Hyd1/C, Au/C and C. The substrate **1** is not soluble in water therefore the addition of a cosolvent was required: 10 vol% acetonitrile was used. Hyd1 is known to have reasonable solvent tolerance from previous studies performed in the group therefore this amount of cosolvent was not expected to significantly decrease the activity of Hyd1.[16] The first set of reactions were run in pH 8, 50 mM potassium phosphate buffer since previous work in the group had shown it was necessary to use a basic pH in order to stop an alkyne hydration side reaction (this was for the substrate 1-ethynyl-4-nitrobenzene).[3] As summarized in **Table 6. 2.**, entry 1, these reactions showed no sign of any products, with only starting material present in the ^{1}H NMR spectra (after 24 and 50 hours). Upon analysing the starting material ^{1}H NMR spectrum it was noticed that it did not appear to be 95% pure as was suggested by the supplier of the chemical. Therefore, it was wondered whether that was causing an effect on the results, so column chromatography on the starting material was carried out to attempt to increase the purity. As estimated by ^{1}H NMR, this was successful in improving the purity of the crude material from 84 to 95% (based on the peaks corresponding to organic aromatics, ignoring residual solvent). This was not accounting for any inorganic

material that may have been present; the silica column collected a layer of insoluble brown material which may have been residual metal species (from previous reaction steps). It was therefore hoped that the purified material would give an improvement on the results, so the same reaction conditions were re-tested using the purified starting material (**Table 6. 2.**, entry 2). After 24 hours at room temperature again no reaction was observed, thus the reaction vessel was heated using a hot plate set to 60 °C. Hyd1 is known to be a thermostable enzyme, with optimal activity observed at around 60 to 70 °C.[6] This increase in temperature did not change the results however. Therefore, the conditions were changed to be more similar to those used when reducing different aryl-nitro compounds with Hyd1/C to see whether this would encourage the reduction of the nitro group in **1** – pH 6, 50 mM sodium phosphate buffer – as well as an increase in the total catalyst loading (**Table 6. 2.**, entry 3). This time the ^{1}H NMR spectra of the reactions containing Hyd1/C or Hyd1-Au/C had changed after the 24-hour time point, while the controls with Au/C or C remained unchanged (**Figure 6. 11.** for ^{1}H NMR spectra). The amine product **3** was clearly identifiable in both Hyd1/C and Hyd1-Au/C reactions (using literature reference to identify corresponding NMR peaks).[11] There was also some hydroxylamine **1b** which has been shown to be an intermediate in comparable reactions[3] as well as some remaining starting material for the reaction in Hyd1-Au/C. To attempt to achieve complete conversion to the amine product **3**, or even to the cyclised indole **2**, the temperature was thereafter increased to 70 °C. After a total of 50.5 hours, there was now no starting material remaining in the reaction with Hyd1-Au/C and there were slightly higher ratios of the amine to hydroxylamine for both Hyd1/C and Hyd1-Au/C. However disappointingly there was still no sign of the indole **2**. Since the study using supported Au NPs for the successful catalysis of **1** to **2** showed that conversion to **2** increased with increasing temperature from 40 to 110 °C, it was decided to try using the product from the reaction using Hyd1/C or Hyd1-Au/C in aqueous conditions (**Table 6. 2.**, entry 3) and use toluene and 90 °C to see if those conditions would allow the Au catalysis step to occur (amine **3** to indole **2**). After 6 hours the reaction was stopped and the ^{1}H NMR spectra showed a completely different set

of peaks with no identifiable products or any of the amine (**Table 6. 2.**, entry 4). The ^{1}H NMR of the reaction sample after 24 hours of the reaction in entry 3 was rerun (this was after 6 days) and it was discovered that the amine had completely decomposed. Therefore, the amine **3** was not stable (at least in $CDCl_3$ which was used for the NMR solvent) and in hindsight the second step of the reaction (heating in toluene) should have been carried out immediately after the amine formation.

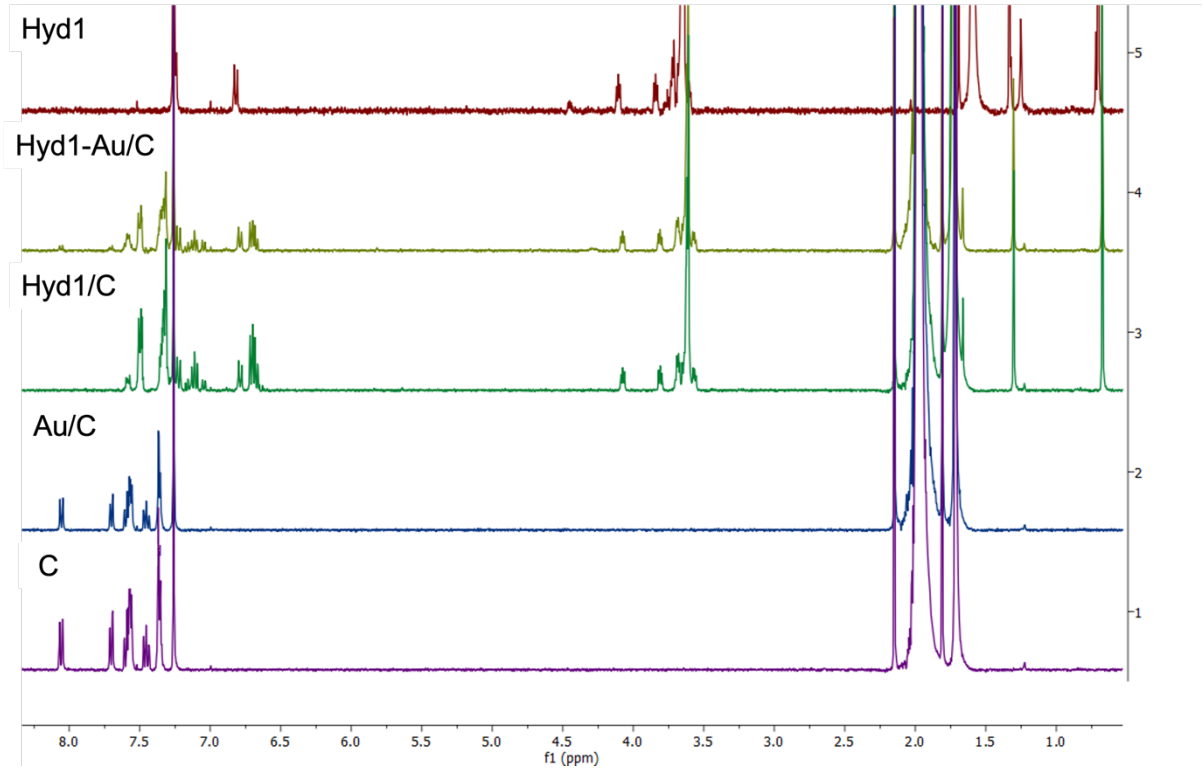


Figure 6. 11. ^{1}H NMR($CDCl_3$) spectra of Hyd1 (extracted straight into $CDCl_3$, to check for peaks corresponding to Hyd1 in the reaction samples) and reaction samples from **Table 6. 2.**, entry 3, after 24-hour timepoint.

Table 6. 2. Summary of results for reactions attempting to carry out the reduction and cyclisation of **1** to **2**, using Hyd1/C or Hyd1-Au/C.[a]

Entry	Initial conditions	Analysis after first time point[b]	Change to conditions?	Analysis after second time point[b]
1	pH 8, 50 mM KPi, room temp.	24 h: only starting material (**1**)	no	50 h: only starting material (**1**)
2	pH 8, 50 mM KPi, room temp.	24 h: only starting material (**1**)	Hot plate to 60 °C	72 h: only starting material (**1**)
3[c]	pH 6, 50 mM NaPi, room temp.	24 h: Hyd1/C, **1**: **1b**: **3** ratio of 0: 0.19: 1 Hyd1-Au/C, **1**: **1b**: **3** ratio of 0: 0.57: 1	Hot plate to 70 °C	50.5 h: Hyd1/C, **1**: **1b**: **3** ratio of 0: 0.19: 1 Hyd1-Au/C, **1**: **1b**: **3** ratio of 0: 0.20: 1
4	Entry 3 products in toluene added to new Hyd1/C and Hyd1-Au/C catalyst,[d] hot plate at 90 °C	6 h: no products identifiable as any of expected possible products[e]	n/a	n/a

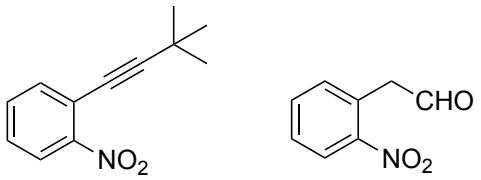
[a] Reaction procedure: Hyd1-Au/C were firstly prepared following the procedure described in **6.2.2** and for Hyd1/C emitting the addition of $HAuCl_4$ salt. Next, these were transferred to 2 mL GC vials, with small stirrer bar, and **1** was added as a solution in acetonitrile and total reaction volume was topped up to 1 mL using aqueous buffer. Caps, with smartSpatula® plastic straw pushed through the pre-slit suba seal (see **Appendix**), were added to GC vials which were then added to pressure vessel which was then filled with H_2 (filling to 2.5 bar and venting x 3, before filling to 1 bar) and put on stirring plate (set to 800 rpm). Reaction conditions: **1** (10 mM), 10 vol% acetonitrile, carbon: Hyd1 mass ratio of 40: 1, Hyd1: Au^{3+} molar ratio 1: 250, 2.64 mg Hyd1 per 1 mmol substrate, 0.6 mol% Au atom/substrate. [b] Analysis was carried out by ^{1}H NMR spectroscopy using the following steps for sample preparation: reaction mixture (480 μL) was removed, $CDCl_3$ (480 μL) was added to extract (shake/vortex), aqueous layer was removed, more $CDCl_3$ (480 μL) was added to the aqueous layer (shake/vortex), $CDCl_3$ extracts were combined, centrifuged to remove catalyst, dried using sodium sulfate, centrifuged to remove sodium sulfate and added to NMR tube. [c] Catalyst loading was increased x 4: therefore 10.56 mg Hyd1 per 1 mmol substrate, 2.4 mol% Au atom/substrate. [d] These had been prepared under the conditions used in entry 2 and subsequently centrifuged to remove aqueous layer and toluene added and repeated (centrifuge, supernatant removed, and toluene added). [e] See discussion, it was discovered that amine had decomposed before the start of the reaction. For analysis, the samples were centrifuged to remove catalyst, toluene was then removed under vacuum and residue dissolved in $CDCl_3$ for ^{1}H NMR.

There are further experiments that could be tested which may lead to the discovery of an improved process for the reduction and cyclisation of **1** to **2** (by at least minimising the use of high pressure H_2); including those described in **Table 6. 3.** which should be followed in the order of the entries. Starting with a repeat of the initial conditions with Hyd1/C to make the amine intermediate **3**, followed by extracting into toluene, adding Hyd1-Au/C and heating to 90 °C. If this does not work (entry 1), this suggest there is an issue with the activity of the Au NPs in the Hyd1-Au/C thus testing Hyd1-Au NPs, with no carbon support, for this second step (entry 2) may be useful to try since these NPs have been shown to exhibit catalytic properties (for increasing flavin reduction rate, *Chapter 5* results). If these conditions are kept as aqueous with 10 vol% acetonitrile and there is no activity with Hyd1-Au NPs, this could be due to the

insolubility of the substrate in water and its planar nature meaning it adsorbs very strongly to the carbon support (perhaps limiting its interaction with the Au NPs). Thus, another option could be to test with higher amounts of cosolvent to see if this helps with increasing the concentration of "free" substrate, that is not stuck to the carbon (entry 3). Further experiments could also be carried out with a different substrate which is less planar (e.g. 1-(3,3-dimethyl-1-butyn-1-yl)-2-nitrobenzene, **5**) and therefore may have less issues with the strong adsorption to carbon. Alternatively, an intramolecular reduction amination reaction could be tested using 2-(2-nitrophenyl)acetaldehyde, **6**, as the substrate (**Figure 6. 12.**). Additionally, the choice of the support from carbon to Fe_2O_3 which was the support used in the literature example for this reaction may be worth investigating.

Table 6. 3. Further experiments for the reduction and cyclisation of **1** to **2**.

Entry	Step 1	Step 2
1	Hyd1/C to make amine	Extract into toluene then add Hyd1-Au/C, heat to 90 °C
2	Hyd1/C to make amine	Add Hyd1-Au NPs
3	Hyd1/C or Hyd1-Au/C, using 50 vol% cosolvents (try acetonitrile, toluene)	For step 1 with Hyd1/C, then add Hyd1-Au/C or Hyd1-Au NPs



5 **6**

Figure 6. 12. Alternative substrates to test for reduction and cyclisation using Hyd1-Au/C hybrid catalyst.

6.4. References

[1] M. P. Thompson, I. Peñafiel, S. C. Cosgrove, N. J. Turner, *Organic Process Research & Development* **2019**, *23*, 9-18.

[2] R. A. Sheldon, S. van Pelt, *Chem. Soc. Rev.* **2013**, *42*, 6223-6235.
[3] D. Sokolova, T. C. Lurshay, J. S. Rowbotham, G. Stonadge, H. A. Reeve, S. E. Cleary, T. Sudmeier, K. A. Vincent, *ChemRxiv preprint* **2024**.
[4] A. Goel, J. B. Howard, J. B. Vander Sande, *Carbon* **2004**, *42*, 1907-1915.
[5] A. Macías-García, M. A. Díaz-Díez, M. Alfaro-Domínguez, J. P. Carrasco-Amador, *Heliyon* **2020**, *6*, e04024.
[6] S. Joseph Srinivasan, S. E. Cleary, M. A. Ramirez, H. A. Reeve, C. E. Paul, K. A. Vincent, *Angew. Chem. Int. Ed.* **2021**, *60*, 13824-13828.
[7] H. A. Reeve, P. A. Ash, H. Park, A. Huang, M. Posidias, C. Tomlinson, O. Lenz, K. A. Vincent, *Biochem. J* **2017**, *474*, 215-230.
[8] L. D. Burke, P. F. Nugent, *Gold Bulletin* **1997**, *30*, 43-53.
[9] V. M. Fernandez, M. L. Rua, P. Reyes, R. Cammack, E. C. Hatchikian, *Eur. J. Biochem.* **1989**, *185*, 449-454.
[10] S. Mourdikoudis, R. M. Pallares, N. T. K. Thanh, *Nanoscale* **2018**, *10*, 12871-12934.
[11] Y. Yamane, X. Liu, A. Hamasaki, T. Ishida, M. Haruta, T. Yokoyama, M. Tokunaga, *Org. Lett.* **2009**, *11*, 5162-5165.
[12] W.-M. Dai, L.-P. Sun, D.-S. Guo, *Tetrahedron Lett.* **2002**, *43*, 7699-7702.
[13] J. S. Kim, J. H. Han, J. J. Lee, Y. M. Jun, B. M. Lee, B. H. Kim, *Tetrahedron Lett.* **2008**, *49*, 3733-3738.
[14] B. J. Murphy, F. Sargent, F. A. Armstrong, *Energy & Environmental Science* **2014**, *7*, 1426-1433.
[15] C. Sandford, M. A. Edwards, K. J. Klunder, D. P. Hickey, M. Li, K. Barman, M. S. Sigman, H. S. White, S. D. Minteer, *Chem. Sci.* **2019**, *10*, 6404-6422.
[16] M. A. Ramirez, S. Joseph Srinivasan, S. E. Cleary, P. M. T. Todd, H. A. Reeve, K. A. Vincent, *Frontiers in Catalysis* **2022**, *2*.

Chapter 7. Conclusions and Future Directions

This thesis sought to investigate the synthesis of metal nanoparticles using isolated enzymes and investigating the properties of resulting metal NP-enzyme hybrids, particularly for catalysis applications. This was firstly investigated (as described in *Chapter 3*) using a NAD^+ reductase (NRase) enzyme moiety that originated from a *soluble hydrogenase,* but which was expressed without the hydrogenase subunit (known to have instability issues as an isolated enzyme), in *E. coli*. This stable enzyme moiety was then supplied with its natural reduced cofactor, NADH, in the presence of Au^{3+} salts. Since the NAD^+ reductase subunit, found in the whole *soluble hydrogenase* protein, relies on receiving electrons from H_2 oxidation, occurring at the hydrogenase subunit, there is a chain of Fe-S clusters which links these subunits and conveniently, in the isolated NRase there is a Fe-S cluster near the surface of the enzyme moiety. This therefore allows for electrons from NADH oxidation to be guided to the surface of the enzyme (away from the active site) where Au^{3+} reduction can then occur, leading to the synthesis of Au NPs, stabilised by the enzyme through electrostatics. This proposed mechanism was evidenced by the following observations: the NPs were uniform in size/shape, the size was dependent on the concentration of enzyme used, NPs were not formed using NADPH (which the enzyme has no activity for) instead of NADH, and the enzyme activity remained after the NP synthesis. This was different from other examples of using isolated enzymes in which either the active site is not actively involved in the NP synthesis and instead surface functional groups are the reducing agents or the metal reduction is carried out directly at the active site resulting in a loss of enzyme activity.[1-2] Cheaper, synthetic cofactors (BNAH and AmNAH) were also tested using this method in place of NADH. These were accepted by the NRase and formed similarly well-controlled Au NPs.

The NRase, NADH system was extended to prepare core-shell NPs by introducing Pt^{4+} salts (and more NADH) after the initial formation of NRase-Au NPs hybrids. These resulting NRase-Au@Pt NPs were tested in a NAD^+ reduction reaction under H_2. Their selectivity for 1,4-NADH product (under conditions with a high enough ratio of NRase to metal) showed that there was electronic contact between the metal NP (where H_2 oxidation occurred and where unselective

NAD^+ reduction was possible) and the NAD^+ reductase (where selective NAD^+ reduction occurred). Finally, this system was tested for its compatibility as a H_2-driven NADH cofactor recycling system for an alcohol dehydrogenase enzyme. This demonstrated good compatibility with no dechlorination observed for the enantioselective ketone reduction of 4'-chloroacetophenone substrate, with the (*S*)-alcohol product obtained in ≥ 99% e.e.

Chapter 4 then moved onto discuss results unrelated to metal NP synthesis, but which laid the groundwork for the next chapter. Here the use of riboflavin, a significantly cheaper flavin than FMN and FAD which are commonly found as a cofactor in biocatalysis applications, was demonstrated to be accepted by commercial ene-reductase enzymes and coupled with a H_2-driven system for the reduction of riboflavin. This involved utilising the high H_2-oxidation activity of Hyd1, an O_2-tolerant hydrogenase from *E. coli*, as had already been shown for FMN and FAD reduction.[3]

Chapter 5 then used a similar principle to *Chapter 4* where the H_2-oxidation activity of Hyd1 was used to reduce Au^{3+} to Au^0. Analogous to using NRase, Fe-S clusters within the enzyme are employed to transfer electrons away from the site of H_2 oxidation to the surface of the enzyme. Thus, again, well-controlled, stabilised Au NPs are formed in the presence of an isolated enzyme. An advantage of this system is the use of H_2, at 1 bar, as the electron source for the metal reduction, allow for a waste-free synthesis procedure. Due to the relative inertness of Au (compared to other metals such as Pt or Pd) there are not many examples of using low pressure H_2 to synthesise Au NPs. The Au NP synthesis using Hyd1 and H_2 was also tested in the presence of riboflavin where it was discovered that the Au NP synthesis rate was increased by the presence of riboflavin and subsequently, after the NP synthesis, an increased rate of riboflavin reduction was observed. This rate enhancement also translated to a faster rate of alkene reduction when coupling the H_2-driven riboflavin reduction using the Hyd1-Au NP biohybrid catalyst with ene-reductase.

Chapter 6 demonstrated that using an isolated enzyme to prepare metal NPs could also be extended to preparing supported metal NPs. This was shown by first adsorbing Hyd1 onto

carbon particles (BP2000) and then introducing Au^{3+} and H_2. Small Au NPs (< 10 nm) were observed, by TEM, to form across the support and shown to have good stability (tested by analysing before and after sonicating by CV). These results showed promising signs that a hybrid chemo-bio catalyst could be prepared under facile and mild conditions and could subsequently be used for a catalysis application where a chemical transformation may require both enzyme and supported metal NPs. Initial tests aiming to demonstrate the application of the hybrid catalyst in a cascade style reaction were attempted for the synthesis of an indole from a nitroaryl alkyne. These were unsuccessful at forming the indole however the amine intermediate (from nitro reduction) was observed. The amine was not observed in any of the controls, showing that the Hyd1 present on the carbon was still active after the NP synthesis (previous studies had shown this nitro reduction activity was only observed when Hyd1 was immobilised onto carbon).[4] Further tests are therefore required to find conditions where the Au NPs were active.

The results detailed in this thesis open up many other possible areas, involving metal NPs and enzymes, worth investigating. Most discernible would be to test other hydrogenase and metal combinations. For example, another [NiFe] hydrogenase "Hyd2" might allow for metals with lower reduction potentials to be reduced; Hyd1 is known to have a H_2 oxidation onset potential of -0.36 $\pm$ 0.01 V vs SHE (pH 7, 37 °C, 1 bar H_2)[5] while Hyd2 has no over-potential therefore has a H_2 oxidation onset potential at the thermodynamic $2H^+/H_2$ couple, -0.43 V vs SHE at the same conditions. For other metals to test, Cu(II)Cl_2 (Cu^{2+}: +0.3419 V) was already tested with Hyd1 on carbon and there was some evidence of Cu^0 from CV but no NPs were seen in TEM. Since Cu^{2+} is known to be a hydrogenase inhibitor[6] it explains why only a small amount of reduction can occur before Hyd1 becomes inactive hence stopping the formation of large NPs. For Cu^{2+} it may be interesting to test the NRase, NADH system to see if Cu^{2+} also inhibits NRase or if Cu NPs can be formed. Cu NPs have shown promise in CO_2 reduction as a cheaper source of metal.[7] Other metals not tested but which could be of interest due to their potential applications are shown in **Table 7. 1.**

Table 7. 1. Other metals not tested in this thesis, but which could be tested as part of future work.

Entry	Metal	Reduction Potential (vs SHE)	Application of Metal NPs	Possible Issues
1	Mo	Mo^{3+}: -0.2 V	medical applications, as an alternative source for ^{99}Mo radioisotope[8]	Most Mo salts are however insoluble in water therefore a cosolvent would be required
2	Ni	Ni^{2+}: -0.257 V	magnetic and antibacterial properties[9]	-
3	Co	Co^{2+}: -0.277 V	magnetic, used for targeted drug delivery[10]	-
4	Ru	Ru^{2+}: +0.45 V	hydrogen evolution reaction catalysts, cheaper than Pt and shown to give higher catalytic activity[11]	-
5	Fe	Fe^{3+}: -0.037 V	non-toxic, magnetic therefore possible application in drug delivery[12]	Usually need to be kept anaerobically to keep as Fe^0 NPs, however, does Hyd1 prevent oxidation?

This system could also be extended to the other types of support such as nitrogen-doped carbon nanotubes which may give increased catalytic properties or to Fe_2O_3 for useful magnetic properties.

Other unexplored areas include testing the NRase-metal NP or hydrogenase-metal NP hybrids for photocatalytic applications where the surface plasmon of the metal NP can be excited. For a hydrogen generation application, the Hyd1-Au NPs could be tested by illuminating in the presence of a sacrificial electron source (triethanolamine). A similar study has been performed which used a cysteine-modified Hyd1 variant to covalently bound a silver nanocluster, this study showed the presence of TiO_2 and/or graphitic carbon nitride were also essential to observe significant H_2 generation with the overall mechanism remaining unclear to the authors.[13]

The scope of the H_2-driven riboflavin reduction could also be extended by testing if riboflavin is accepted by nitroreductase enzymes and if the same increase in rate when using Hyd1-Au NPs compared to Hyd1 alone is observed.

In summary this thesis has demonstrated the biocatalytic approach for metal NP synthesis using either a NAD^+ reductase or hydrogenase enzyme, under mild conditions. In the process

of characterising the resulting metal NP hybrids, the enzyme remained active after the NP synthesis and thus catalytic behaviour was shown from both enzyme and metal NP components.

References

[1] A. Rangnekar, T. K. Sarma, A. K. Singh, J. Deka, A. Ramesh, A. Chattopadhyay, *Langmuir* **2007**, *23*, 5700-5706.
[2] D. Scott, M. Toney, M. Muzikár, *J. Am. Chem. Soc.* **2008**, *130*, 865-874.
[3] S. Joseph Srinivasan, S. E. Cleary, M. A. Ramirez, H. A. Reeve, C. E. Paul, K. A. Vincent, *Angew. Chem. Int. Ed.* **2021**, *60*, 13824-13828.
[4] D. Sokolova, T. C. Lurshay, J. S. Rowbotham, G. Stonadge, H. A. Reeve, S. E. Cleary, T. Sudmeier, K. A. Vincent, *ChemRxiv preprint* **2024**.
[5] B. J. Murphy, F. Sargent, F. A. Armstrong, *Energy & Environmental Science* **2014**, *7*, 1426-1433.
[6] R. M. Fitz, H. Cypionka, *Arch. Microbiol.* **1991**, *155*, 444-448.
[7] S. Dongare, N. Singh, H. Bhunia, *Appl. Surf. Sci.* **2021**, *537*, 148020.
[8] Á. Arnosa-Prieto, M. A. González-Gómez, P. García-Acevedo, L. de Castro-Alves, Y. Piñeiro, J. Rivas, *Materials Today Chemistry* **2024**, *35*, 101854.
[9] M. R. Ahghari, V. Soltaninejad, A. Maleki, *Scientific Reports* **2020**, *10*, 12627.
[10] A. A. Vodyashkin, P. Kezimana, F. Y. Prokonov, I. A. Vasilenko, Y. M. Stanishevskiy, in *Crystals, Vol. 12*, **2022**.
[11] J. Wang, Z. Wei, S. Mao, H. Li, Y. Wang, *Energy & Environmental Science* **2018**, *11*, 800-806.
[12] F. Batool, M. S. Iqbal, S.-U.-D. Khan, J. Khan, B. Ahmed, M. I. Qadir, *Scientific Reports* **2021**, *11*, 22132.
[13] L. Zhang, G. Morello, S. B. Carr, F. A. Armstrong, *J. Am. Chem. Soc.* **2020**, *142*, 12699-12707.

Appendix: Reaction Set-up

GC vial set-up for small-scale heterogeneous reactions (to go inside pressure vessel filled with H_2)



Left side-on view and right top-view: of 2 mL GC vial with small stirrer bar inside, 1 mL reaction solution (photo is just water) and smartSpatula® (by LevGo, Catalog No. 17231B) cut into approx. 1 cm length piece and used to push through pre-slit GC seal (to keep reaction exposed to H_2 and minimise experimental variability).